ANALYSIS OF HEAVY ION RADIATION DAMAGE IN TITANIUM AND TITANIUM ALLOYS

By

Aida Amroussia

A DISSERTATION

Submitted to
Michigan State University
in partial fulfillment of the requirements
for the degree of

Materials Science and Engineering – Doctor of Philosophy

2020

ABSTRACT

ANALYSIS OF HEAVY ION RADIATION DAMAGE IN TITANIUM AND TITANIUM ALLOYS

By

Aida Amroussia

Titanium (Ti) alloys are widely used in the biomedical, aerospace and automobile industry thanks to their high specific strength, excellent fatigue and creep properties, corrosion resistance, high workability, good weldability as well as their commercial availability. Ti-alloys are also currently investigated for several applications in the nuclear industry and especially as a structural material for the beam dump for the Facility for Rare Isotope Beams (FRIB) at Michigan State University due to their low activation in radioactive environments. This dissertation investigates the effect of heavy ion radiation damage on the microstructure and the nano-hardness in Ti and Ti alloys, namely commercially pure (CP) Ti and a two-phase α+β Ti-6Al-4V alloy processed through two different methods: conventional powder metallurgy rolling (PM) and additive manufacturing (AM).

The microstructures of the as-received materials are characterized using scanning electron microscopy (SEM) and electron backscattered diffraction (EBSD). Nano-indentation was performed on samples irradiated *ex situ* with Ar ion beams at 30 ℃ and 350 ℃ to investigate the change in mechanical properties in the three materials. Additionally, a study of the evolution of radiation damage in CP Ti irradiated *in situ* with krypton (Kr) ion beams was performed at the IVEM-Tandem facility at Argonne National Laboratory, USA. The results of the observations of the nucleation and growth of dislocation loops using transmission electron microscopy (TEM) are reported.

Radiation hardening was observed in all materials irradiated *ex situ* at 30 ℃ and 360 ℃. This hardening was insensitive to electronic excitation and was caused by ballistic effects. A strong dose dependence was observed mainly for the PM α+β Ti-alloy. The resistance to radiation hardening in the AM Ti-alloy was higher than that for the PM rolled alloy due to the significant α-phase grain refinement.

The current study is the first to quantify the radiation-induced dislocation loop evolution at different temperatures and doses in Ti and AM Ti-6Al-4V (wt.%). The primary mechanism of loop growth was coalescence and their size increased proportionally with the irradiation dose. *In situ* TEM irradiation observation shows that c-component loops were only observed after reaching a threshold incubation dose (TID). In CP Ti, these loops nucleated at much lower doses than Zr, and the TID decreased with increasing temperature: 1.4 dpa, 0.6 dpa and 0.24 dpa for irradiation temperatures of 30 ℃, 360 ℃ and 430 ℃, respectively. The TID for AM Ti-6Al-4V (wt.%) at 360 ℃ was lower than for CP Ti, confirming previous observations where alloying elements assisted c-component loop nucleation. The dispersed barrier hardening model is used to analyze structure-mechanics relationships after irradiation in CP Ti. A good agreement between the experimental measurements of the hardening in irradiated CP Ti and the calculated contributions from dislocation loops is found.

Through this work, an improved understanding of the influence of radiation-induced dislocation loops on the mechanical properties, and in particular, the hardness of Ti alloys as a function of the irradiation conditions and the alloy microstructure is gained. These insights can further the development of radiation-resistant Ti-alloys for use in radioactive environments.

وَمَا زال فِي الدَّرب دربٌ .وما زال في الدرب مُتّسعٌ للرَّحيلْ
محمود درويش

ACKNOWLEDGMENTS

I want to express my sincere gratitude to those who supported me academically and personally in the past few years. First, I would like to thank my advisor, Prof. Carl Boehlert, for his support and guidance during the different research stages and for helping me become a better technical writer. I would also like to acknowledge the invaluable help I received from my committee members Dr. Frederique Pellemoine, Prof. David S. Grummon and Prof. Thomas Bieler. I feel incredibly fortunate to have started my Ph.D. journey with an internship with Dr. Pellemoine, who continuously supported and believed in me. I am also thankful to Prof. Grummon for his help in structuring my ideas and developing my technical writing skills. I want to express my deep gratitude for Prof. Wolfgang Mittig, who, while not in my committee, has been an invaluable source of inspiration, support and wisdom.

I would like to also thank the members of the metal group, professors and students who have helped me grow as a researcher. I want to especially express my deep thanks to Ms. Uche Okeke whose friendship has been an unfailing source of encouragement. I also would like to thank Dr. Per Askeland and Dr. Ed Drown for their help with instruments at The Composite Materials and Structures Center, MSU. I want to recognize the valuable help in operating TEMs that I received from Dr. Alicia Withrow and Dr. Xudong Fan from The Center for Advanced Microscopy, MSU.

I would like to acknowledge that this work was partially supported by the U.S. Department of Energy, Office of Science under Cooperative Agreement DE-SC0000661. This work was also supported by Michigan State University under the Strategic Partnership Grant "FRIB - Materials in Extreme Environments". The *in situ* TEM irradiations at the Intermediate

Voltage Electron Microscopy (IVEM)-Tandem Facility, Argonne National Laboratory, IL, USA, and post-irradiation characterization at Oak Ridge National Laboratory (ORNL), TN, USA were supported by the U.S. Department of Energy, Office of Nuclear Energy under DOE Idaho Operations Office Contract DE-AC07- 051D14517 as part of a Nuclear Science User Facilities experiment. The use of the Center for Nanoscale Materials (CNM), an Office of Science user facility, was supported by the U.S. Department of Energy under Contract No. DE-AC02-06CH11357.

This work would not have been possible without the valuable collaborations we have established over the years. I would like to thank our collaborators from GANIL-CIMAP, France, Dr. Isabelle Monet, Dr. Clara Grygiel and Dr. Florent Durantel for their assistance during irradiation experiments and valuable contributions later on through discussions. I am also thankful to our collaborators at the Notre Dame University, ID, USA, Prof. Tan Ahn, Prof. Daniel Robertson and Prof. Edward Stech, for helping us perform part of our *ex situ* irradiation experiments at their facility. Next, I would like to thank the staff members at the IVEM-Tandem Facility, Dr. Memei Li, Dr. Mark Kirk, Mr. Pete Baldo, Mr. Ed Ryan, Dr. Jing Hu and Dr. Wei-Ying Chen for their support during *in situ* TEM experiments. I would like to acknowledge the help of Dr. Haihua Liu from the CNM for his help during the post-irradiation characterization. I would also like to thank Dr. Keith Leonard and Dr. Kurt Terrani for offering me excellent learning opportunities through the Nuclear Engineering Science Laboratory Synthesis (NESLS) program at ORNL. I would like to express my gratitude to all researchers and staff at ORNL for their valuable help and advice during my visits.

I would not have survived the Ph. D process without the emotional support of the many dear friends I have in Tunisia, France and the US. Our friendships nourished my soul and helped

me grow tremendously. I am forever grateful that our paths crossed.

Finally, my deepest gratitude goes to my family. Your unwavering support over the years and your unconditional love have always encouraged and inspired me. Yemna, Ammar, Nada and Maha, this Ph. D. is dedicated to you.

TABLE OF CONTENTS

LIST OF TABLES

LIST OF FIGURES

KEY TO SYMBOLS AND ABREVIATIONS

a	Hexagonal lattice parameter in the basal plane
<a> loops	Dislocation loops in prismatic planes
b	Burgers Vector
Al	Aluminum
AM	Additive manufacturing
Ar	Argon
ASTM	American society for testing and materials
b	Dislocation Burgers vector
BCC	Body center cubic
B.D.	Beam dump
BF	Bright field
BSE	Backscattered electron
c	Hexagonal lattice parameter normal to the basal plan
c- component loops	Dislocation loops in basal planes
CP	Commercially pure
Cu	Copper
DAD	Diffusional anisotropy difference
DBH	Dispersed Barrier Hardening
DED	Direct Energy Deposition
DF	Dark field
dpa	Displacements per atom
EBM	Electron Beam Melted
EBSD	Electron backscattered diffraction

EDS	Energy Dispersive Spectroscopy
Fe	Iron
FIB	Focused Ion Beams
Fiji	Fiji Is Just ImageJ
g	Diffraction g vector
GB	Grain boundary
GND	Geometrially necessary dislocation
hcp	Hexagonal closed-packed
HIP	Hot isostatic pressing
H_{irr}	Average hardness of irradiated material (GPa)
$H_{non\ irr}$	Average hardness of unirradiated material (GPa)
$\Delta Hardness$	Difference between average hardness measurements (GPa)
IPF	Inverse pole figure
Kr	Krypton
Ni	Nickel
O	Oxygen
PKA	Primary knock-on atom
RIS	Radiation Induced Segregation
RT	Room temperature
SE	Secondary electron
s_{error}	Statistical error calculated for nanoindentation hardness measurements
s_{eDiff}	Statistical error calculated for $\Delta Hardness$ measurements
SEM	Scanning electron microscopy
SIA	Single Interstitial Atom
SiC	Silicon carbide

SLM	Selective Laser Melted
Sn	Tin
SPP	Secondary Phase Precipitates
STEM	Scanning transmission electron microscopy
T	Temperature
T_d	Threshold displacement energy
TEM	Transmission electron microscopy
Ti	Titanium
TID	Threshold Incubation Dose
T_{irr}	Irradiation Temperature
V	Vanadium
wt.%	Weight percent
YS	Yield strength
Zr	Zirconium
α	Hexagonal close packed phase
β	Body center cubic phase
ω	Hexagonal phase
σ	The standard deviation for the nanoindentation measurements
$\Delta\sigma_y$	The change in yield stress as a result of irradaition
θ_B	Bragg's angle
λ	Wavelength
τ	Orowen Shear stress
μ	Material's shear modulus

CHAPTER 1
INTRODUCTION

1.1. MOTIVATION

Titanium alloys are widely used in the biomedical, aerospace and automobile industry due to their high specific strength, excellent fatigue and creep properties, corrosion resistance, good workability and weldability, as well as their commercial availability. Ti-alloys are also attractive for nuclear applications thanks to their compatibility with coolants (lithium, helium, water) and low activation in radioactive environments [1]. The low activation of Ti alloys present significant advantages for low-level waste management, reactor exploitation and decommissioning. As a result, Ti-alloys and especially Ti-6Al-4V (wt.%) [*] are currently considered for several applications in the nuclear industry, including:

- Metal canisters for geological disposal facilities to contain used nuclear fuel or high-level radioactive waste [2].
- Ti-6Al-4V is a candidate metal matrix for targeted composite materials for the Next Generation Nuclear Reactors [3].
- Flexible support for blanket attachments in ITER fusion reactor [4, 5].

Ti-6Al-4V is also the selected structural material for the Facility for Rare Isotope Beams (FRIB) beam dump at Michigan State University [6]. The FRIB is a new generation accelerator with high power heavy ion beams. It will provide primary beams from oxygen (O) to uranium (U) with energies of 200 MeV/u for heavy-ion beams and higher energies for lighter beams [7, 8]. FRIB will allow unique investigations and discoveries of properties of rare isotopes in order

[*] From this point forward, all alloy compositions are given in weight percent.

to advance nuclear astrophysics and fundamental studies. The applications of these discoveries can have a broad range of impacts on areas including medicine with the harvesting of radioisotopes [9], homeland security, and industry [10].

In the FRIB, the accelerated primary beam hits a graphite target to generate a beam of interest containing the isotopes that will be analyzed by nuclear physicists. The remaining beam, constituting a significant portion of the unreacted primary beam, will be "stopped" and absorbed in a beam dump (B.D.), which is one of the critical components of the accelerator. The selected design for the B.D. (see Figure 1) is a rotating water-filled drum with the following dimensions: 0.5 mm wall thickness and 70 cm diameter. The shape of the drum was designed to optimize water flow and minimize the temperature of the shell. The widely used Ti-6Al-4V alloy was selected as the structural material for the beam dump and additive manufacturing (AM) is the selected method to manufacture the drum's complex shape along with its thin wall [11]. The B.D. faces several materials engineering challenges, such as corrosion, cavitation erosion and radiation damage. The expected accumulated dose over one year is 7 dpa and the Ti-alloy shell must be maintained at a temperature below 150 ℃ [7].

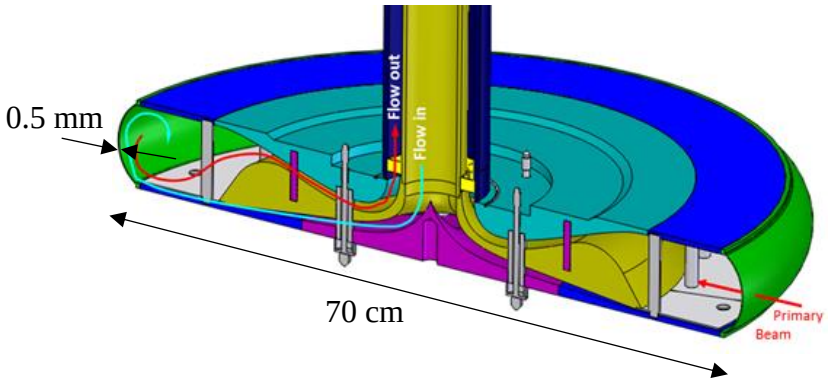

Figure 1. FRIB primary beam dump concept adapted from [7].

This dissertation research was motivated by the need to investigate the effect of the low temperature, high dose irradiation on the mechanical properties of AM Ti-6Al-4V. Few studies

have investigated the radiation damage in some conventionally manufactured Ti-alloys, with neutrons [12], protons [13, 14] and ions [11, 15, 16, 17] for doses lower than 7 dpa. A dual dose and temperature dependence was observed on the mechanical properties of irradiated Ti-6Al-4V; samples irradiated at higher temperatures exhibited higher hardening at higher doses.

In all previous studies, only the final irradiated microstructure at a certain dose level was investigated, preventing a deeper understanding of the evolution of the damage structures at different doses and temperatures. *In situ* Transmission Electron Microscopy (TEM) irradiation offers the unique capability to investigate the evolution of radiation damage through continual imaging and observation, and allows for quantitative and qualitative microstructural studies [18, 19]. *In situ* TEM irradiation studies were able to image the dislocation loop evolution in zirconium and its alloys at different doses and their interactions [20, 21]. The current work focuses on the nucleation of radiation-induced dislocation loops and their accumulation at higher doses [22, 23].

The mechanical properties of Ti-6Al-4V are highly dependent on thermomechanical processing [24-26]. Thermomechanical processing influences the grain size and phase compositions (i.e., the ratio of α to β compositions and contents). Improving the resistance of materials to radiation damage has been the subject of a few studies that focused on the effect of grain boundaries and grain size. A higher density of grain boundaries, such as in nanocrystalline materials, resulted in a higher radiation resistance [27-30]. Additionally, the effect of the grain size on irradiation-induced void formation was investigated in copper [31] and steel [32]. To investigate grain size effect in Ti alloys, the current study proposes to investigate the radiation damage in Ti-6Al-4V processed through powder metallurgy (PM) rolling ,wich produces a microstructure containing predominantly equiaxed or globular grains, and direct metal laser

sintering, an AM technique which produces samples with lamellar microstructure. Thus, this study enables not only the evaluation of the effect of alloy content (i.e. commercially pure (CP) Ti versus Ti-6Al-4V) but also processing/microstructure (i.e. equaixed versus lamellar) on ion radiation damage.

In summary, the primary objective of this dissertation research is to provide a deeper understanding of structure–mechanical behavior relationships in ion-irradiated Ti and Ti-6Al-4V by combining nanoindentation testing and TEM characterization. To that end, a microstructural study, providing both quantitative (defect formation, defect densities) and qualitative (defect interaction, defect growth) data and its analysis was performed.

1.2. WORK PERFORMED AND DISSERTATION STRUCTURE

This dissertation investigates the effect of heavy ion radiation damage on the microstructure and the nano-hardness in three materials, namely fully-α CP Ti and the two-phase α+β Ti-6Al-4V alloy processed through PM rolling and AM.

In Chapter 2, background information on Ti and Ti alloys is presented, including the presentation of the crystal structure, alloy descriptions, and different microstructures of the studied materials. A review of the current understanding of the radiation damage in metals, and more specifically, in Ti and Ti alloys is also provided.

In Chapter 3, the materials and experimental procedures used in this work are described. The experimental conditions for *in situ* and *ex situ* irradiations are presented. The details of the TEM specimen preparation and the characterization methods are also included. Finally, the nanoindentation testing method and the dispersed barrier hardening model, used to clarify structure-mechanics relationships, are presented.

In Chapter 4, the results from the as-received microstructure characterization, the nanoindentation experiments, and the *in situ* TEM irradiation experiments are provided. For each material, the grain size and texture were characterized using scanning electron microscopy (SEM) and electron backscattered diffraction (EBSD). Nano-indentation was performed on samples irradiated *ex situ* with Ar beams to investigate the change in mechanical properties in the three materials. The radiation hardening was determined at 30 ℃ and 350 ℃ from the nano-hardness results. To understand the effect of radiation damage structures on the radiation hardening, a study of the evolution of the radiation damage in CP Ti irradiated *in situ* with Kr ion beams was performed at the IVEM-Tandem facility at Argonne National Laboratory. The irradiation temperatures in these experiments were 30 ℃, 360 ℃ and 430 ℃ and results of the observations of the nucleation and growth of <a> and c-component dislocation loops are reported.

In Chapter 5, a discussion of the radiation damage in Ti and Ti alloys is presented. The results of the TEM investigations were compared to previously published results. The dispersed barrier hardening model was used to analyze structure-mechanics relationships after irradiation for CP Ti. A good agreement between experimental measurements of the hardening in irradiated CP Ti and the calculated contributions from dislocation loops was found. The barrier strength factors of <a> and c-component dislocation loops were validated as equal to 0.15 and 0.02 (unitless) respectively confirming that <a> loops act as strong barriers to dislocation motion in ion irradiated Ti [33]. Finally, the effect of the composition and microstructure (grain size and morphology) on the radiation resistance among the three materials is examined. The irradiation dose and temperature dependence in hardening was analyzed for the PM Ti-6Al-4V. The effect of the initial microstructure on the resistance to radiation-induced hardening was also

investigated using low-temperature irradiation with a 4 MeV Ar ion beam in the AM and PM alloy. The significant grain refinement in the AM alloy enhanced its radiation resistance.

In Chapter 6, conclusions and recommendations for future work are presented.

CHAPTER 2
LITERATURE REVIEW

In this chapter, background information on Ti and the studied Ti alloys are provided. A literature review of the current understanding of the radiation damage mechanisms in metals, hexagonal close-packed (hcp) materials, and the investigated Ti alloys is also included.

2.1. TITANIUM AND TITANIUM ALLOYS

Pure Ti is subject to an allotropic transformation from a hexagonal close-packed crystal structure, called the α-phase, to a body-centered-cubic bcc crystal structure, called the β-phase, at the β-transus temperature [34] (882 ^{o}C for pure Ti and 910 ^{o}C for CP Ti [35]). It can also exhibit a non-equilibrium hexagonal ω-phase [36]. The crystal lattice parameters for each of these phases are presented in Table 1.

Table 1. Crystal lattice parameters for the different phases in pure Ti [35].

Phase	Crystal lattice parameters
α (hcp)	a = 0.295 nm, c = 0.468 nm at RT
β (bcc)	a = 0.332 nm at 900 °C
ω (h)	a = 0.2813 nm, c=0.4625 nm

The transformation of the metastable β phase to the stable α phase is characterized by the following orientation relationship: the close-packed planes $\{0001\}_{\alpha}$ / $\{110\}_{\beta}$ and the close-packed directions $\langle 11\bar{2}0\rangle_{\alpha}/\langle 111\rangle_{\beta}$ are parallel [37, 38] .

Depending on the alloying elements, either the α or β phase, or both, can be retained and stabilized in Ti-alloys. The elements that either maintain or increase the equilibrium temperature

range of the α phase-field are called α-stabilizers, such as aluminum (Al). The elements that either maintain or increase the equilibrium temperature range of the β phase field are called β-stabilizers. The most common β-stabilizers are vanadium (V), iron (Fe), and molybdenum (Mo). Other alloying elements are neutral, such as zirconium (Zr) and tin (Sn). Depending on the retained phase or phases, Ti alloys are classified as either α, β and α+β alloys [34].

A three-dimensional phase diagram of Ti, with Al and V alloying additions, is presented in Figure 2. The alloys that are investigated in the current work are based on Ti-6Al-4V, and were processed using conventional PM rolling and AM techniques. Throughout this dissertation, ASTM (American society for testing and materials) grades for three Ti alloys are used and their definition is given in Table 2.

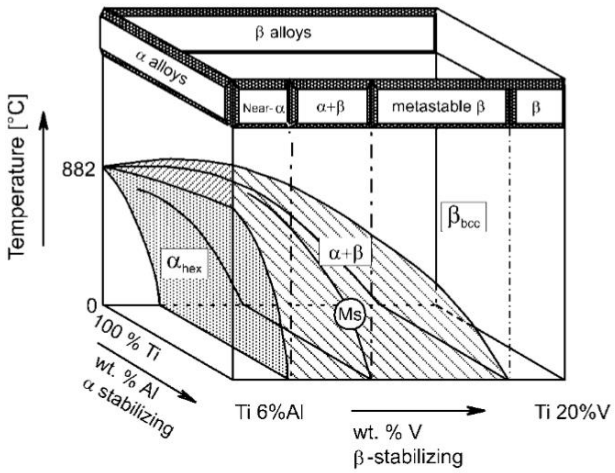

Figure 2. Three-dimensional phase diagram to classify Ti alloys containing V and Al (reproduced from [37]).

Table 2. Chemical composition ranges for some relevant ASTM Grade Ti alloys.

ASTM Grade	Range		Maximum content					
	Aluminum	Vanadium	Carbon,	Oxygen	Nitrogen	Hydrogen	Iron	Other Elements
2/2H	- -	- -	0.08	0.25	0.03	0.015	0.3	0.4
5	5.5-6.75	3.5-4.5	0.08	0.2	0.05	0.015	0.4	0.4
23	5.5- 6.5	3.5-4.5	0.08	0.13	0.03	0.0125	0.25	0.4

A detailed description of the standard microstructures and the mechanical properties of interest for the materials studied in this work are presented in the following section.

2.1.1. CP Ti

CP Ti (grade 2 ASTM) is characterized by its α-phase microstructure and the presence of certain impurity elements (carbon, oxygen, nitrogen, iron) that increase its β-transus temperature (~ 910 °C) [35]. The morphology of the grains depends on the cooling rate from the β-transus temperature. With a fast cooling rate, CP Ti exhibits a lamellar or lath-type morphology [39] (see Figure 3-a). In contrast, equiaxed grains are obtained with slower cooling rates [40] (see Figure 3-b). The room temperature (RT) tensile properties of the Grade 2 CP Ti with these different grain morphologies are presented in Table 3. The most active deformation modes in CP Ti are prismatic dislocation slip and twinning, both of which are not strongly temperature sensitive for temperatures between 23 °C and 455 °C [40].

Thermomechanical processing affects the mechanical properties of CP Ti significantly through changing the grain morphology and size. Lamellar grains lead to an increase in the ultimate tensile strength (UTS) and yield stress (YS) and typically reduces the elongation-to-failure [35] (see Table 3). Grain refinement through severe plastic deformation improves the strength, fatigue and creep properties but decreases the elongation-to-failure [41 - 43].

Table 3. Tensile properties for different CP Ti microstructures.

	UTS (MPa)	YS (MPa)	Elongation (%)	Ref
Lamellar α grain morphology	673 ± 11	523 ± 11	24 ±1	[39]
Equiaxed α grain morphology	564	440	-	[40]
Minimum values for CP Ti	343	275	20	[35]

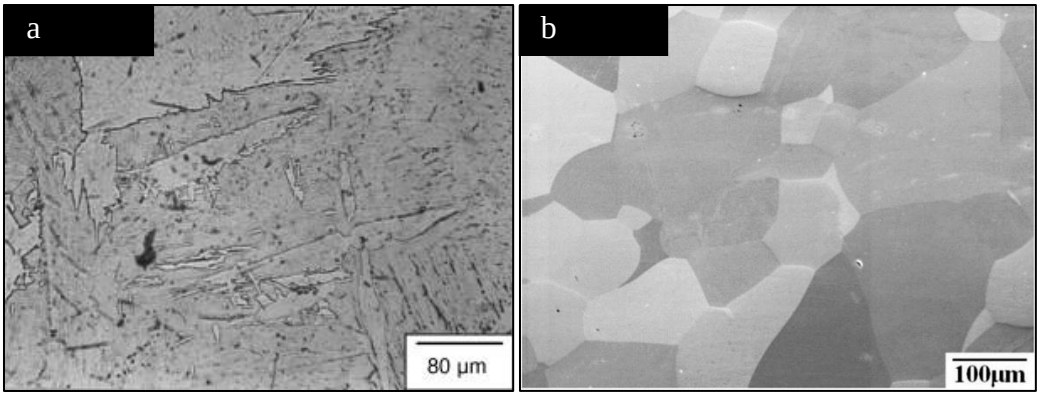

Figure 3. Example of the grain morphology in CP Ti: a) lath type morphology [39], b) equiaxed morphology [40].

2.1.2. Ti-6Al-4V

The second material used in this work is Ti-6Al-4V (Grade 5 ASTM). This alloy is the most commonly used Ti-alloy, especially in the aerospace and biomedical industries. In addition to Al and V, this alloy contains impurity elements such as C, O, N, Fe and Si [35]. The β transus temperature for this alloy is ~ 995 °C [35]. Ti-6Al-4V is a two-phase alloy, meaning that both α and β phases are present in the material at RT. The β-phase volume percentage varies between 5 and 10 vol. % [35].

The thermomechanical processing of this alloy, usually performed in the α + β two-phase field, affects the grain morphology. As the material is cooled from the β-transus temperature into the α + β two-phase field, α-phase plates nucleate from the grain boundary of β-phase. The final microstructure, which depends on the cooling rates and thermomechanical processing, can be classified into three primary grain morphologies [35]:

- Lamellar (see Figure 4-a): The thickness of individual α-phase lamellae and the size of the prior-β colonies can vary depending on the cooling rate. High cooling rates result in a martensitic structure (acicular), whereas lower cooling rates result in the formation of a

lamellar α + β microstructure. Decreasing the cooling rate causes an increase both in the thickness of individual α-phase lamellae and in the size of the prior- β colonies.

- Equiaxed (see Figure 4-b): Significant mechanical working (above 75%) and subsequent heat treatment in the α + β two-phase field can result in an equiaxed and recrystallized grain microstructure [37]. The temperature of the heat treatments affects the α-phase volume fraction and the grain size.
- Bimodal (see Figure 4-c): A mixture of lamellar and equiaxed grains is present in the final microstructure.

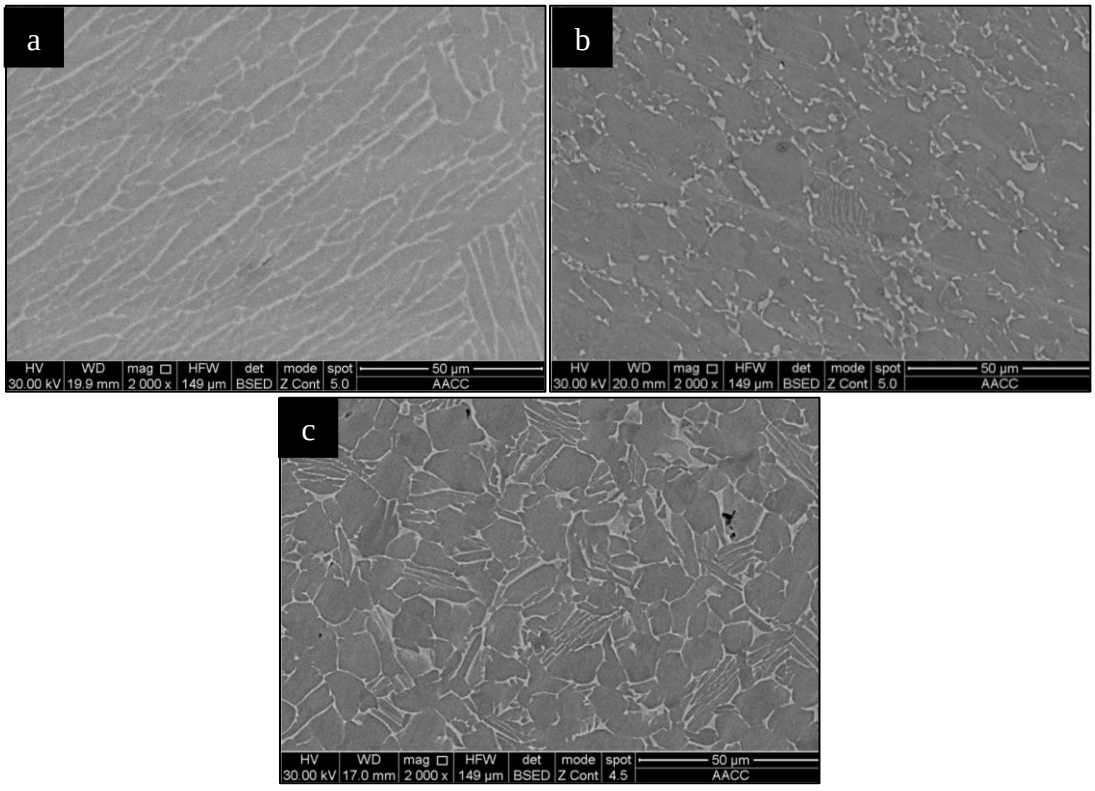

Figure 4. Examples of the different microstructures found in Ti-6Al-4V: a) Lamellar, b) Equiaxed; c) Bimodal. Figures are adapted from [44].

The mechanical properties of Ti-6Al-4V depend on the obtained microstructure, and in particular, the distribution of the β and α phases and their relative volume fractions [45].

2.1.3. Additive manufacturing (AM) of Ti-6Al-4V

The traditional manufacturing of Ti-alloy parts can be difficult, time-consuming and have both high material wastage and manufacturing costs. Additive manufacturing (AM) presents an attractive alternative due to its capability to produce near-net-shape components with less production time and material waste [46]. The growing interest in AM as a viable processing solution to manufacture complex shapes led to the choice of AM Ti-6Al-4V to be investigated in this study. Examples of the different microstructures in Ti-6Al-4V produced by the three main AM techniques, namely Direct Energy Deposition (DED), Selective Laser Melting (SLM) and Electron Beam Melting (EBM) are shown in Figure 5. The AM Ti-6Al-4V usually exhibits a lamellar grain structure at the surface (see Figure 6-a) and an elongated columnar prior β-grains (see Figure 6-b) along the build direction due to the rapid cooling rates [46].

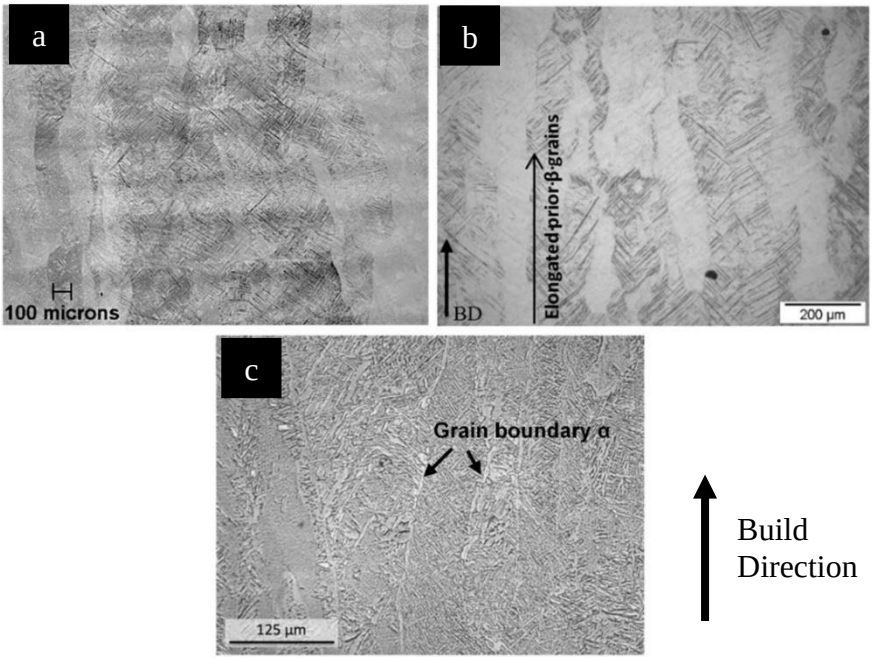

Figure 5. The morphology of prior β grains formed in Ti-6Al-4V by: a) DED [47]; b) SLM [48], c) EBM [49]. Figure reproduced from [47]. For all these images, the build direction was vertical.

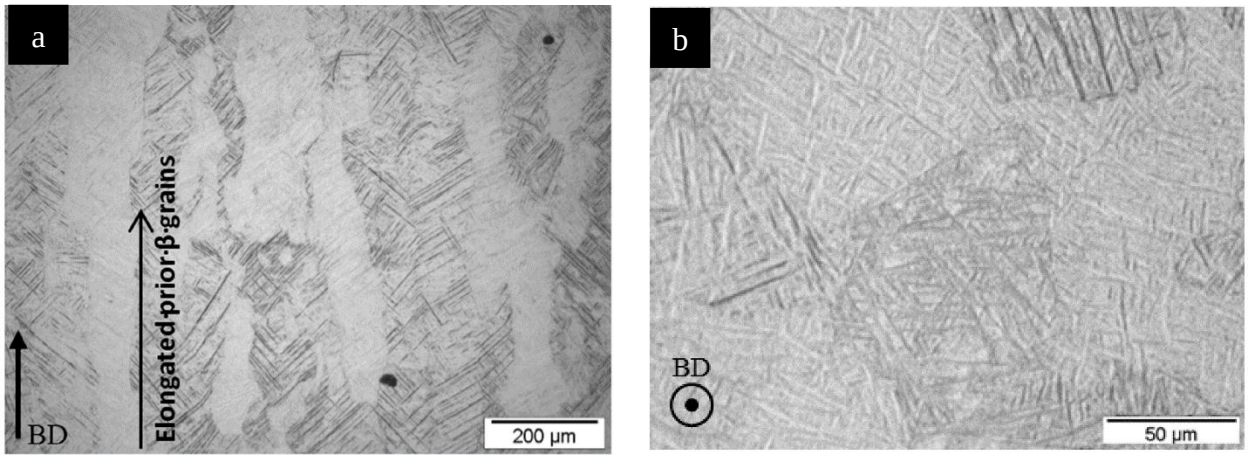

Figure 6. Micrographs of the macrostructure of Ti6Al4V SLM: a) side view parallel to the building direction (BD) showing the elongated prior β grains; b) top view perpendicular to the BD showing the lamellar grain morphology. Figure reproduced from [48].

AM of Ti-6Al-4V typically produces parts that are harder than conventionally-manufactured Ti-6Al-4V, i.e., higher YS and UTS, but with slightly lower elongation-to-failure [46, 50, 51].

2.2. RADIATION DAMAGE IN MATERIALS

2.2.1. Radiation damage event

G. Was [23] describes the radiation damage event as the energy transfer from the irradiating particle as it impacts a lattice atom [23]. The scattering of energetic particles from irradiation exposure imparts recoil energy to the atoms in the materials. When this recoil energy exceeds a critical value, called the threshold displacement energy (T_d), a primary knock-on atom (PKA) is created displacing the atoms in the crystal lattice. The T_d for Ti is 19.2+/-1 eV [52]. Other knock-on atoms will be created inside the material resulting in a displacement cascade or a collection of point defects. Finally, the PKA terminates at an interstitial site in the lattice.

The evolution of collision cascades can be divided into the following stages [23]:

i. Collision stage: PKA displaces the atoms creating a cascade.

ii. Thermal spike: This stage is characterized by a local increase in temperature due to the energy transfer. The atoms can be in a near molten stage.

iii. Quenched stage: The cooling down and recombination of some of the point defects results in stable vacancies (V) and self-interstitial atoms (SIA).

iv. Annealing stage: The recombination of the final damaged microstructure is assisted by thermal diffusion. This final stage lasts until all mobile defects escape the cascade region. At this stage, defects can be observed as small black dots in TEM.

Each damage cascade is thought to create a cluster of vacancies surrounded by the ejected interstitial atoms from the cascade core [53]. As a result of these damage cascades, high concentrations of point defects (PDs), both vacancies and interstitials, are present in irradiated materials. These PDs are free to move in the material and can interact with each other or with defect sinks (dislocations, grain boundaries, free surface, interfaces). These interactions are defined as:

- Recombination: The annihilation of V-SIA pairs.
- Clustering: V-V and SIA-SIA interactions resulting in a cluster of defects.
- Loss at defect sinks.

The evolution of defect concentrations are described as a function of these interactions using diffusional and rate theory [54] per the following equation:

$$\frac{dC_v}{dt} = K_0 - K_{vi}C_vC_i - K_{vs}C_vC_s \; ; \; \frac{dC_i}{dt} = K_0 - K_{vi}C_iC_v - K_{is}C_iC_s \qquad \text{Eq. 1}$$

Where:

C_v = vacancy concentration;

C_i = interstitial concentration;

K_0 = defect production rate;

K_{vi} = vacancy–interstitial recombination rate coefficient;

K_{vs} = vacancy–sink reaction rate coefficient;

K_{is} = interstitial–sink reaction rate coefficient.

Radiation damage is, therefore, controlled by competing processes of clustering and loss at defect sinks. Vacancy clustering results in the formation of an atomic scale disc-shaped cavity that collapses into a Frank dislocation loop with Burgers vector normal to the plane of the loop [55]. Similarly, interstitial clustering can result in the formation of interstitial Frank loop by inserting an extra layer of atoms between two normal planes [56].

2.2.2. Radiation-induced diffusion

The high point defect concentrations (C_v and C_i) created as a result of irradiation significantly enhance solid-state diffusion (much higher than in the case of thermal diffusion) and depend on several parameters such as temperature, initial sink density, and irradiation dose rate* [57, 58]. The diffusion coefficient D_{rad} for an irradiated pure metal is defined as a function of the diffusion coefficients for vacancies and interstitials and their corresponding defect concentrations:

$$D_{rad} = D_i C_i + D_v C_v \qquad \text{Eq. 2}$$

* Equivalent to the defect production rate.

An example of the evolution of D_{rad} as a function of temperature ($\frac{1}{T}$) for different dose rates and defect sink concentrations in copper (Cu) is presented in Figure 7 [57]. As the temperature increases, D_{rad} increases. The curves labeled 1, 2 and 3, enable a comparison of the effect of sink concentration (in this case dislocation densities ρ_d) at the same defect production rate. At the same temperature, for example, 555 ℃ (see dashed red line in Figure 7), D_{rad} decreases as a function of the increasing sink density. Increasing the dose rate (see curve 4) significantly increases the diffusion.

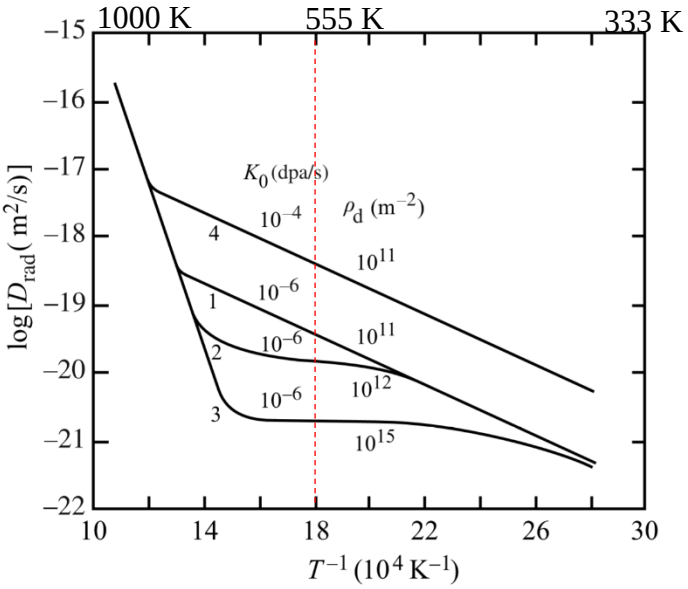

Figure 7. Calculated D_{rad} for self-diffusion of Cu as a function of temperature for different combinations of defect production rates and dislocation densities. 1: $K_0 = 10^{-6}$ dpa/s, $\rho_d = 10^{11}$ m^{-2}, 2: $K_0 = 10^{-6}$ dpa/s, $\rho_d = 10^{14}$ m^{-2}, 3: $K_0 = 10^{-6}$ dpa/s, $\rho_d = 10^{15}$ m^{-2}, 4: $K_0 = 10^{-4}$ dpa/s, $\rho_d = 10^{11}$ m^{-2}. Figure adapted from [57, 59]**.**

At lower temperatures, most point defects are annihilated by recombination. At higher temperatures, point defect diffusion to sinks causes an inverse flux of solute elements from defect sinks through inverse Kirkendall and "dragging" effects, respectively, for vacancy and interstitial type point defects. These biased fluxes of point defects and solutes and/or alloying elements lead to enrichment or depletion close to sinks, known as radiation-induced segregation

(RIS) [23, 60]. Figure 8 presents an example of solute segregation at the grain boundaries as a result of RIS in a neutron-irradiated 300 series stainless steel. Cr, Ni, Si and P concentrations across the grain boundary were homogeneous before irradiation. After being exposed to neutrons at 300 ℃, the depletion of Cr is shown, while the Ni, Si and P concentrations increased [59].

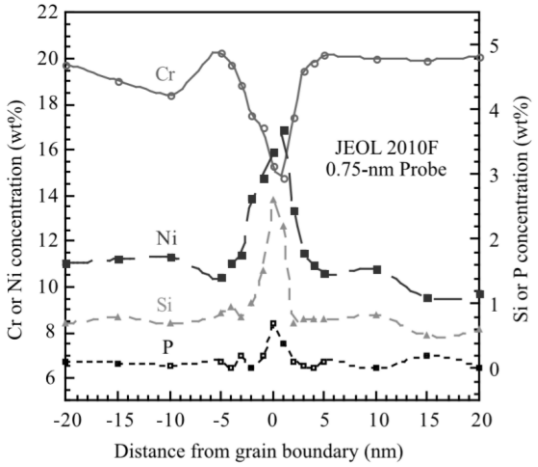

Figure 8. Radiation-induced segregation of Cr, Ni, Si and P at the grain boundary of a 300 series stainless steel irradiated in a light water reactor core to several dpa at~300 ℃. Figure reproduced from [57] (after [59]).

At even higher temperatures, the segregated elements diffuse back into defect sinks and a quasi-steady state may be reached during irradiation.

Figure 9 summarizes the effect of temperature and dose rate on the diffusion and highlights the three different domains: Recombination, RIS and back diffusion. For CP Ti and using a melting temperature T_m equal to 1600 ℃ (1360 K) [35], the equivalent irradiation temperatures T(℃) are indicated on the right-hand axis.

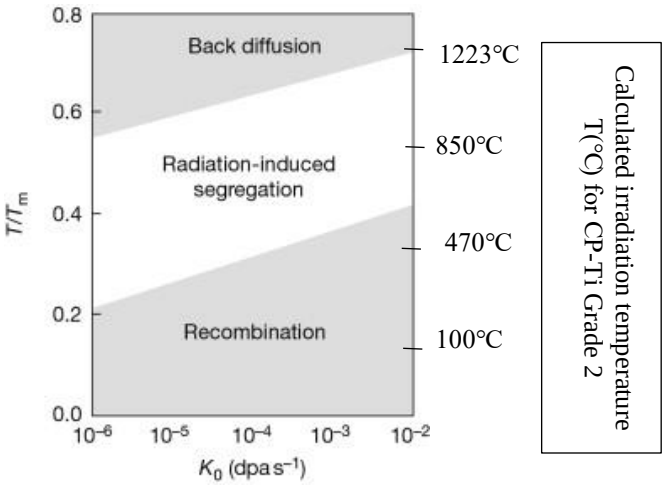

Figure 9. Temperature and dose rate (dpa/s) effect on RIS. The figure is adapted from [61]. The temperature in the left-hand axis is in K. For CP Ti and using a melting temperature (T_m) of 1600 °C (1360 K) [35], the equivalent irradiation temperatures T(°C) are indicated on the right-hand axis.

This radiation-enhanced diffusion promotes the motion of point defects inside the material and causes profound changes to the microstructure such as dislocation loops, bubbles and voids [23]. Phase transformations can also occur in the material due to local enrichment or depletion of solutes [23]. A description of the radiation-induced microstructural changes in Ti alloys is provided in section 2.3.

2.2.3. Influence of the irradiating particle

Radiation damage in Ti alloys was investigated using neutrons [12], protons [13, 14] and ions [11, 15]. Therefore, understanding the effect of the irradiating particle is necessary.

First, a fundamental parameter that describes the radiation-induced lattice displacement events needs to be defined. The term “dpa” or displacement per atom is the unit conventionally used to quantify the radiation damage [23]. It is a damage-based exposure unit and represents the number of atoms displaced from their regular lattice sites as a result of energetic particle bombardment. Dpa is also used to compare radiation damage by different radiation sources.

The main differences between these irradiations are damage depth and the dose rate. The smaller the projectile, the smaller the energy transfer to the impacted lattice atoms and the longer its trajectory resulting in greater damage depth [23]. Large particles, such as heavy ions, displace more atoms in their trajectories but are stopped much sooner. A schematic representation of the cascade morphologies (displaced atoms along the trajectory of the incident particle) as a result of 1 MeV ion, proton, and neutron irradiation in Ni is shown in Figure 10.

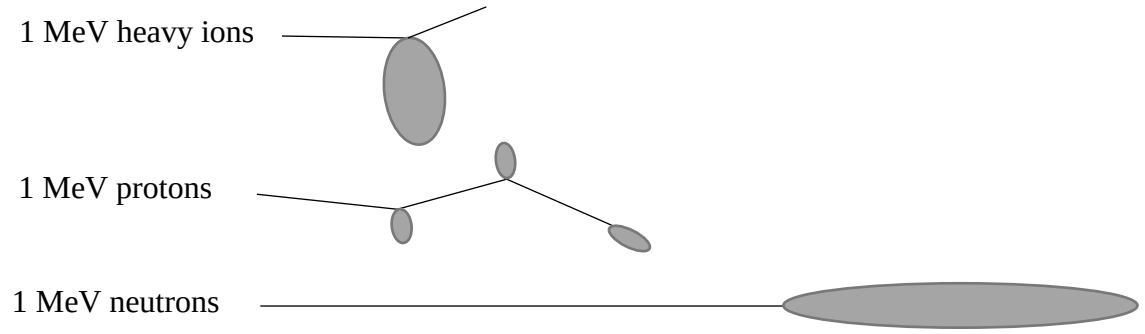

Figure 10. Damage cascade morphologies for different irradiating particles with the same incident energy of 1 MeV. The figure is adapted from [23].

Neutron irradiations have dose rates (dpa/s) that are typically 10^2 -10^3 lower than for proton irradiations, which are 2-3 times lower than ion irradiations [62]. Additionally, neutron irradiation in a nuclear reactor environment is characterized by transmutation reactions, most importantly, helium (He) production that can further embrittle the material.

Ion irradiation experiments have been used to simulate radiation damage in nuclear environments for decades. The advantages of using this type of particles are mainly the high dose levels achieved in extremely short irradiation times and the non-activation of the samples allowing their manipulation outside of hot cells* [62]. The extent of the induced damage

* Shielded nuclear radiation containment chambers.

depends on the size of the projectiles and their energy. The lower the energy of the ion beam, the higher the damage created [23].

The range of slow charged ions in the material is small and their energy loss is dominated by elastic collisions (nuclear stopping). Ions of high kinetic energy, or Swift Heavy Ions (SHI), do not interact directly with the atoms but rather with the electrons of the target, inducing ionization and electronic excitation processes. The ion range is then extensive and a cylindrical region of extremely high ionization density along the ion path can be observed. This amorphized area is referred to as ion tracks [63]. Ion irradiation does not only change the arrangement of atoms inside the material, but it can also cause a chemical modification of the composition in the case of implantation.

2.2.4. Irradiation damage in hcp metals

2.2.4.1. Microscopic effects

2.2.4.1.1. Dislocation loop formation

The main defects observed in irradiated metals are dislocation loops resulting from vacancy and interstitial clusters. Depending on the flux of point defects, these loops can either shrink or grow [23]. Additionally, in non-cubic metals, the point-defect diffusion, called diffusional anisotropy difference (DAD), was shown to be anisotropic through atomistic computations, especially for SIA migration [64]. Once the loops reach a critical size, they become stable and grow until they unfault by either interaction with other loops or with the network dislocation density [23].

The different dislocation loops observed in hcp materials are summarized in Table 4. In irradiated hcp materials, the most commonly observed loops are those nucleating in the basal and prismatic planes referred to as c-component loops and <a> loops respectively [65].

Table 4. Dislocation loops in hcp materials, their habit planes and Burgers vectors.[66]

Notation	Habit plane	Burgers vector
<c>	{0001}	$\frac{1}{2}[0001]$
<c+p>	{0001}	$\frac{1}{6}<20\bar{2}3>$
<a>	$\{10\bar{1}0\}$	$\frac{1}{3}<2\bar{1}\bar{1}0>$
<c+a>	$\{10\bar{1}1\}$	$\frac{1}{3}<11\bar{2}3>$

During the collision stage of the cascade evolution, the crystal structure is not important since the high kinetic energy of the cascading atoms is significant and ballistic effects cause the displacement of the atoms. Later on, during the cooling down, when the kinetic energy decreases significantly, the evolution of the defects (defect motion) depends on the crystal structure [67]. Molecular dynamic (MD) simulations yielded a possible relationship between loop habit nucleation planes and the c/a ratio in hcp materials [68]. The anisotropy of the interstitial diffusion is expected to depend on this c/a ratio, where it is weakest for values close to the ideal ratio ($\sqrt{3}$) [69]. Since c/a ratios for Ti (1.586) and Zr (1.59) are below this ideal ratio, similar radiation damage structures with dominant basal loops were expected.

Experimentally, this rule was proven to be inaccurate for both Ti [70] and Zr [71] as both basal and prismatic loops were observed. Basal and prismatic loops formed at different levels of

irradiation and were shown to have different impacts on the property degradation of these alloys [65, 72 - 76].

For Zr, the size of the <a> loops increases non-linearly with temperature, while the loop density decreases as temperature increases [77]. An example of the observed <a> loops in Zr is shown in Figure 11. The existence of these small loops in the microstructure was the cause of the strength increase and elongation-to-failure reduction in irradiated materials [21, 72].

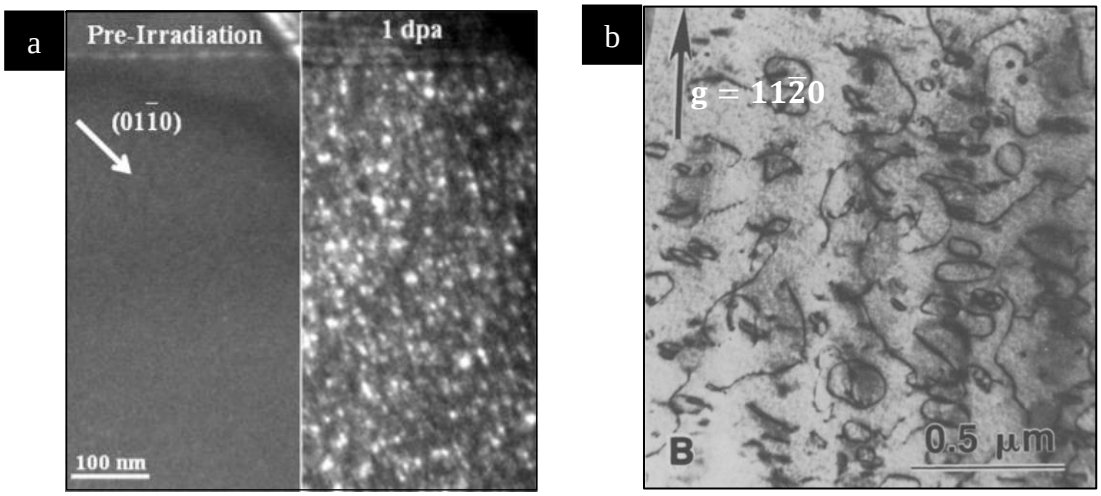

Figure 11. Prismatic <a> dislocation loops observed in Zr at different irradiation conditions: a) Pre-irradiated area and after irradiation with 1 MeV Kr ions at 500 ℃ up to 1 dpa with $\mathbf{g} = 01\bar{1}0$ and beam direction B~[0001] [20]; b) After neutron irradiation at about 430 ℃ and up to a dose of ~ 50 dpa. Diffracting vector $\mathbf{g} = 11\bar{2}0$, beam direction $B = 1\bar{1}00$ [76].

The c-component loops nucleate at higher doses and temperatures and are associated with accelerated irradiation-induced growth or swelling [74, 77]. C-component dislocation loop nucleation is thought to occur during the collision cascade stage [66] and they can be both vacancy and interstitial type in Zr, Ti and Mg [75]. Figure 12 shows an example of c-component loops observed in electron irradiated Zn and neutron-irradiated Zr. When imaged with a diffraction vector g = 0002, only c-component loops are visible (<a> loops invisible) and they are oriented edge-on (Figure 12-b).

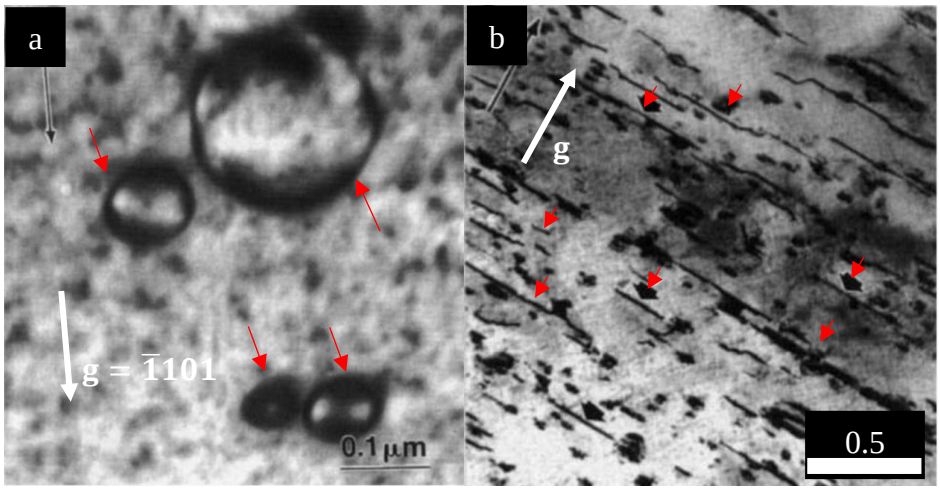

Figure 12. Basal-plane dislocation loops observed in : a) Electron irradiated Zn (hcp) at 0 °C imaged with $\mathbf{g} = \bar{1}101$, beam direction near $[1\bar{2}13]$; b) Zr following neutron irradiation to a fluence of 1.5 x $l0^{26}$ neutrons.m^{-2} at 427 °C. The c-component loops are in an edge-on orientation (red arrowed) with **g** = 0002. The figure is adapted from [75].

The c-component dislocation loop stability and evolution depend on the temperature, the dose, and the present alloying and impurity elements [74, 77, 20]. In Zr, c-component loops were only observed after reaching a threshold incubation dose (TID) that was dependent on the temperature and the distribution of impurities [78]. TID decreased as the temperature increased and the presence of large $Zr_3(Mo,Nb,Fe)_4$ secondary phase precipitates (SPPs) was linked to the earlier nucleation of c-component loops (See Figure 13). Fe content specifically promoted c-component loop nucleation [78].

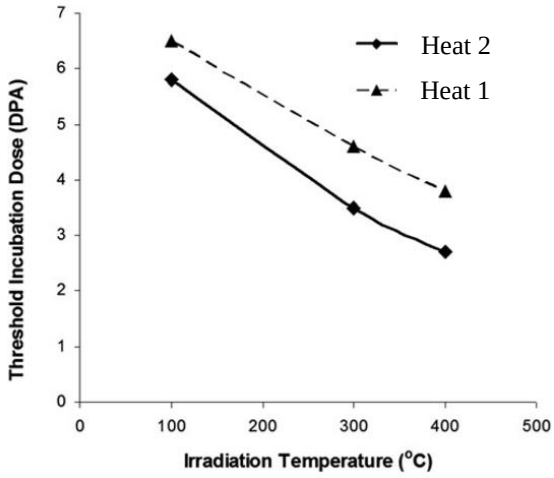

Figure 13. TID for the formation of c-component loops plotted as a function of temperature for two Excel alloys after two different heat treatments: Heat 1: Zr-Excel after two hours of solution treatment at 890°C followed by water quenching and one-hour aging at 450°C not showing any SPPs; Heat 2: Zr-Excel after being solution treated and aged for 550 h at 500 °C containing SPPs. The figure is reproduced from [78].

2.2.4.1.2. Chemical changes

Irradiation can cause chemical changes in materials as a result of the ballistic effects* and the RIS under certain combinations of dose rate and temperatures (see Figure 9). These transformations are not dependent on the crystal structure and have been observed in a variety of materials ([61, 60, 79, 80]). An example of RIS of Fe and Sn at grain boundaries of α-phase grains observed in Zr-Excel alloys after 1 MeV Kr ion irradiation at 400 °C and 10 dpa is shown in Figure 14 [78]. In the same Zr-alloy, precipitate formation, dissolution, and amorphization were also observed [78].

*i.e. Ejection of atoms during collision cascades.

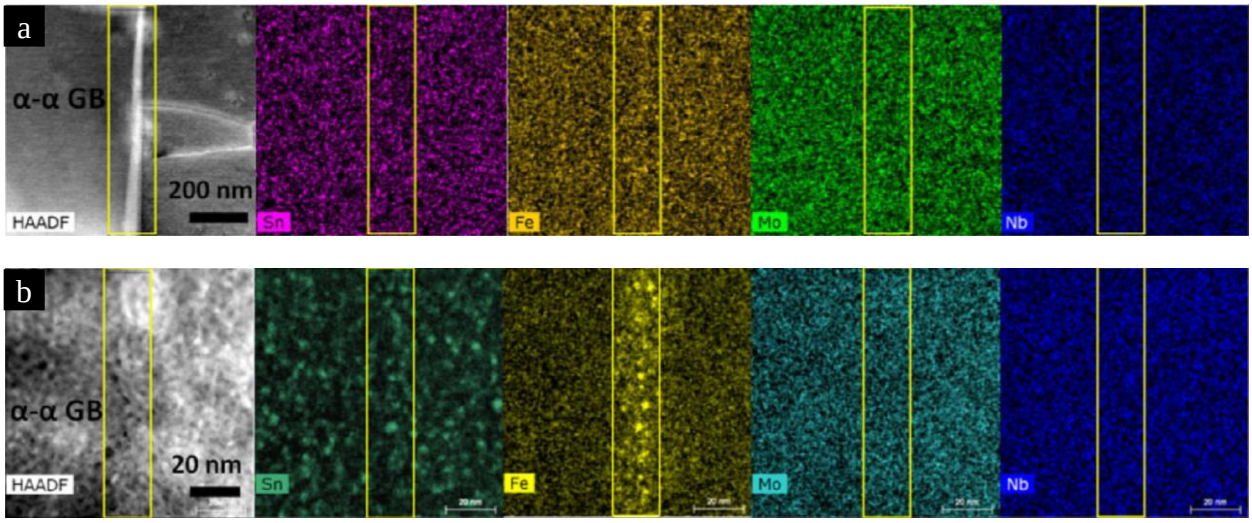

Figure 14. EDS mapping on an α–α grain boundary where the β phase is absent, in Zr-Excel sample: a) Unirradiated sample; b) After irradiation up to 10 dpa at 400 °C showing segregation of Fe and Sn clusters along the grain boundary. The figure is reproduced from [78].

2.2.4.2. Macroscopic effects

2.2.4.2.1. Radiation hardening

Glide or conservative motion occurs when a dislocation line moves in the surface that contains both its line and its Burgers vector [81]. A dislocation able to move in this way is called glissile, while one that cannot is called sessile. Climb or nonconservative motion occurs when the dislocation moves out of the glide surface and thus normal to the Burgers vector. Glide of many dislocations results in slip, which is the most common manifestation of plastic deformation in crystalline solids. Slip is the sliding or successive displacement of one plane of atoms over another on slip planes. The discrete blocks of crystals between two slip planes remain undistorted. Further deformation occurs either by more movement on existing slip planes or by the formation of new slip planes [82].

The mobility of the defects depends on the nature of the dislocations (sessile or glissile), which depend on the crystal structure (see Table 5) and the stacking fault energy [83]. Sessile loops cannot glide and can act as nucleation sites for the growth of extended defects [83, 81]. The intrinsic glissile/sessile nature of dislocations, both interstitial and vacancy in metals with different crystal structures, are presented in Table 5.

Table 5. Summary of Burgers vectors of glissile and sessile loops in fcc, bcc and hcp lattices. This table is reproduced from [81]

BCC	$\mathbf{b} = \frac{1}{2} < 111 >$	Glissile
	$\mathbf{b} = \frac{1}{3} < 100 >$	Glissile
FCC	$\mathbf{b} = \frac{1}{2} < 110 >$	Glissile
	$\mathbf{b} = \frac{1}{3} < 111 >$	Sessile
HCP	$\mathbf{b} = \frac{1}{3} < 11\bar{2}0 >$	Glissile
	$\mathbf{b} = \frac{1}{2} < 10\bar{1}0 >$	Sessile

2.2.4.2.2. Radiation-induced swelling*

Radiation-induced swelling is the dimensional change that occurs without applied stress in hcp metals [23]. The mechanisms of this swelling in recrystallized Zr can be summarized in three stages [64] (see Figure 16) and are explained by the diffusional anisotropy difference (DAD). In the DAD model, SIAs are more mobile on the basal plane and vacancies have anisotropic diffusion. As a result, grain boundaries and dislocations parallel to the c-component axis absorb most interstitial atoms formed after irradiation leading to elongation along the <a> axis and a contraction along the <c> axis [64]. In the first stage (1), fast growth is observed due to the absorption of a high concentration of SIAs. In the second stage (2), stationary growth is

*Also called irradiation growth (IG).

reached with a high density of interstitial <a> loops. The last stage (3), referred to as breakaway growth, is characterized by the high density of c-component loops.

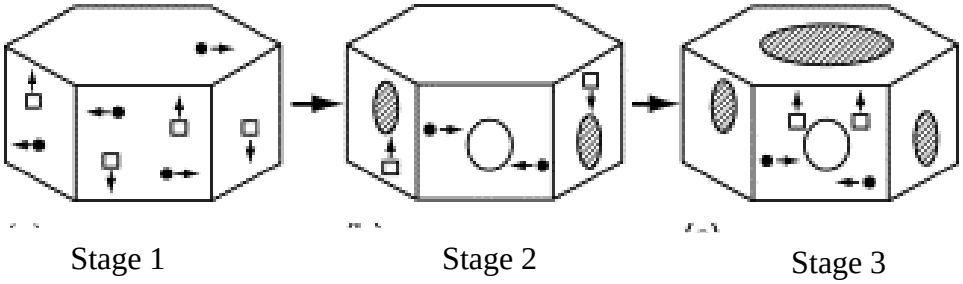

Figure 15. Schematic representation of the three stages of irradiation-induced swelling in recrystallized zirconium alloys [64].

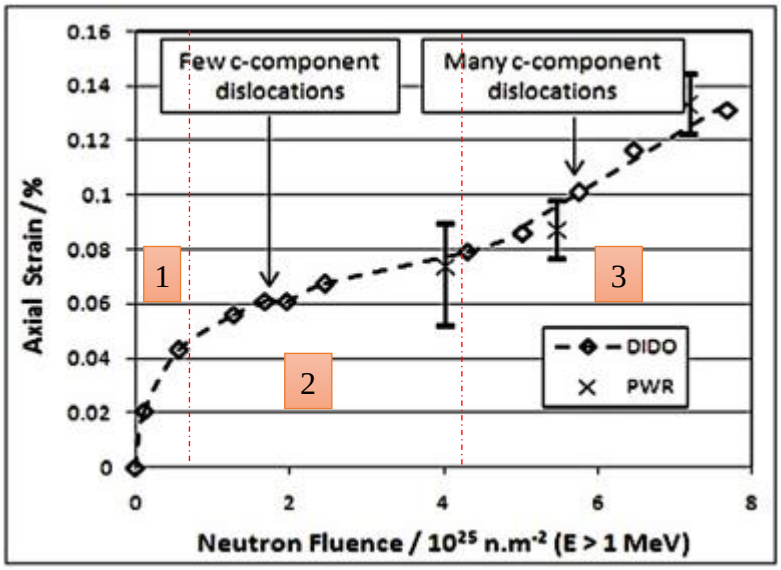

Figure 16. Irradiation-induced swelling in annealed (RXA) Zircaloy at 550 K–580 K, showing accelerating growth after a fluence of about 4×10^{25} nm^{-2} (E > 1 MeV). The figure is reproduced from [84].

2.3. RADIATION DAMAGE IN TI-ALLOYS

In the following sections, a survey of the published data on radiation damage in Ti and Ti-6Al-4V will be presented, starting with the microstructural changes and later describing the effect on the mechanical properties.

2.3.1. Changes in microstructure

2.3.1.1. In Ti

Similar to other hcp metals, the dislocation loops formed in irradiated α-phase Ti are <a> type dislocation loops with the Burgers vector $\mathbf{b} = \frac{1}{3} < 2\bar{1}\bar{1}0 >$ and c-component loops with Burgers vectors $\mathbf{b} = \frac{1}{2}[0001]$ and $\mathbf{b} = \frac{1}{6} < 2023 >$ [70].

Examples of the reported <a> dislocation loops in Ti irradiated with neutrons [70], protons [14, 85] and ions [86] are presented in Figure 17, Figure 18 and Figure 19 respectively. These loops were homogeneously distributed in the grain at the different temperatures and doses. Preferential alignment of <a> type loops in bands parallel with (0001) was only observed in neutron-irradiated cold worked Ti (see Figure 17-b). In Ti, <a> type loops are mainly interstitial, while most c-component loops are vacancy type [70].

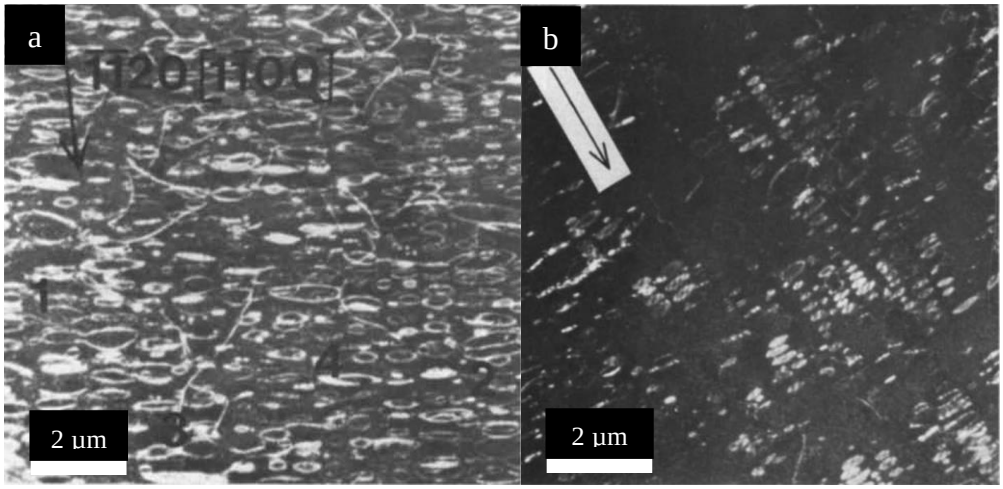

Figure 17. <a> dislocation loops in neutron-irradiated samples at 347 ℃: a) annealed Ti irradiated to a fluence of 3.4×10^{25} n.m^{-2} ; b) 64% cold-worked Ti irradiated to a fluence of 4.03×10^{25} n.m^{-2}[70].

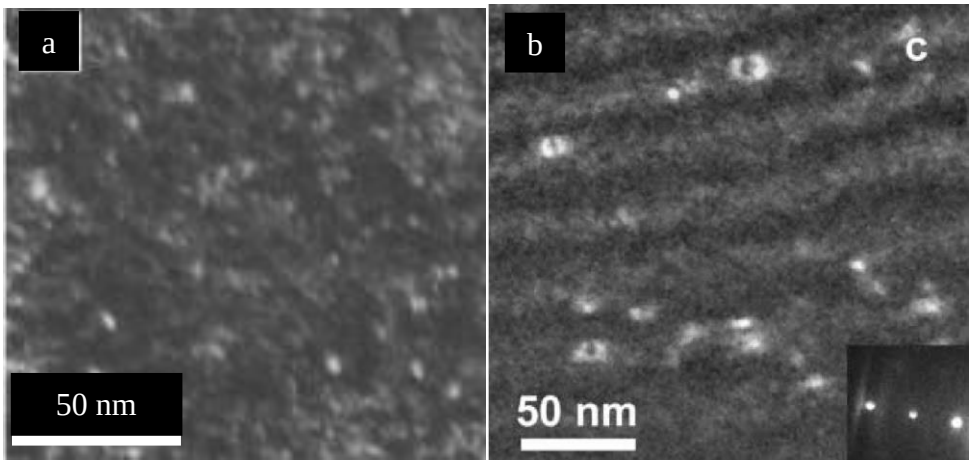

Figure 18. High purity Ti irradiated with 590 MeV protons at: a) 25 ℃ and 0.03 dpa [85], b) 250 ℃ and 0.09 dpa, $\mathbf{g} = 10\bar{1}1[0001]$ [14].

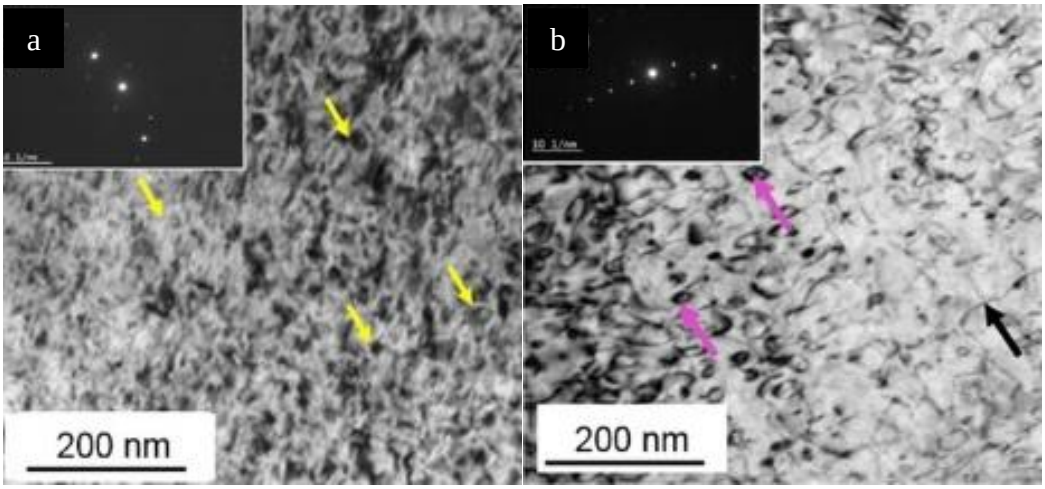

Figure 19. Microstructure of CP Ti grade 2 showing <a>-type dislocation loops after irradiation at a dose of 3 dpa with 6 MeV Ti ions at: a) 300 °C; b) 430 °C [86].

Observations of c-component loops in Ti were reported in [70] and [86]. An example of these loops is shown in Figure 20 for grade 2 Ti irradiated with 6 MeV Ti ions up to 3 dpa [86]. Compared to c-component loops in Zr (see Figure 12-b), these edge-on loops were not straight. Their curved appearance is enhanced at higher temperatures (see Figure 20). This phenomenon could be explained by dislocation loop climbing as a result of vacancy absorption which is enhanced at higher temperatures [87].

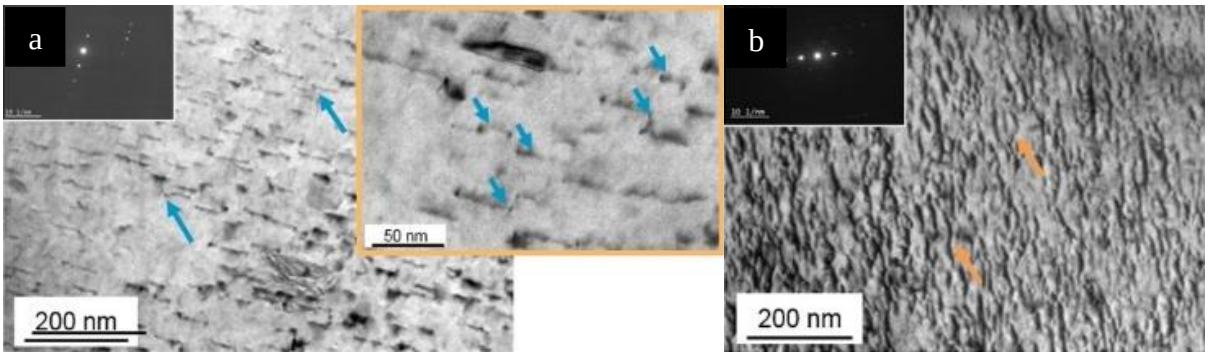

Figure 20. The microstructure of CP Ti grade 2 showing c-component dislocation loops after irradiation at a dose of 3 dpa with 6 MeV Ti ions at a) 300°C; b) 430°C [86].

2.3.1.2. In Ti-6Al-4V

The reported changes in the microstructure of the α+β Ti-alloy were similar to CP Ti except for radiation-induced precipitation. Examples of the observed <a> type dislocations in irradiated Ti-6Al-4V with neutron [88] and ions [17] are shown in Figure 21. At high temperature (starting from 300 ℃), V-rich precipitates were observed as a result of irradiation (see Figure 22).

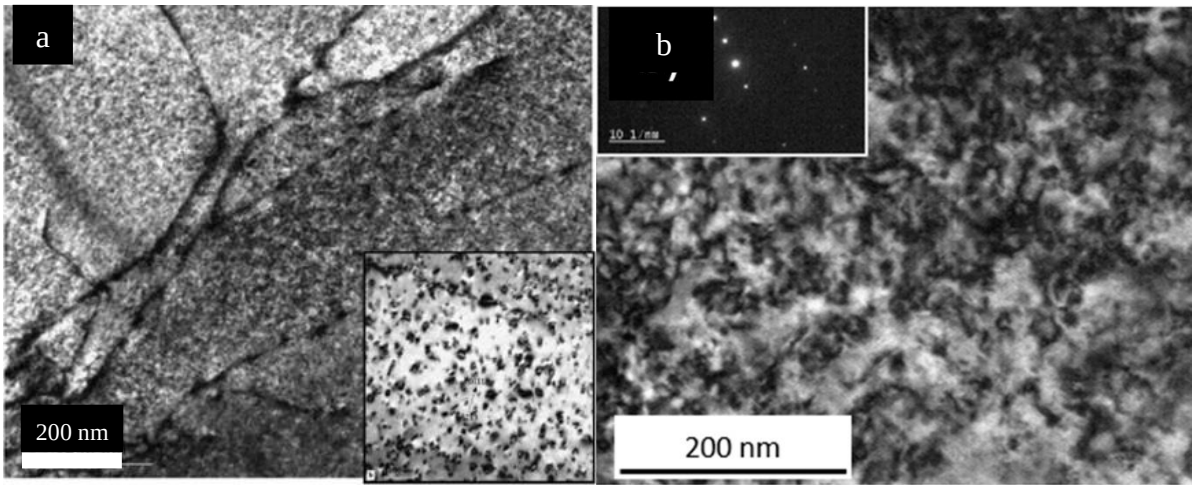

Figure 21. Microstructure after irradiation of Ti-6Al-4V with: a) Neutrons at 50 ℃ and up to 0.3 dpa [88]; b) 6 MeV ions at 430 ℃ 0.6 dpa [17].

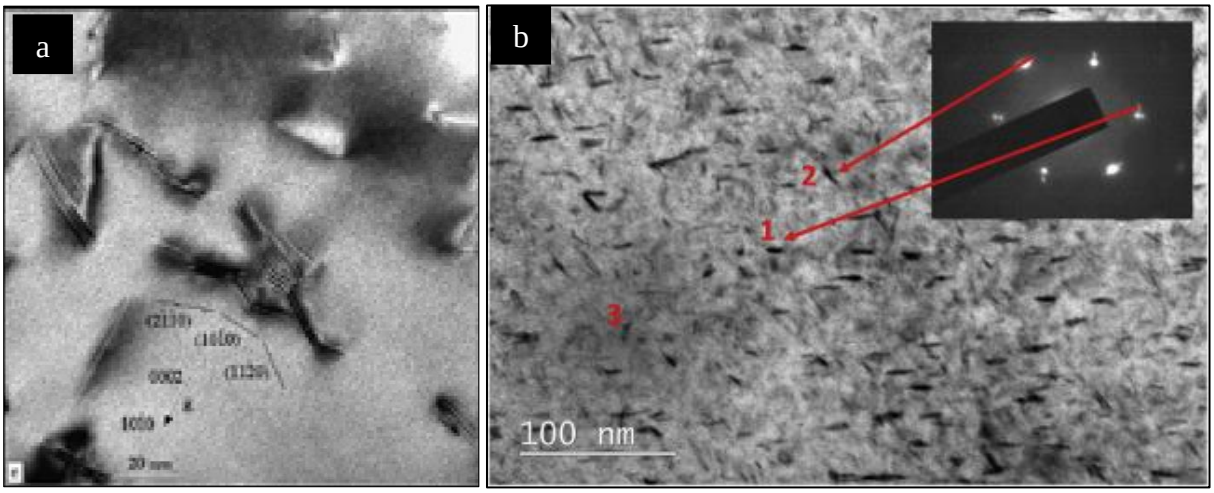

Figure 22. Precipitates observed in Ti-6Al-4V irradiated with: a) neutrons at 50 ℃ and up to 0.3 dpa [88]; b) 6 MeV ions at 430 ℃ and for a dose of 3 dpa [17].

A detailed summary of the changes in the microstructure of Ti-6Al-4V at different doses and temperatures is presented in Table 6. As previously discussed, radiation-enhanced diffusion promotes the mobility of point defects inside the Ti-alloy leading to the formation of the reported dislocation loops at all temperatures [60]. The effect of the dose on the density and size of these loops was not significant [17, 88]. However, the increase in temperature was followed by an increase in the loop size. At temperatures above 300 °C, V-rich precipitates formed in the α-phase grains [88 - 90] (see Figure 23). It seems that this local enrichment in V, which is a β-stabilizer, is related to phase transformations. In fact, at temperatures higher than 350 °C and for doses above 2.1 dpa, α-to-β phase transformation was reported [89, 90].

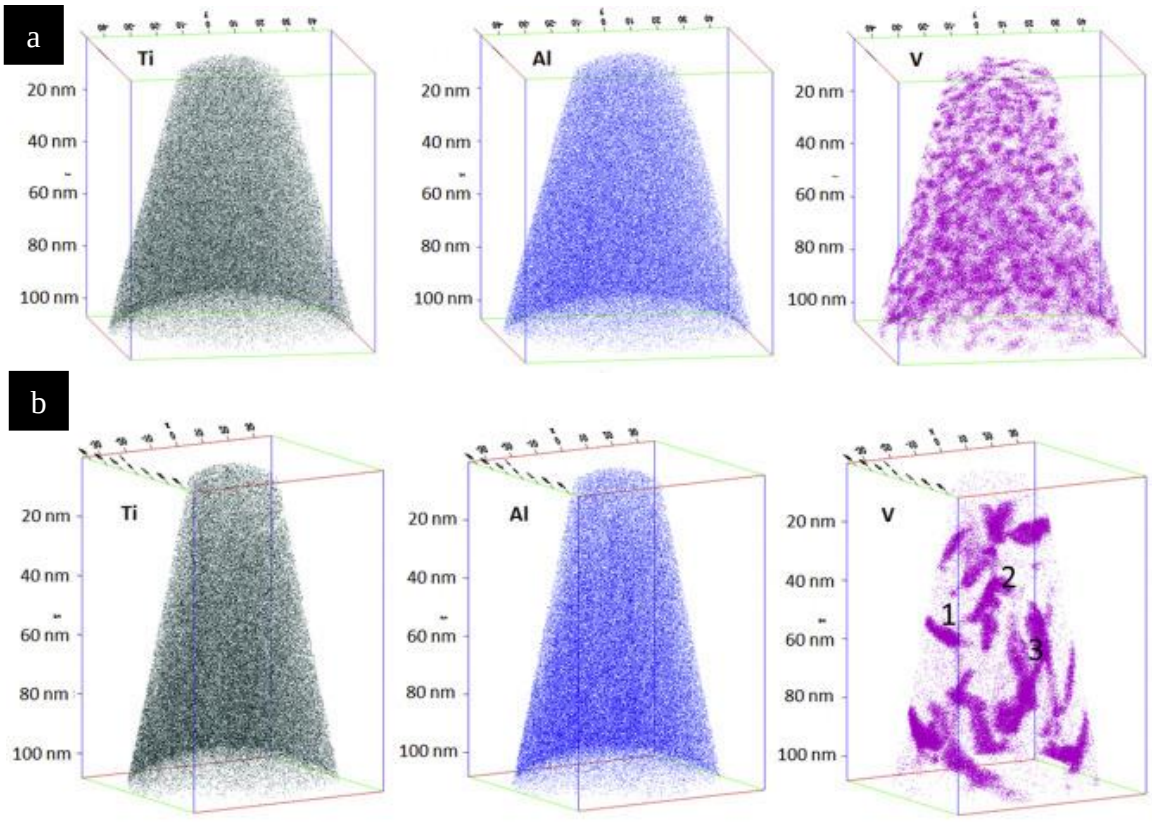

Figure 23. Needle tip 3D reconstruction (Atom Probe Tomography (APT) analysis): spatial distribution of Ti, Al, and V in Ti-6Al-4V alloy irradiated at the dose of 3 dpa, high flux, at the temperature of: a) 300 °C and b) 430 °C. Figure reproduced from [17].

Table 6. Summary of TEM observations in irradiated Ti-6Al-4V [17, 88 - 90]**.**

Irradiating particle	Temperature and dose	Microstructure change observations	Ref
Neutrons	50 ℃, 0.3 dpa	A high concentration of uniformly distributed defect clusters in the α-phase	[88]
Neutrons	150 ℃, ~0.05 dpa	Defect clusters density 3×10^{22} m^{-3}	[91]
Neutrons	260 ℃, ~0.25 dpa	Defect clusters density 2×10^{22} m^{-3}	[91]
17.5 MeV Cu^{4+}	250 and 350 ℃, 1.5 dpa	Small and dense dislocation loops	[16]
Neutrons	350 ℃, 0.3 dpa	Coarse dislocation loops Vanadium precipitates (40 nm× 5 nm)	[88]
6 MeV Ti ions	300 ℃, 0.6 and 3 dpa	Dislocation loops (~ 7 nm diameter) and very small precipitates (less than nm)	[17]
6 MeV Ti ions	430 ℃, 0.6 and 3 dpa	Dislocation loops (~ 9 to 8 nm diameter) Platelet like precipitates 16 nm × 3 nm and decreased to 14 nm × 3 at the higher dose.	[17]
17.5 MeV Cu^{4+}	450 ℃, 1.5 dpa	Dislocation loops up to 350 ºC At 450ºC β-phase precipitates in α phase	[16]
Neutrons	450 ℃, 2.1 and 32 dpa	β-phase precipitates in α phase	[90]
9 MeV Al ions	500 ℃, 2 dpa	β-phase precipitates in α phase 65 nm and a density of 1.2 10^{15} m^{-3}	[92]
9 MeV Al ions	550 ℃, 2 dpa	β-phase precipitates in α phase 87 nm and a density of 2 10^{15} m^{-3}	[92]
Neutrons	550 ℃, 32 dpa	Extensive void formation Coarse β-precipitates	[90]
9 MeV Al ions	600 ℃, 2 dpa	β-phase precipitates in α phase 140 nm and a density of 5.3 10^{14} m^{-3}	[92]
9 MeV Al ions	650 ℃, 2 dpa	β-phase precipitates in α phase 400 nm and a density of 6 10^{12} m^{-3}	[92]
9 MeV Al ions	700 ℃, 2 dpa	none	[92]

2.3.2. Changes in mechanical properties

These radiation-induced microstructural changes in Ti and Ti-6Al-4V are expected to cause changes in the mechanical properties.

Similar to Zr, radiation-induced swelling is expected for Ti [70] and was found to be between 1.5% and 5% for neutron-irradiated Ti-6Al-4V at temperatures between 450 °C and 550 °C [90].

The radiation-induced hardening as a function of dose and temperature for Ti and Ti-6Al-4V is plotted in Figure 24 and Figure 25. At low temperatures, an increase in the dose (up to 0.03 dpa) was linked to an increase in hardness for both materials [12, 14, 33, 93]. For CP Ti and Ti-6Al-4V, the effect of the temperature is unclear as there is not enough data for trends to emerge. This will be addressed and evaluated in this dissertation work.

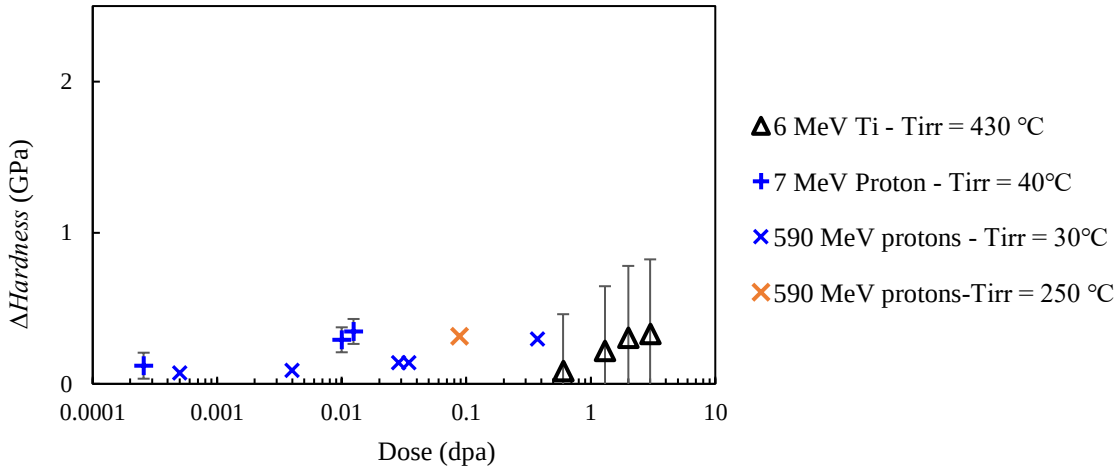

Figure 24. Change in hardness plotted for CP Ti samples: Irradiated with 6 MeV Ti ion beams from [33] (empty black triangle); Irradiated with 7 MeV proton beam from [93] (blue +); High purity Ti irradiated with 590 MeV proton beam from [14] (blue and red ×); The irradiation temperature for each set of samples is indicated in the legend.

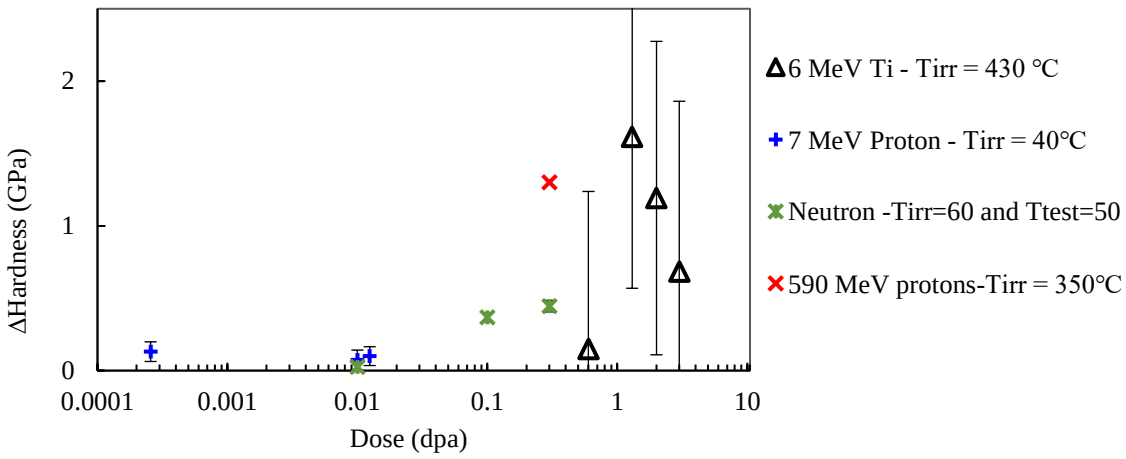

Figure 25. Change in hardness plotted for Ti-6Al-4V samples: Irradiated with 6 MeV Ti ion beams from [33] (empty black triangle); Irradiated with 7 MeV proton beam from [93] (blue +); Irradiated with neutrons from [12] (green *); Irradiated with 590 MeV proton beam from [13] (red ×); The irradiation temperature for each set of samples is indicated in the legend.

In addition to this increase in hardness, neutron irradiations decreased both the initiation fracture toughness [88] (see Figure 26-a) and the total and uniform elongation in Ti-6Al-4V (see Figure 26-b **)** [4].

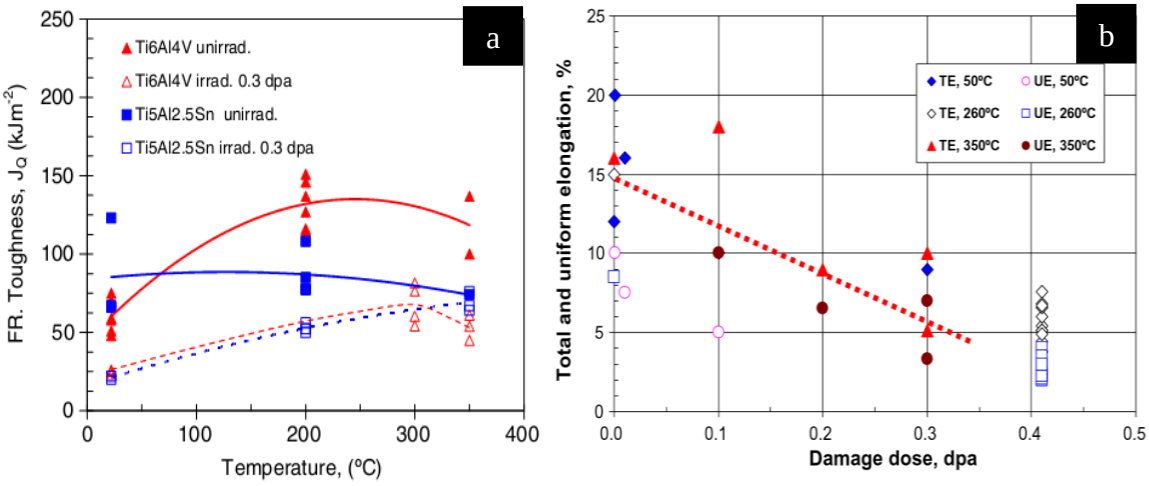

Figure 26. Effect of neutron irradiation in Ti-6Al-4V on: a) Fracture toughness [88]; b) Total (TE) and uniform elongation (UE) of Ti–6Al–4V [4].

2.4. SUMMARY

This background chapter explored published information on the microstructure of Ti and Ti-alloys and the changes in microstructure and mechanical properties as a result of radiation damage, highlighting aspects that are relevant to the current work. A summary of the reviewed effects of thermomechanical processing on the properties of unirradiated Ti alloys is presented in Table 7. Radiation damage mechanisms in materials in general and, more specifically, in conventionally manufactured Ti alloys were reviewed and the main effects are listed in Table 8.

Table 7. Summary of the effect of the microstructure on the properties of Ti alloys (adapted from [94]).

	Microstructure	Strength	Ductility	Fracture toughness
Grain Morphology	Lamellar	+	–	+
	Equiaxed	+	+	–
Grain size	Fine grain	+	–	+
	Coarse grain	–	+	–
Alloy phase	α-type	–	–	+
	α+β-type	+	+	++

Table 8. Radiation effects and their results in the material.

Effect	Consequence in material	Type of degradation in component
Displacement damage	Formation of point defect clusters	Hardening, embrittlement
Irradiation-induced segregation	Diffusion of detrimental elements to grain boundaries	Embrittlement, grain boundary cracking
Irradiation-induced phase transitions	Formation of phases not expected according to phase diagram, phase dissolution	Embrittlement, softening
Swelling	Volume increase due to defect clusters and voids	Local deformation, eventually residual stresses

A critical review of the literature reveals the following knowledge gaps relevant to radiation damage in Ti alloys:

(1) Generally, there is a lack of data on radiation damage in Ti alloys compared to other materials such as iron and zirconium alloys.

(2) The evolution of radiation hardening due to high-temperature irradiations, especially at temperatures of interest to the nuclear industry (350 ℃) has yet to be investigated at different doses.

(3) The quantification of the radiation-induced dislocation loops as a function of dose and temperature is limited.

(4) The c-component loops are rarely characterized and their threshold incubation dose has yet to be investigated.

(5) All defects were characterized after irradiations. Observation of the evolution of damage structures as a function of dose and temperature through *in situ* TEM irradiation experiments has yet to be performed.

(6) The effect of the thermomechanical processing on the radiation damage resistance has not been clearly studied.

(7) The effect of alloying on the radiation damage in Ti-6Al-4V by varying alloy composition has yet to be investigated.

(8) Bulk mechanical testing of irradiated materials would allow for a better understanding of the dose/temperature dependence in Ti-alloys.

This dissertation work addresses a few of these gaps, namely (1) and (2), by performing ion-irradiation experiments on the commonly used Ti-6Al-4V alloy at two different temperatures (30 and 350 ℃) and different doses. The above-listed points, (6) and (7), are addressed by

comparing radiation damage in CP Ti and two Ti-6Al-4V alloys with different microstructures and slightly different chemical compositions. Finally, *in situ* TEM irradiation at the IVEM facility was used to investigate the evolution of radiation damage and perform quantitative microstructural studies [18] [19]. This dissertation focuses on the nucleation of radiation-induced defects, specifically dislocation loops (<a> and c-component loops), at initial damage stages and their accumulation at higher dose levels resulting in the final complex microstructure (see points (3)-(5)). Neutron irradiation experiments and subsequent mechanical testing are outside of the scope of this work and are recommended for future work in Chapter 6.

CHAPTER 3
EXPERIMENTAL METHODS

In this chapter, the materials and experimental procedures used in this dissertation work are described. The experimental conditions for *in situ* and *ex situ* irradiations are presented. The details of the TEM specimen preparation and the characterization methods are also included. Finally, the nanoindentation testing method and the dispersed barrier hardening model used to clarify structure-mechanics relationships are described.

3.1. MATERIALS

Three different materials were investigated in this study: CP Ti (ASTM Grade 2), Ti-6Al-4V (ASTM Grade 5) PM rolled and Ti-6Al-4V (ASTM Grade 23) AM[*]. The description of the Grade 2 CP Ti material, provided by the National Energy Technology Laboratory (NETL) in Albany, Oregon, can be found in [95]. The original CP Ti powder was produced through the Armstrong process [96], which is a metal halide reduction process where Ti tetrachloride metal gas is injected in liquid sodium to produce Ti metal. The Ti sponge, which is an output of the Armstrong process, was later compacted into an electrode and melted. The resulting 150 mm diameter ingot was triple vacuum arc remelted and then upset forged, forge flattened, and squared before rolling. The forging steps were performed above the β transus temperature, while the rolling passes were performed at temperatures below the β transus.

The AM Ti-6Al-4V samples in this study were provided by Linear Mold, Livonia, Michigan. The thermomechanical process used in this case was direct metal laser sintering

[*] See Table 2 for the description of ASTM grades.

(DMLS) followed by hot isostatic pressing (HIP) at 1050 ºC. The AM process is depicted in Figure 27. DMLS is a laser-based technique where the metal part is built layer by layer [97]. First, the printing machine deposits a film of the metal powder. Then, the high power laser beam, directed on the powder bed, fuses the metal powders present in its focal zone, according to a computer-assisted-design (CAD) file. This creates one metal layer. The platform moves down the preprogrammed layer thickness and the process described above is repeated until the part is fabricated [98, 99]. Since the build direction is an important parameter for AM [100 - 102], all samples used in this study were from the same build direction. The build direction for the samples used in the current work is illustrated in Figure 28. The layers were added horizontally from the bottom to the top as shown in Figure 28. The Grade 23 Ti-6Al-4V powder used was provided by Linear Mold and its composition is presented in Table 9. The powder had a spherical geometry and an average diameter of 45 μm.

The exact processing history of the Ti-6Al-4V Grade 5 powder metallurgy rolled samples are not known. The samples studied in this dissertation were all made from a rolled plate of 0.5 mm thickness.

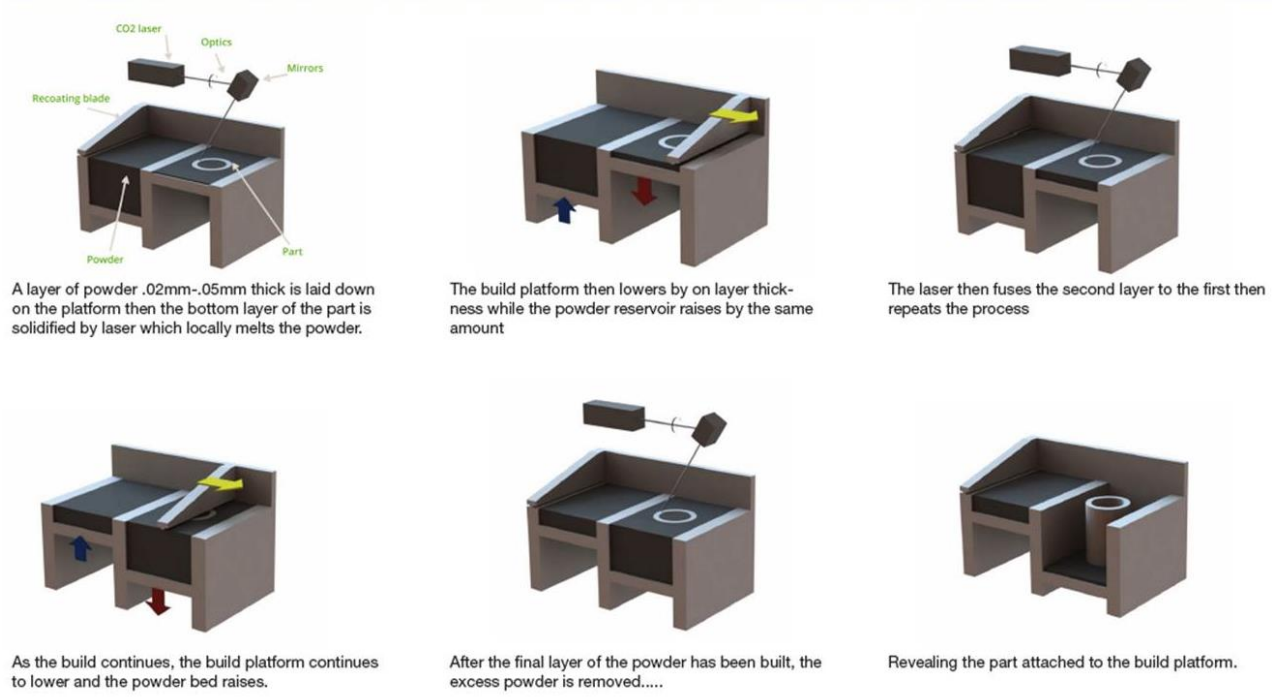

Figure 27. Representation of the powder bed process used by Linear mold © for the AM of the Ti-6Al-4V alloy. This figure was provided by Linear Mold, Livonia, Michigan.

Table 9. Ti-6Al-4V – Grade 23 powder composition used in the DMLS process.

	Ti	Al	V	Fe	O	N	C
wt.%	Bal	6.3-6.4	4	0.18	0.09-0.13	0.02	0.01

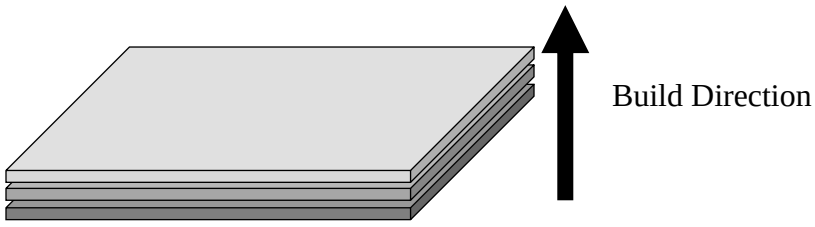

Figure 28. Schematic representation of the build direction during DMLS. Three layers of the deposited material are represented.

3.2. SAMPLE PREPARATION

3.2.1. Metallurgical samples

The samples were mechanically polished using silicon carbide (SiC) planar grinding papers starting from 600 up to 4000 grit. Water and dish soap were used for lubrication as well as rinsing the specimen before proceeding to the next grinding step. Each of these polishing steps lasted between 30 seconds to 120 seconds. The specimens were then polished sequentially using 6 µm, 3 µm, and 1 µm diamond paste, respectively. Each of these polishing steps lasted 10 to 15 minutes. Water and soap were used as lubricants and the specimens were cleaned with ethanol after the final polishing step. To achieve a mirror finish, the samples were polished between 1 and 2 hours with a chemical etching solution of 1 part H_2O_2 to 5 parts Struers OP-S colloidal silica (0.04 µm). To remove the residual colloidal silica after this step, each specimen was rinsed immediately under running water, gently wiped with a finger or a cotton swab moistened with dishwashing soap, then quickly rinsed and blow-dried. The entire cleaning process after the colloidal silica step lasted less than 5 seconds.

3.2.2. TEM samples

Metal sheets (0.5 mm initial thickness) were mechanically ground to a thickness of 300 µm using silicon carbide (SiC) planar grinding papers up to 2000 grit. After reaching a thickness of 300 µm, the sheets were gently polished down to 200 µm using 6 µm, 3 µm, and 1 µm diamond paste. Special care was taken to not apply too much force during the last polishing steps. Finally, a 0.5 µm diamond paste was used to polish the sheets down to a thickness between 100 and 150 µm. 3 mm discs were then carefully punched using a manual punch. The discs were electropolished using a Struers Tenupol 5 twin-jet electropolisher at a temperature

between -44 ºC and -30 ºC. A solution bath of 300 mL methanol, 175 mL 2-butanol, and 30 mL perchloric acid was used. The thickness of the transparent thin area in the TEM foils was estimated to be less than 100 nm. Low keV ion milling was performed as the last step to remove contaminants and improve TEM foil quality. The beam energy was between 2 and 3 keV and the milling angle was varied incrementally between 8º to 4º.

For samples irradiated *ex situ*, the samples were thinned to a thickness between 100 and 150 µm by mechanical grinding on the unirradiated side only. The irradiated surface was covered in Lacomit Varnish from Agar Scientific Ltd as shown in Figure 29-a. Afterword, during the electropolishing step, the material was only removed from the unirradiated side (see Figure 29-b). The samples were immersed in Lacomit varnish remover after electropolishing. Low keV ion milling was also performed to remove contaminants and improve TEM foil quality.

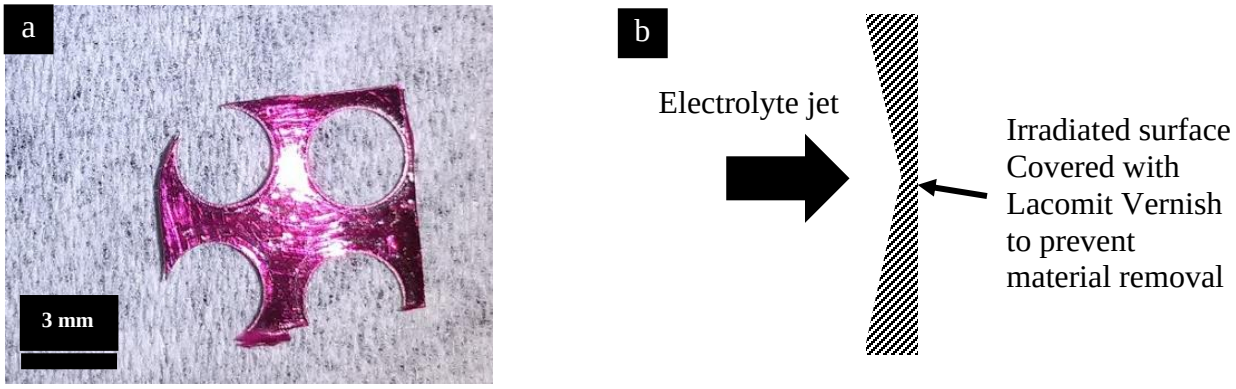

Figure 29. TEM preparation for a sample irradiated *ex situ*: a) The irradiated surface is covered by Lacomit varnish (Pink tint) after thinning and punching out 3 mm discs; b) Representation of the electropolishing for these foils.

3.3. IRRADIATION CONDITIONS

All ion beam irradiation energies used in this work were below the Coulomb Barrier energy. By having irradiation energies lower than this limit, the samples were not activated, which allowed their safe handling outside of hot cells. It also permitted the irradiation of relatively thick samples, which made it easier to evaluate the mechanical properties and deformation behavior. The experiments were performed at three different facilities:

- The IRRSUD beamline, part of the GANIL-CIMAP (Grand Accélérateur National d'Ions Lourds - Centre de Recherche sur les Ions, les Matériaux et la Photonique) in Caen, France was used. This beamline allows low-energy irradiation experiments (up to 1 MeV/A) with continuous measurement of the ion flux during irradiation.
- Sta. ANA (Stable ion Accelerator for Nuclear Astrophysics) or the 5U accelerator at the University of Notre Dame, IN was used in collaboration with The Institute for Structure and Nuclear Astrophysics (ISNAP). This is a single-ended vertical pelletron providing ion beam energies up to 5 MeV.
- The Intermediate Voltage Electron Microscopy (IVEM)-Tandem Facility of Argonne National Laboratory (Chicago, IL) was used. The TEM interfaces with an ion beamline with ion energies up to 1 MeV and is incident from above at 30° to the electron beam, allowing *in situ* irradiations during observation under controlled sample and diffraction conditions.

3.3.1. Dose calculation

The software 'The Stopping and Range of Ions in Matter' (SRIM-2013) [103] was used to determine ion ranges, collision events, and deposited energy. This Monte Carlo simulation

code uses different ion stopping theories, such as Brandt–Kitagawa theory and Lindhard, Scharff and Schiott theory (LSS-theory), to calculate the ion stopping power and range from a large selection of ions and different target materials (compounds included) [103]. Figure 30 presents an example of the output files from SRIM [103] for the irradiation of Ti-6Al-4V with Ar ions at an energy of 36 MeV. The trajectories of simulated 5000 Ar ions, the ions ranges, and the simulated collision events are illustrated in Figure 30.

The Displacement per Atom (dpa) estimation is performed using the software Transport of Ions in Matter (TRIM) [103]. The equation for the dpa rate follows:

$$dpa\ rate\ (\frac{dpa}{s}) = D \times \frac{F}{N} \quad \text{Eq. 3}$$

- *D*: Damage rate in the sample from the TRIM [103] output file [vacancies/(ion-Angstrom)];
- *F*: Ion fluence, $F = I/(q*A)$ [ions.cm^{-2}.s^{-1}], *I* - Beam current, *q* - Charge, *A* – Irradiation area;
- *N*: Atom number density, $N = N_A * \rho / M$ [cm^{-3}], $N_A = 6.022.10^{23}$ mol^{-1} – Avogadro number, *M* – molecular mass (g.mol^{-1}), ρ – mass density (g.cm^{-3})

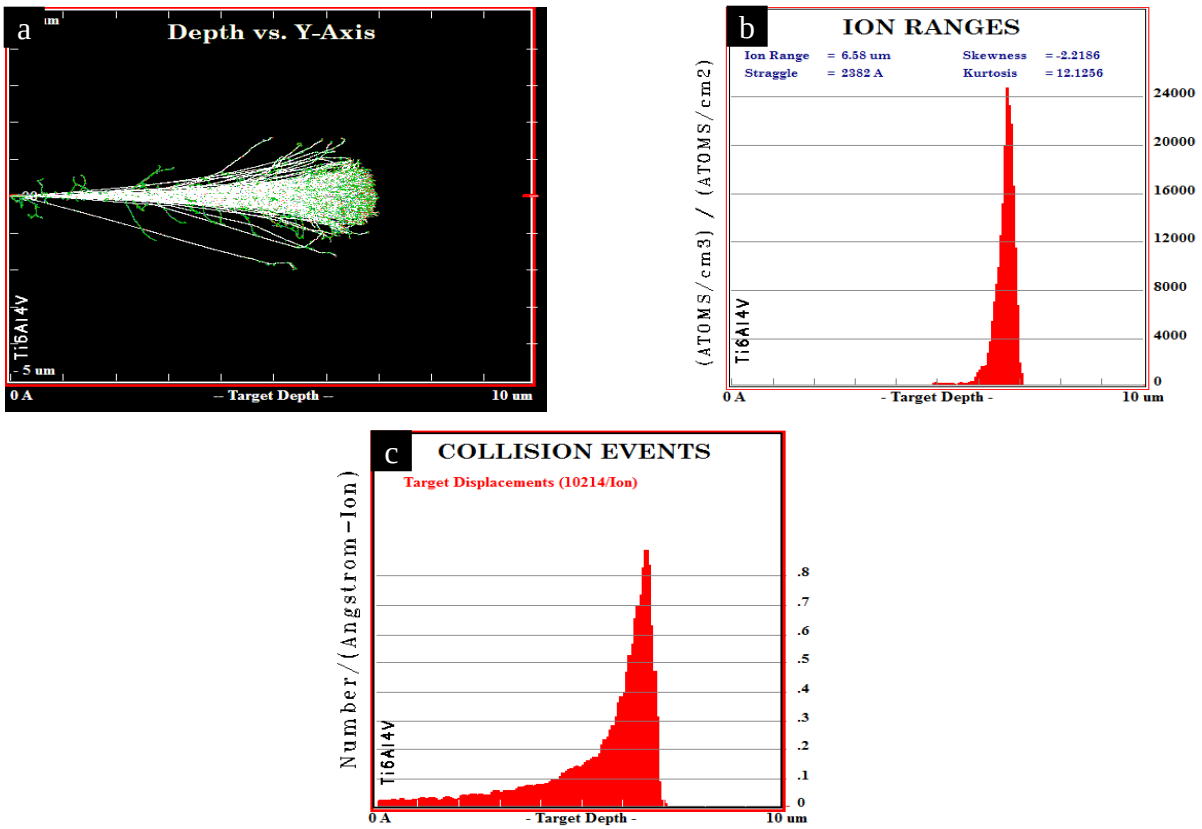

Figure 30. Example output plots from SRIM [103] calculation using a Ti-6Al-4V target irradiated with a 36 MeV Ar ion beam: a) Cross section view of the simulated trajectories of 5000 ions in a 10 um, b) Ion ranges as a function of the target depth; c) Collision events as a function of the target depth.

3.3.2. *Ex situ* irradiation experiments

Table 10 contains a description of the irradiation conditions as well as the irradiated materials in all the *ex situ* experiments presented in this dissertation. Bulk samples were irradiated using three different ion beams (see Table 10). The irradiation temperatures were selected as 30 ℃ and 350 ℃. Cooling or heating systems were used to maintain the desired temperature during the irradiation experiment. The temperature was measured during the experiments using thermocouples attached to the back of the copper plate where the samples

were mounted using conductive silver paste (PELCO ® High Performance Silver Paste, Product No 16047). This paste can be diluted with water after the irradiation to remove the samples.

Lower dose irradiations, up to 1 dpa, were only performed on Ti-6Al-4V PM rolled samples. Additionally, with the ^{36}Ar at 36 MeV beam, two of the Ti-6Al-4V samples were irradiated with a 6 µm CP Ti foil on the surface. This foil was used as a beam degrader in order to have a higher damage dose closer to the surface, as shown in Figure 31. The electronic energy loss S_e and the nuclear stopping power S_n for these samples were calculated using SRIM [103]. The sample with the Ti-foil on the surface exhibited a higher electronic excitation energy S_n on the surface (~ 0.25 keV nm^{-1}) and lower S_e (~1.4 keV nm^{-1}) compared to the sample without the Ti-foil (S_n ~ 0.015 keV nm^{-1} and S_e ~7.4 keV nm^{-1}).

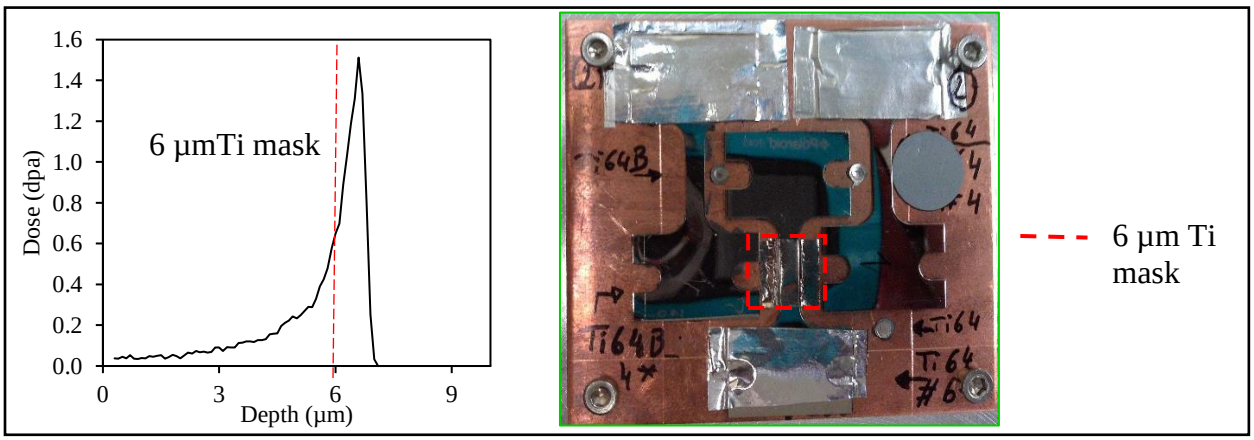

Figure 31. The SRIM-2013 [103] calculation of the dose in a Ti-6Al-4V sample for the ^{36}Ar beam @ 36 MeV with a fluence of 10^{15} ions.cm^{-2}.

All beam dose profiles are illustrated in Figure 32. At the Bragg peak, corresponding to a maximum irradiation dose, the ions from the irradiating beam are implanted in the material. For the high dose irradiation with Ar @ 4 MeV, the Bragg* peak was located 2.9 µm below the

* Not to be confused with the X-ray diffraction Bragg peak. As the ions pass through the material, they lose energy. The curve of the ion energy loss rate is referred to as the Bragg curve, exhibiting a peak where the ions stop. This peak is called the Bragg peak.

surface and for the Ar @ 36 MeV the peak was 6.6 µm below the surface. The Bragg Peak depth is important in determining the ion implantation depth for each of the conditions. Since studying ion implantation is outside of the scope of this study, nano-indentation measurements were all performed at a depth well above the Bragg peak for most irradiated samples.

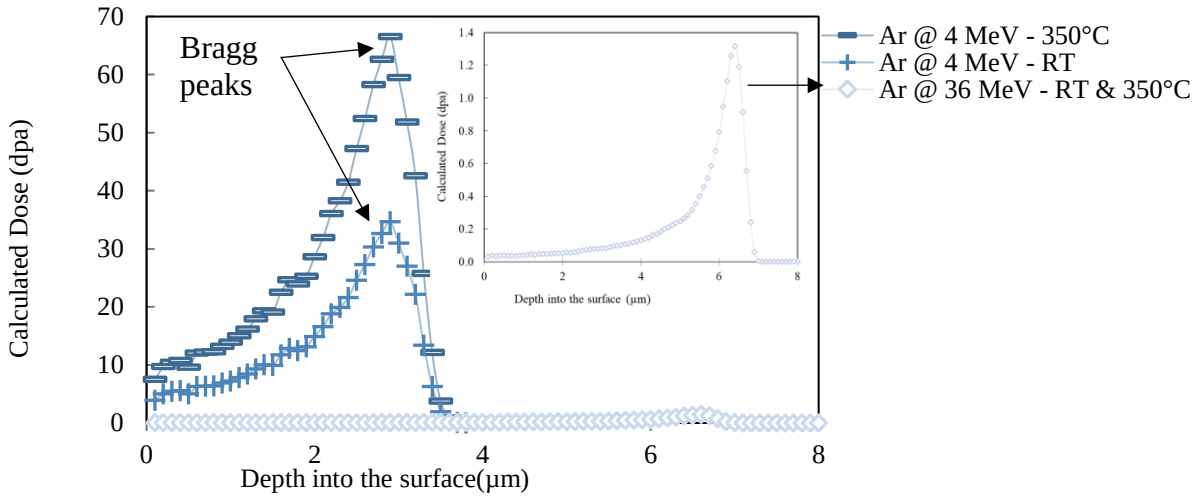

Figure 32. Irradiation dose as a function of depth below the material surface for all the ion beams used in the *ex situ* irradiation.

Table 10. Summary of the *ex situ* irradiation conditions. The irradiation dose indicated is the dose at the probed depth by nanoindentation.

Beam	Energy (MeV)	Ion range (µm)	Se (keV/nm)	Flux (ions/cm^2.s^{-1})	Fluence (ions/cm^2)	T (°C)	Dose (dpa)	Material
^{36}Ar	36	6.8	7.5	2.10^{10}	10^{15}	30	0.08	Ti-6Al-4V PM
^{36}Ar	0.76	0.6	1.4	2.10^{10}	10^{15}	30	1.03	Ti-6Al-4V PM
^{36}Ar	36	6.8	7.5	4.10^{10}	10^{15}	350	0.08	Ti-6Al-4V PM
^{36}Ar	0.76	0.6	1.4	4.10^{10}	10^{15}	350	1.03	Ti-6Al-4V PM
^{40}Ar	4	3.8	3.16	$2.18.\ 10^{13}$	$4.8.10^{16}$	350	16	Ti-6Al-4V PM, Ti-6Al-4V AM, CP Ti
^{40}Ar	4	3.8	3.16	$3.5\ 10^{13}$	$2.5.10^{16}$	30	8.0	Ti-6Al-4V PM, Ti-6Al-4V AM, CP Ti

3.3.3. *In situ* irradiation experiment

In situ irradiation experiments were performed using a Hitachi H-9000NAR transmission electron microscope (TEM) interfaced with a tandem ion accelerator at the (IVEM) - Tandem Facility of Argonne National Laboratory (Chicago, IL). The range of Kr ions in a Ti-6Al-4V target, estimated with SRIM, is 389 nm. A typical TEM sample thickness of 100 nm allows for homogeneous irradiation of the whole thickness. The dose profile for the different *in situ* irradiation experiments is shown in Figure 33. The remaining details of the *in situ* irradiations are provided in Table 11. The samples were mounted in a double-tilt heating holder and were tilted around an angle of 15° to maintain a normal incidence angle of the Kr ion beam to the surface sample.

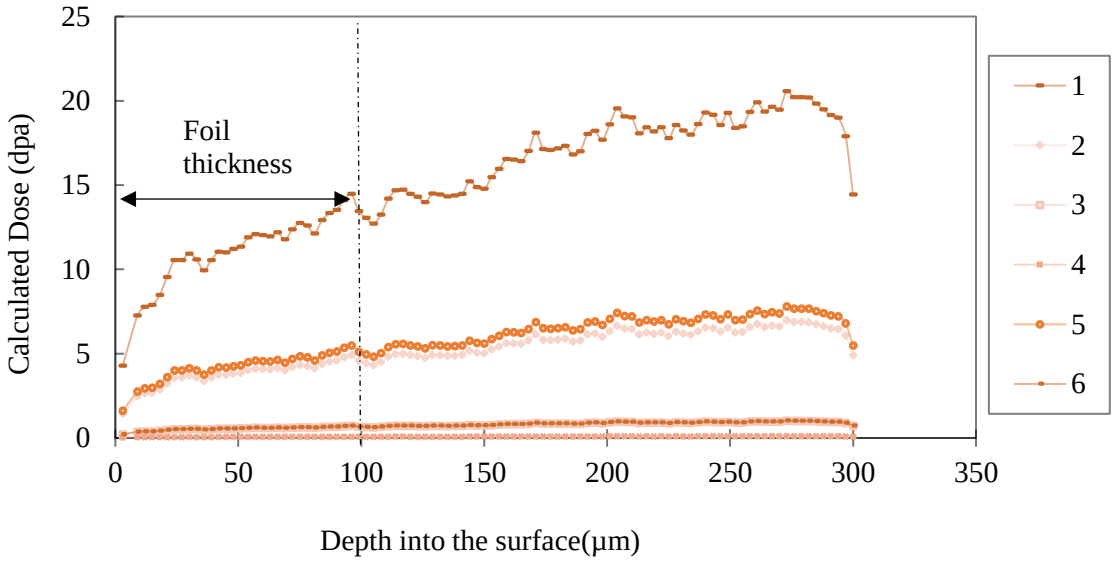

Figure 33. Irradiation dose of Kr ion beam in Ti-6Al-4V as a function of depth below the material surface for all the different *in situ* irradiation experiments. The numbers in the legend refer to the experiment numbers provided in Table 11.

Table 11. Summary of the *in situ* irradiation conditions with 1 MeV ^{82}Kr ions.

Beam	Energy (MeV)	Range (um)	Se (keV/nm)	Flux (ions.cm^2.s^{-1})	Fluence (ions.cm^{-2})	T (°C)	Material	Dose (dpa)	Exp #
$^{82}Kr^{+1}$	1	0.4	2.3	3.8×10^{11}	5×10^{15}	30	CP-Ti	11.13	1
				3.8×10^{11}	1.7×10^{15}	350		3.79	2
				3.8×10^{11}	2.5×10^{15}	430		0.56	3
				6.3×10^{10}	2.5×10^{15}	450		0.06	4
				3.8×10^{11}	1.9×10^{15}	350	Ti-6Al-4V – (AM)	3.74	5
				3.8×10^{11}	2.5×10^{15}	430		0.56	6
				6.3×10^{10}	1×10^{15}	450		0.22	4

3.4. TEM IMAGING AND COUNTING METHODS

3.4.1. TEM Weak Beam imaging

TEM is routinely used to observe and image irradiation-induced defects in metals. In simple terms, TEM is based on the interaction of the incident electron beam with a thin foil containing a few atom planes arranged according to the crystal structure of the material [104]. Bragg's law provides a useful depiction of the main interaction of interest to this work, namely the diffraction of the incident electron beam by the material, see Figure 34. The equation relating the diffraction angle θ, the distance d between the atomic planes, and the mean free path of an electron between scattering events λ is called Bragg's law:

$$\lambda = 2dsin(\theta) \qquad \text{Eq. 4}$$

As depicted in Figure 34, the diffracting planes act as mirrors for the incident electron beam. These diffracted beams produce the diffraction spots in the Selected Area Electron Diffraction Pattern (SAEDP). An example of the zone axis SAEDP is shown in Figure 35-a. These spots are called reflections and the vector between the direct beam and one of the reflections is called the diffraction vector **g**. The Miller-Bravais notation *hkil* is used to refer to

the indices of the diffracted planes and are equivalent to the Miller indices (hkl) of the diffracting crystal plane (or some multiple thereof).

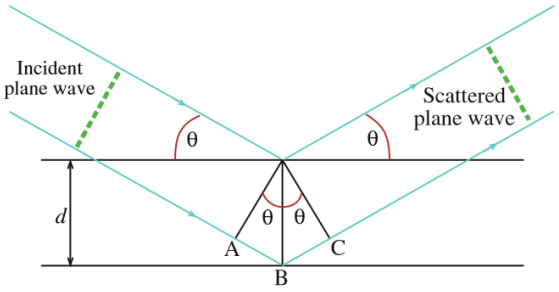

Figure 34. The Bragg description of diffraction in terms of the reflection of a plane wave incident at an angle θ to atomic planes of spacing d. The path difference between reflected waves is AB + BC [104].

The recommended method for imaging dislocations and specifically dislocation loops is weak beam (WB) diffraction in either the dark field (DF) or bright field (BF) mode [105]. A description of the set up of the condition for WB BF imaging is presented in Figure 35. The choice of the diffraction conditions, namely the initial zone axis diffraction condition and the selected ***g*** vector, is the first step in acquiring useful images for the defect characterization.

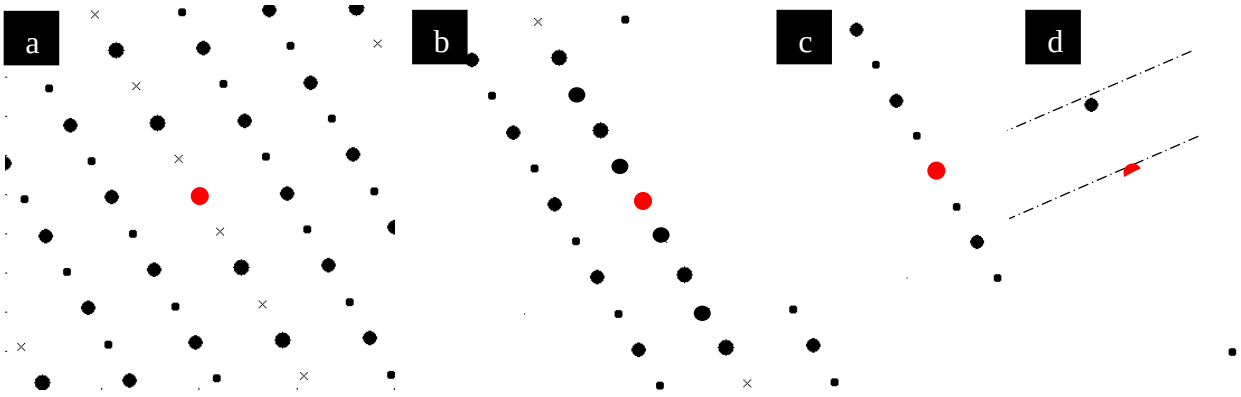

Figure 35. Schematic representation of the set up for a WB diffraction condition for the $[2\bar{1}\bar{1}0]$ zone axis with the direct beam highlighted in red: a) Tilting the foil to the $[2\bar{1}\bar{1}0]$ zone axis; b) Tilting away from the zone axis; c) Condition where the desired row of **g** vectors is excited; d) Condition where only the direct beam and 2**g** are excited and Kikuchi lines are presented as a dashed black line. These diffraction patterns were simulated for the α-phase Ti using the software CrysTBox [106].

The current study focuses on the nucleation and growth of dislocation loops in Ti-alloys. Therefore, two types of dislocation loops were investigated:

- <a> type dislocation loops with a Burgers vector $\mathbf{b} = \frac{1}{3} < 2\bar{1}\bar{1}0 >$ that can be imaged with $\mathbf{g}=01\bar{1}0$.
- c-component dislocation loops in the basal planes that can be imaged with $\mathbf{g} = 0002$.

The habit nucleation planes for <a> loops and c-component loops are illustrated in Figure 36.

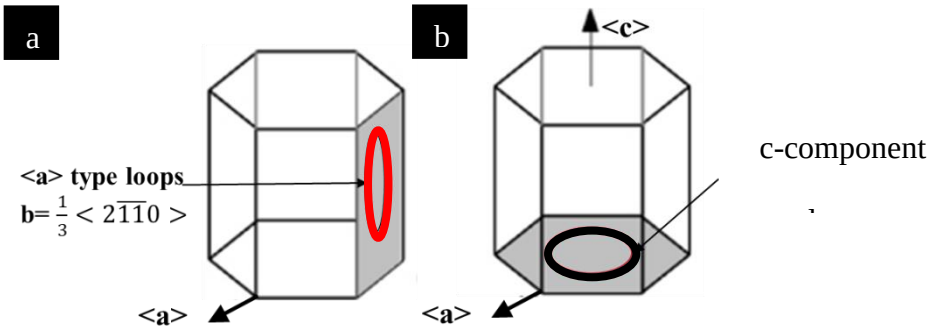

Figure 36 . Nucleation planes for (a) <a> and (b) c-component dislocation loops in hcp materials.

The selection of the TEM diffraction imaging conditions is essential for the characterization of these dislocation loops. Tilting to the $[2\bar{1}\bar{1}0]$ zone axis (see Figure 37) allows for the distinction between <a> and c-component loops since perpendicular g vectors can be selected to image each type of loops. The diffraction conditions to observe the loops were set up close to the Weak Beam (WB) BF condition for the $[2\bar{1}\bar{1}0]$ zone axis. The **g** vectors used to image each of the loops are shown in Figure 37 and Figure 38.

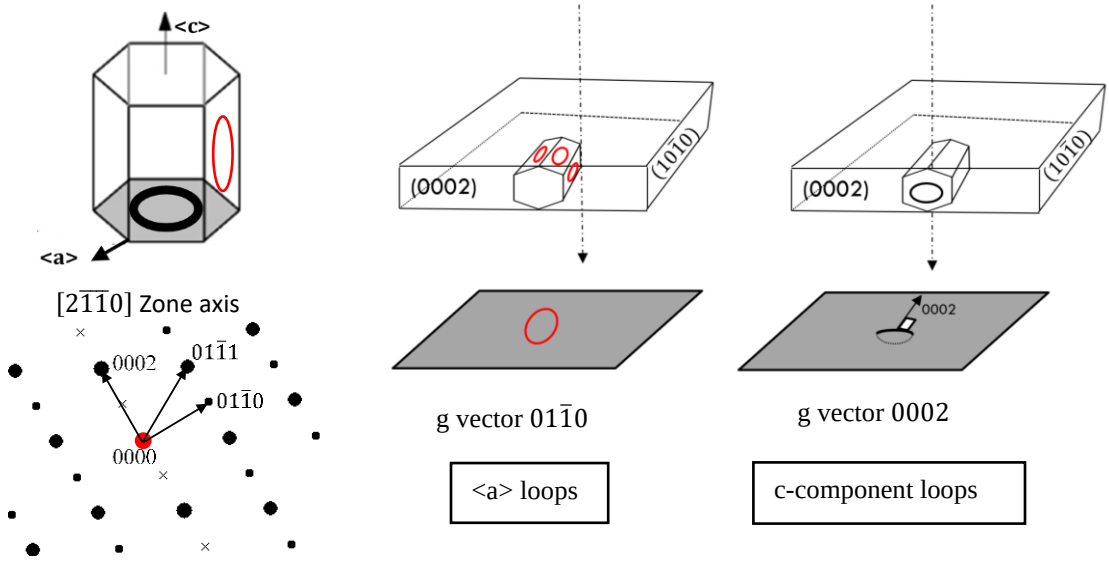

Figure 37. Schematic representation of the TEM imaging of <a> and c-component loops in a [2$\bar{1}\bar{1}$0] zone axis in using the two **g** vectors 01$\bar{1}$0 and 0002.

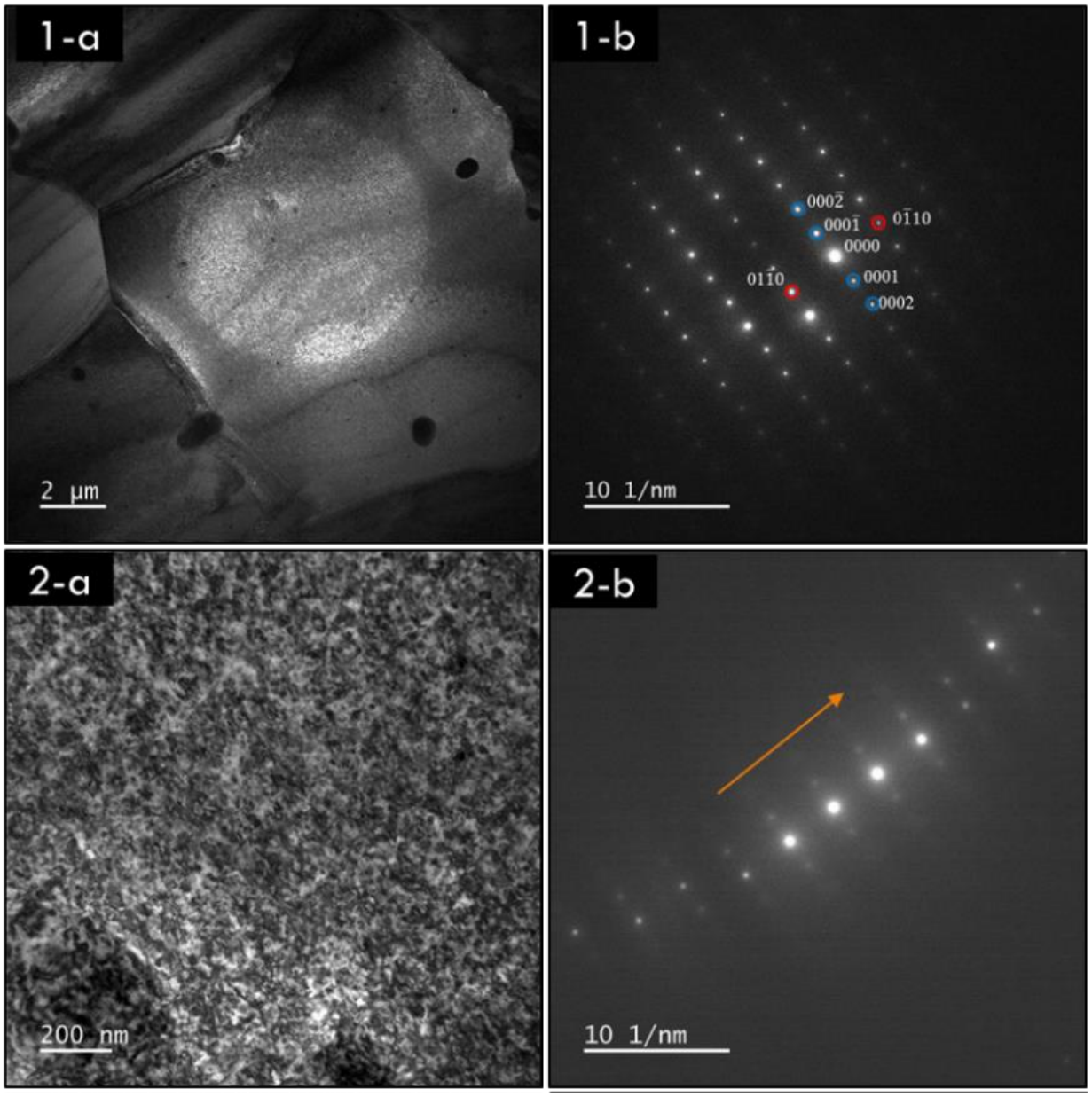

Figure 38. Example of the identification of dislocation loops in CP Ti irradiated with 1 MeV Kr ions at 450 ℃: 1-a) Selected grain and (1-b) its corresponding diffraction pattern close to the $[2\bar{1}\bar{1}0]$ ZA, 2-a) BF TEM photomicrograph with 2-b) its corresponding diffraction condition for **g**=$01\bar{1}0$, 3-a) BF TEM photomicrograph with 3-b) its corresponding diffraction condition for **g**=0002, 4-a) Magnified BF image showing c-component loops indicated with blue arrows and 4-b) Magnified BF image showing <a> loops indicated with red arrows.

Figure 38. (cont'd)

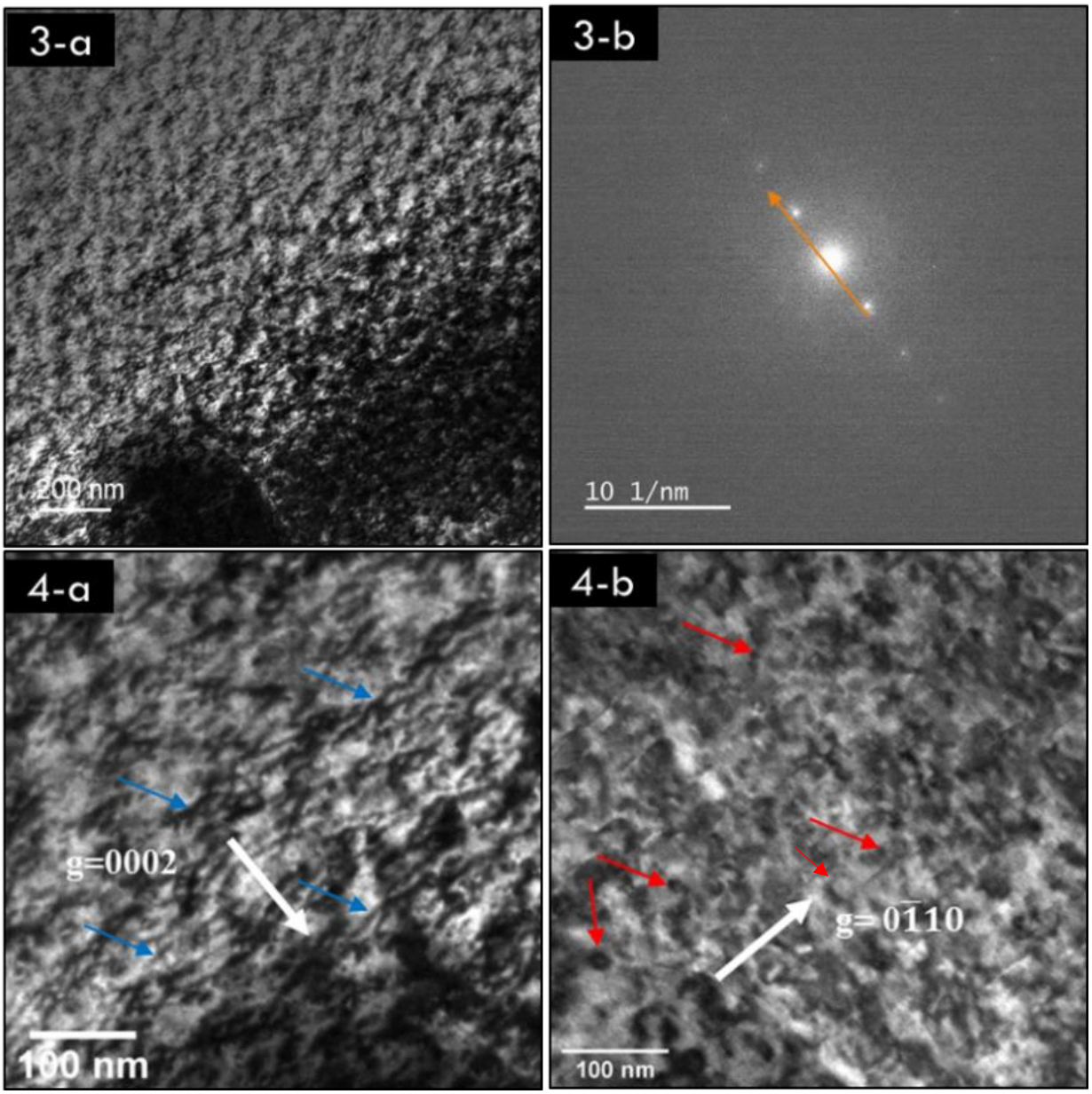

3.4.2. Transmission Kikuchi Diffraction (TKD)

Transmission Kikuchi diffraction was used to characterize the foils prior to the TEM characterization. The goal of this characterization was to locate grains that were oriented close

to the $[2\bar{1}\bar{1}0]$ zone axis. Such grains are desirable for performing the described TEM characterization in 3.4.3 and 3.4.4.

The samples were loaded on a particular sample holder capable of imaging thin foils. The Transmission-EBSD Sample Holder, specifically designed to hold 3 mm foils, was purchased from EDAX-TSL (Mahwah, NJ). An electron reflection plate was used to account for the thickness difference in each sample. The sample holder was mounted inside a field emission Tescan Mira3 SEM equipped with an EDAX-TSL EBSD system.

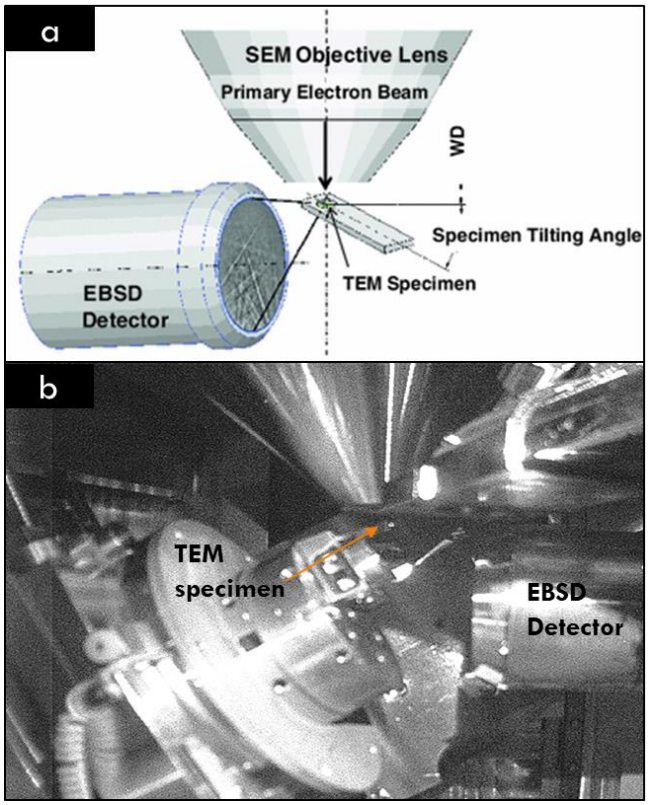

Figure 39. TEM specimen setting arrangement for TKD: a) General layout [107], b) Image of the set up inside the MIRA 3 SEM chamber.

Figure 39 shows the tilted stage and the detector position. A sample tilting angle of -20° was used. The working voltage was 30 kV. The working distance was approximately 4.3 mm. The spot size varied between 20 to 50 nm. Grain orientation maps were then acquired using

TEAM software from Oxford. A step size between 50 and 100 nm was used. A 1×1 binning setting and an acquisition speed of about 5 points per second were used for all the TKD scans.

Figure 40 illustrates the typical images acquired during the TKD characterization used to locate grains that were oriented between $[2\bar{1}\bar{1}0]$ and $[10\bar{1}0]$ zone axis (with visible 0002 Kikuchi line). The difference between the orientation of the foil between TKD and TEM observation was not measured. After finding the desired grains, the samples were imaged using a 100CX JEOL TEM to confirm the selected orientations.

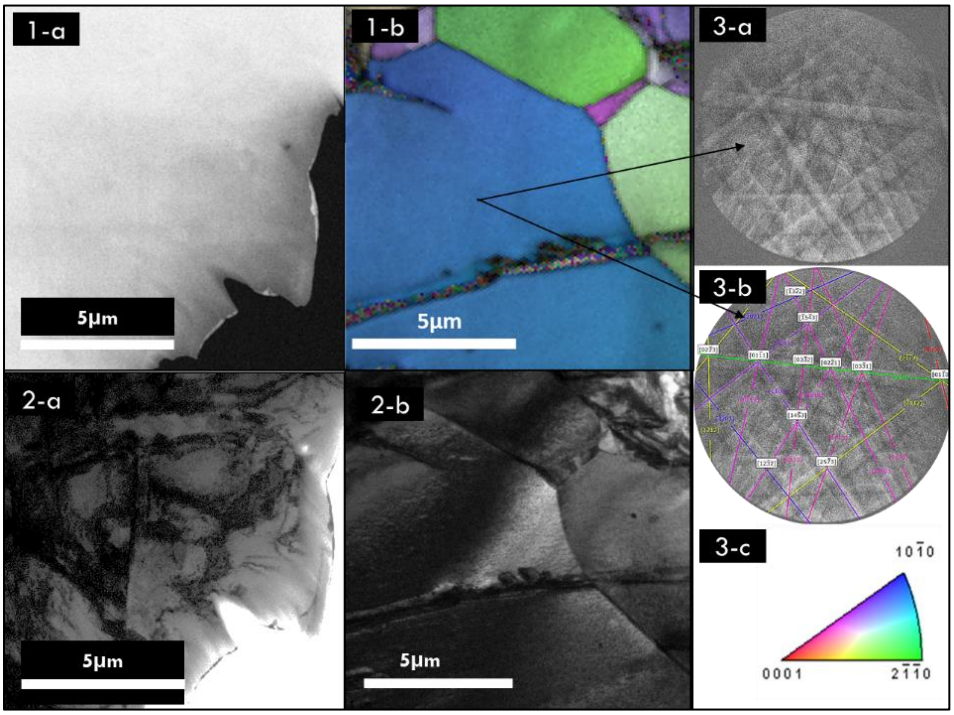

Figure 40. Illustration of an example of grain identification for TEM using TKD. The grain orientation was between $[2\bar{1}\bar{1}0]$ and $[10\bar{1}0]$ ZA: 1-a) SEM image of the distinctive edge used as a marker, 1-b) EBSD inverse pole figure of the selected area, 2-a) Low magnification TEM micrograph of the distinctive edge used as a marker, 2-b)) High-magnification TEM photomicrograph of the selected area; 3-a) Unindexed Kikuchi pattern in the selected grain; 3-b) Indexed Kikuchi pattern in the selected grain; 3-c) corresponding color scale unit triangle for image 1-b.

3.4.3. Counting of <a> loops

BF and DF TEM photomicrographs were acquired using **g** = $01\bar{1}0$, to observe <a> loops. This **g** vector is obtained by tilting the TEM foil to the weak beam condition, **g** = $01\bar{1}0$, after identifying the $[2\bar{1}\bar{1}0]$ zone axis, as shown in Figure 37. An example of a DF TEM photomicrograph is shown in Figure 41-a. The outlines of the <a> loops were traced in the Fiji software [108] using a Microsoft pen on a touch screen surface for high precision line tracing. An example of identified <a> loops is provided in Figure 41-b.

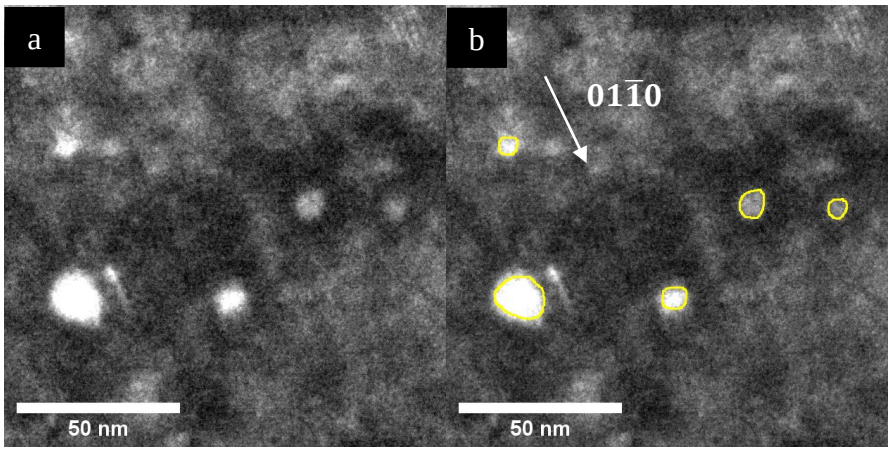

Figure 41. Example of identification of <a> loops: a) DF TEM photomicrograph showing the <a> type dislocation loops for CP Ti irradiated with 1 MeV Kr ion beams at 350 °C. The loops appear circular when imaged using **g** = $01\bar{1}0$; b) Identified loops with the highlighted outlines in yellow.

3.4.4. Counting of c-component loops

TEM BF photomicrographs were acquired under specific diffraction conditions to observe the c-component loops and distinguish them from <a> loops. C-component loops appear as a line when imaged edge on using **g** = 0002 as shown in Figure 42. This **g** vector is obtained by tilting the TEM foil in the weak beam condition **g** = 0002 after identifying the $[2\bar{1}\bar{1}0]$ zone axis as shown in Figure 37.

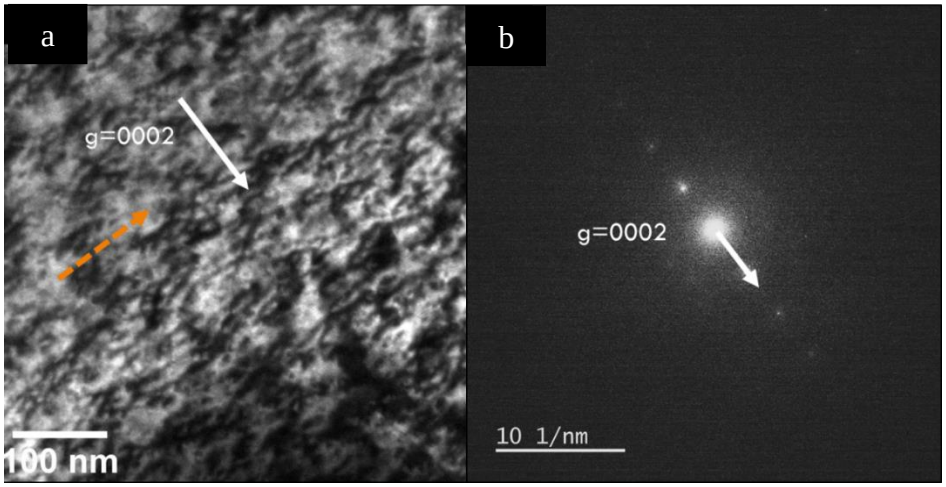

Figure 42. Example of identification of c-component loops: a) BF TEM photomicrograph showing the c-component dislocation loops in CP Ti irradiated with 1 MeV Kr ion beams at 430 °C. The loops appear as lines parallel to the direction of the orange arrow when imaged using **g**=0002; b) Corresponding diffraction pattern.

The BF TEM photomicrographs of ion irradiated CP Ti samples were uploaded to Fiji [108], the image processing software used in this characterization. In each image (880.8 nm x 880.8 nm), 3 to 5 areas (880.8 nm x 201 nm) were selected and magnified to assist with the counting of c-component loops.

The c-component loops were identified by the Burgers vector **b**, which is perpendicular to **g** = 0002. The Fiji software [108] was used to draw the outline of each identified dislocation line and number them as shown in Figure 43. The outline of each c-component loop was overlayed to the direction perpendicular to **g** = 0002. To be included, the outline of the loop was required to lie within an angle of 5º to the theoretical direction of the c-component loops[*]. After validation of the selected loops, their length was generated automatically by Fiji [108].

[*] Perpendicular to **g** = 0002.

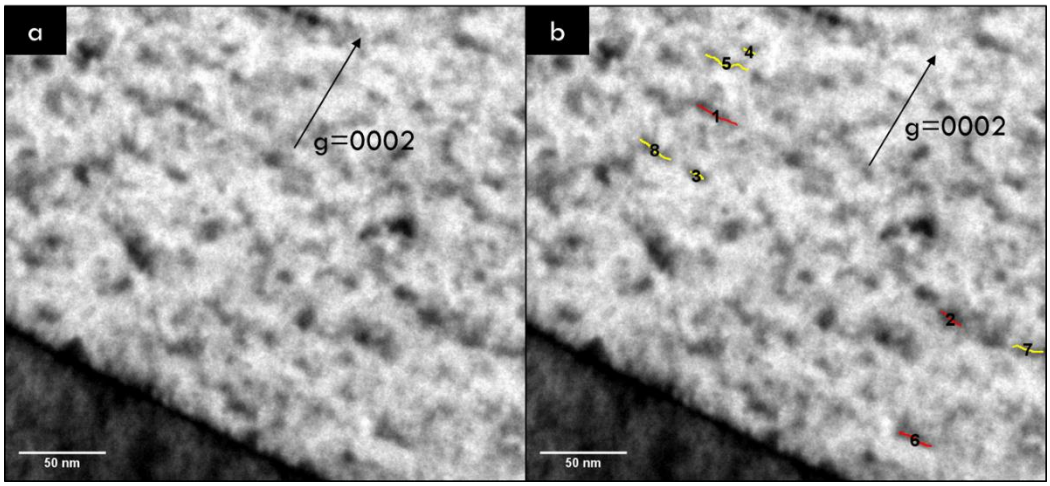

Figure 43. Magnified image showing a) BF TEM photomicrograph showing the c-component dislocation loops in CP Ti irradiated with 1 MeV Kr ion beam at 30 ℃. The loops appear as lines perpendicular to the direction of the imaging g vector, **g** = 0002; b) Eight possible loops were identified.

In Figure 44, the identified loops in Figure 43 were overlaid with the theoretical direction[*] for c-component loops represented by a white arrow. Based on the above-mentioned criteria, the loops 3, 4, 5, 7 and 8 were confirmed as c-component loops. Loops 1, 2, and 7 deviated more than 5 degrees from the theoretical direction for the c-component loops and were therefore not included in the analysis.

[*] Perpendicular to **g** = 0002.

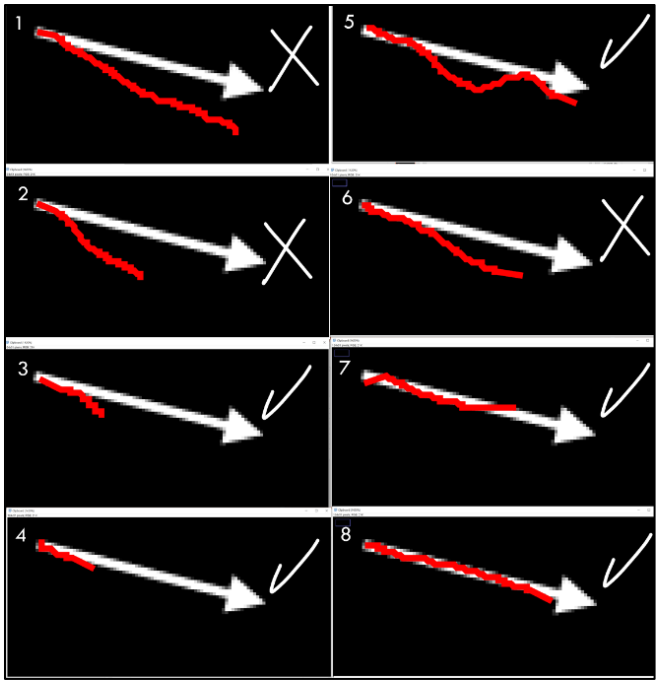

Figure 44. The 8 loops identified in Figure 43 overlaid with the direction perpendicular to the **g** vector 0002. Loops 3, 4, 5, 7 and 8 were confirmed as c-component loops, while loops 1, 2, and 7 deviated more than 5º from the theoretical direction for the c-component loops and were therefore not included in the analysis.

3.4.5. Measurements

3.4.5.1. Size of the dislocation loops

The size of the <a> loops was defined as the observed length of the loop (nm). Figure 45 illustrates an example of <a> dislocation loops, and their size is reported in Table 12. For the c-component loops, the size of the loops was defined as the length of the observed dislocation length when observed edge-on. An example of the identification of c-component loops is shown in Figure 46. Their lengths are reported in Table 13. Figure 47 shows the distribution of the length of c-component dislocation loops.

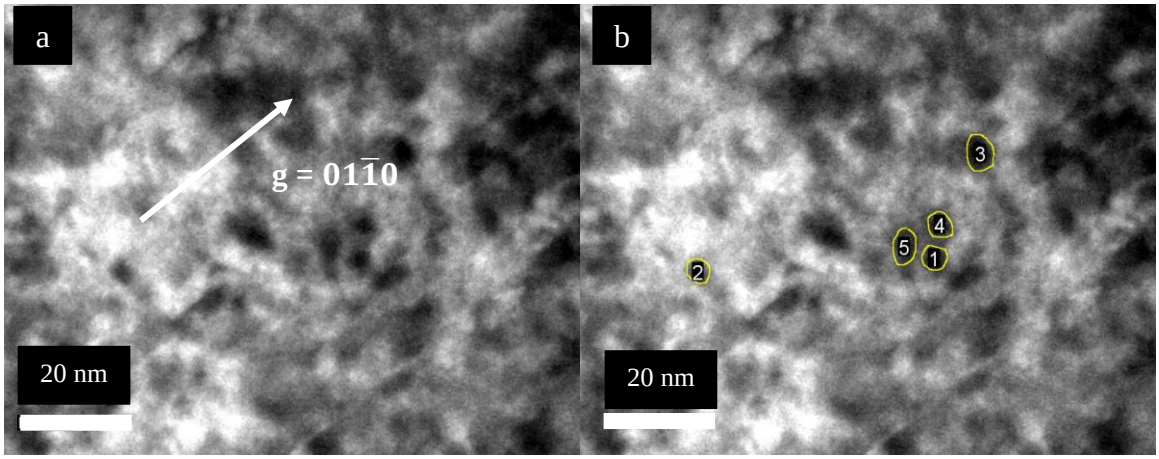

Figure 45. Identified 5 <a> loops in CP Ti irradiated *in situ* with 1 MeV Kr ions at 430 ℃: a- BF photomicrograph of an area imaged using **g** = 01$\bar{1}$0; b- Outline of the 5 <a> loops (Note that there are other loops in this figure that are not highlighted).

Table 12. The measurements of the <a> loops identified in Figure 45 using Fiji [108]

Loop #	Area (nm^2)	Perimeter (nm)
1	35.837	30.056
2	34.681	29.271
3	46.241	39.4
4	37.456	31.8
5	43.929	36.5

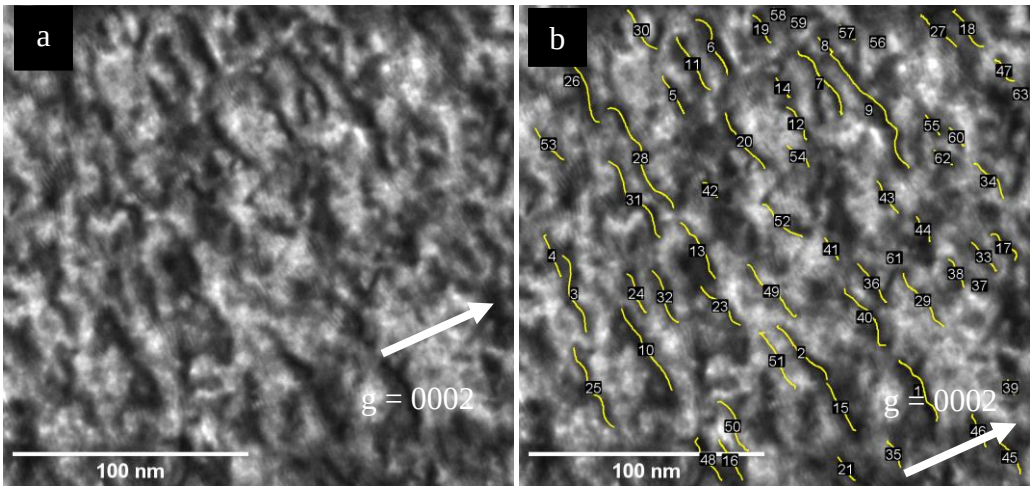

Figure 46. Identified c-component loops in CP Ti irradiated *in situ* with 1 MeV Kr ions at 360 ℃ at a dose of 1.9 dpa: a- BF photomicrograph of an area imaged using **g** = 0002; b- Outline of the c-component loops highlighted in yellow.

Table 13. The measurements of the diameter of c-component loop identified in Figure 46 using Fiji [108]

Loop number	Loop diameter (nm)
1	32.576
2	32.523
3	35.514
4	19.153
5	18.478
6	29.008
7	36.249
8	9.071
9	63.159
10	41.033
11	26.902
12	17.101
13	28.797
14	10.438
15	23.684
16	19.942
17	17.602
18	21.542
19	14.326
20	29.321
21	12.221
22	24.137
23	18.935
24	40.374
25	45.156
26	20.711
27	54.333
28	29.533
29	21.298
30	41.425
31	25.2
32	15.917

Loop number	Loop diameter (nm)
33	20.666
34	13.106
35	20.454
36	6.442
37	13.699
38	6.666
39	32.405
40	10.807
41	9.162
42	16.504
43	12.413
44	17.437
45	14.966
46	13.356
47	21.756
48	31.482
49	26.658
50	30.658
51	22.449
52	18.319
53	13.257
54	10.254
55	6.512
56	8.952
57	6.869
58	5.381
59	9.976
60	3.482
61	9.928
62	5.704

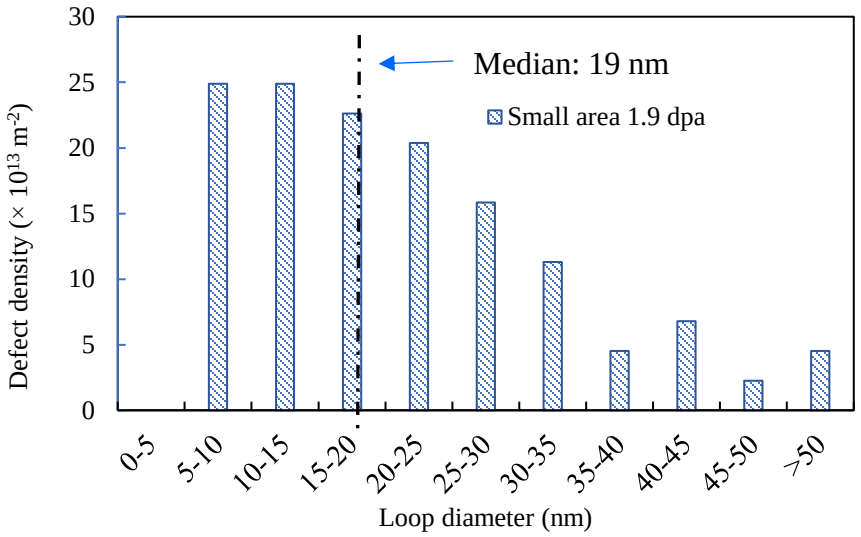

Figure 47. The distribution of c-component loop diameters quantified in Figure 46. The y-axis corresponds to the number of the loops in each diameter bin divided by the total area studied.

3.4.5.2. Dislocation density

The dislocation density is calculated from the acquired TEM photomicrographs at the specified diffraction conditions. The evolution of the defect density as a function of irradiation dose is observed in the same area and as a result, in the same volume for each sample. The two measurements of the dislocation densities used are defined below:

- **Area dislocation number density:** This is a measure of the number of specific dislocation loop types (<a> or c-component) in a unit area.
- **Dislocation number density:** This is a measure of the number of specific dislocation loop types (<a> or c-component) in a unit volume.
- **Linear area dislocation density:** This is a measure of the sum of the length of the specific dislocation loop types in a unit area

3.5. NANOINDENTATION EXPERIMENTS AND METHODS

3.5.1. Experimental

Nanoindentation measurements were carried out using an Agilent Technologies G200 Nano Indenter. The continuous stiffness measurement (CSM) module used in the present study exhibits a displacement resolution below 0.01 nm. A Berkovich tip was used with a strain rate of 0.05 s^{-1}. The distance between indents was 100 μm and the value for the Poisson ratio was 0.33.

Multiple indents were performed on each of the studied samples (between 36 and 100 indents). Figure 48 shows an example of indent matrices on the surface of irradiated CP Ti at 30 °C and 350 °C. Due to indenter size effects* (ISE) [110], values of hardness for indentation depths below 100 nm were not considered. The Berkovich tip used in the nano-indentation experiments provided a compromise between a moderate pile-up and a small plastic zone size [111]. The median values were used for the analysis to minimize the effect of outliers.

* This refers to the apparent increase in hardness at shalloy depths during indentation experiments. Nix and Gao [109] explained this strain gradient, most significant at small indentation depths, to be an effect of geometrically necessary dislocations (GND). As the indenter pushes into the surface, these GNDs are required to account for the permanent deformation and thus will contribute to the measured hardness of the material.

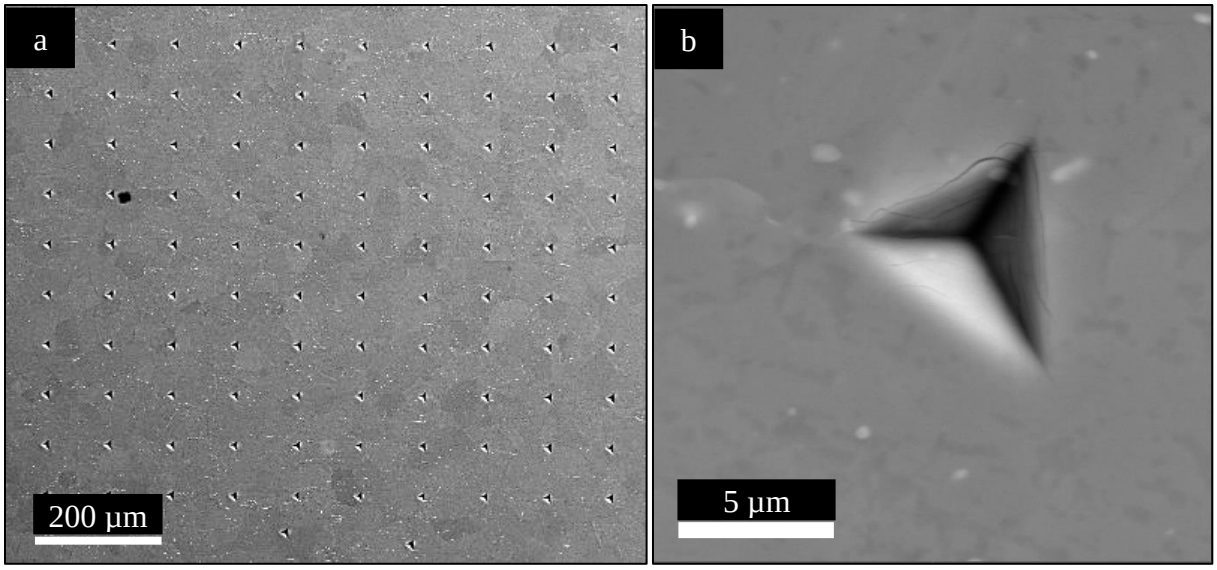

Figure 48. BSE SEM photomicrographs showing an example of the indents in CP Ti sample irradiated with Ar @ 4 MeV at 350 ℃ up to 16.2 dpa: a) Lower-magnification photomicrograph of the indentation grid; b) Higher-magnification photomicrograph depicting only one indent.

For ion irradiated FeCrAl alloy, Hardie et al. [111] proposed an adjustment of the measured hardness by accounting for the difference between the contact area, as given by the nanoindentation instrument, and what they defined as the actual contact area, measured directly on SEM images of the indents at different depths. They estimated the error on the hardness measurements, at depths between 50 nm and 200 nm, to be between 10% and 50%. As a result, only hardness values at depths between 200 nm and 400 nm were included in the discussion of the results from the current work.

For each set of measurements, the standard deviation for the nanoindentation measurements, σ, was calculated. Assuming a confidence interval of 95% (two sided T-test), the plotted error is the standard error of the mean (SEM) multiplied by a factor 2* for a sampling size *n* (number of indents) between 36 and 100 [112]. The error was expressed as:

* Corresponds to the critical *t* value for a two sided T-test with n values between 36 and 100 and a confidence interval of 95%.

$$s_{error} = 2 \times \frac{\sigma}{\sqrt{n}}, \quad \text{Eq. 5}$$

The change in hardness value was calculated by subtracting the hardness of the unirradiated sample from the hardness of the irradiated sample at the same depth:

$$\Delta Hardness = H_{irradiated} - H_{non\ irradiated} \quad \text{Eq. 6}$$

The error corresponding to $\Delta Hardness$ was estimated using the propagation law for uncertainty [113], and is calculated using the formula:

$$s_{eDiff} = \sqrt{(s_{error})_{irradiated}{}^2 + (s_{error})_{non\ irradiated}{}^2} \quad \text{Eq.7}$$

3.5.2. Dispersed Barrier Hardening (DBH)

In the dispersed barrier hardening model, the short-range interactions between the moving dislocation as it comes into direct contact with the obstacles are quantified [114 - 116]. For a moving dislocation line to pass around strong barriers separated by a distance *l*, as illustrated in Figure 49, the applied stress must be at least equal to the average internal stress, and for spherical particles, this is given by the shear stress τ [117]. These obstacles are assumed to be randomly distributed on the slip plane of the dislocations.

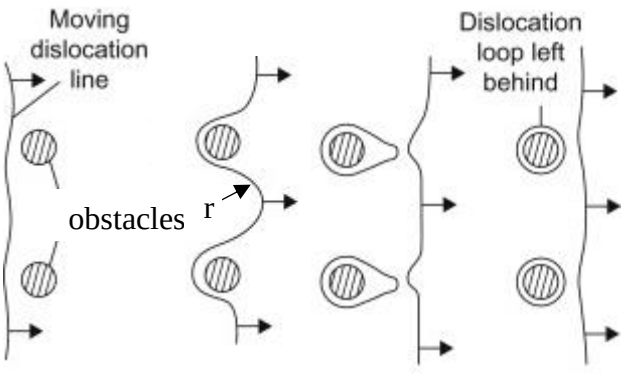

Figure 49. Schematic representation of Orowan bowing: A dislocation in motion encounters two obstacles, bows to a radius r before passing and leaving dislocation loop behind around the obstacle. This illustration is adapted from [117].

In dispersion hardening, the obstacles remain undeformed and the yield stress is the stress necessary to expand a loop of dislocation between them [118]. The maximum curvature *r* that this dislocation can bow to is the distance *l* separating these obstacles. This is described by the following equation, known as Orowan stress [119]:

$$\tau = \frac{\alpha \mu b}{l} \qquad \text{Eq. 8}$$

- α is the obstacle strength factor, varies in the range of 0–1 and strongly depends on the types of defects.
- μ is the shear modulus of the material.
- *b* is the magnitude of the Burgers vector.

Estimating the value of *l* is necessary to find the value of τ. In the case of DBH, the friction stress due to a dispersion of barriers depends on the distance *l* between the obstacles in the slip plane of the moving dislocation. This distance separating two obstacles having a radius *r* and intersecting a unit area of the slip plane is shown in Figure 50. The distance between these obstacles can be estimated using the obstacle number density ρ_n, representing the concentration of these randomly distributed obstacles in a unit volume [120]. The number of obstacles in this

volume element is estimated to be equal to the number of intersections per unit area on the slip plane $2r\rho_n$ [120].

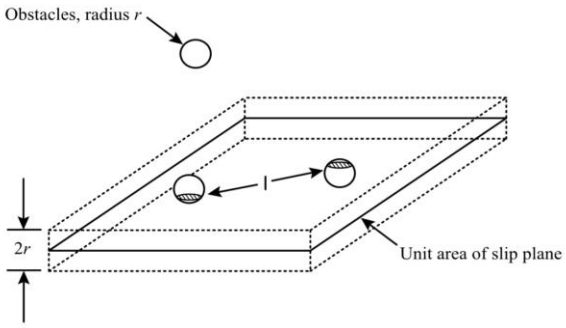

Figure 50. Graphic representation of the intersection of spherical obstacles of radius *r* and spacing *l* with a unit area of a slip plane. This figure is reproduced from [116, 120].

As a result, the distance *l*, defined as the average obstacle spacing along the slip plane is calculated as:

$$l = \frac{1}{\sqrt{2r\rho_n}} \qquad \text{Eq. 9}$$

This shear stress τ can be related to the yield stress σ_y by the Taylor factor [121]:

$$\sigma_y = \mathrm{M} \times \tau = \frac{\mathrm{M}\alpha\mu\mathrm{b}}{\mathrm{l}} \qquad \text{Eq. 10}$$

Radiation-induced defects such as dislocation loops are considered obstacles to dislocation motion. The contribution of these defects to the increase in the yield stress as a result of irradiation can be quantified using the following equation [122] [23]:

$$\Delta\sigma_{yDefects} = \alpha_{defects}.M\mu b\sqrt{(\rho_n.d)} \qquad \text{Eq. 11}$$

For Ti, the magnitude of the Burgers vector for prism slip is equal to 0.295 nm. The value to be used for the shear modulus μ is 38 GPa [16]. The factor $\alpha_{defects}$ is defined as the barrier strength, and accounts for the fact that some obstacles may be partially cut or sheared as the dislocation segments bow out and break away. For impenetrable Orowan obstacles, α is equal to 1. The values of the factor $\alpha_{defects}$ were mainly inferred from fitting experimental data.

In the current work where dislocation loops are the obstacles, α has values between 0.02 and 0.15 for Ti, as shown in Table 14. Dislocation loops can be considered relatively weak, meaning they can be sheared by gliding dislocations during deformation (Friedel cutting) [123]. The clearing of these defects during deformation can produce dislocation channels and highly localized deformation [124].

Table 14. Examples of values of barrier strength factors for irradiated materials from the literature.

Materials	Irradiation beam	T (°C)	Dose (dpa)	Barrier strength factor		Ref
				Dislocation loops	Precipitates	
Pure Zr	5 MeV Zr	300	0.5, 5	0.1	-	[125]
Zr-2.5Nb				0.1		
Zr-5Nb				0.1		
Pure W	Neutron	-	0.03 -2.2	0.15		[126]
Pure Ti	6 MeV Ti	430	0.6-3	0.15 (<a> loops), 0.02 (c-component loops)		[33]
Ti-6Al-4V	6 MeV Ti	430	0.6-3	0.9 (<a> loops)	1	[33]
Pure Ti	520 MeV Protons	RT	4×10^{-4}, 4×10^{-3} and 3×10^{-2}	0.04 <a> loops		[14]
Pure Cu	14-MeV neutron	RT	-	0.23		[127]

For CP Ti, the factor α representing the obstacle strength of <a> and c-component loops can be taken initially as equal to 0.15 and 0.02, respectively [33]. These coefficients were inferred from experimental data of grade 2 Ti irradiated with 6 MeV Ti ions at 430 °C up to a dose of 3 dpa. Since the application of the dispersed barrier model may result in irradiation dose-dependent barrier strength factors [127], these values may be tuned later. With the values of α between 0.01 and 0.5, an updated version of Eq. 10, here called Modified DBH, can be used [128]:

$$\Delta\sigma_{ydefects} = \alpha'_{defects}.M\mu b\sqrt{N.d}\left[1+\sqrt{\frac{\pi\rho_n.d^3}{6\alpha}}\right]$$

With: $\alpha'_{defects} = \sqrt{\frac{2\pi\alpha^3}{3}}$ Eq. 12

The Taylor factor M for α-phase Ti varies between 5 [129] and 2.5 [33] depending on the texture of the material [130]. For low-temperature deformation and assuming type 1 prism mode, the value of 2.5 was chosen for this study [131]. This value was used to study a similar Grade 2 Ti [33].

Table 15. Summary of the parameters used in this analysis

Parameter	Value
M	2.5
μ	38 GPa
$\alpha_{<a> loops}$	0.15
$\alpha_{c\text{-component loops}}$	0.02
$b_{gliding\ dislocation}$	0.295 nm

3.5.3. Estimation of the dose at the indentation depth

Figure 51 is an illustration of the nanoindentation on the surface of irradiated samples. It shows the probed depth and the plastic zone radius [110]. Estimating the irradiation dose for the measured hardness results was performed by taking into account the interaction volume.

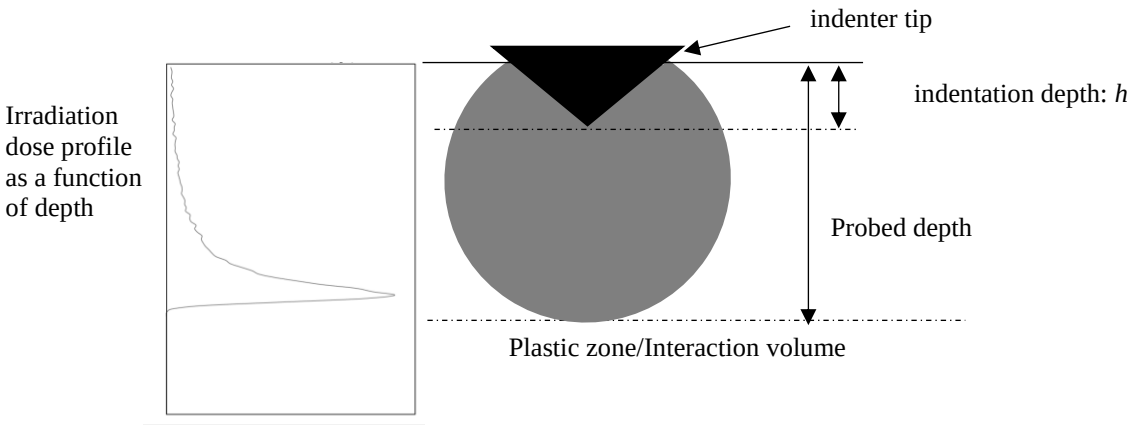

Figure 51. Schematic representation of the indentation on the surface of the irradiated samples.

The plastic zone radius increased proportionally to the indentation depth based on measurements on TEM micrographs of Focused Ion Beam (FIB) liftout samples of ion irradiated FeCrAl alloy [111]. In Figure 52, the data from Hardie's paper [111] is reproduced. It is noted that the data shown in Figure 52 is only for the measurements made using a Berkovich tip since this was the indenter tip used in the current study. Based on the slope of the plastic zone radius as a function of depth, the probed depth equivalent to the radius of the plastic zone was approximately four times the indentation depth. This approximation will be applied to Ti and Ti-alloys in the curent work.

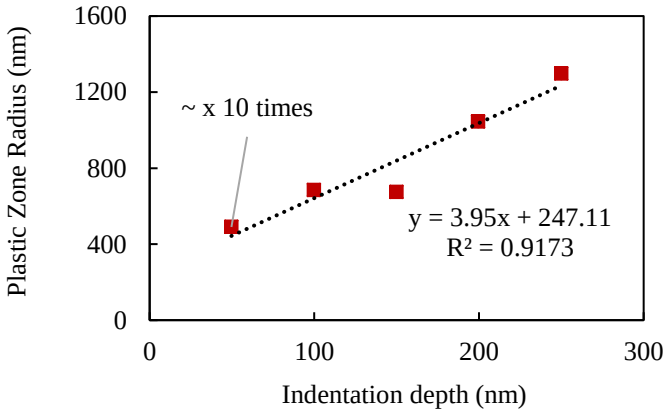

Figure 52. Plastic zone radius as a function of indentation depth for ion irradiated Fe12%Cr Alloy. This graph is adapted from [111].

The irradiation dose profiles were adjusted by taking into account this plastic zone and are shown in Figure 53. The corrected dose in Figure 53-b is the average of the irradiation dose calculated from SRIM [103] (Figure 53-a) over the probed depth (~ four times the indentation depth).

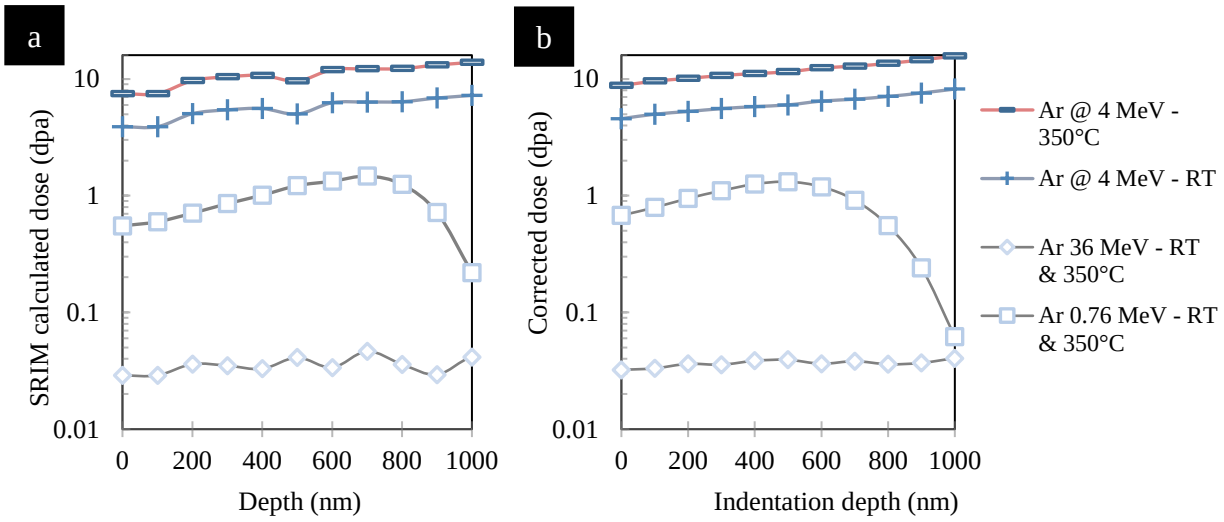

Figure 53. Dose profiles for the different ion beam irradiation energies: a) Irradiation dose as calculated previously from SRIM [103] as a function of material depth, b) Corrected dose for the measured indentation depth. Note that dose on the y axis is in the logarithmic scale.

3.5.4. Comparing results with different irradiation particles

In this work, dislocation loop evolution as a function of temperature and dose was investigated. In the discussion Chapter 5, results from the current ion irradiations were compared to previously published results on Ti and Ti-alloys.

In comparing the results of different irradiating particles, the effect of the temperature and dose rate on the diffusion of point defects should be taken into account [61]. In the current work, the dpa rate for *in situ* experiments was between 8.4×10^{-4} dpa/s and 10^{-3} dpa/s. As for the *ex situ* irradiation experiments, the dose rate was between 6.5×10^{-3} dpa/s and 9×10^{-3} dpa/s. Figure 54 [61, 132] is a representation of the effect of dose rate and temperature on the

production of freely migrating defects. In the recombination domain, a large fraction of created vacancies and interstitials recombine, leading to either annihilation of these defects or the formation of defect clusters. At higher temperatures, radiation-enhanced diffusion leads to a local chemical redistribution identified as RIS [133].

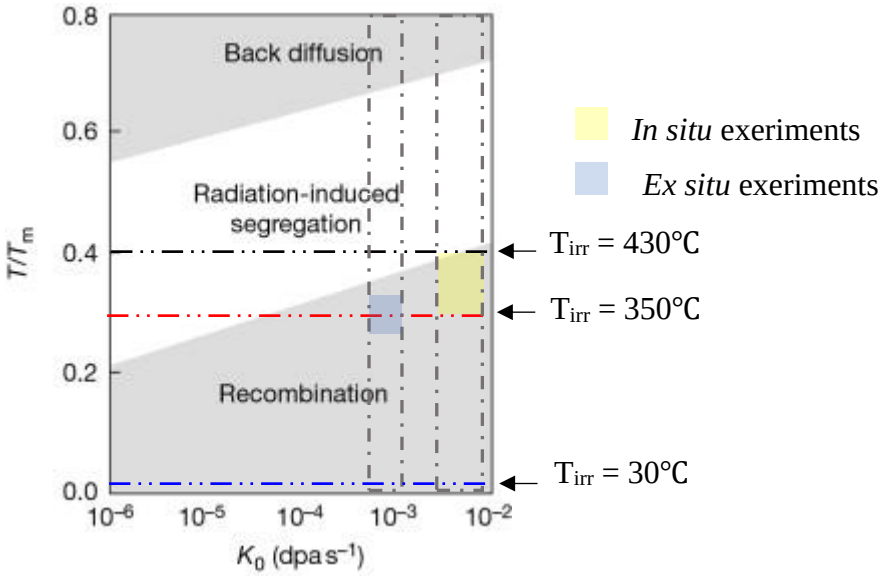

Figure 54. Temperature and dose rate effect on radiation-induced segregation. Figure is adapted from [61].

As can be seen in Figure 54, the ratio T/T_m of the temperatures used both *in situ* and *ex situ* experiments in the current work, 430 ℃, 350 ℃ and 30 ℃ are represented by a black, red and blue dashed line respectively. All these irradiation conditions fall into the recombination dominant regime. To account for the difference between the different irradiating particles, when the temperature is within the recombination-dominated regime and if the net flux of vacancies over interstitials to a particular type of sinks is invariant, a temperature shift can be calculated [17, 134]. Increasing the irradiation dose rate can be considered equivalent to increasing the temperature. This shift between irradiation with a higher dose rate at T_2 and a lower dose rate at T_1 is calculated using the following equation [17, 134]:

$$T_2 - T_1 = \frac{\left(\frac{kT_1{}^2}{E_{vm}+2E_{vf}}\right)\ln\left(\frac{K_2}{K_1}\right)}{1-\left(\frac{kT_1}{E_{vm}+2E_{vf}}\right)\ln\left(\frac{K_2}{K_1}\right)} \quad \text{Eq. 13}$$

E_{vm} is the migration energy of vacancies (For Ti, $E_{vm} = 0.50$ eV [135]) and E_{vf} is the vacancy formation energy ($E_{vf} = 1.96$ eV [135]). K_1 and K_2 are the dose rates and k is Boltzman's constant $k = 8.617 \times 10^{-5}$ eV/K.

Two other experiments will be used in the discussion section where proton [14] and neutron [12] irradiations were performed to probe radiation damage in Ti alloys. The temperature shift to be considered is presented in Table 16.

Table 16. The temperature shift calculated for two different irradiations conditions in [12, 14] using the dose rate for 1 MeV Kr irradiations.

Tirr (℃)	Dose rate (dpa/s)	ΔT	Irradiating particle	Reference
40	3×10^{-6}	12	590 MeV Proton	[14]
250	4×10^{-6}	31	590 MeV Proton	[14]
50	5×10^{-9}	27	Neutron	[12]
350	5×10^{-9}	108	Neutron	[12]

CHAPTER 4
RESULTS

In this chapter, the results from the as-received microstructure characterization, the nanoindentation experiments, and the *in situ* TEM irradiation experiments are provided. For each material, the grain size was measured, and the texture was characterized using electron backscattered diffraction (EBSD). Next, nanoindentation results of samples irradiated *ex situ* with Ar beams were presented to probe the change in mechanical properties in the three materials. The radiation hardening was determined at 30 ℃ and 350 ℃ from the nano-hardness results.

To understand the effect of radiation damage structures on the radiation hardening, a study of the evolution of the radiation damage in CP Ti irradiated *in situ* with Kr ion beams was performed at the IVEM-Tandem facility at Argonne National Laboratory. The irradiation temperatures in these experiments were 30 ℃, 360 ℃ and 430 ℃ and results of the observations of the nucleation and growth of <a> and c-component dislocation loops are reported.

4.1. MICROSTRUCTURE OF THE AS-RECEIVED SAMPLES

4.1.1. CP Ti

Electron Backscatter Diffraction (EBSD) and Scanning Electron Microscopy (SEM) imaging techniques were used to characterize the microstructure of the samples.

Representative SEM images of the microstructure of CP Ti (Grade 2) are shown in Figure 55. The microstructure consisted of large α-phase grains (between 20 and 40 μm). The average grain size was 30 μm, measured using the line intercept method [136]. As shown in Figure 56-a,

the EBSD orientation map exhibited a variety of colors* for the scanned area with no strongly prevalent color observed. In Figure 56-b, the {0001} peak locations were aligned almost perpendicular to the x-direction and a moderate fiber texture (approximately 6 times random) was observed. The TEM photomicrographs in Figure 57 show the initial, as-received grain structure where precipitates of 1 μm size were observed. EDS (Energy Dispersive Spectroscopy) characterization of these precipitates indicated that they were Fe rich, see Figure 58.

* In EBSD orientation maps, colors represent different grain orientation, see color scale unit triangle in Figure 56-a.

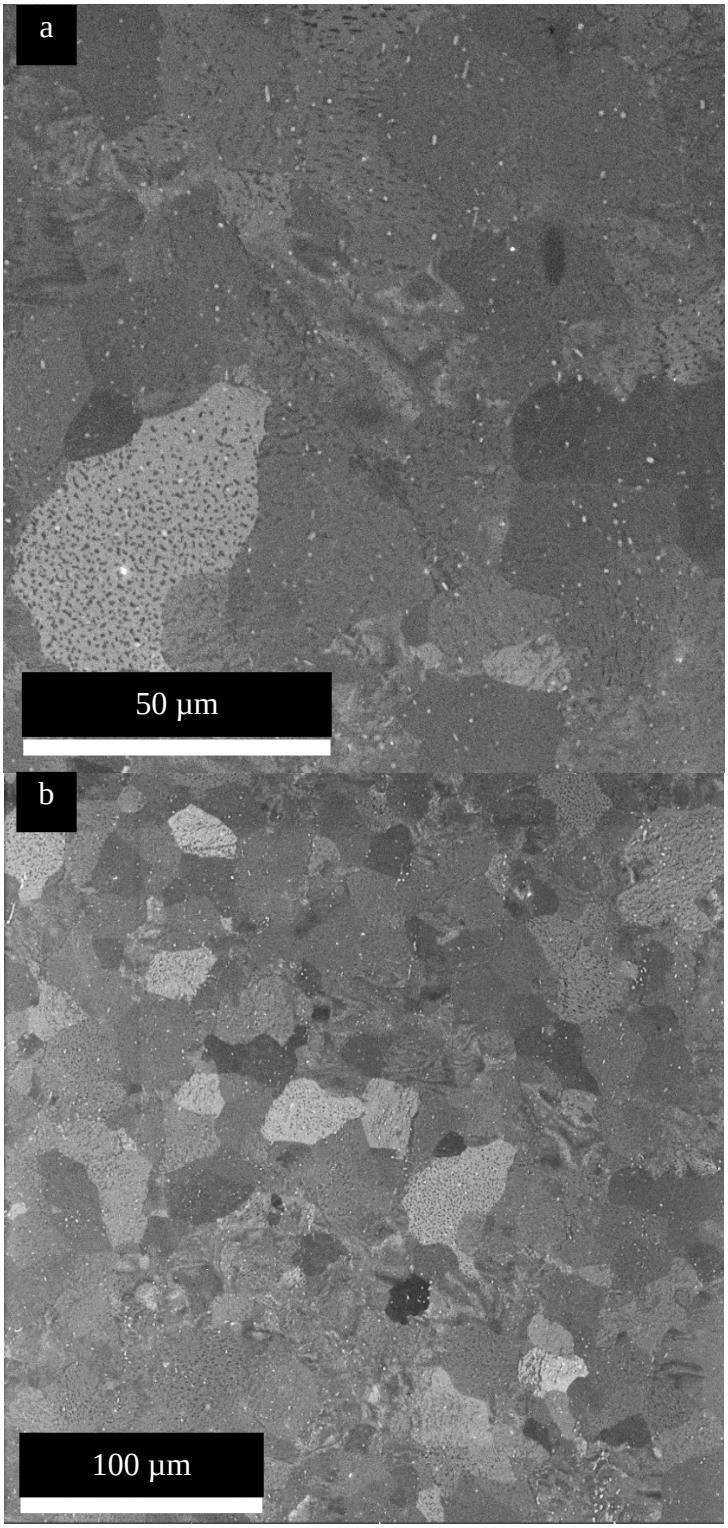

Figure 55. SE SEM photomicrographs showing the representative microstructure of CP Ti: (a) high- and (b) low magnifications.

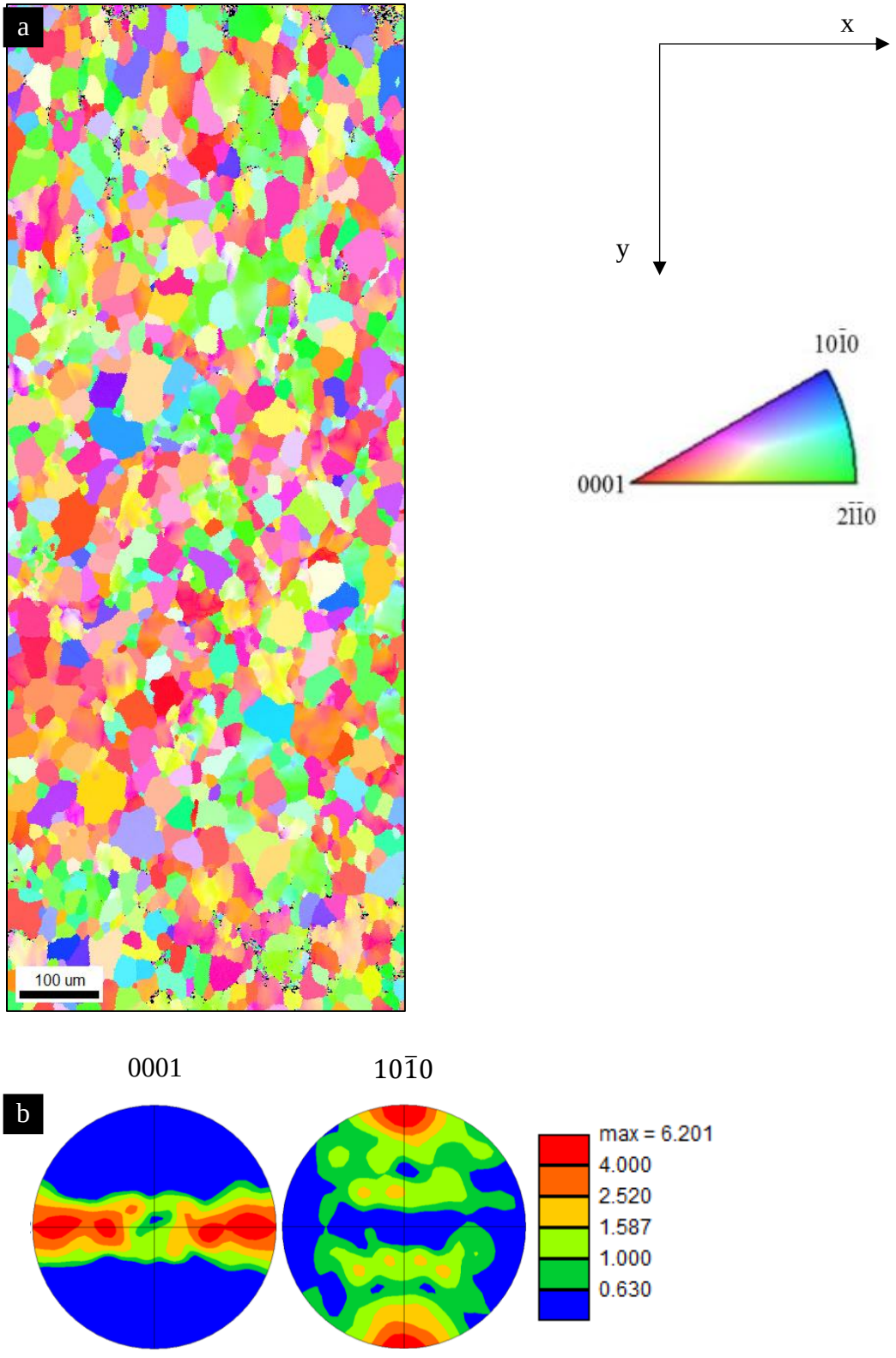

Figure 56. EBSD data of the CP Ti used in this study: a) EBSD IPF (Inverse Pole Figure) map with the corresponding color scale unit triangle; b) The {0001} and the {$10\bar{1}0$} pole figures.

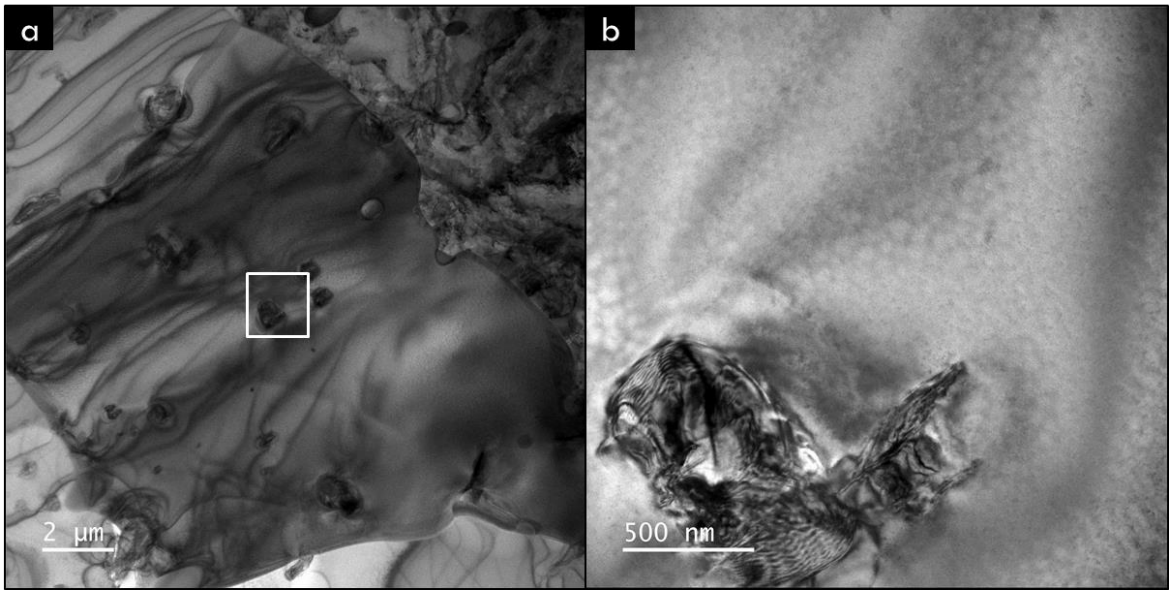

Figure 57. TEM photomicrographs of CP Ti: a- An image of a 20 µm diameter α-phase grain containing the highlighted precipitate, b- A magnified image of the precipitate highlighted in (a).

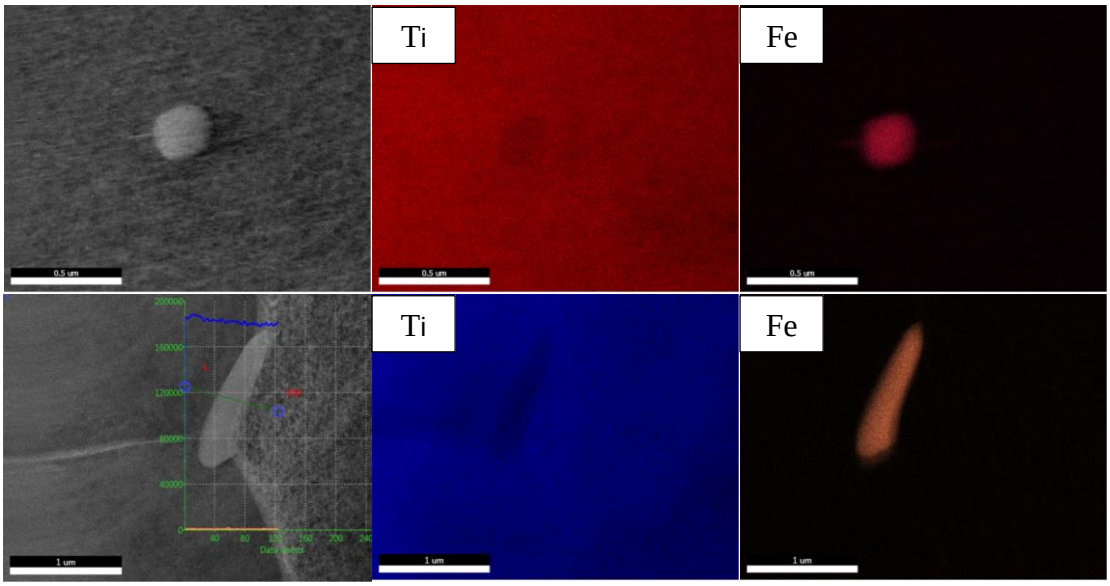

Figure 58. EDS analysis showing the composition of two of the precipitates observed in CP Ti.

4.1.2. Ti-6Al-4V AM

Representative SEM images of the microstructure of the Ti-6Al-4V AM samples are shown in Figure 59. The samples exhibited a lamellar α+β microstructure, typical of AM samples [46]. The α-phase lamellae width ranged between 0.5 and 2 μm and their length varied between 2 and 20 μm. The TEM BF photomicrographs show the presence of small equiaxed grains as highlighted by the red circles in Figure 60-a, in addition to the lamellar α-grains. The β-phase grains appearing as lighter color in the SEM images in Figure 59 were intergranular. The volume percent of the β-phase was calculated from several acquired SEM micrographs (see Figure 59) using Fiji [108], and it was approximately equal to 14 vol.%. The volume percentage of the α phase was approximately equal to 86 vol.%.

As shown in Figure 61, the prior β grains could be more easily distinguished in the IPF maps compared to the SEM images. These grains were large and had an equiaxed morphology since the hot isostatic pressing occurred at supertransus temperature (1035 °C) [137]. This material showed a higher fiber texture (approximately 8.5 times random) compared to the CP Ti sample (see Figure 61-b)).

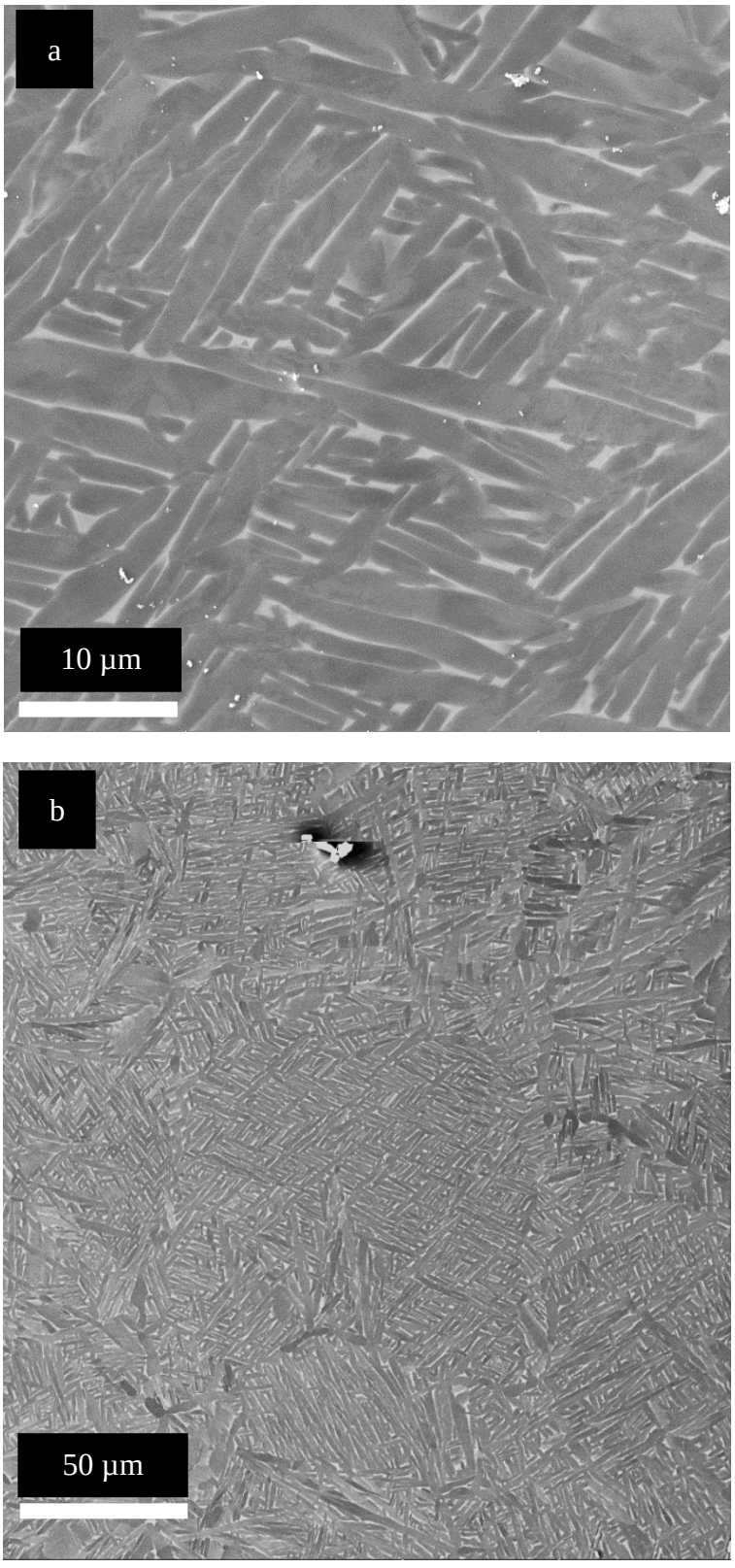

Figure 59. SE SEM photomicrographs showing the representative microstructure of Ti-6Al-4V AM: (a) high- and (b) low magnifications.

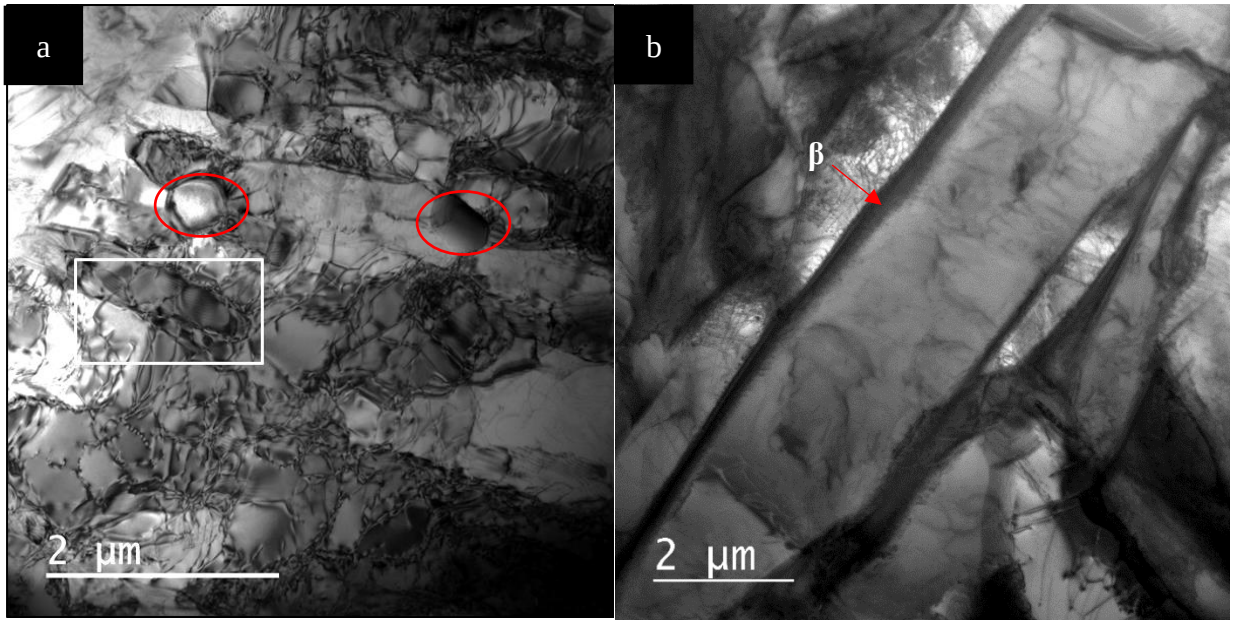

Figure 60. TEM photomicrographs of Ti-6Al-4V (AM): a- BF image of showing the lamellar α phase grain structure indicated with a white rectangle and some equiaxed grains highlighted with red circles, b- A magnified image of the highlighted α grain lamellae in white with intergranular β-phase grains indicated with a red arrow. The diffraction conditions in a and b are different.

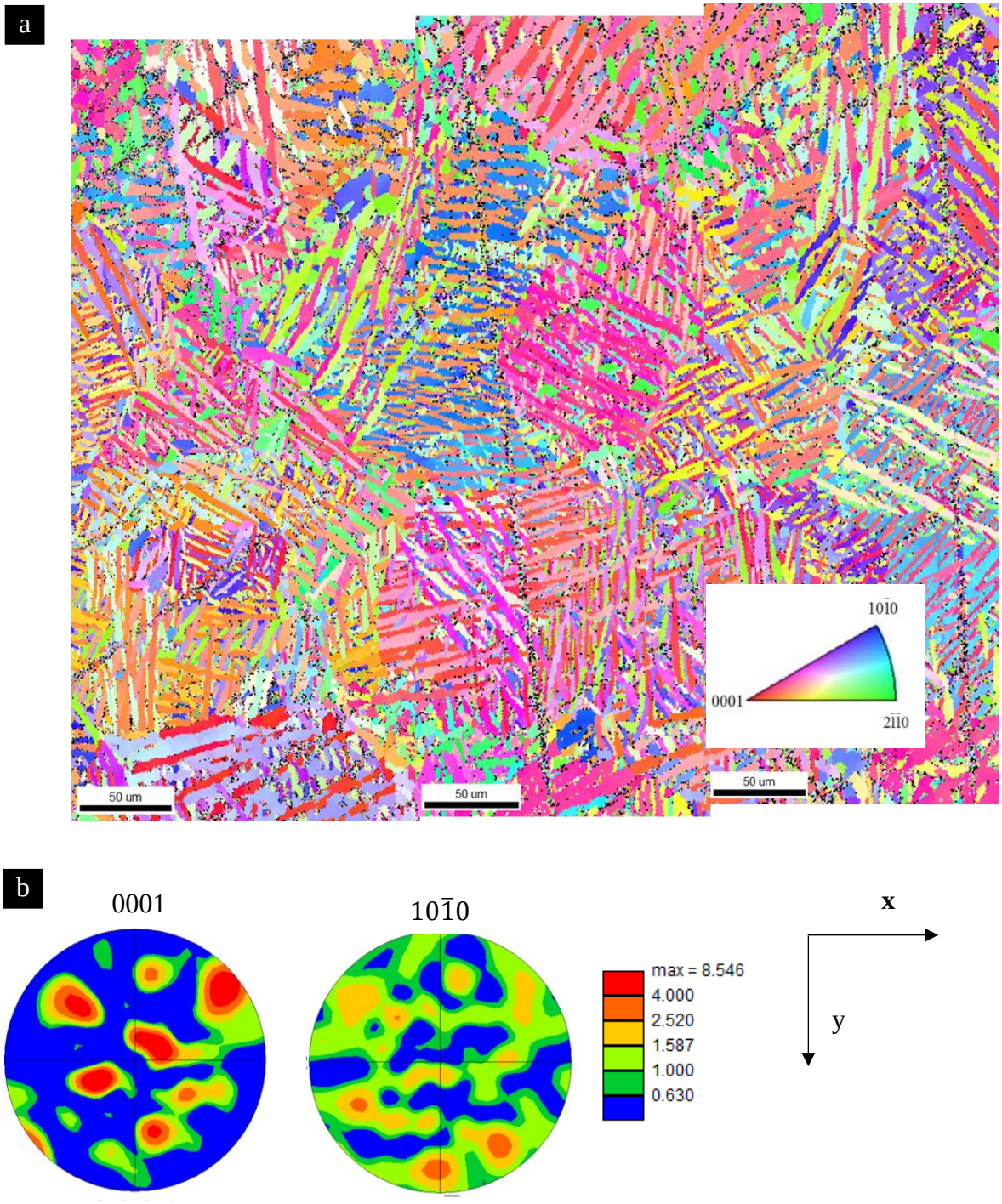

Figure 61. EBSD data of the Ti-6Al-4V AM used in this study: a) Manually stitched EBSD IPF (Inverse Pole Figure) map with the corresponding color scale unit triangle; b) The {0001} and the $\{10\bar{1}0\}$ pole figures.

4.1.3. Ti-6Al-4V PM

These samples exhibited a lenticular α-phase with mostly an intergranular β-phase. Intra-granular β-phase was also observed. The volume percentage of the β-phase was calculated from several acquired SEM images using Fiji [108], and it was approximately equal to 7 vol.% . The volume percentage of the α phase was approximately equal to 93 vol.%. The average grain size was measured using the line intercept method and is approximately equal to 10.2 μm. The size of the α-phase grains varied between 10 and 40 μm. This material showed a higher fiber texture (approximately 9.4 times random) compared to the CP Ti and Ti-6Al-4V AM samples (see Figure 63-b)).

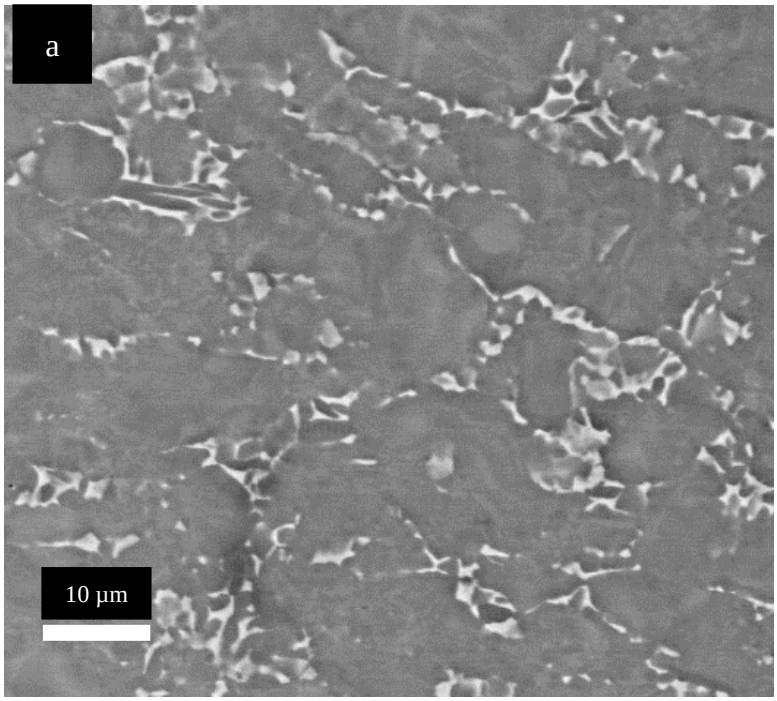

Figure 62. BSE SEM photomicrographs showing the representative microstructure of Ti-6Al-4V PM: (a) high- and (b) low magnifications.

Figure 62. (cont'd)

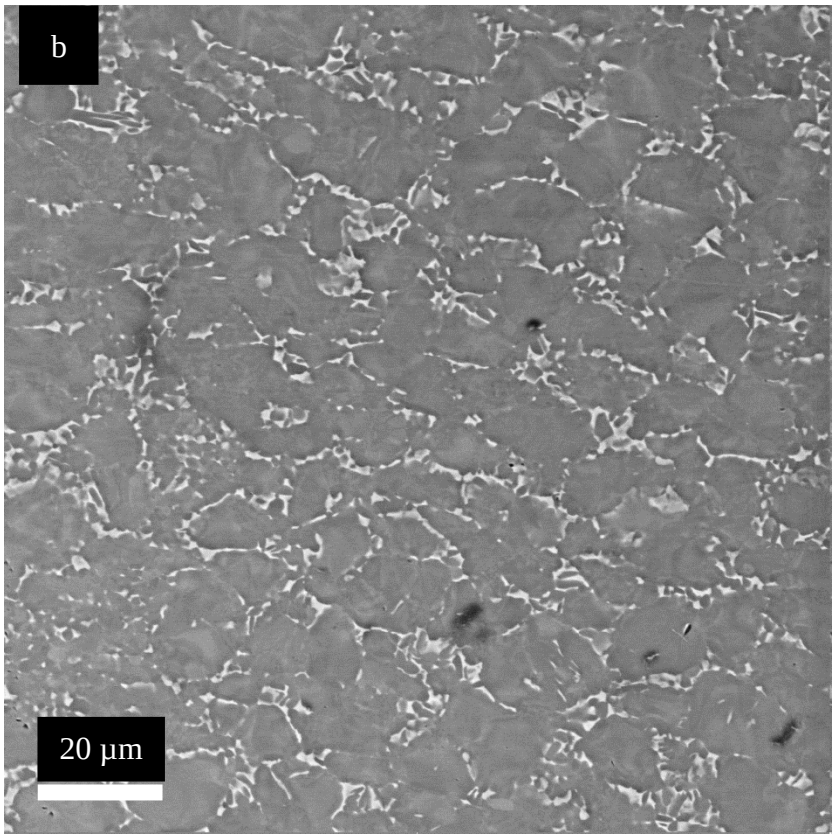

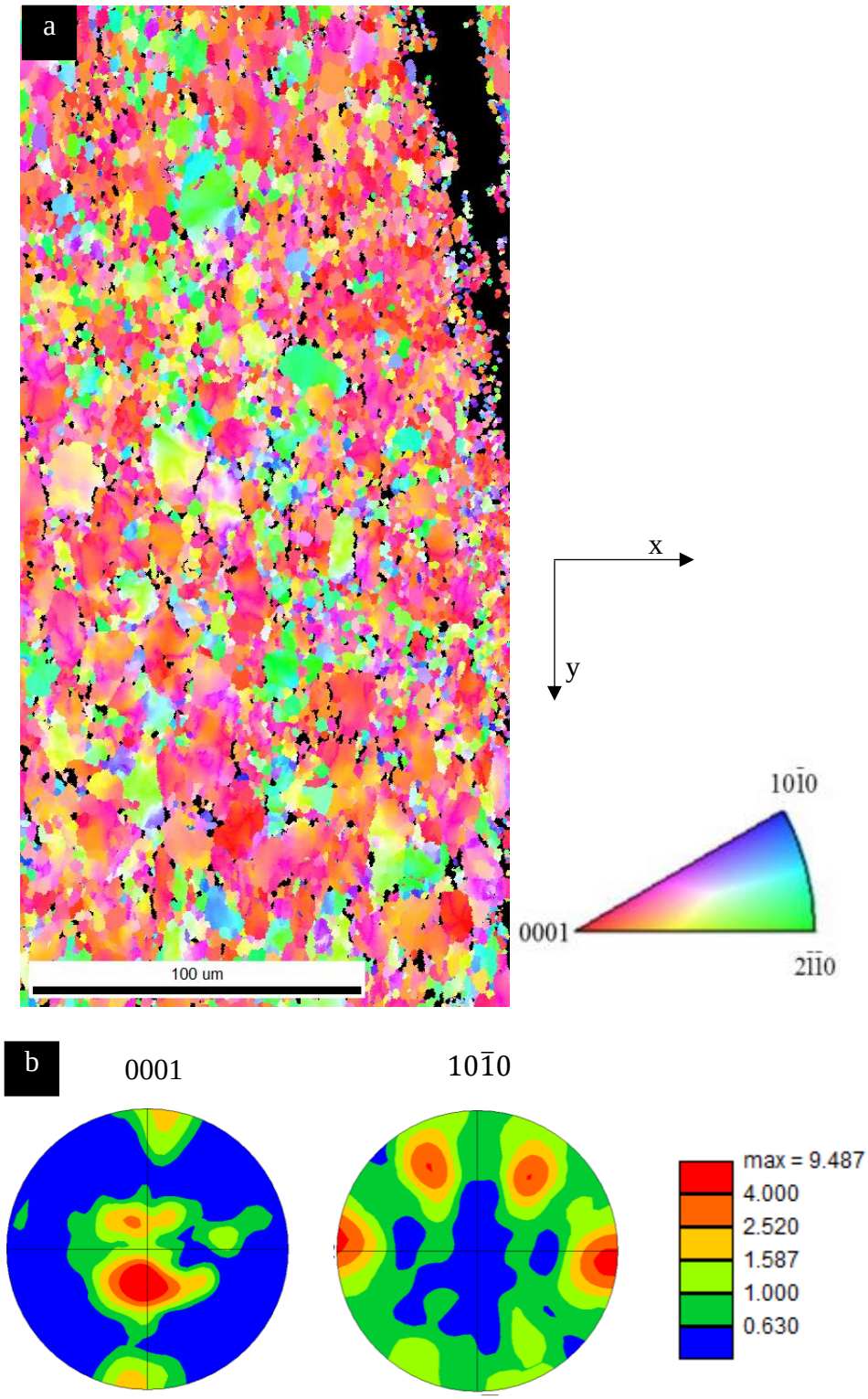

Figure 63. EBSD data of the Ti-6Al-4V PM used in this study: a) EBSD IPF (Inverse Pole Figure) map with the corresponding color scale unit triangle; b) The {0001} and the {$10\bar{1}0$} pole figures. Note that only the α phase is indicated in this figure and the data corresponding to the β phase regions in (a) are black.

4.2. NANOINDENTATION RESULTS

In this section, the results of the nanoindentation tests on samples irradiated *ex situ* are presented. First, the results of irradiation with Ar at different energies in PM rolled Ti-6Al-4V are provided. Then a comparison of the hardness between CP Ti, Ti-6Al-4V PM and AM Ti-6Al-4V irradiated under the same conditions is provided.

4.2.1 Results for all materials

4.2.1.1. Ti-6Al-4V PM

PM rolled Ti-6Al-4V samples were irradiated *ex situ* with Ar beams at different energies: 36 MeV, 0.76 MeV and 4 MeV. The full description of the irradiation conditions is provided in Table 10. The plotted irradiation dose profiles in Figure 64 and Figure 65 correspond to the dose at the probed depth. The dose at each point was estimated by taking the average of the dose over the probed depth[*].

The hardness as a function of indenter tip depth is plotted in **Figure 64** (for an irradiation temperature of 350 °C) and Figure 65 (for an irradiation temperature of 30 °C) for the irradiated and the reference (not irradiated) samples. The hardness values are the calculated average of the hardness over depth intervals equal to 100 nm. For all samples, a decrease in the measured hardness as a function of depth was observed. A steep increase in hardness at the surface of all samples was observed. This increase in hardness could be attributed to the indentation size effect [110, 111]. In fact, and as indicated in Figure 52, the plastic zone was 10 times the indentation depth for the irradiated samples at the shallower indentation depth of 50 nm [111].

[*] See 2.5.3 for the full description of the method used to estimate the irradiation dose for a certain indentation depth.

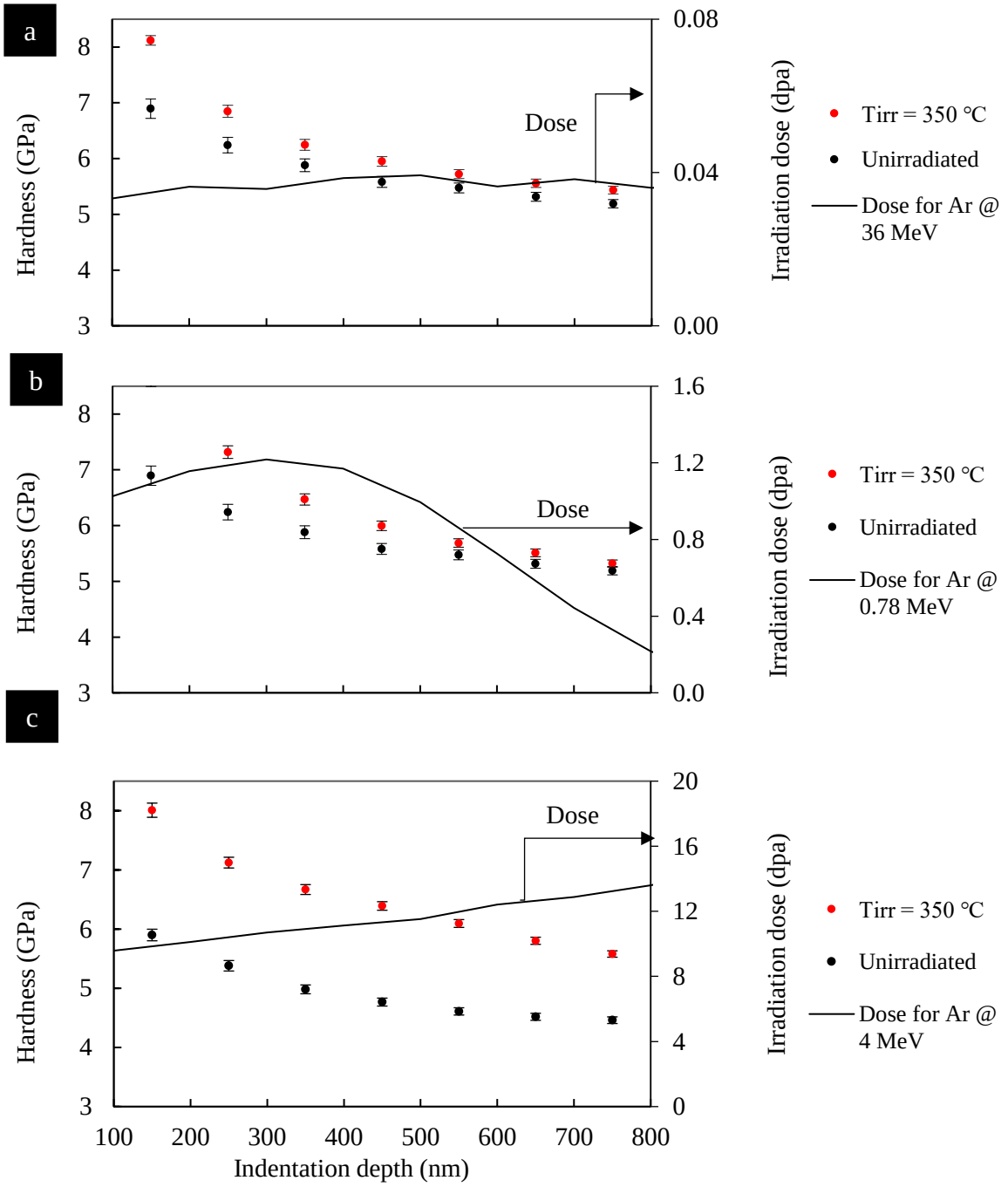

Figure 64. Hardness as a function of depth for Ti-6Al-4V PM irradiated at 350 °C with the following beam energies presented in increasing irradiation dose: a) 36 MeV Ar; b) 0.76 MeV Ar; c) 4 MeV Ar. The plotted error bars correspond to the calculated s_{error}. The probed irradiation dose as a function of depth is also plotted for each sample.

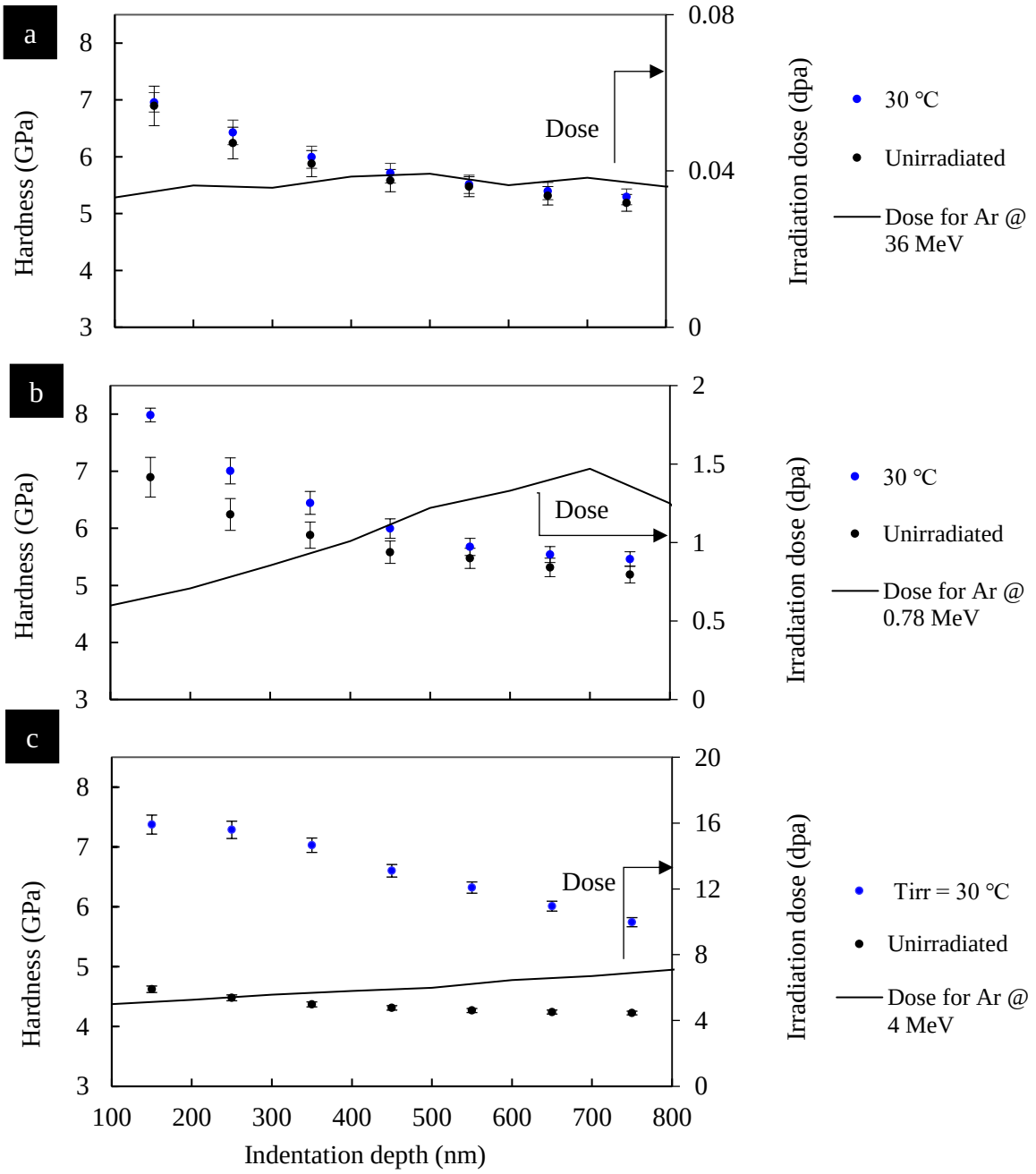

Figure 65. Hardness as a function of depth for Ti-6Al-4V PM irradiated at 30 ℃ with the following beam energies presented in increasing irradiation dose : a) 36 MeV Ar; b) 0.76 MeV Ar; c) 4 MeV Ar. The plotted error bars correspond to the calculated s_{error}. The probed irradiation dose as a function of depth is plotted for each sample.

As the dose increased, the hardness of the irradiated material increased (see both Figure 64 and Figure 65). To better investigate the effect of irradiation on the hardness, the change in hardness was calculated for the same condition. This value was calculated by subtracting the hardness of the unirradiated sample from the hardness of the irradiated sample at the same depth:

$$\Delta Hardness = H_{irradiated} - H_{non\ irradiated} \quad \text{Eq. 14}$$

This change in hardness ($\Delta Hardness$) is plotted in Figure 66 as a function of indentation depth for samples irradiated at 350 ℃. The hardness decreased as a function of depth for all doses.

The change in hardness for PM samples irradiated at 30 ℃ is plotted in Figure 67. The hardness did not change significantly as a function of depth for the sample irradiated with Ar at the energy of 36 MeV at 30 ℃ (Figure 67-a). However, the hardness decreased as a function of depth for the sample irradiated with Ar at an energy of 0.78 MeV at 30 ℃ (Figure 67-b). The sample irradiated with Ar at an energy of 4 MeV and 30 ℃ (Figure 67-c) was the only sample to exhibit an increase in hardness from 1.5 GPa to 2 GPa for depths between 100 nm and 400 nm before decreasing again.

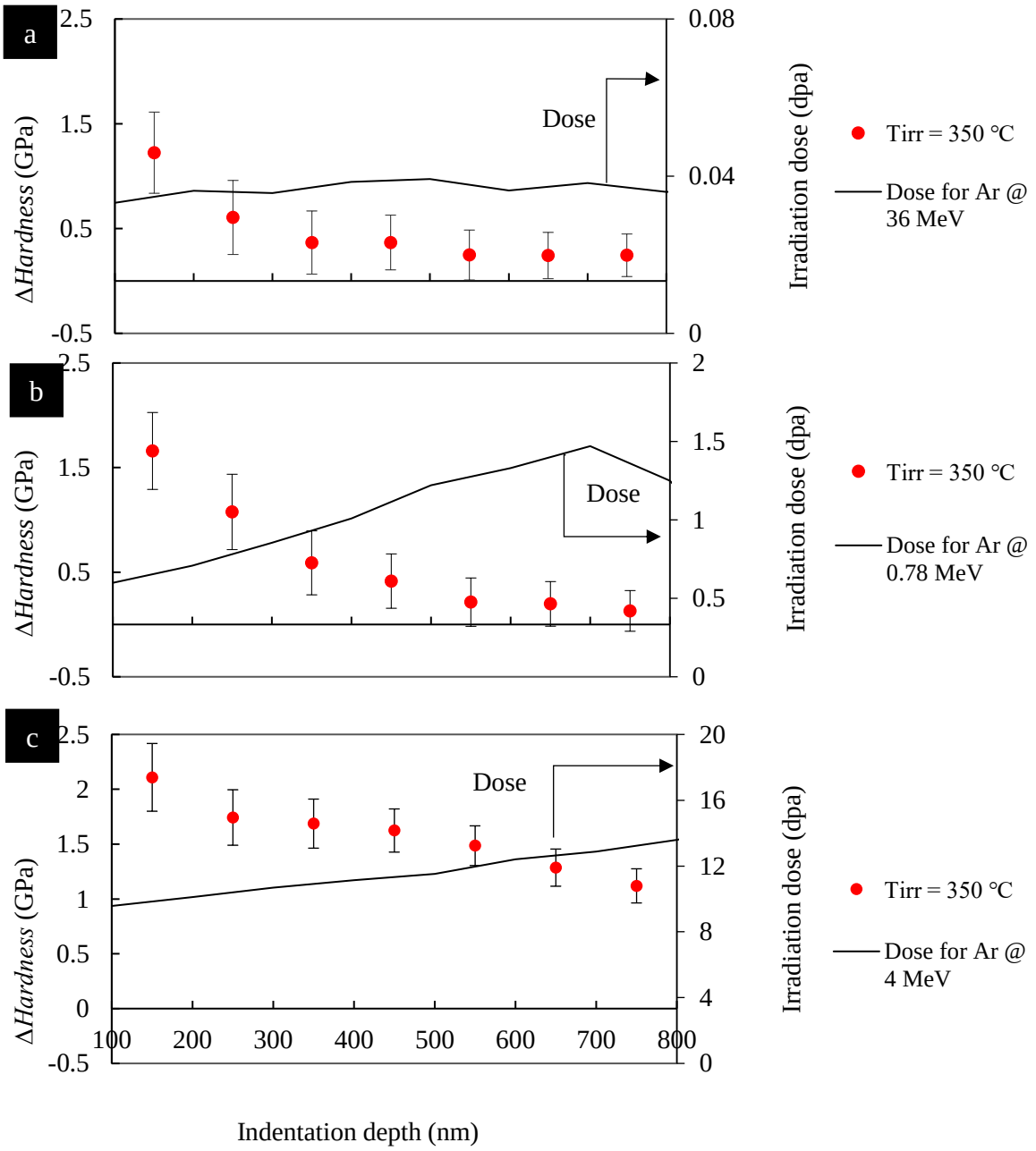

Figure 66. Δ*Hardness* as a function of depth for Ti-6Al-4V PM irradiated at 350 °C with the following beam energies presented in increasing irradiation dose: a) 36 MeV Ar; b) 0.76 MeV Ar; c) 4 MeV Ar. The error bars correspond to the calculated s_{eDiff}. The probed irradiation dose as a function of depth is also plotted for each sample.

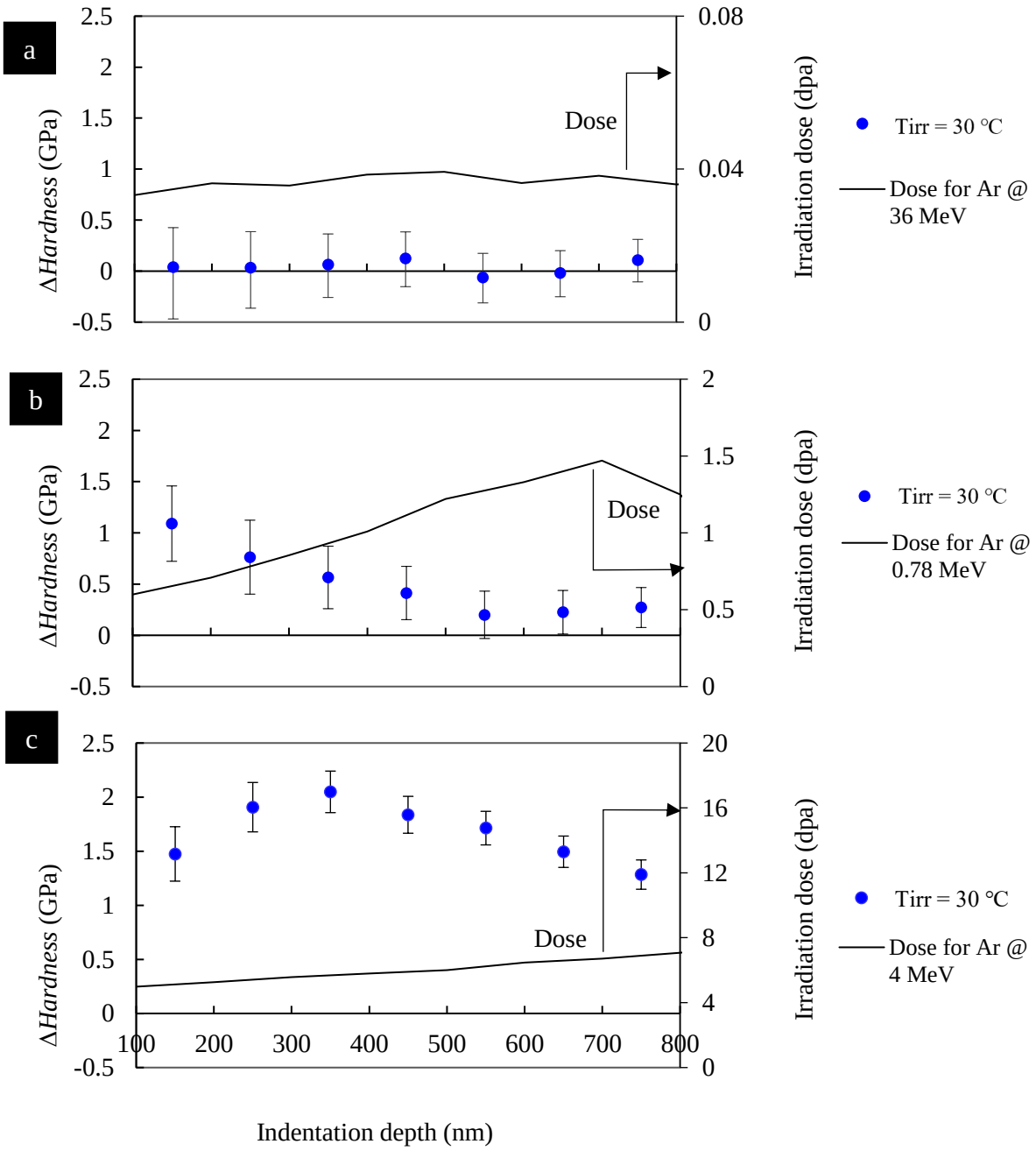

Figure 67. Δ*Hardness* as a function of depth for Ti-6Al-4V PM irradiated at 30 °C with: a) 36 MeV Ar; b) 0.76 MeV Ar; c) 4 MeV Ar. The error bars correspond to the calculated s_{eDiff}. The probed irradiation dose as a function of depth is also plotted for each sample.

4.2.1.2. CP Ti

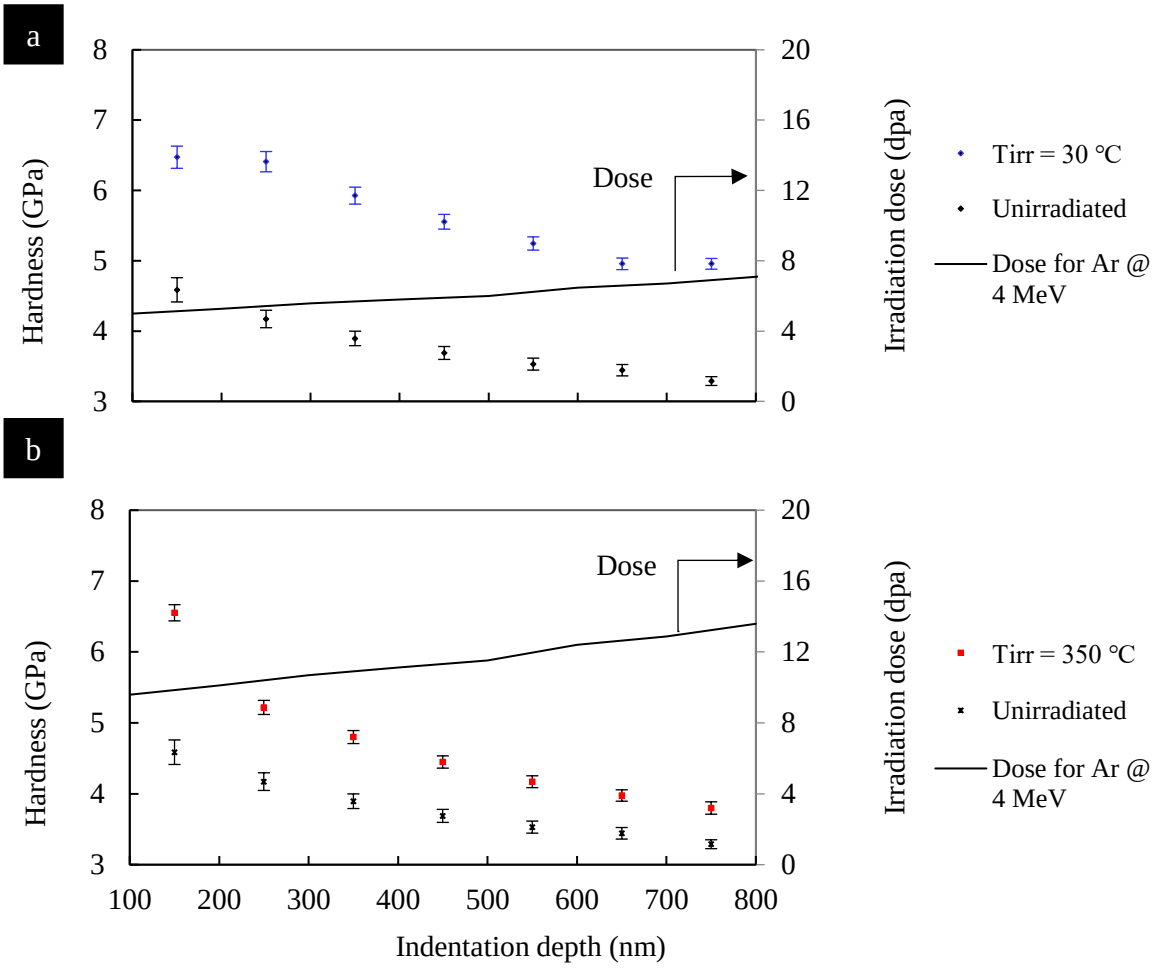

Figure 68. Hardness as a function of depth for CP Ti irradiated with 4 MeV Ar beams at: a) 30 ℃; b) 350 ℃. The error bars correspond to the calculated s_{error}. The probed irradiation dose as a function of depth is also plotted for each sample.

The hardness as a function of depth for the CP Ti sample irradiated with 4 MeV Ar ions beams at two different doses is plotted in Figure 68 for temperatures of 30 ℃ and 350 ℃. For all samples, the hardness decreased with increasing depth, and the samples irradiated at a higher temperature and dose exhibited less hardening. This observation is confirmed in Figure 69, which shows the change in hardness as a function of depth.

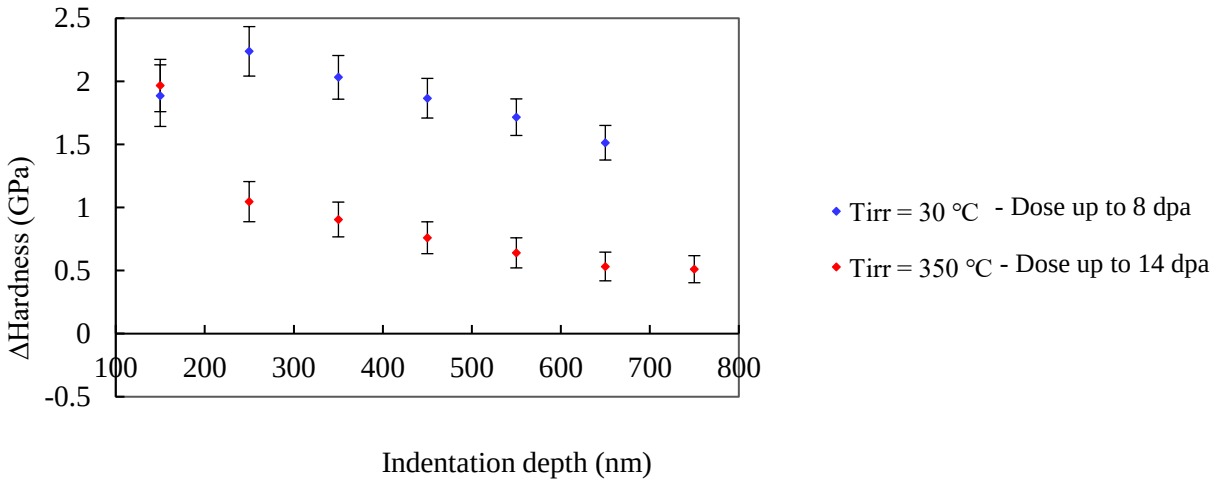

Figure 69. Δ*Hardness* as a function of depth for CP Ti irradiated with 4 MeV Ar beams at 30 ℃ and 350 ℃. The plotted error bars correspond to the calculated s_{eDiff}. The maximum probed irradiation dose is indicated for each sample.

4.2.1.3. Ti-6Al-4V AM

Only one sample of the Ti-6Al-4V AM irradiated at 30 ℃ was available for this investigation. Nanoindentation was performed similarly to the Ti-6Al-4V PM and CP Ti samples. For this sample, the hardness as a function of depth is plotted in Figure 70. As can be seen, the hardness decreased as the indentation depth increased for the irradiated sample. The unirradiated sample exhibited an almost constant hardness value of 5.1 GPa.

The change in hardness for the irradiated sample is plotted as a function of depth in Figure 71. This sample exhibited a decrease of Δ*Hardness* from 1.1 GPa to 0 GPa over indentation depths between 100 and 900 nm.

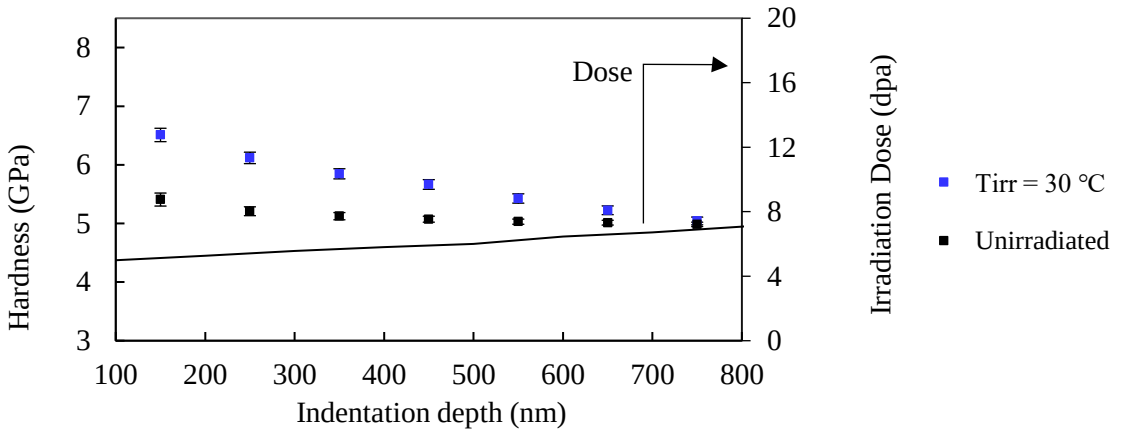

Figure 70. Hardness as a function of depth for AM Ti-6Al-4V irradiated with 4 MeV Ar beams at 30 ℃. The plotted error bars correspond to the calculated statistical error. The probed irradiation dose as a function of depth is also plotted.

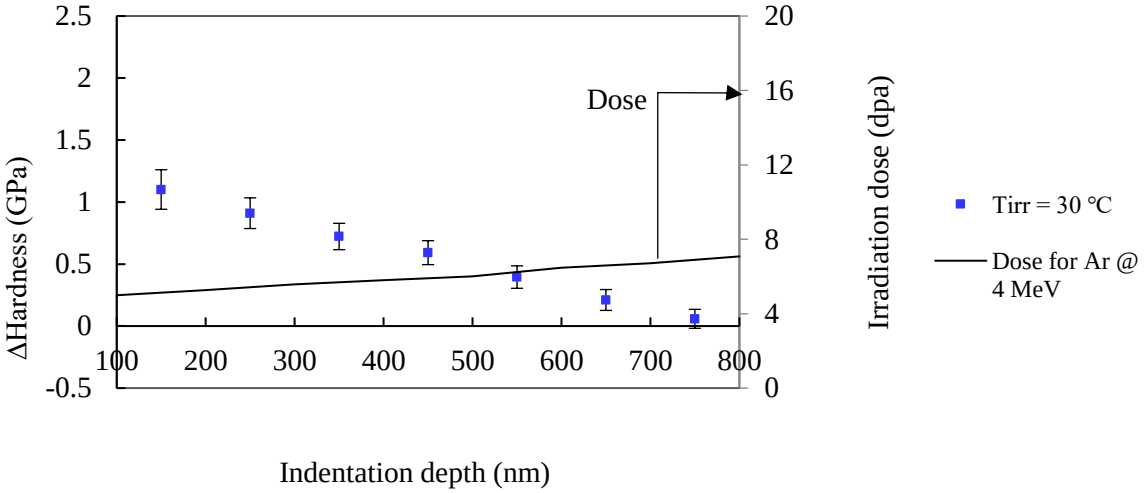

Figure 71. Δ*Hardness* as a function of depth for AM Ti-6Al-4V irradiated with 4 MeV Ar beams at 30 ℃. The error bars correspond to the calculated s_{eDiff}. The probed irradiation dose is also provided.

4.2.2. Comparison between different materials

A comparison between the three different materials irradiated with the same 4 MeV Ar ion beams at 30 ℃ was performed. A plot of the hardness of the unirradiated materials is provided in Figure 72. The hardness decreased significantly from 4.6 to 3.3 GPa for CP Ti, and

from 5.9 to 4.3 GPa for Ti-6Al-4V PM between indentation depths between 100 nm and 750 nm. For AM Ti-6Al-4V, the hardness did not decrease as significantly and was close to 5.1 GPa.

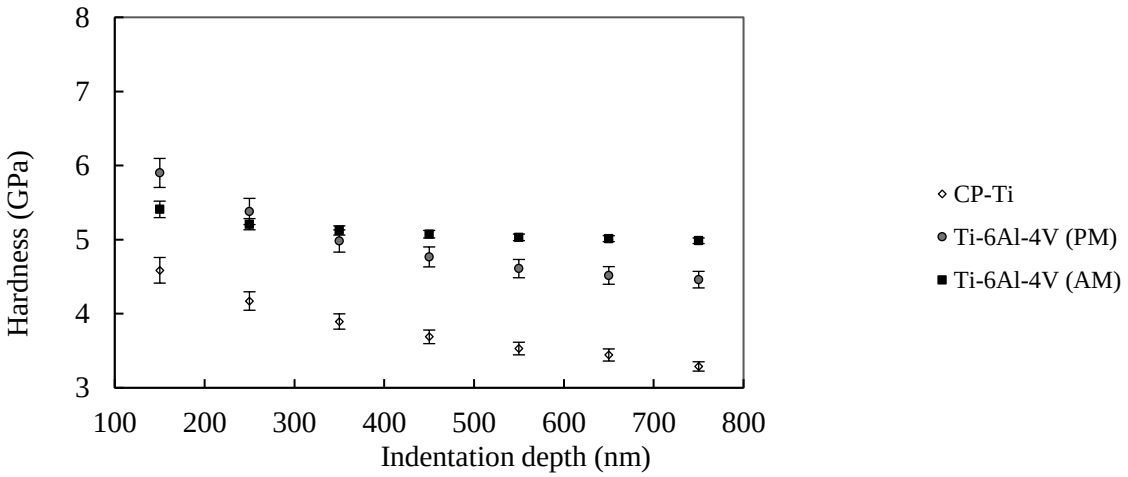

Figure 72. Hardness as a function of depth for the unirradiated samples of CP Ti, Ti-6Al-4V PM and AM. The error bars correspond to the calculated statistical error s_{error}.

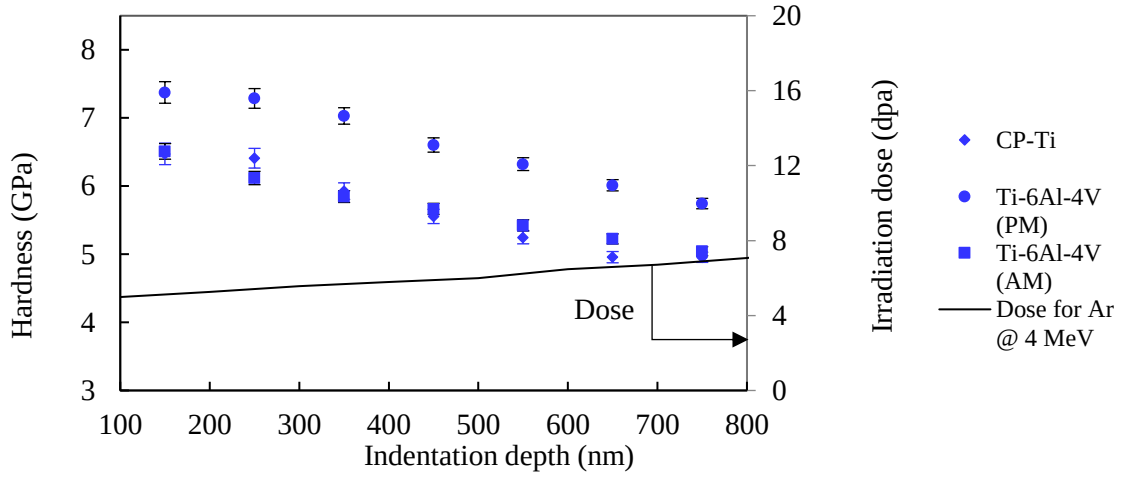

Figure 73. Hardness as a function of depth for irradiated samples of CP Ti, Ti-6Al-4V PM and AM irradiated with 4 MeV Ar beams at 30 ℃. The error bars correspond to the calculated s_{error}The probed irradiation dose is also provided.

The hardness values at indentation depths between 200 nm and 400 nm were averaged for each sample to allow for a comparison between the three materials. The results are presented in Figure 74 and Figure 75. In terms of average hardness, the unirradiated samples can be ranked from higher to lower as follows: Ti-6Al-4V PM, Ti-6Al-4V AM, and CP Ti with the

corresponding values of 5.4 GPa, 5.2 GPa, and 4 GPa respectively. After irradiation with the same ion beam at 30 ℃, Ti-6Al-4V (PM) exhibited the highest average hardness of 7.15 GPa. The CP Ti and Ti-6Al-4V AM samples had similar hardness values of 6.12 GPa and 6 GPa, respectively. After irradiation at 350 ℃, the average hardness of CP Ti and Ti-6Al-4V (PM) increased to 5 GPa and 7.2 GPa, respectively.

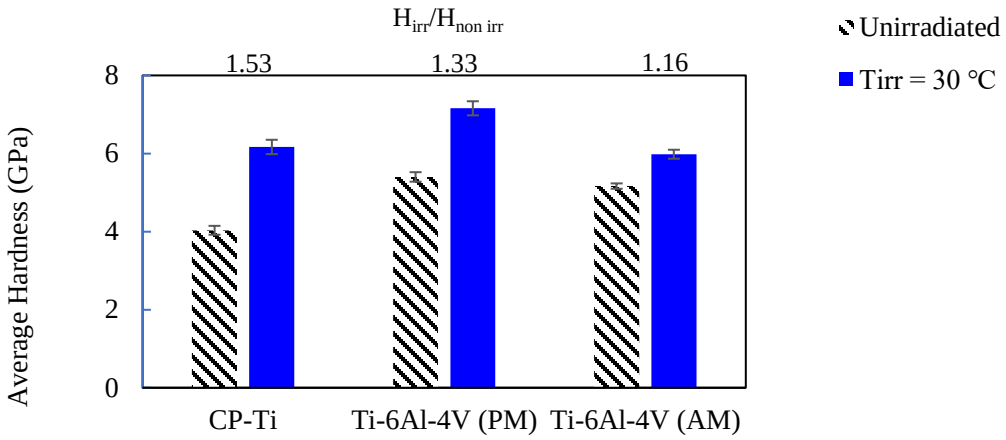

Figure 74. Average Hardness of CP Ti, Ti-6Al-4V PM and AM Ti-6Al-4V samples unirradiated (black pattern fill) and irradiated with 4 MeV Ar beams at 30 ℃ (solid blue fill). The irradiation dose is 5.4 dpa. The error bars correspond to the calculated s_{error}.

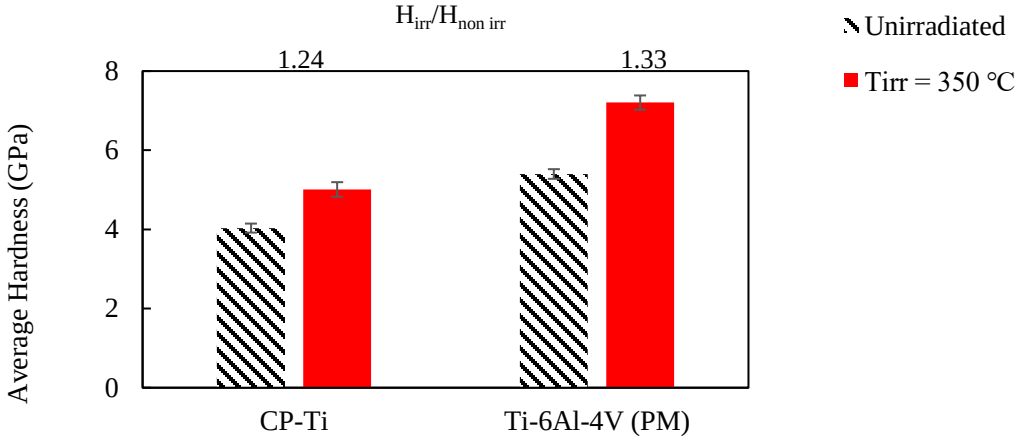

Figure 75. Average Hardness (indentation depth between 200 and 400 nm) of CP Ti, Ti-6Al-4V PM and AM Ti-6Al-4V samples unirradiated (black pattern fill) and irradiated with 4 MeV Ar beams at 350 ℃ (solid blue fill). The irradiation dose is 10 dpa. The error bars correspond to the calculated s_{error}.

A summary of the results was presented in Figure 76, where Δ*Hardness* was calculated for each irradiated sample. At low irradiation temperature, CP Ti and Ti-6Al-4V PM exhibited the highest hardening. The Ti-6Al-4V AM exhibited the lowest hardening after RT irradiation. At a higher temperature, the average hardness of the irradiated α+β alloy Ti-6Al-4V PM was higher than CP Ti after irradiation up to 10 dpa.

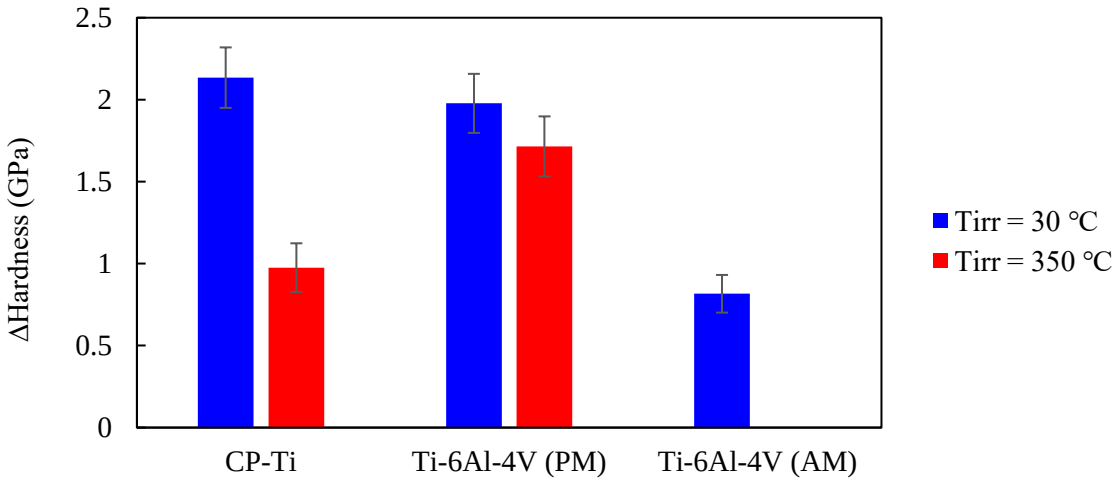

Figure 76. Average Δ*Hardness* (indentation depth between 200 and 400 nm) for CP Ti, Ti-6Al-4V PM and AM irradiated with 4 MeV Ar beams. The probed irradiation dose at 30 °C is 5.4 dpa and at 350 °C is 10 dpa. The error bars correspond to the calculated s_{eDiff}.

4.2.3. Effect of dose and temperature

Since only multiple samples of Ti-6Al-4V PM were irradiated at different doses and temperatures, the effect of dose and temperature on the hardness was only investigated for this alloy. For this analysis, the change of hardness between 200 nm and 400 nm was averaged and used as a measure of the hardening at the corresponding dose. The results are plotted in Figure 77.

At the lowest temperature, there was no change in hardness at the dose of 0.036 dpa. Δ*Hardness* increased from 0.67 GPa to 2 GPa between 1.1 dpa and 5.4 dpa, respectively. For the

samples irradiated 350 ℃, radiation hardening was observed in all the samples at doses between 0.036 dpa to 10 dpa. Δ*Hardness* increased from 0.5 to 1.7 GPa between 0.036 dpa and 1.1 dpa, respectively. At low doses, the hardening at 350 ℃ was higher than hardening observed at 30 ℃. At the highest dose, Δ*Hardness* was lower at a higher temperature.

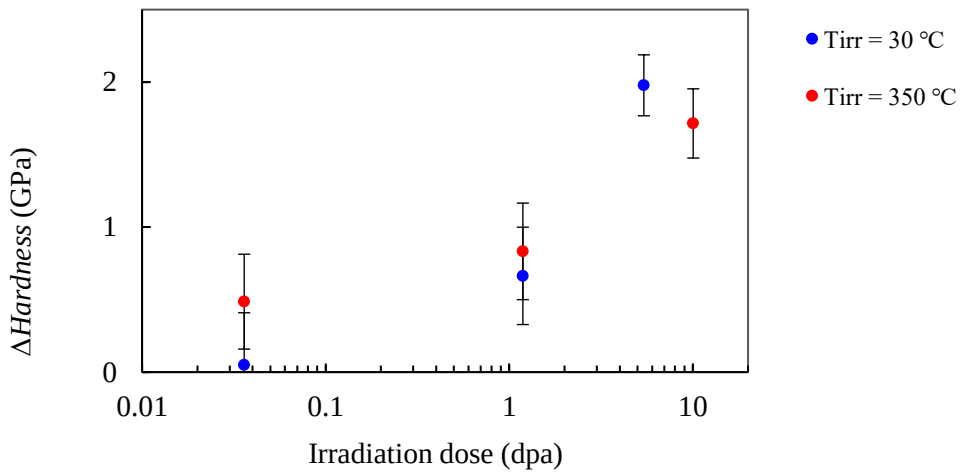

Figure 77. Δ*Hardness* as a function of the irradiation dose for PM rolled Ti-6Al-4V irradiated with Ar ion beams at different energies and at temperatures of 30 ℃ and 350 ℃.

4.2.4. Summary of the nanoindentation results

The hardness of CP Ti, Ti-6Al-4V PM and AM were investigated using nanoindentation before and after irradiation with Ar ion beams at 30 ℃ and 350 ℃. In all samples, a decrease in the hardness as a function of indentation depth was observed. This depth-dependent decrease in hardness is referred to in the literature as the indentation size effect (ISE) [109, 110, 138]. Nix and Gao [109] explained this strain gradient, most significant at small indentation depths, as an effect of geometrically necessary dislocations (GND). As the indenter tip pushes into the surface, GNDs are required to account for the permanent deformation and thus will contribute to the measured hardness of the material. The change of hardness $\Delta Hardness$ was calculated using the hardness of the irradiated and unirradiated materials at the same depth to account for this measurement artifact.

The hardness of the reference unirradiated materials is presented in Table 17. The hardness values at indentation depths between 200 nm and 400 nm were used to estimate $\Delta Hardness$. The hardness at a depth of 800 nm, where there was a minimal indentation size effect, is also included.

Table 17. Summary of the hardness measurement of the unirradiated materials.

Material	H_{unirr} (GPa) Depth: 200 - 400 nm	H_{unirr} (GPa) Depth: ~ 800 nm
CP Ti	4 +/- 0.1	3.3 +/-0.3
Ti-6Al-4V (PM)	5.4 +/- 0.12	4.3 +/-0.2
Ti-6Al-4V (AM)	5.2+/- 0.06	5+/-0.19

After irradiation with the 4 MeV Ar ion beam, the change in hardness was investigated in CP Ti, Ti-6Al-4V PM, and AM. At low temperature, CP Ti exhibited the highest hardening (~ 2.1 GPa) for irradiation doses up to 5.4 dpa. Both α+β Ti alloys exhibited less hardening

(1.8 GPa for Ti-6Al-4V PM and 0.8 GPa for AM). A summary of the hardness of these samples irradiated with 4 MeV Ar ions is provided at both temperatures in Table 18.

Table 18. Hardness measurements of the samples irradiated with 4 MeV Ar beams.

Material	Hirr (GPa) Depth: 200 - 400 nm	
	Tirr = 30 ℃ Dose= 5.4 dpa	Tirr = 350 ℃ Dose= 10 dpa
CP Ti	6.17 +/- 0.15	5 +/- 0.1
Ti-6Al-4V (PM)	7.15 +/- 0.13	7.2 +/- 0.14
Ti-6Al-4V (AM)	6 +/-0.09	-

The effect of the irradiation temperature was investigated in PM rolled Ti-6Al-4V. At doses below 1 dpa, samples irradiated at 350 ℃ showed higher hardening values than samples irradiated at 30 ℃. The trend observed in Figure 77 suggests that the hardening at lower temperatures was more significant at higher doses.

4.3. OBSERVATIONS OF <A> DISLOCATION LOOPS

This section presents the observations and quantification of prismatic <a> dislocation loops in CP Ti and Ti-6Al-4V AM during *in situ* TEM irradiations with 1 MeV Kr ions at the IVEM Facility at different temperatures and dose. The habit nucleation plane of these dislocation loops is {1120} and their Burgers vector is $\mathbf{b} = \frac{1}{3} < 2\bar{1}\bar{1}0 >$ [65]. These small loops are correlated to the increase in hardness and reduction in the elongation-to-failure of irradiated hcp materials [65]. The nucleation and growth [71, 139, 140] of these loops have been extensively studied in Zr and Zr alloys as well as their effect on the hardening [140 - 144]. Although these loops were observed in irradiated Ti [15, 145, 70], there is no prior systematic investigation of the effect of the dose and temperature. In the following section, prismatic loops

are systematically characterized in CP Ti <a> at different temperatures and doses. Observation of <a> loops in Ti-6Al-4V AM were also made at high temperature.

4.3.1. CP Ti

4.3.1.1. *In situ* irradiation

First, the low dose damage structure was investigated in CP Ti irradiated *in situ* at 30 °C, 360 °C and 430 °C. The samples were observed during irradiation at doses between 0.05 dpa and 0.06 dpa. At these low doses, the <a> loops appear to be homogeneously distributed throughout the grains. As shown in Figure 78, Figure 79 and Figure 80, these loops have a dark contrast in BF images and appeared as bright dots in DF images.

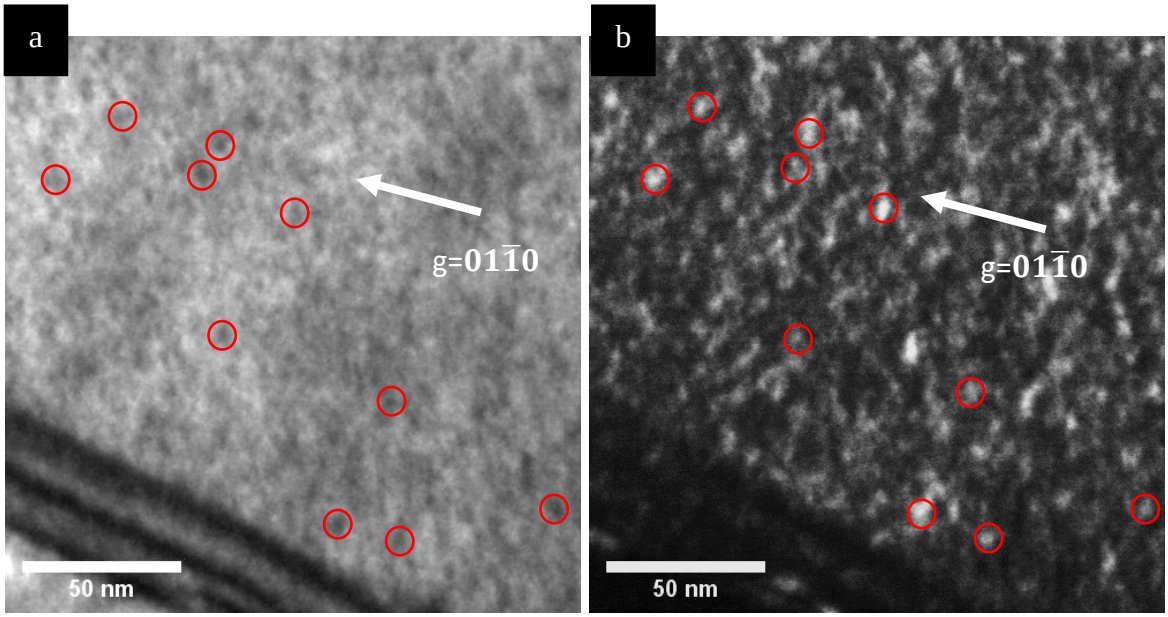

Figure 78. TEM photomicrographs showing the microstructure of CP Ti irradiated with 1 MeV Kr ions at a dose of 0.05 dpa with **g** = 01$\bar{1}$0 and at 30 °C: a) BF condition, b) DF condition. The same <a> loops are circled in red in both images.

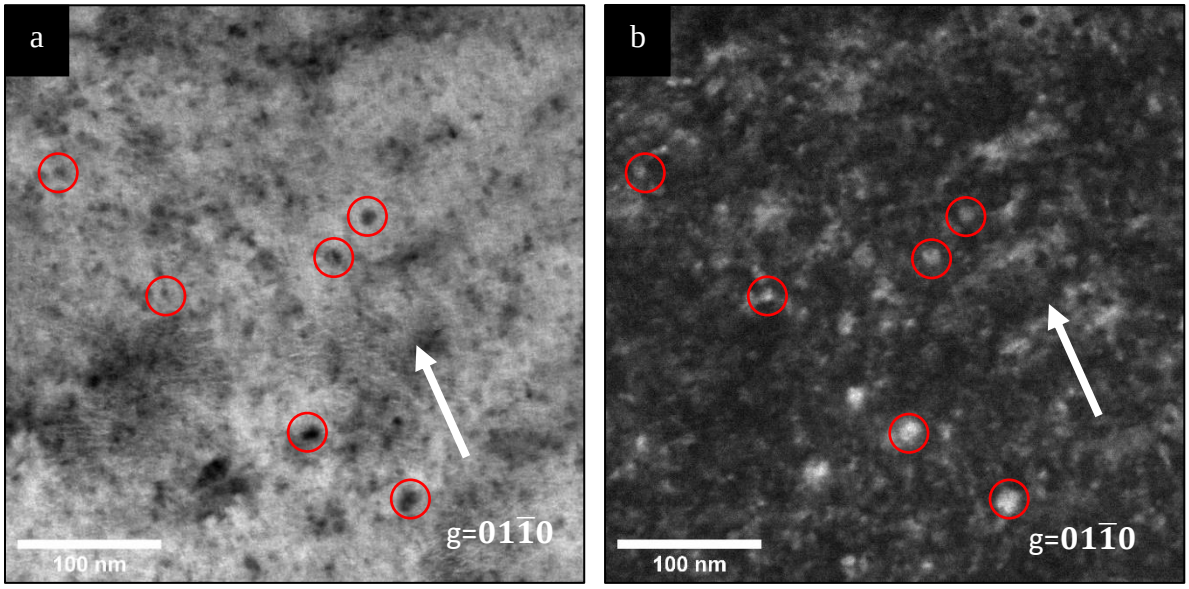

Figure 79. TEM photomicrographs showing the microstructure of CP Ti irradiated at 360 ℃ with 1 MeV Kr ions at a dose of 0.06 dpa with **g** = 01$\bar{1}$0: a) BF condition, b) DF condition. The same <a> loops are identified in both conditions.

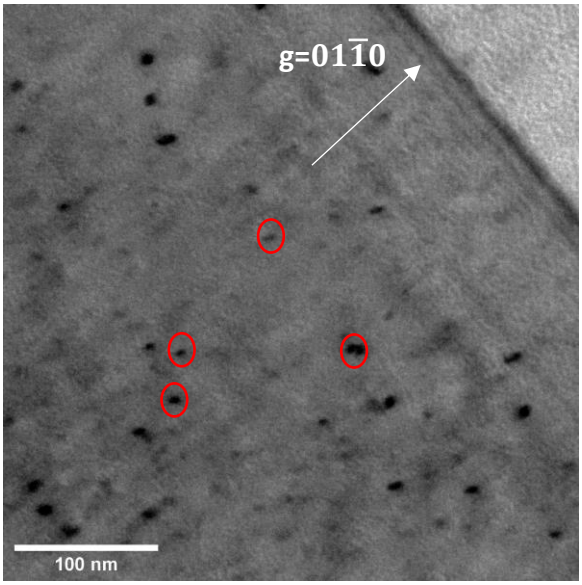

Figure 80. BF TEM photomicrograph showing the microstructure of CP Ti irradiated at 450 ℃ with 1 MeV Kr ions at a dose of 0.05 dpa with **g** = 01$\bar{1}$0. Some of the observed <a> loops are circled in red.

At higher doses, the final damage structure in CP Ti was investigated at 11 dpa at 30 ℃ (see Figure 81), 3.7 dpa at 360 ℃ (see Figure 82) and 0.55 dpa at 430 ℃ (see Figure 83). The <a> loops exhibited an elliptical shape and a larger size at these irradiation temperatures and

doses. Unfaulting of the loops was observed as evidenced by the lack of stacking fault contrast in some of the loops. Black dots or very small <a> loops are still present at these high doses as well as the large unfaulted loops and dislocation lines. Dislocation networks were observed in the foil irradiated at 430 ℃ (see Figure 83).

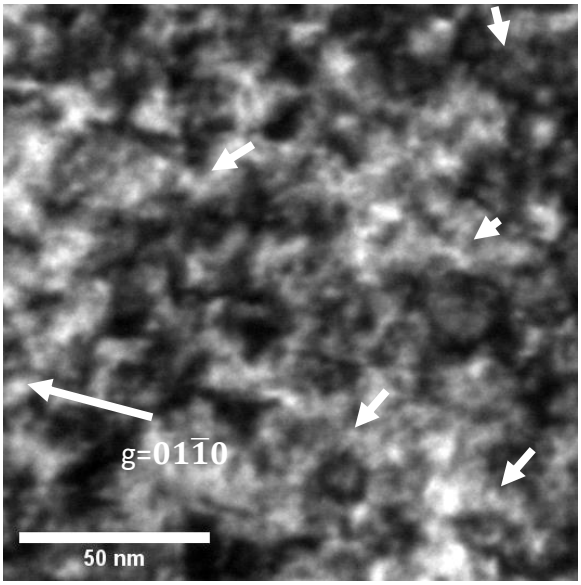

Figure 81. BF TEM photomicrograph showing the <a> loops observed in the sample irradiated up to 11 dpa at 30 ℃ with **g** = 01$\bar{1}$0. Some of the large <a> loops are indicated with white arrows.

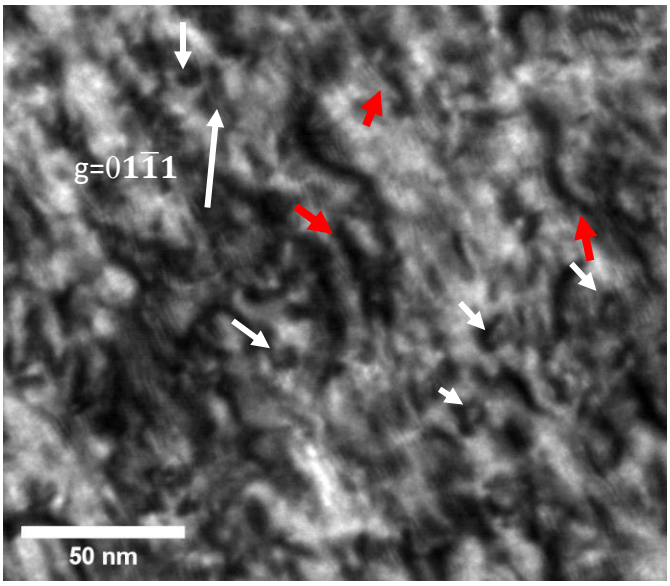

Figure 82. BF TEM photomicrograph showing the <a> loops observed in the sample irradiated up to 0.55 dpa at 360 °C. The **g** vector used in this condition was **g** = 01$\bar{1}$1. Under this condition, both <a> loops and c-component loops are visible. In the figure, <a> loops are distinguished by their elliptical shape. White arrows highlight some of the <a> loops. Red arrows indicate some of the c-component loops.

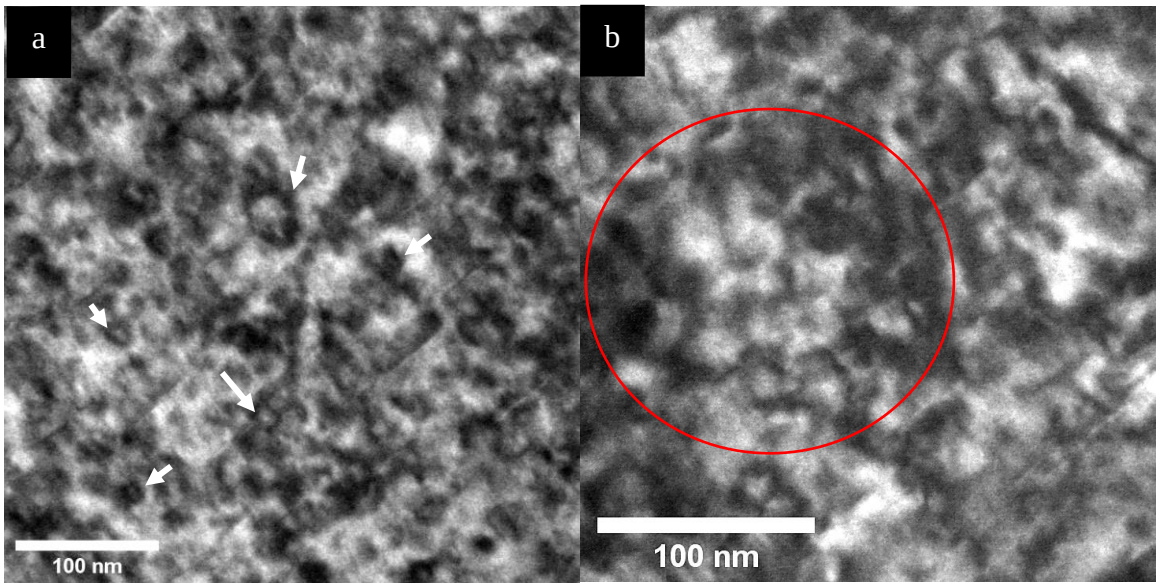

Figure 83. BF TEM photomicrograph of the CP Ti sample irradiated up to 0.55 dpa at 430 °C, **g** = 01$\bar{1}$0: a) White arrows point to some of the observed <a> loops; b) Higher magnification photomicrograph showing an observed dislocation network circled in red.

The length distributions of <a> loops in the samples irradiated at 30 ℃, 360 ℃ and 430 ℃ are illustrated in Figure 84. For samples irradiated at 30 ℃, as illustrated in Figure 78, <a> loops were observed at 0.05 dpa and the average size of the loops was 9 nm. Since the loops were too small and dense for precise length quantifications in this condition (30 ℃ and 0.05 dpa), the number of these defects was counted using brightness maxima in Fiji [146].

All the distributions of the length of the loops were sightly right-skewed. For each irradiation temperature, as the dose increased, the skewness moved further left. As a result, the median values of the <a> loop length increased as a function of dose for each irradiation temperature (see Figure 84 b and c). The area under the curve also increased as the dose increased, which suggests a cumulative increase in total defect number density.

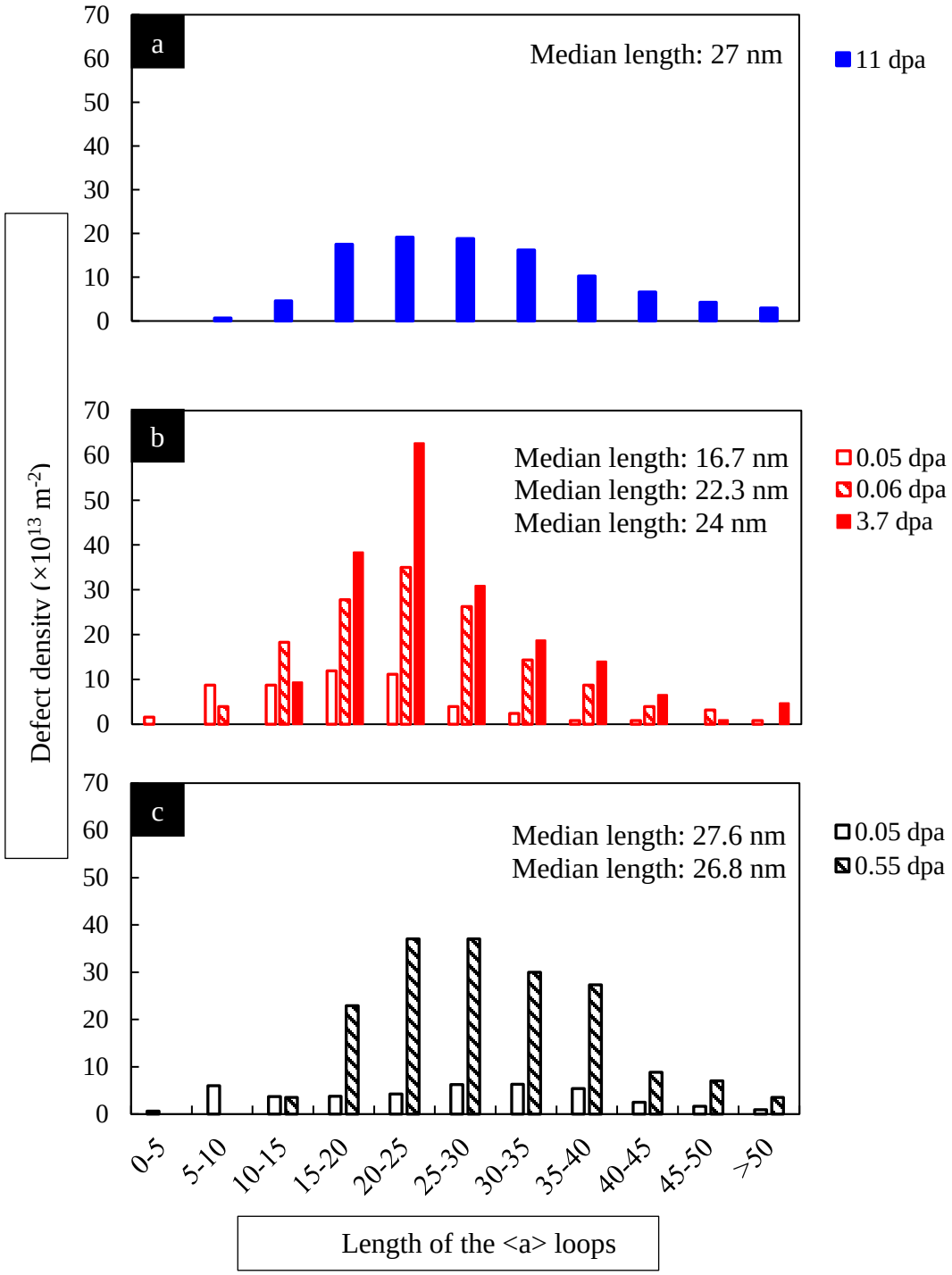

Figure 84. Distribution of the length of <a> loops in CP Ti irradiated *in situ* with 1 MeV Kr at: a) 30 ℃, b) 360 ℃ and c) 430 ℃.

4.3.1.2. *Ex situ* irradiation

TEM foils were made from the CP Ti samples irradiated *ex situ* with 4 MeV Ar ion beams. Since only the unirradiated side was electropolished as explained in 3.2.2 (see Figure 29), the irradiation dose corresponds to the dose at the surface of the sample 4.1 dpa and 7.5 dpa for the irradiation temperature of 30 °C and 350 °C, respectively. These samples contained <a> dislocation lines, as well as <a> loops. The loops are indicated by white arrows in Figure 85. The size of the loops was larger in the sample irradiated at 350 °C (Figure 85-b).

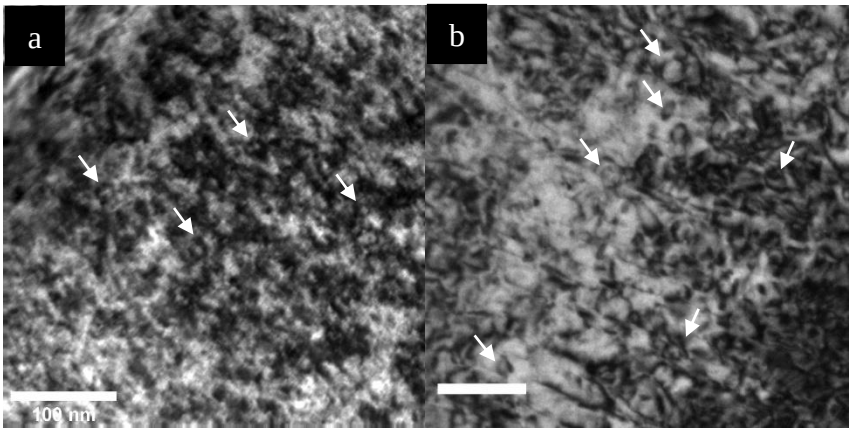

Figure 85. BF TEM photomicrographs showing the CP Ti sample irradiated *ex situ* with 4 MeV Ar ions imaged with **g** = $01\bar{1}0$: a) Sample irradiated at 30 °C and with the dose at the surface of 4.1 dpa; b) Sample irradiated at 350 °C and with the dose at the surface of 7.5 dpa. The white arrows indicate some of the <a> loops.

4.3.1.3. Effect of dose and temperature

The area <a> loop number density* and their median length as a function of dose for CP Ti irradiated *in situ* at different temperatures are presented in Figure 86 and Figure 87, respectively. For the sample irradiated at 30 °C, the area <a> loop number density decreased from ~10^{16} .m^{-2} to 10^{15} .m^{-2} between the doses of 0.06 dpa and 11 dpa, respectively. This

* Defined as the number of specific dislocation loop types (<a> or c-component) in a unit area [m^{-2}] (see 3.4.5.2.)

significant decrease in number density per unit area occurred with a significant increase in the median loop size from 9 nm to 27 nm. In the sample irradiated at 360 °C, the area <a> loop number density increased from $10^{15}.m^{-2}$ to $1.4\times10^{15}.m^{-2}$ for the doses of 0.05 to 0.06 dpa. The median loop size went from 11.7 nm to 22 nm. At the higher dose of 3.7 dpa, the area <a> loop number density seems to saturate and reach the value of $1.8\times10^{15}.m^{-2}$. The area <a> loop number density for the sample irradiated at 430 °C went from $4\times10^{14}.m^{-2}$ to $1.8\times10^{15}.m^{-2}$, but the loop size did not increase significantly.

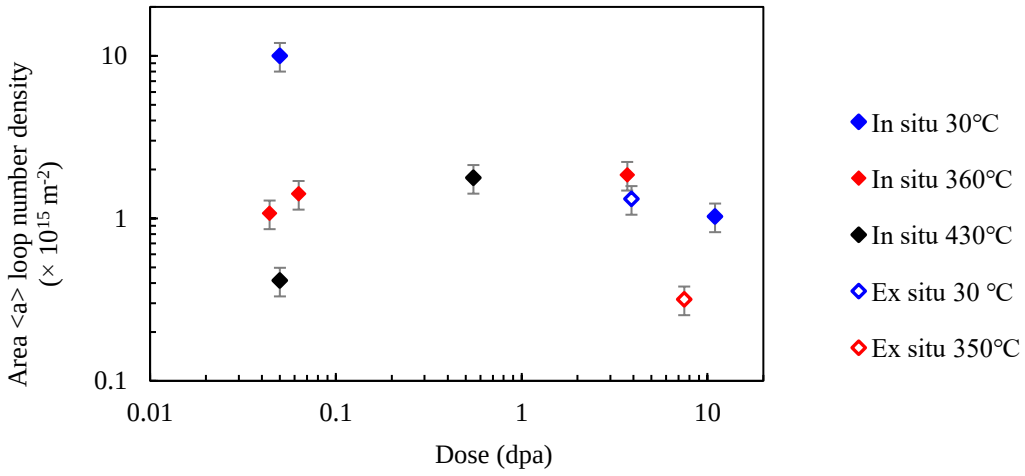

Figure 86. Area <a> loop number density in CP Ti irradiated *in situ* with 1 MeV Kr and *ex situ* with 4 MeV Ar as a function of dose and at different temperatures. The irradiation conditions are indicated in the legend.

The effect of the irradiation temperature on the <a> nucleation in CP Ti was investigated at the low irradiation dose of 0.05 dpa. The sample irradiated at the lowest temperature had a much higher defect density and a smaller loop size. As the temperature increased, the defect number density decreased, and the loop size increased.

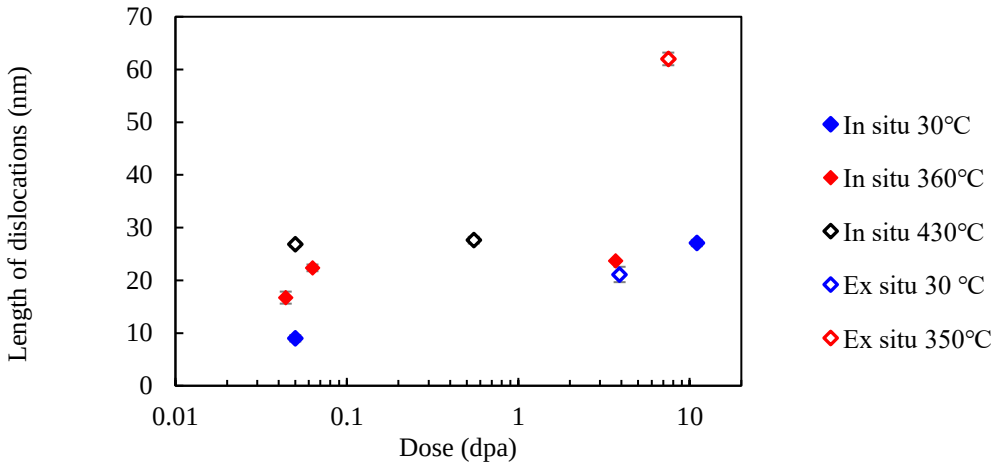

Figure 87. The median length of <a> loops observed in CP Ti irradiated with 1 MeV Kr as a function of dose.

4.3.2. Ti-6Al-4V AM

Prismatic loops were also observed in the irradiated Ti-6Al-4V AM at low irradiation doses at 450 °C and a higher dose at 340 °C.

The evolution of the microstructure during *in situ* irradiation at 450 °C can be seen in Figure 88. Similar to the observations in CP Ti, the number and the size of the <a> loops increased as the dose increased. The distribution of the <a> loop evolution for Ti-6Al-4V AM is presented in Figure 89. As the dose increased from 0.06 to 0.22 dpa, the median loop length increased from 40.6 nm to 55.2 nm, respectively.

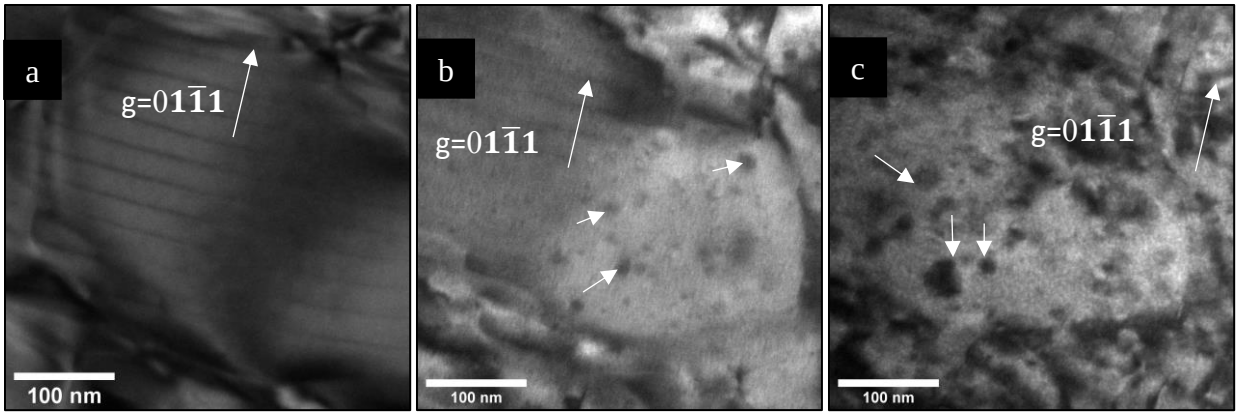

Figure 88. BF TEM photomicrograph showing the same area in AM Ti-6Al-4V irradiated *in situ* with 1 MeV Kr ions at 450 °C imaged with **g** = 01$\bar{1}$0 with increasing doses: a) 0 dpa; b) 0.06 dpa; c) 0.22 dpa. White arrows indicated some of the observed <a> loops in b) and c).

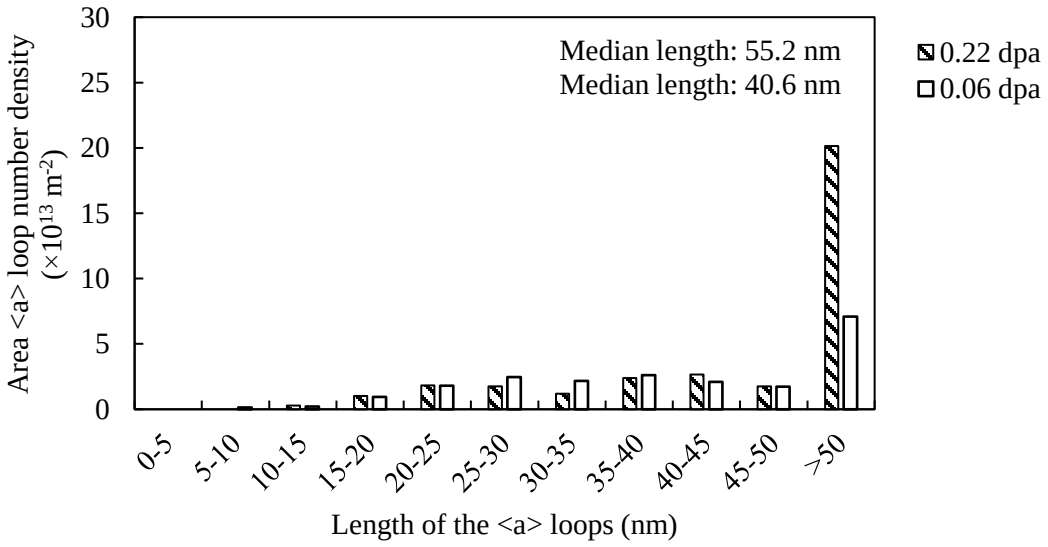

Figure 89. Distribution of the length of <a> loops in Ti-6Al-4V AM irradiated *in situ* with 1 MeV Kr at 450 °C.

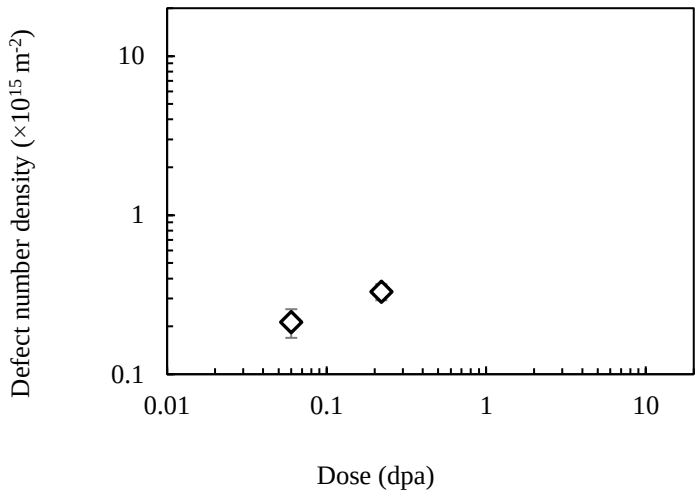

Figure 90. Area <a> loop number density in AM Ti-6Al-4V irradiated *in situ* at 450 ℃ with 1 MeV Kr as a function of dose.

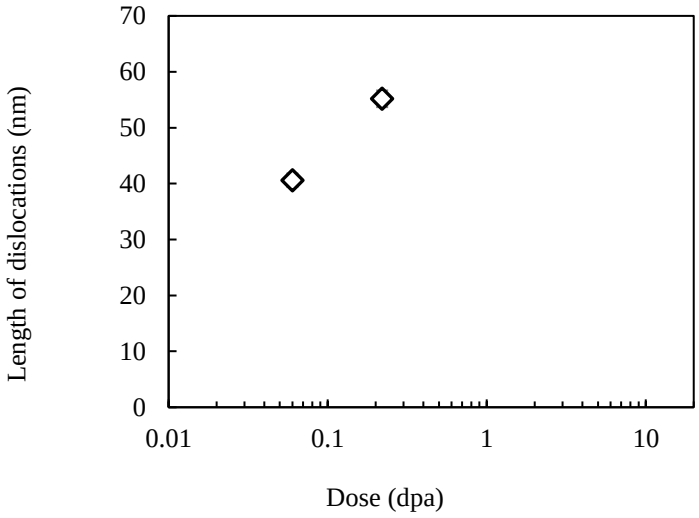

Figure 91. The median length of <a> loops observed in AM Ti-6Al-4V irradiated with 1 MeV Kr as a function of dose at 450 ℃.

An example of the damage structure at a dose of 3.7 dpa is presented in Figure 92. In addition to <a> dislocation loops (note their elliptical shapes), dislocation networks were also observed as shown in Figure 92-b.

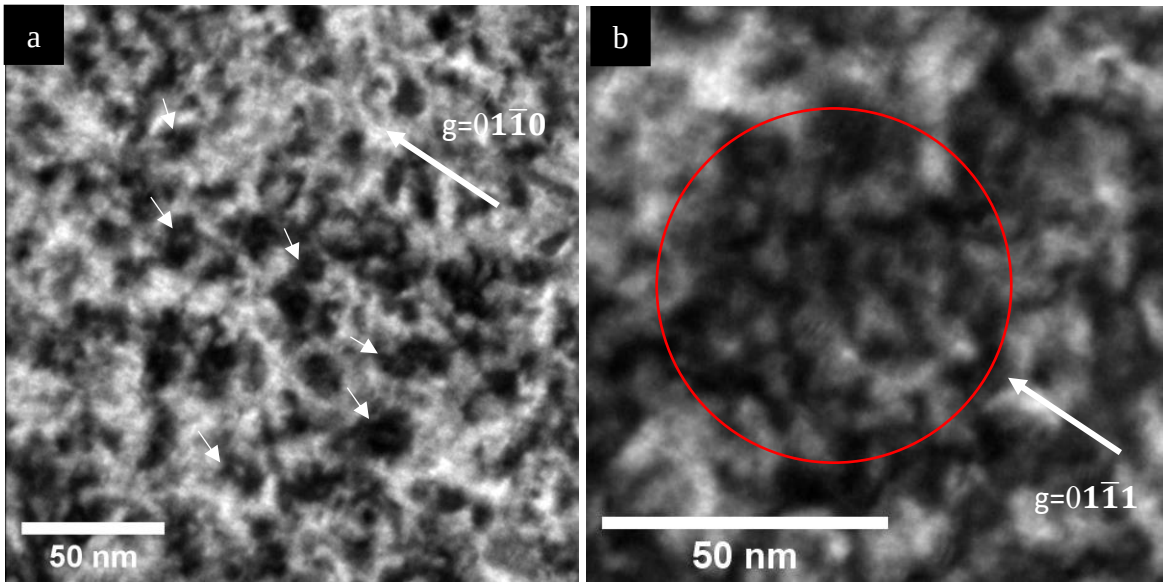

Figure 92. BF TEM photomicrograph showing the same area in AM Ti-6Al-4V irradiated *in situ* with 1 MeV Kr ions at 360 °C imaged with **g** = 01$\bar{1}$0 at the final dose of 3.7 dpa: a) Lower magnification photomicrograph with <a> loop pointed with white arrows; b) Higher magnification micrograph with an observed dislocation network circled in red.

4.4. OBSERVATIONS OF C-COMPONENT DISLOCATION LOOPS

This section presents the observations and quantification of basal c-component dislocation loops in CP Ti and AM Ti-6Al-4V during *in situ* TEM irradiation experiments with 1 MeV Kr ions at the IVEM Facility at different temperatures and doses. The basal loop nucleation is thought to occur during the collision cascade stage [147]. The stability and evolution of these loops depend on the presence of impurities, the temperature, the dose and their threshold incubation dose (TID) [20, 65]. In Zr, these loops were found to be mostly vacancy faulted loops [148]. The interest in these loops stems from concerns about irradiation-induced swelling that can have detrimental effects on metals used in nuclear applications [23]. In Ti, these loops also participate in radiation hardening at lower doses [15].

In the following section, a systematic characterization of basal loops in CP Ti at different temperatures and doses is presented. Observations of c-component loops in AM Ti-6Al-4V at 360 ℃ are also reported.

4.4.1. CP Ti

4.4.1.1. *In situ* irradiation

In situ TEM irradiation allowed for the observation of the nucleation and growth of c-component loops. Through the analysis of the acquired images and videos, the threshold incubation dose (TID) of c-component loops in CP Ti was identified. In Figure 93, the identified c-component loops in CP Ti irradiated at 360 ℃ were highlighted with blue arrows. Figure 93-b shows the irradiation dose (0.6 dpa) at which c-component loops were identified through the procedure described in 3.4.4. This dose was recorded as the TID for CP Ti at 360 ℃.

The TID for c-component loops as a function of irradiation temperature is plotted in Figure 94 for different temperatures. The TID decreased from 1.4 dpa to 0.2 dpa as the irradiation temperatures increased from 30 ℃ to 360 ℃. These observations are consistent with the trends observed in Zr (see Figure 13) [66].

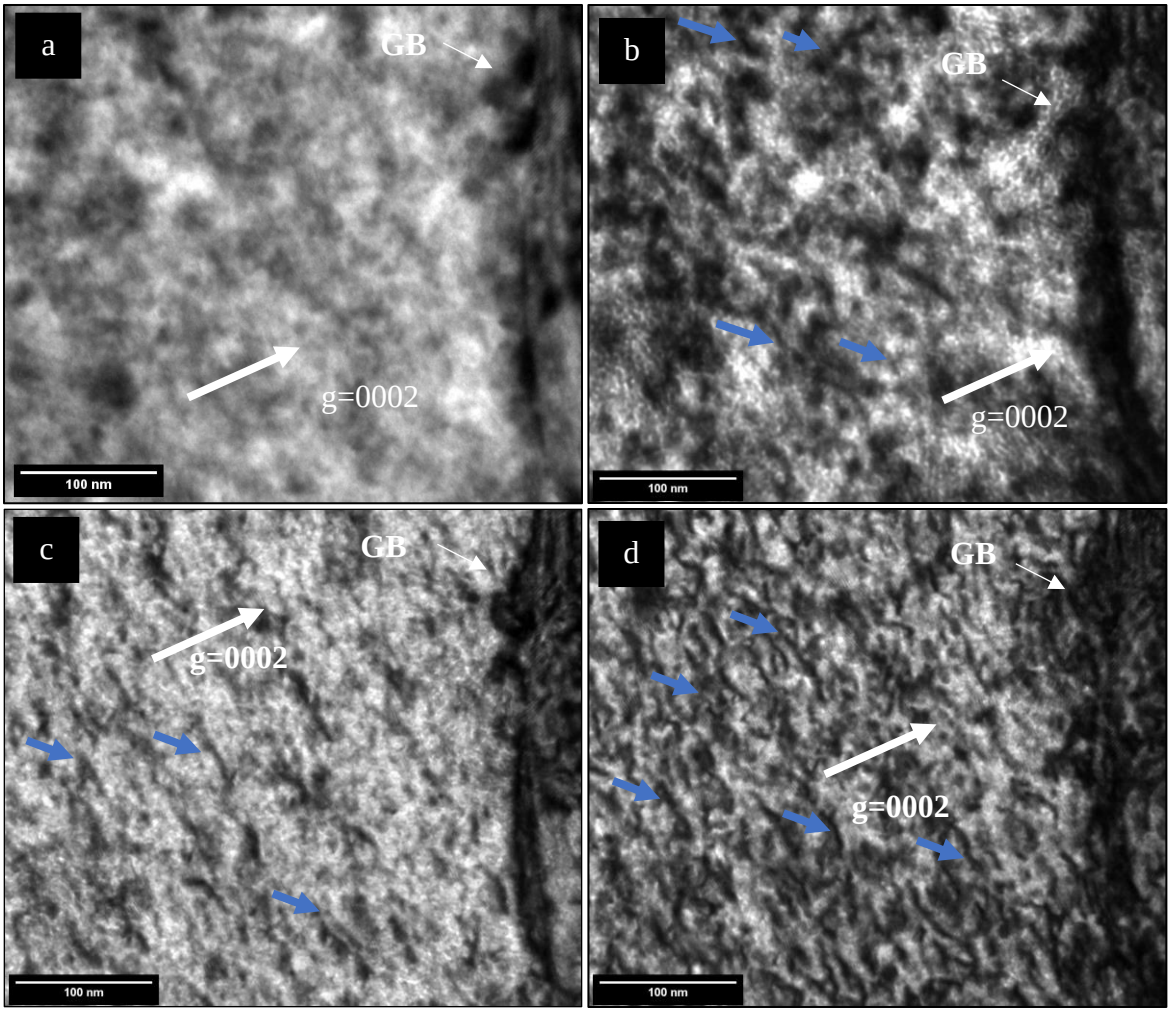

Figure 93. BF TEM photomicrographs showing the microstructural evolution in CP Ti irradiated with 1 MeV Kr at 360 °C at increasing doses in the same area: a) Area before irradiation; b) Area at a dose of 0.6 dpa; c) Area at a dose of 1.8 dpa d) Area at a dose of 3.7 dpa. The grain boundary (GB) is indicated with a white arrow in each photomicrograph. Blue arrows indicate some of the observed c-component loops.

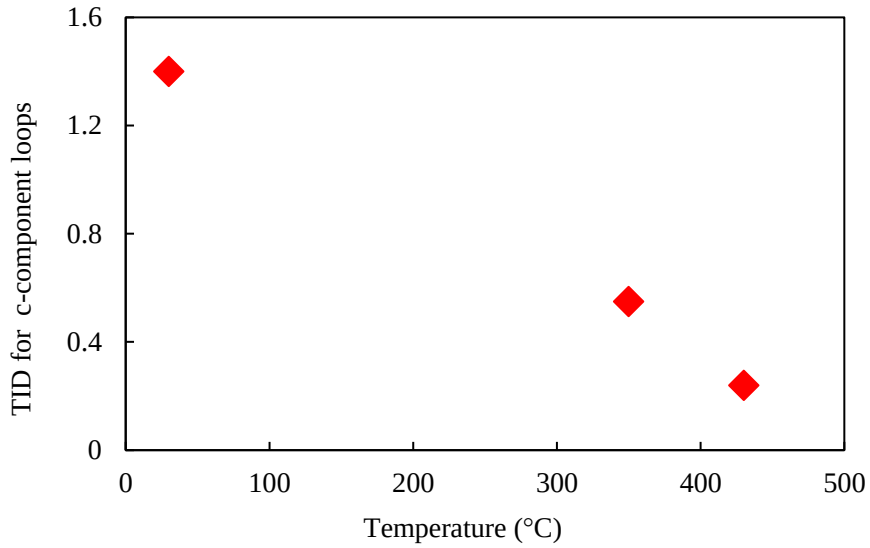

Figure 94. Threshold incubation dose (TID) for c-component loops in CP Ti irradiated *in situ* with 1 MeV Kr ion beam as a function of temperature.

Figure 93, Figure 95 and Figure 97 illustrate the observed increase in c-component loop nucleation as a function of increasing dose in the same area of a CP Ti foil. Denuded zones* at the grain boundary were not observed in irradiated CP Ti at any of the temperatures examined, as illustrated in Figure 95 and Figure 97. In fact, c-component loops were observed at a distance less than 10 nm from the grain boundary in all samples. Figure 96 shows the coalescence of smaller neighboring loops to form longer strings easily identifiable as c-component loops in the CP Ti irradiated with 1 MeV Kr.

The distributions of the length of the c-component loops in CP Ti irradiated *in situ* at 30 ℃, 360 ℃ and 430 ℃ for different doses are shown in Figure 98. All the distributions are right-skewed. As the dose increases, the right-skewed distributions move further to the left. As a result, the median values of the c-component loop length increase as a function of dose for each

*Dislocation free zone observed in the case of irradiated Zr alloys [66].

temperature. For the irradiation temperature of 360 ℃ and between the doses of 1.9 and 3 dpa, the loops that already nucleated grew in size while a few new loops formed (see Figure 98-b).

A similar trend was observed for the sample irradiated at 430 ℃. The increase in c-component loops length above 50 nm with increased dose is significant (see Figure 98-c). At the final irradiation dose of 0.55 dpa, both small (between 5 and 10 nm) and large (above 50 nm) loops were present in the foils and as shown in Figure 98-c, and the two highest loop diameter peaks were indicated by red arrows.

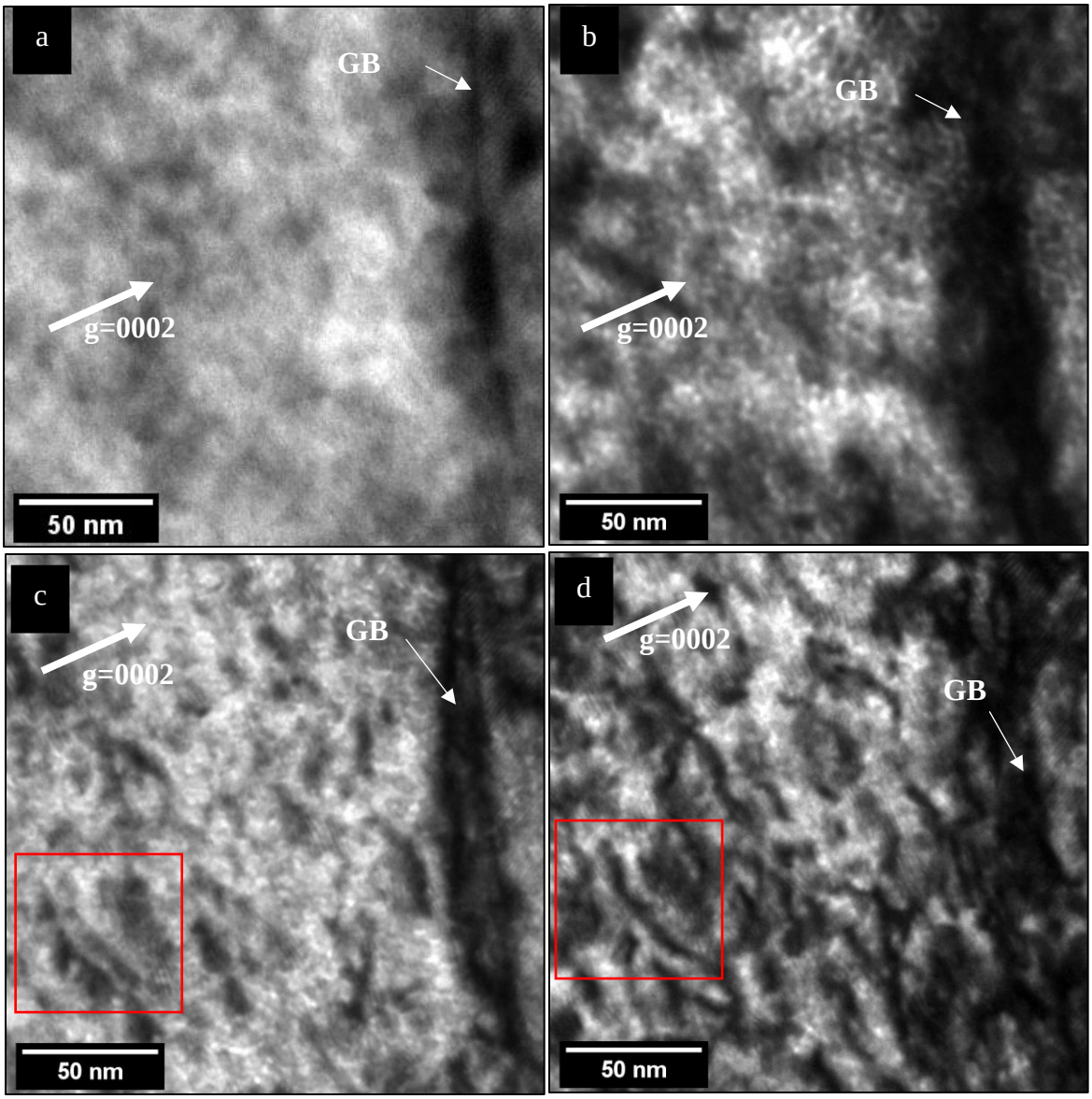

Figure 95. BF TEM photomicrographs showing the microstructural evolution in CP Ti irradiated with 1 MeV Kr at 360 °C at increasing doses in the same area: a) Area before irradiation; b) Area at a dose of 0.6 dpa; c) Area at a dose of 1.8 dpa; d) Area at a dose of 3.7 dpa. The grain boundary (GB) is indicated with a white arrow. The red box highlights the same area that is magnified in Figure 96.

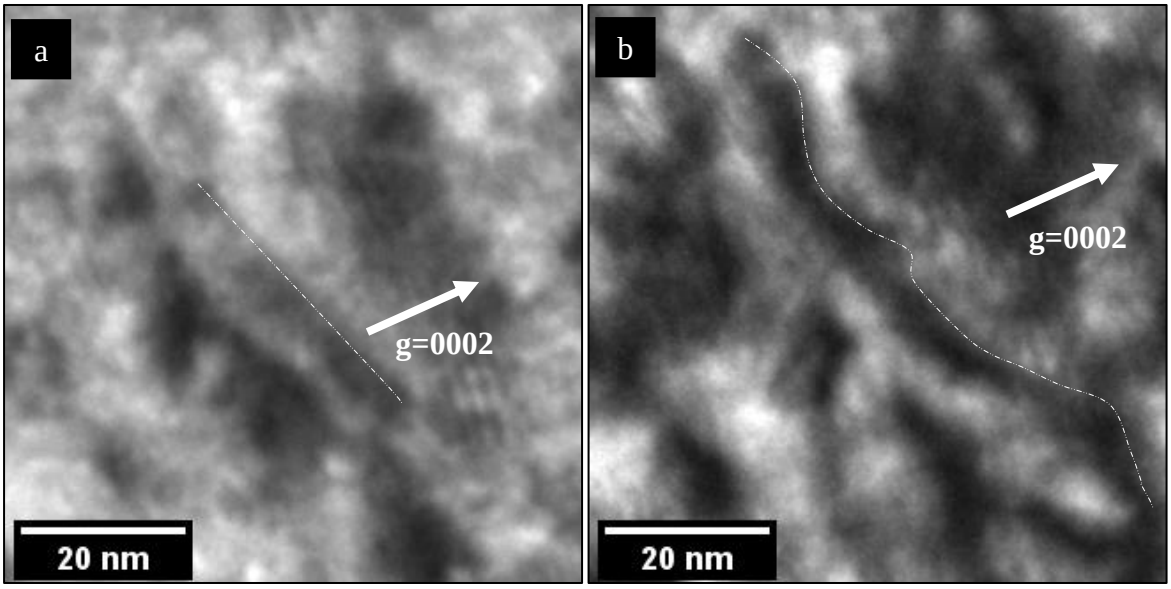

Figure 96. BF TEM photomicrographs showing coalescence of smaller neighboring loops to form longer strings easily identifiable as c-component type loops in CP Ti irradiated with 1 MeV Kr at 360 ℃ at different doses: a) Area at a dose of 1.8 dpa ; b) Area at a dose of 3.7 dpa.

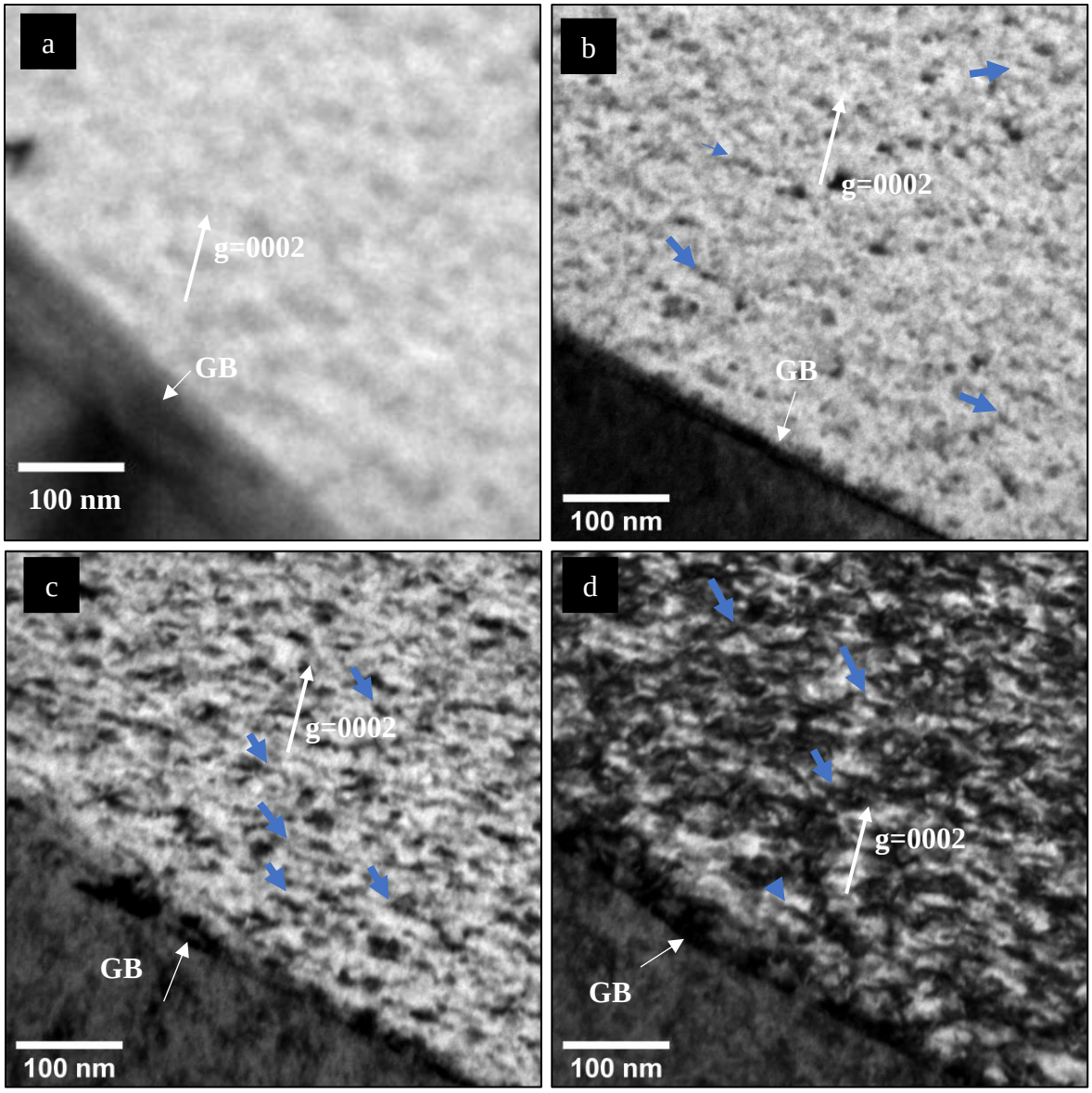

Figure 97. BF TEM photomicrographs showing the microstructural evolution in CP Ti irradiated with 1 MeV Kr at 30 ℃ at increasing doses in the same area: a) Area before irradiation; b) Area at a dose of 1.4 dpa; c) Area at a dose of 4.1 dpa d) Area at a dose of 11 dpa. Blue arrows point to some of the observed c-component loops in each micrograph. The grain boundary (GB) is indicated with a white arrow. Blue arrows indicate some of the observed c-component loops.

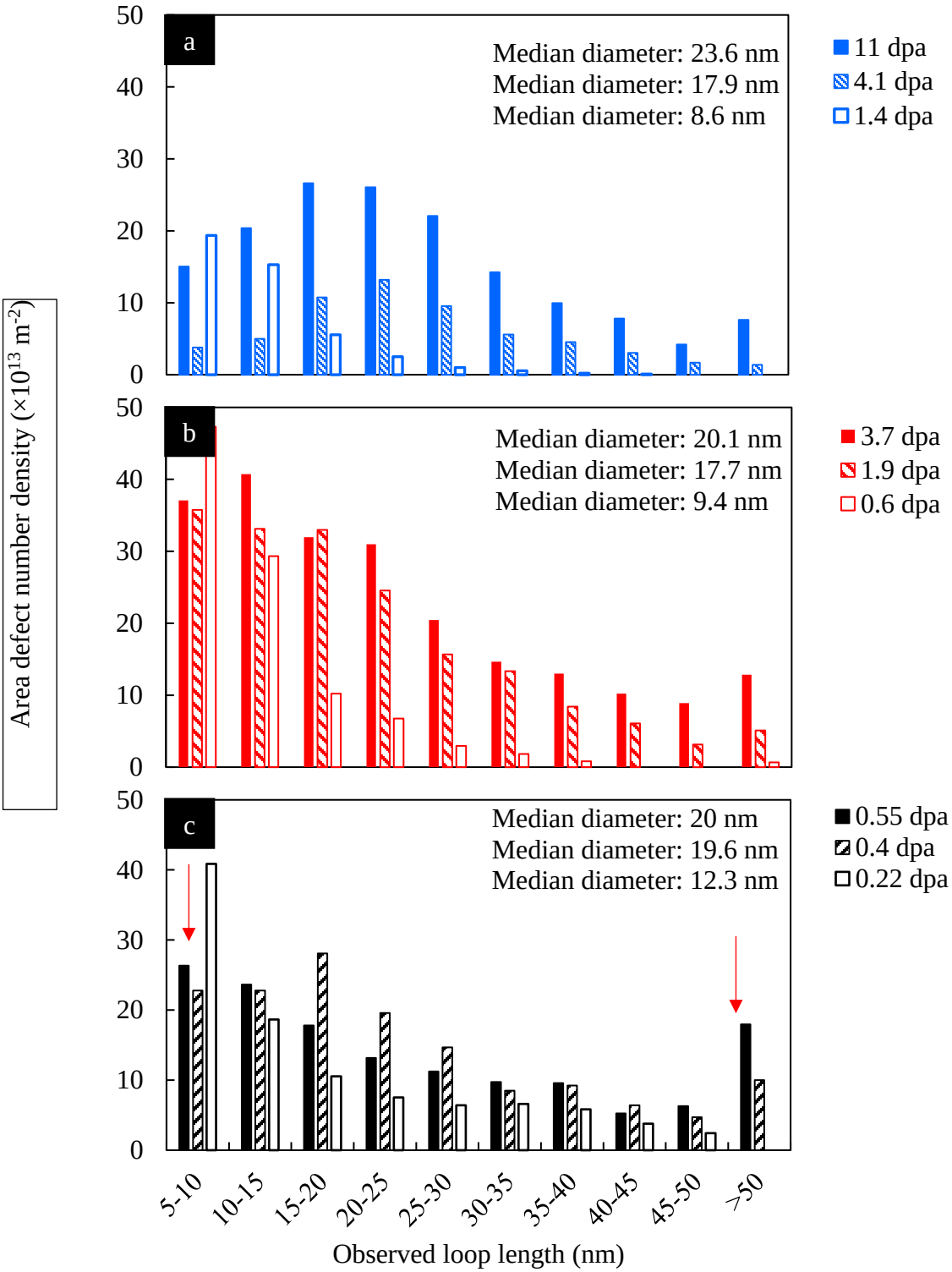

Figure 98. Distributions of the observed length of c-component loops in CP Ti irradiated *in situ* with 1 MeV Kr at: a) 30 ℃; b) 360 ℃; and c) 430 ℃. Red arrows in c) point to the two peak densities in the sample irradiated up to a dose of 0.55 dpa.

4.4.1.2. *Ex situ* irradiation

TEM foils made from CP Ti samples irradiated *ex situ* with 4 MeV Ar ion beams at 30 ℃ and 350 ℃ were also examined. As the temperature increased, the c-component loop length increased significantly as can be seen in Figure 99.

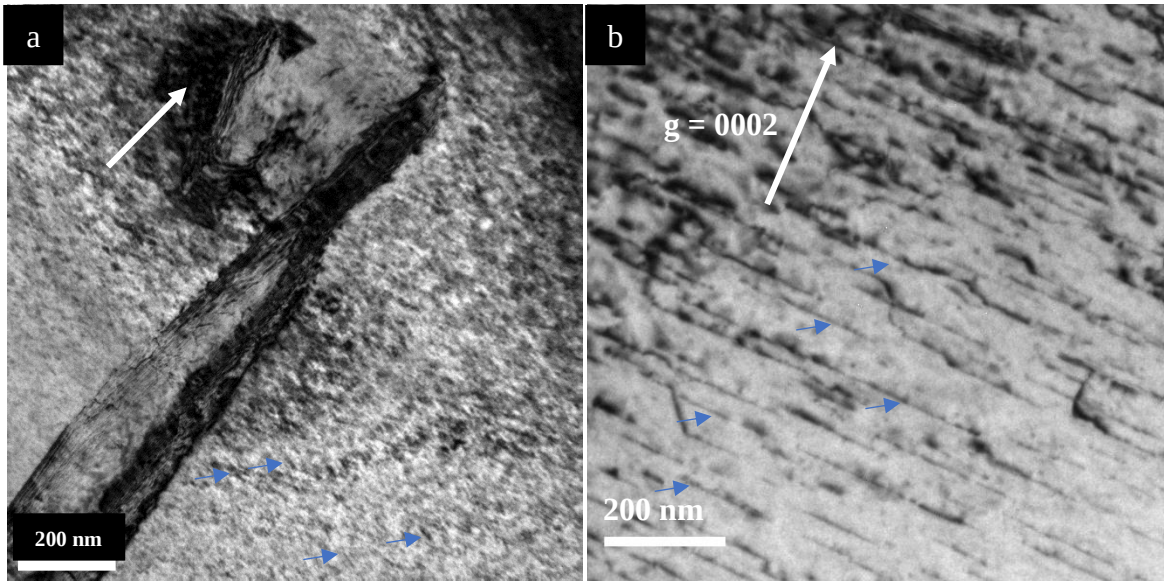

Figure 99. BF TEM photomicrographs showing the CP Ti samples irradiated *ex situ* with 4 MeV Ar ions imaged with **g** = 0002: a) Sample irradiated at 30 ℃ and with the dose at the surface of 4.1 dpa; b) Sample irradiated at 350 ℃ and with the dose at the surface of 7.5 dpa. Blue arrows indicate some of the observed c-component loops.

4.4.1.3. Effect of dose and temperature

To better understand the effect of the dose and temperature on the evolution of c-component loops in CP Ti at different temperatures and doses, defect number densities and linear densities were calculated (see Figure 100 and Figure 101). The median values of the c-component loop length as a function of dose and temperature are plotted in Figure 102. The defect number densities for the sample irradiated at 30 ℃ were the lowest and they increased

as a function of dose. As for the sample irradiated at 360 ℃, a slower increase in the defect number density between 0.6 dpa and 3 dpa was observed with an increase in the loop length from 9 nm to 20 nm. The sample irradiated at 430 ℃, exhibited a significant increase in c-component loop area density (see Figure 100) and length (see Figure 102) between doses of 0.22 and 0.4 dpa. Additional higher dose data points are needed to verify whether the c-component loops evolution saturates at ~ 0.55 dpa.

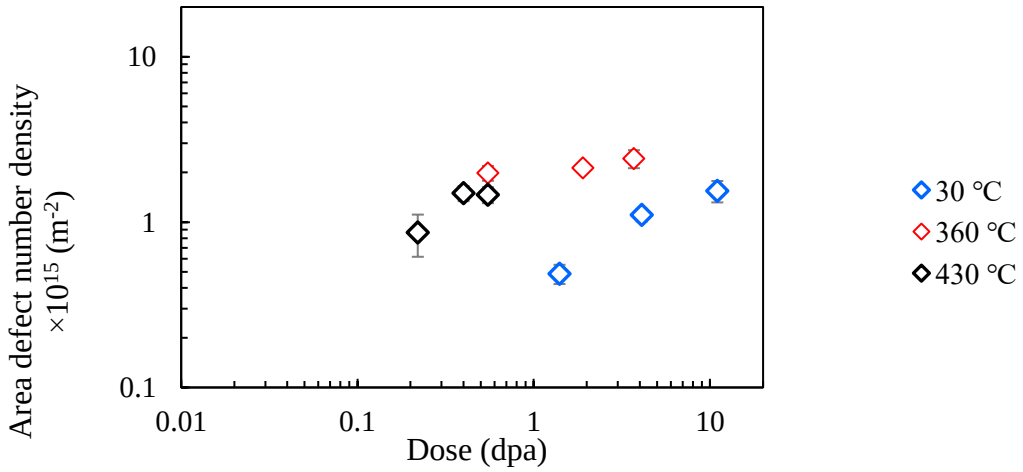

Figure 100. Defect number density as a function of dose and temperature for CP Ti.

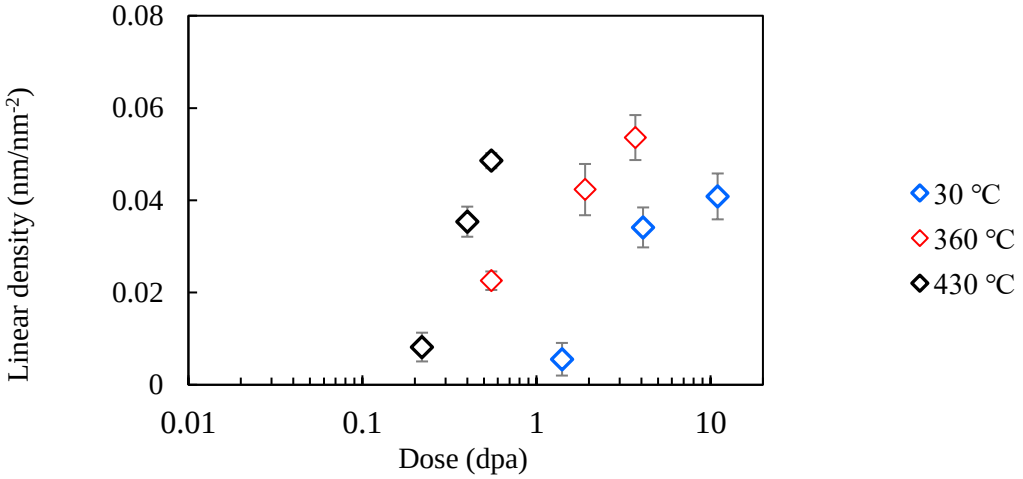

Figure 101. Defect linear density as a function of dose and temperature for CP Ti.

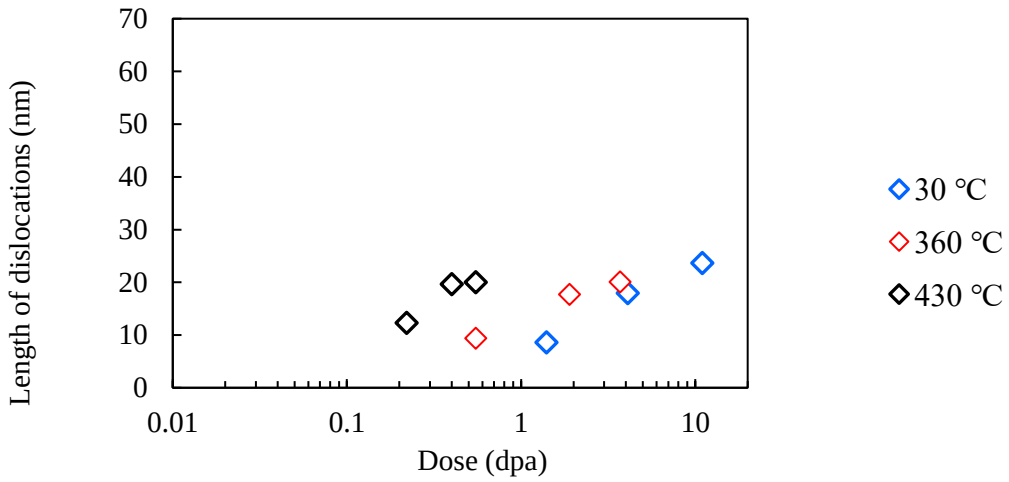

Figure 102. The median observed length of c-component loops as a function of dose and temperature.

4.4.2. Ti-6Al-4V AM

In situ TEM irradiation experiments at 360 ℃ and 430 ℃ were performed on Ti-6Al-4V AM in order to observe c-component loop nucleation and growth.

The evolution of c-component loop nucleation in Ti-6Al-4V AM is presented in Figure 103 for a sample irradiated at 360 ℃ up to a dose of 3.7 dpa. The TID at this temperature was 0.43 dpa as shown in Figure 103-b. The observation of dislocation loops in this Ti alloy was complicated by the appearance of small features visible under this imaging condition ($\mathbf{g} = 0002$) (see Figure 103-(b-d)). As such, the quantification of basal c-component loops was only performed at a dose of 3.7 dpa (see Figure 104).

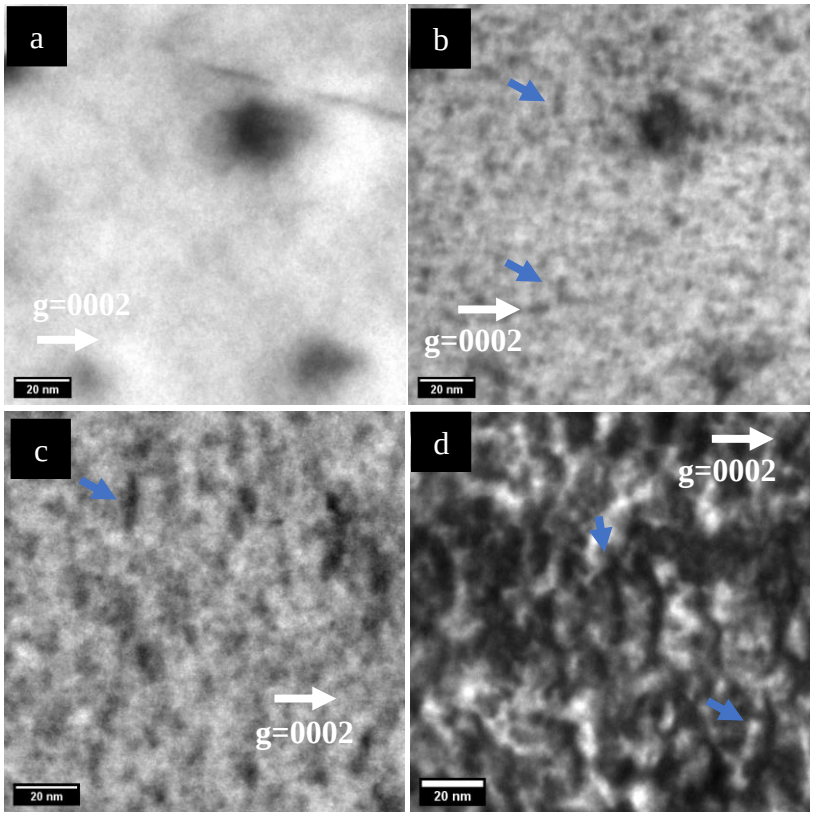

Figure 103. TEM BF photomicrographs showing the evolution of the microstructure in AM Ti-6Al-4V irradiated with 1 MeV Kr ions at 360 °C at increasing doses in the same area: a) Area before irradiation; b) Area at a dose of 0.43 dpa; c) Area at a dose of 1.9 dpa; b) Area at a dose of 3.7 dpa. Some of the c-component loops are indicated with a blue arrow.

The distributions of the observed length of basal loops in the AM Ti-6Al-4V are shown in Figure 104. Similar to CP Ti (see Figure 98), this distribution was also right-skewed. The median c-component loop length was equal to 10.7 nm, which is much smaller than the c-component loop length observed in CP Ti at the same irradiation condition. The calculated c-component loop number density was 2.18×10^{15} m^{-2} and the linear density was 3.1×10^{7} m/m^{2}.

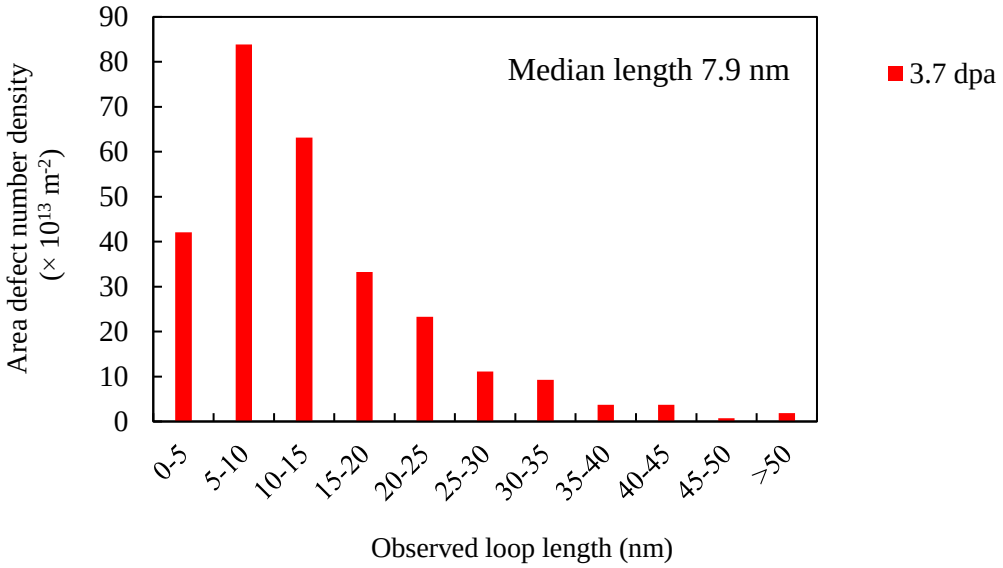

Figure 104. Distribution of the observed length of c-component loops in CP Ti irradiated *in situ* with 1 MeV Kr at 360 °C.

The area defect number density at 360 °C was similar to the one calculated in CP Ti at the same irradiation conditions (see Figure 105). However, as can be seen in Figure 106, the c-component loop length in Ti-6Al-4V AM was significantly shorter.

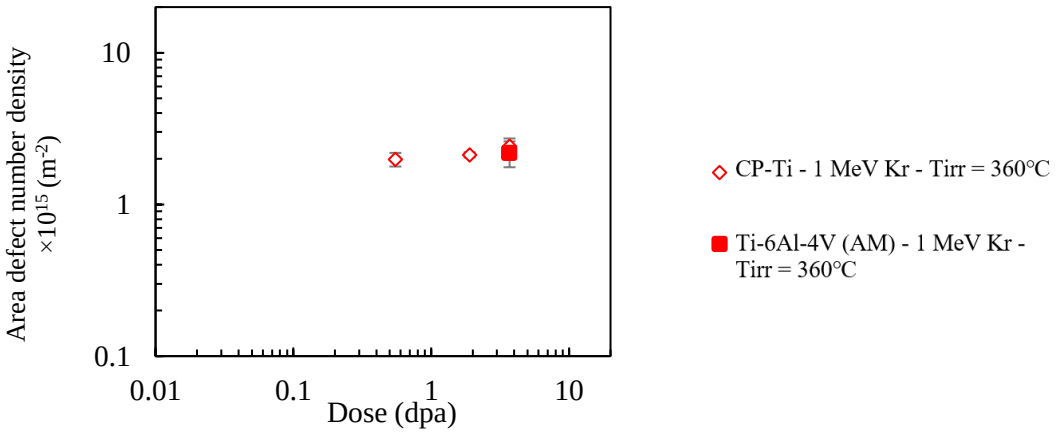

Figure 105. Area c-component loop number density as a function of dose for CP Ti and AM Ti-6Al-4V irradiated at 360 °C with1 MeV Kr ion beams.

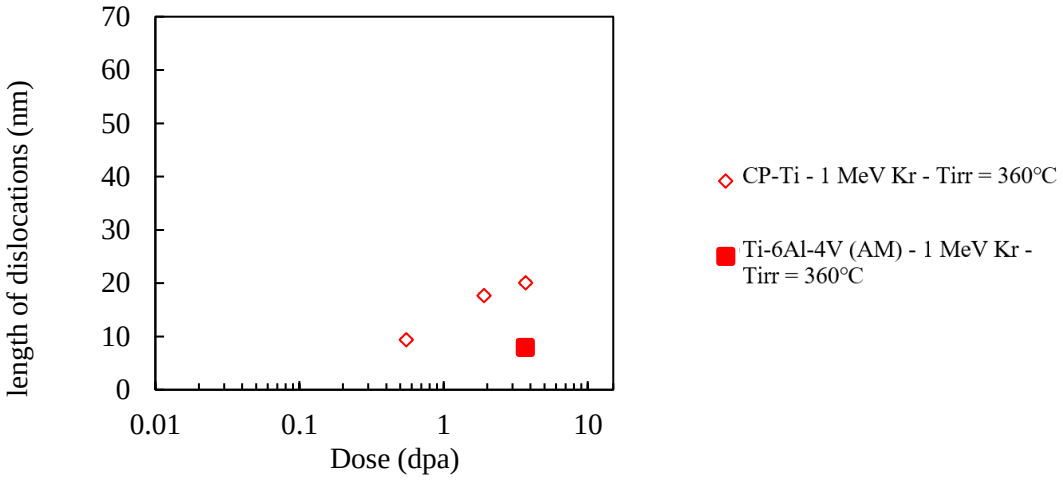

Figure 106. C-component loop length as a function of dose for CP Ti and AM Ti-6Al-4V irradiated at 360 °C with 1 MeV Kr ion beams.

Analyzing c-component loops was not possible for the sample irradiated at 430 °C due to complex features appearing under the imaging conditions selected for this experiment (**g** = 0002) and that were not c-component loops (See Figure 107-b). These linear features already appeared after heating the sample, as can be seen in Figure 107-a.

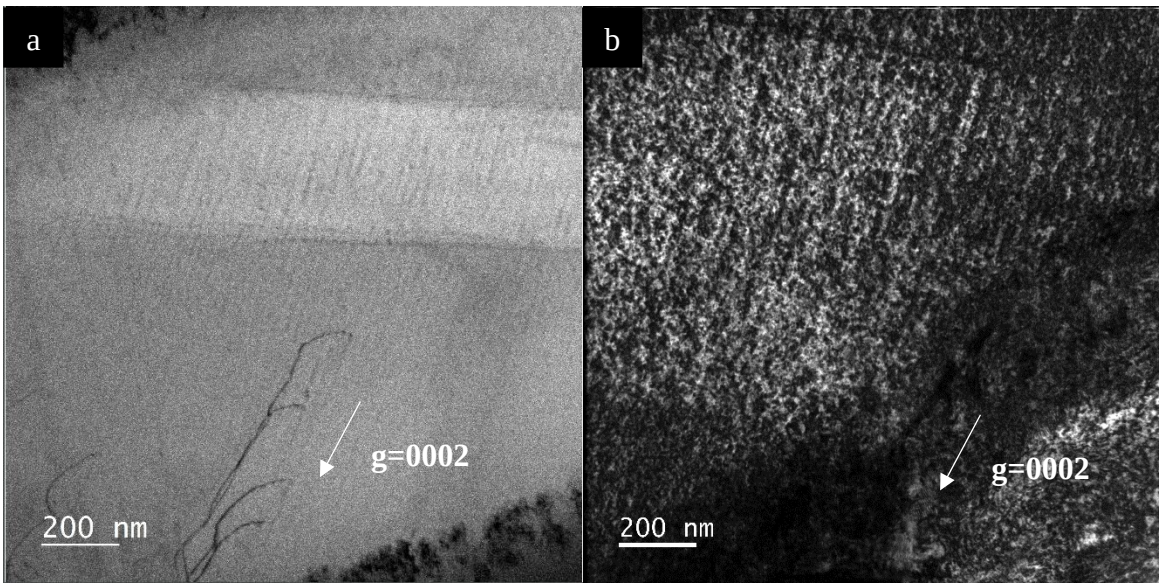

Figure 107. TEM BF photomicrographs showing the microstructural evolution in AM Ti-6Al-4V irradiated with 1 MeV Kr at 430 °C: a) Area before irradiation; b) Area at a dose of 0.55 dpa.

CHAPTER 5
DISCUSSION

In this chapter, a discussion of the radiation damage in Ti and Ti alloys is provided. The results of the TEM investigation are compared to previously published results to validate the findings. The dispersed barrier hardening model is used in CP-Ti to analyze structure-mechanics relationships after irradiation. A good agreement between experimental measurements of the hardening in irradiated CP Ti and the calculated contributions from dislocation loops is found. The barrier strength factors of the <a> and c-component dislocation loops are 0.15 and 0.02, respectively confirming that <a> loops act as strong barriers to dislocation motion in ion irradiated Ti [33]. Finally, the effect of the microstructure and grain size among the three materials is discussed.

The irradiation dose and temperature dependence in hardening is analyzed for the Ti-6Al-4V PM. The effect of the initial microstructure on the resistance to radiation-induced hardening in low-temperature irradiation with a 4 MeV Ar ion beam in the AM and PM alloys is discussed.

5.1. DISCUSSION OF DISLOCATION LOOP CHARACTERIZATION

5.1.1. Evolution of <a> loops

The defect number density of <a> dislocation loops and their equivalent diameter in CP Ti from the current work were compared to the results of ion [33] and proton [14] irradiation in Figure 108 and Figure 109. As expected, temperature and dose dependence was observed for all samples. At a low temperature, high defect densities and smaller defect sizes were observed in the samples irradiated with 1 MeV Kr and 590 MeV protons [13]. The defect density decreased

for higher temperatures while the loop size increased. Since the dose rate was lower, a temperature shift of 30 ℃ was considered for the irradiation with 590 MeV protons at 250 ℃, as shown in Table 16. Hence, the equivalent temperature for this 590 MeV protons irradiation [13] is 290 ℃, closer to the irradiation temperature in [33]. The defect densities resulting from proton irradiations [14] is higher than ion irradiation results from both the current work and [33].

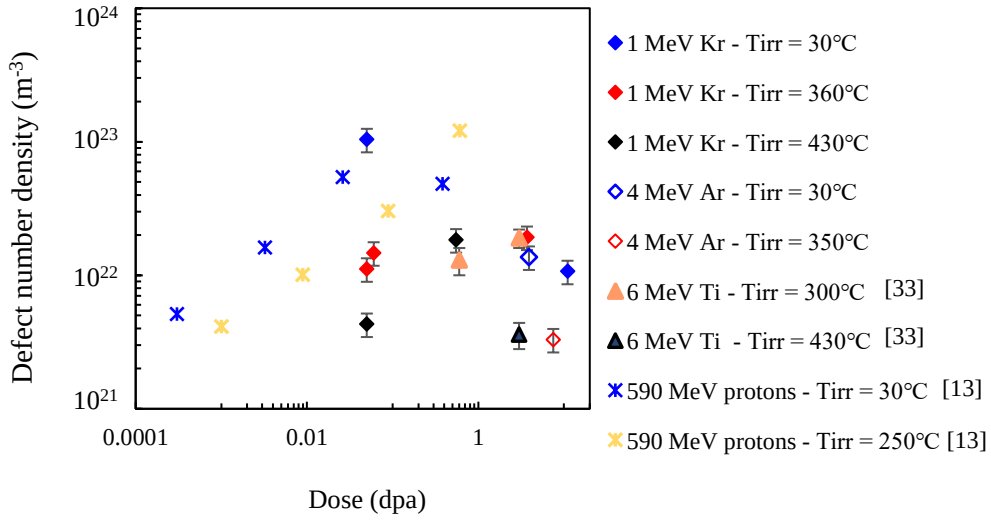

Figure 108. Comparison of the results from current work and literature for defect number density of <a> loops for Ti: Irradiated with 1 MeV Kr and 4 MeV Ar ion beams from the current work (CP Ti); Irradiated with 6 MeV Ti ion beams from [33] (CP Ti); Irradiated with 590 MeV proton beam from [13] (High purity Ti). The irradiation temperature for each set of samples is indicated in the legend.

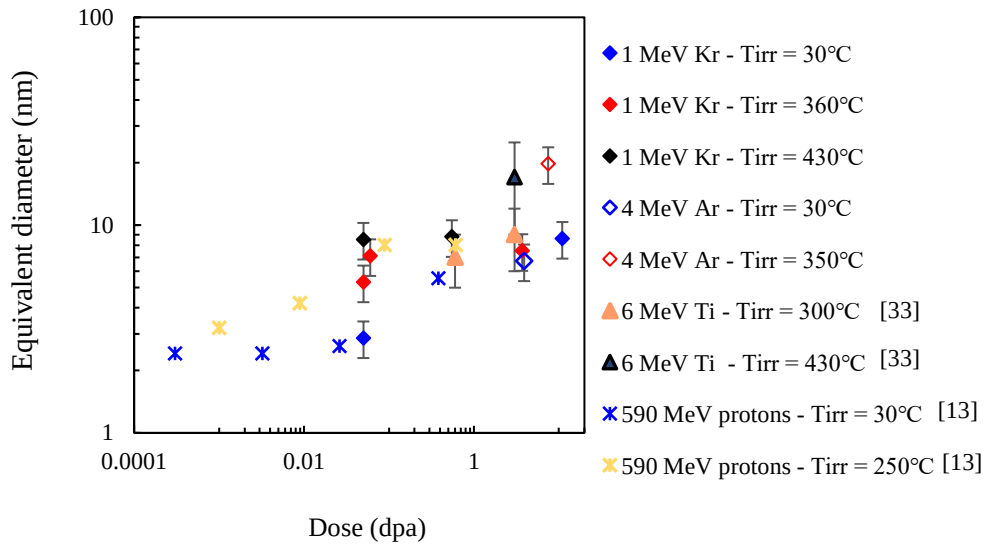

Figure 109. Comparison of the results from current work and literature for the evolution of equivalent diameter of <a> loops for Ti: Irradiated with 1 MeV Kr and 4 MeV Ar ion beams from the current work (CP Ti); Irradiated with 6 MeV Ti ion beams from [33] (CP Ti); Irradiated with 590 MeV proton beam from [13] (High purity Ti). The irradiation temperature for each set of samples were indicated in the legend.

The defect yield, DY, defined as the probability for an incident ion to produce a visible defect, is an important parameter to consider for radiation resistance. In the plot of defect number densities (Figure 108), the defect yield decreased with temperature due to the enhanced mobility of point defects and their recombination [66].

The microstructure of irradiated Ti–6Al–4V PM was investigated after neutron [12, 149], proton [150 - 152], and heavy-ion irradiations [11, 16, 17, 33, 92, 153]. Special attention was given to the irradiation-induced precipitation, especially at high temperatures (RIS domain illustrated in Figure 54). Either V-rich precipitates [12, 17] or β phase precipitates [16] were observed at doses between 0.3 dpa and 3 dpa and at temperatures above 300 °C. At lower temperatures, TEM investigations showed mainly a high density of dislocation loops [12].

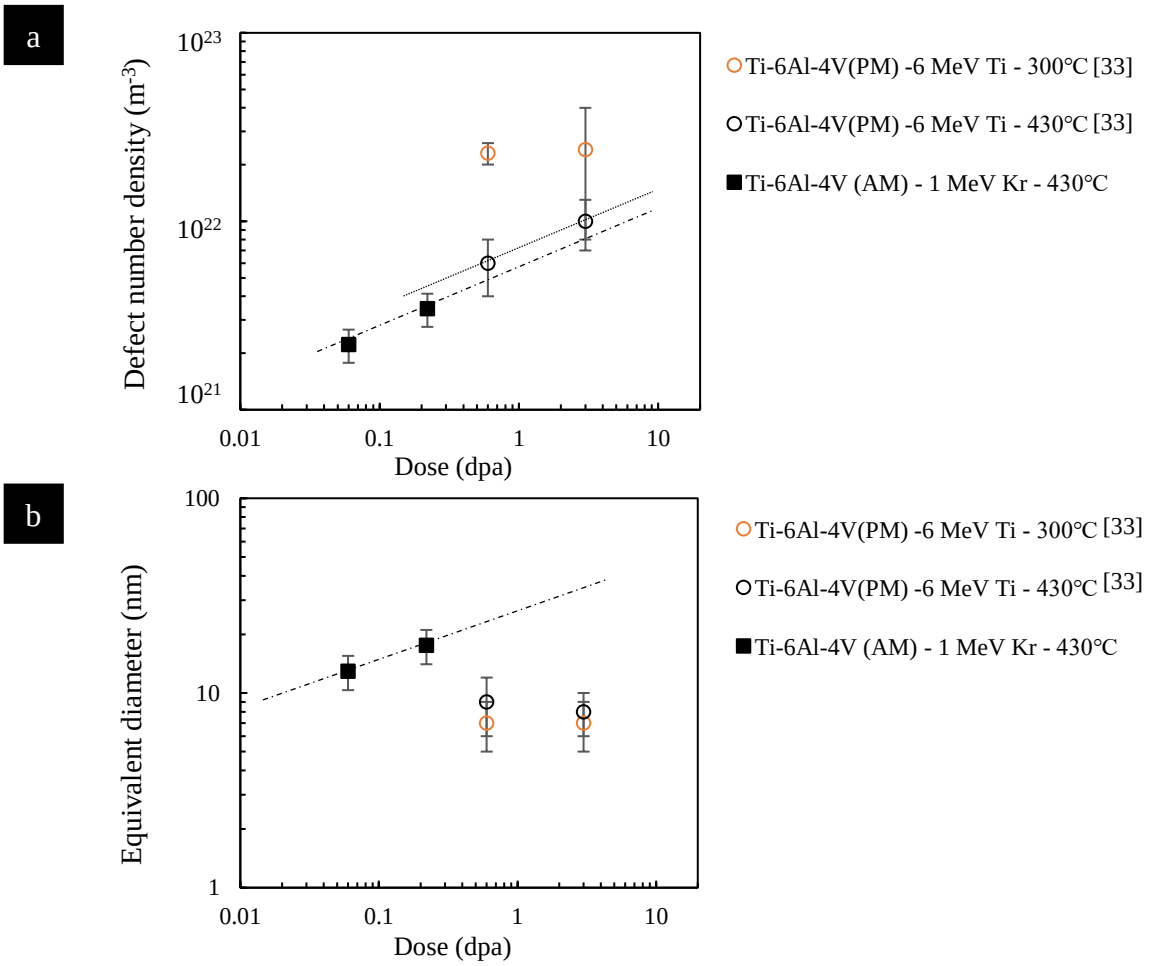

Figure 110. Comparison of the results from current work and literature for the evolution of <a> loops: a) Defect number density and b) Equivalent diameter in two different Ti-6Al-4V alloys: AM and irradiated with 1 MeV Kr and at 430 °C from the current work; PM Irradiated with 6 MeV Ti ion beams from [33]. The irradiation temperature for each set of samples is indicated in the legend.

A comparison between <a> loops in Ti-6Al-4V alloys AM irradiated with ion beams from the current work and PM from [33] is presented in Figure 110. In both ion irradiations at 430 °C of the AM and PM [33] alloys, an increase of the defect density was observed. In Ti-6Al-4V PM irradiated at 300 °C, the <a> loop number density did not change between 0.6 and 3 dpa. In terms of the defect size, the equivalent diameter of AM Ti-6Al-4V was higher than for the PM alloy. For the irradiations with 6 MeV Ti ions [33], the dose rate was very similar (~2×10^{-4} dpa/s) and that could not account for the higher defect size. Investigating, Ti-6Al-4V

AM samples irradiated at lower temperatures might lead to a better understanding of the effect of the grain refinement on the dislocation loop structure. A discussion of the effect of the grain size on radiation resistance is presented in 5.2.1.6.

Irradiation temperatures below 500 °C, as was the case in the current work, fall whithin intermediate temperature stage* [58], where point defects, including self-interstitial atoms (SIAs) and vacancies, are mobile. At lower doses, these loops appear as black dots, such as the observed loops in CP Ti sample irradiated at 30 °C at a dose of 0.05 dpa. These small defects were also observed in Zr [66] and are identified as <a> dislocation loops formed by the collapse of vacancy and interstitial clusters [70]. As the irradiation dose increased, the size of these loops increased, as observed for all irradiation temperatures. Similar to the case of Zr [66], loop growth is thought to occur as a result of loop calescence , i.e. the absorption of smaller loops by larger loops [17, 23, 33]. Alongside the coalescence of already formed loops, new small defects were also present. The final damage structure at 430 °C, included dislocation networks both for CP Ti and AM Ti-6Al-4V (see Figure 83 and Figure 92). Interactions between dislocation loops and dislocation networks may result in loop unfaulting [23]. These unfaulted loops can then contribute to the dislocation network.

5.1.2. Formation of c-component loops and threshold incubation dose (TID)

Radiation-induced swelling in hcp metals depends on the dislocation density, grain size, shape and texture and irradiation temperature. Swelling is enhanced for samples containing c-component loops [74]. This is the reason that c-component loop nucleation was extensively studied in Zr and Zr alloys [74, 76, 154]. Investigations of c-component loops in Ti are very

* Point defect recovery stages that can identify the temperature at which point defects are mobile: Low temperature stage, intermediate temperature stage and high temperature stage [58].

limited [33] and the current study is the first to investigate their evolution at different temperatures and doses. Similar to Zr alloys [66], the current work showed that c-component loops were only observed after reaching a threshold incubation dose (TID).

In CP Ti, c-component loops nucleated more easily in samples irradiated at higher temperatures, as can be seen in Figure 111. The TID in the current work was reported in the same way*. The migration and formation energies of vacancies and interstitials in Zr being higher than those of Ti [155] could explain the lower doses at which c-component loop were observed in the current work. One of the main mechanisms assisting the formation of c-component loops is the presence of alloying elements in the metal, especially the presence of Fe [20]. Fe being a fast diffuser [156], the radiation-induced dissolution of precipitates increases the interstitial diffusion of Fe in the Ti matrix. This enhanced diffusion can decrease the stacking fault energy of the Ti matrix, which assists the nucleation of c-component loops [76]. The Fe-rich precipitates observed in the current study in CP Ti (see Figure 58) could explain the lower TID values as opposed to those for pure Zr in [20], where no precipitates were observed. In fact, for pure Zr, c-component loops were not observed at temperatures below 400 °C. The TID for Ti-6Al-4V AM at 360 °C was 0.22 dpa. This dose was lower than for CP Ti, which is consistent with a decrease in stacking fault energy with increasing Al content in Ti alloys [157]. These results are coherent with observations in Zr alloys, where certain alloying elements promote the c-component loop nucleation [76].

* TID is the dose at which c-component loops were unambiguously identified in a TEM photomicrograph.

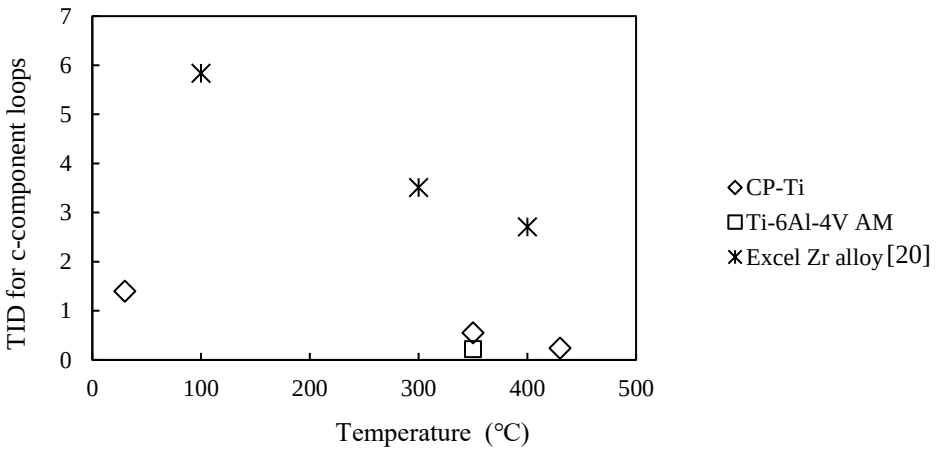

Figure 111. Threshold incubation dose for c-component loops in samples irradiated with 1 MeV Kr ions: CP Ti and Ti-6Al-4V AM results are from the current work and the Excel Zr results are from [20]. All irradiations were performed at the IVEM facility with 1 MeV Kr ion beams.

The defect densities for <a> and c-component dislocation loops in CP Ti irradiated *in situ* with 1 MeV Kr ions are plotted in Figure 112. For irradiations at 30 °C and 360 °C, the number density of <a> loops decreased as the c-component loop density increased, supporting the hypothesis that the nucleation of c-component loops is assisted by <a> loops [125].

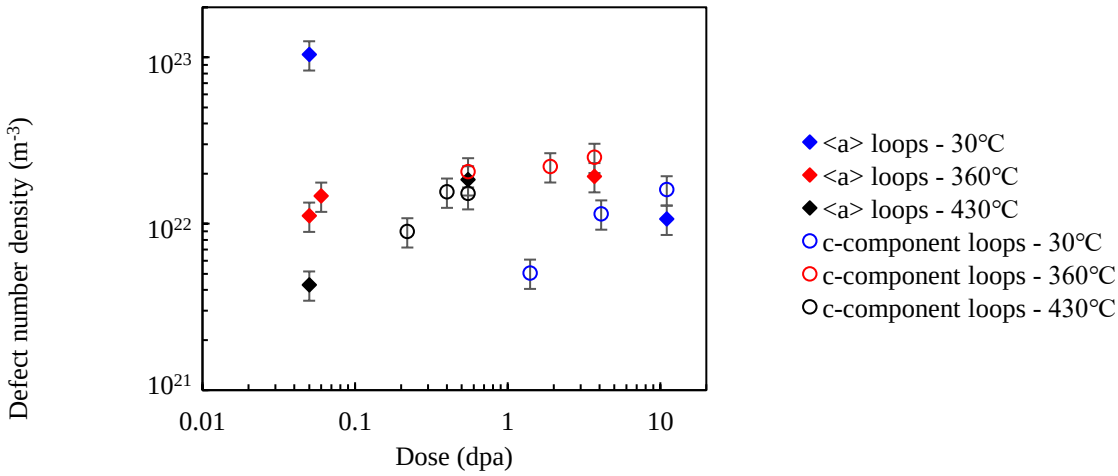

Figure 112. Defect number densities of dislocation loops in CP Ti irradiated *in situ* with 1 MeV Kr ions at different temperatures as indicated on the legend.

Although the presence of c-component loops was previously reported [65, 70], Jouanny [36] was the first to quantify them for CP Ti samples irradiated at 300 °C [33]. A comparison

between the results reported by Jouanny [33] and the current results is presented in Figure 113. Samples irradiated *ex situ* with 6 MeV Ti and 4 MeV Ar ion beams at a temperature of 300 ℃ and 350 ℃ had similar linear loop densities. The higher linear defect densities observed for the sample irradiated *in situ* with 1 MeV Kr ion beam at and 360 ℃ may be a result of the surface stress in the foil [20]. This stress was suggested as a factor assisting c-component loop nucleation during in situ TEM irradiations of Zr [148].

The linear defect density of the Ti-6Al-4V AM was significantly lower than that for CP Ti irradiated with the same 1 MeV Kr ions and at 360 ℃ and a similar dose of ~ 3 dpa. Although c-component loops nucleate at lower doses in the Ti-alloy compared to CP Ti, their growth is less important subsequently. This observation suggests a lower radiation-induced swelling in Ti-6Al-4V AM compared to CP Ti.

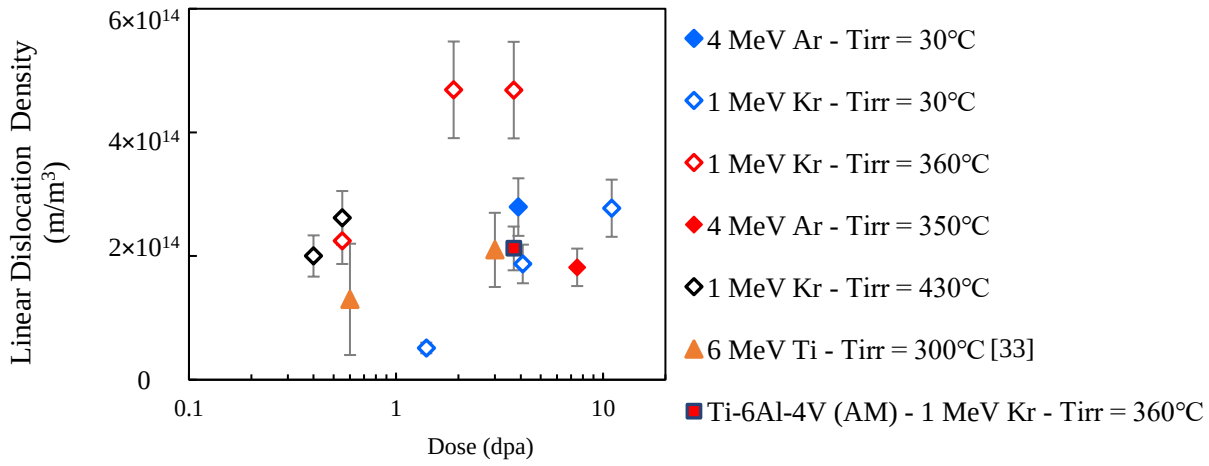

Figure 113. The linear defect density of c-component dislocation loops as a function of dose in CP Ti and Ti-6Al-4V AM irradiated with 1 MeV Kr and 4 MeV Ar ion beams from current work. Data for CP Ti sample irradiated with 6 MeV Ti at 300 ℃ were extracted from [33].

A comparison between the evolution of c-component loops in CP Ti and Zr [20] during irradiation with 1 MeV Kr ions is presented in Figure 114. Although the area defect number densities were comparable, the average lengths of the observed c- component loops are higher in

Zr than CP Ti. Radiation-induced swelling is therefore expected to be higher in Zr. Data on the swelling of Ti was not available to confirm this hypothesis.

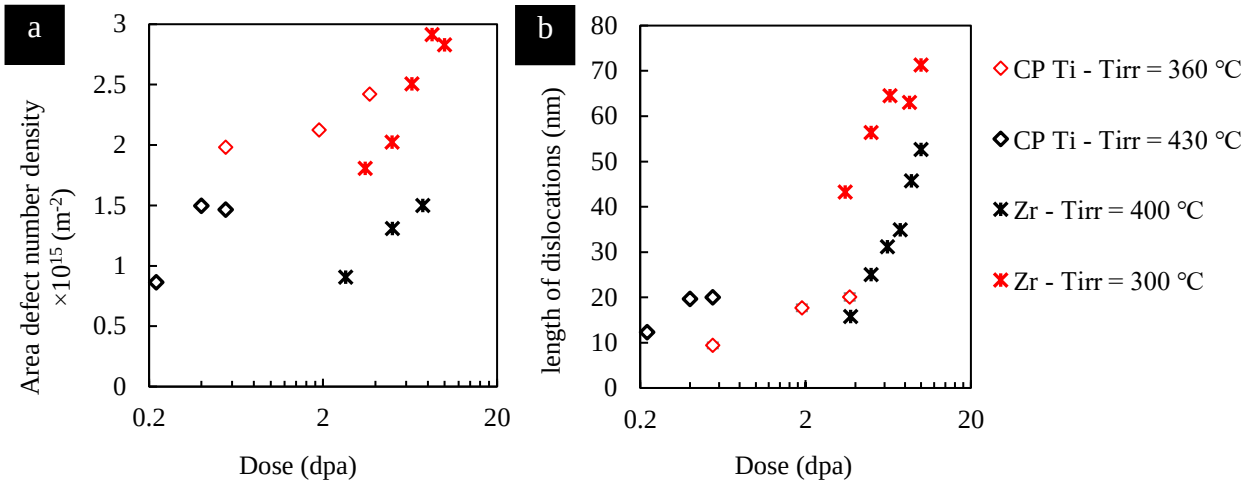

Figure 114. Comparison between the evolution of c-component dislocation loops as a function of dose in CP Ti (current work) and Zr [20] irradiated with 1 MeV Kr ion beams: a- Area defect number density and b) Average length of the loops observed edge-on.

5.1.3. Denuded zones

Denuded zones or defect-free zones at the grain boundaries were not observed in any of the irradiated samples in this study. In fact, grain boundary sink efficiency has often been linked to the size of denuded zones through experimental observations [66, 158 - 161]. The large width of a denuded zone near a grain boundary demonstrates a high sink efficiency for the boundary [158]. The suppression of dislocation loop formation near the boundary is likely due to the enhanced interstitial diffusion toward grain boundary at high temperatures [162]. However, their sink efficiency can depend on the GB type [158]. Additionally, for grain sizes above 100 nm, the effect of the grain boundary on the defect density is not clear[159]. Although the lack of observed denuded zones in the current work could be due to the limited number of investigated grains, the lower increase in hardness after low-temperature irradiation of Ti-6Al-4V AM compared to AM can not be explained only by the increased GB surface area.

5.2. DISCUSSION OF NANOINDENTATION RESULTS

5.2.1. Comparison of the hardness results with the literature

5.2.1.1. Unirradiated materials

Table 19 is a summary of the comparison between the hardness for each of the materials studied here and those found in the literature measured using nanoindentation with a Berkovich indenter tip at depths above 700 nm. The comparison of current work's results to Jouanny's [33] is particularly important since it also investigated radiation damage in similar Ti alloys irradiated with ions. The hardness of the CP Ti Grade 2 in this dissertation is similar to the hardness reported in other works [33, 163]. The current hardness of the PM rolled Ti-6Al-4V with equiaxed grains was lower than that reported in [33], where the Ti-alloy had a bimodal microstructure with globular 10 μm α-phase grains in addition to lamellar grains. The AM Ti-6Al-4V manufactured through direct metal laser sintering was similar to the sample produced through selective laser melting and HIPed in [164].

Table 19. Summary of the hardness values of the unirradiated materials.

Material	H_{unirr} (GPa)	Reference
CP Ti	3.3 ± 0.3	This work
	3.4 ± 0.36	[33]
	2.9 ± 0.4	[163]
Ti-6Al-4V (PM)	4.3 ± 0.2	This work
	5.84 ± 0.84	[33]
	5.0 ± 0.2	[164]
Ti-6Al-4V (AM)	5 ± 0.19	This work
	5.24 - 6.52 Electron Beam Melting	[165]
	5.1 ± 0.5 Selective laser melting & HIPed	[164]

5.2.1.2. Irradiated material

5.2.1.2.1. CP Ti

Limited irradiation experiments were available for comparison with the results of this study, especially for CP Ti. A summary of the available hardness change after irradiation with ion beams and proton beams is presented in Figure 115. As can be seen, ion irradiation allowed for the investigation of higher doses than in proton irradiation. It should be noted that in [14], high purity Ti was used as opposed to CP Ti in both [33] and [93]. At low irradiation temperature and low doses, higher purity Ti samples [14] exhibited almost no hardening compared to the lower-purity CP Ti in [93]. In both materials, the hardness increased as a function of dose. For samples irradiated at higher doses, a temperature effect is evident as the Δ*Hardness* values were higher for samples irradiated at lower temperatures.

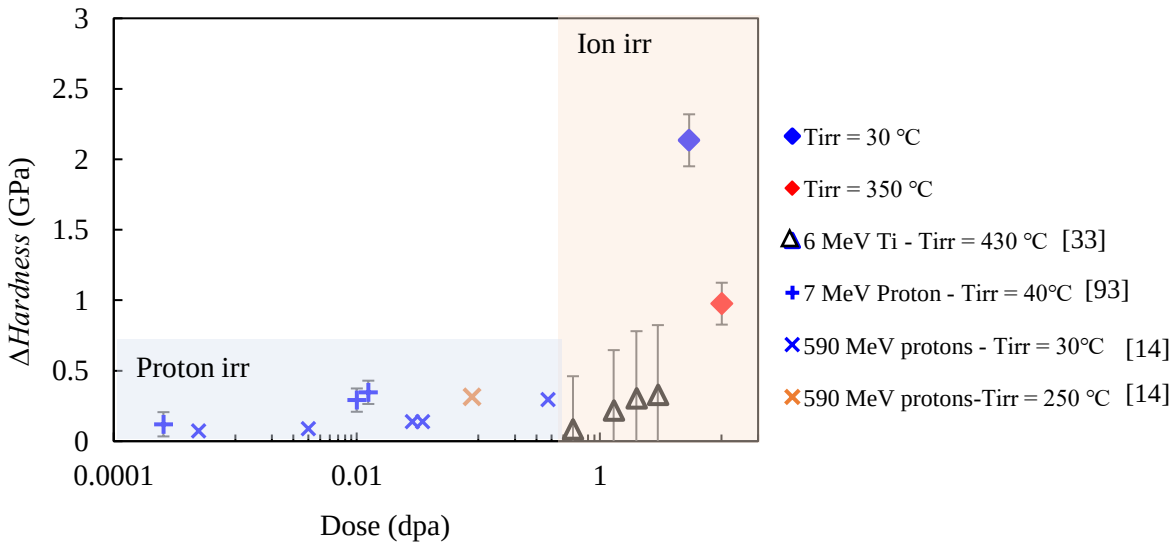

Figure 115. Change in hardness plotted for CP Ti samples: Irradiated with 4 MeV Ar ion beams from this work (filled diamond symbols); Irradiated with 6 MeV Ti ion beams from [33] (empty black triangle); Irradiated with 7 MeV proton beam from [93] (blue +); High purity Ti irradiated with 590 MeV proton beam from [14] (blue and red ×); The irradiation temperature for each set of samples is indicated in the legend.

5.2.1.2.2. Ti-6Al-4V

Since no other studies have been performed on the Ti-6Al-4V AM, a comparison with the literature is not possible for this material. The hardness of the irradiated PM rolled Ti-6Al-4V was compared to other conventionally rolled Ti-6Al-4V irradiated with neutrons [12], protons [14, 93] and ion beams [33] at low temperature (below 50 ℃) and high temperature (above 300 ℃). A summary of the comparison is shown in Figure 116. At an irradiation dose below 1 dpa, the hardening at low temperature for Ti-6Al-4V samples irradiated with neutrons at 50 ℃ [12] and protons at 40 ℃ [93] was lower than for samples irradiated at 350 ℃. The large variability of the data for Ti-6Al-4V irradiated with 6 MeV Ti ion beams [33] at 430 ℃ would suggest that no significant change in hardness was observed for these samples.

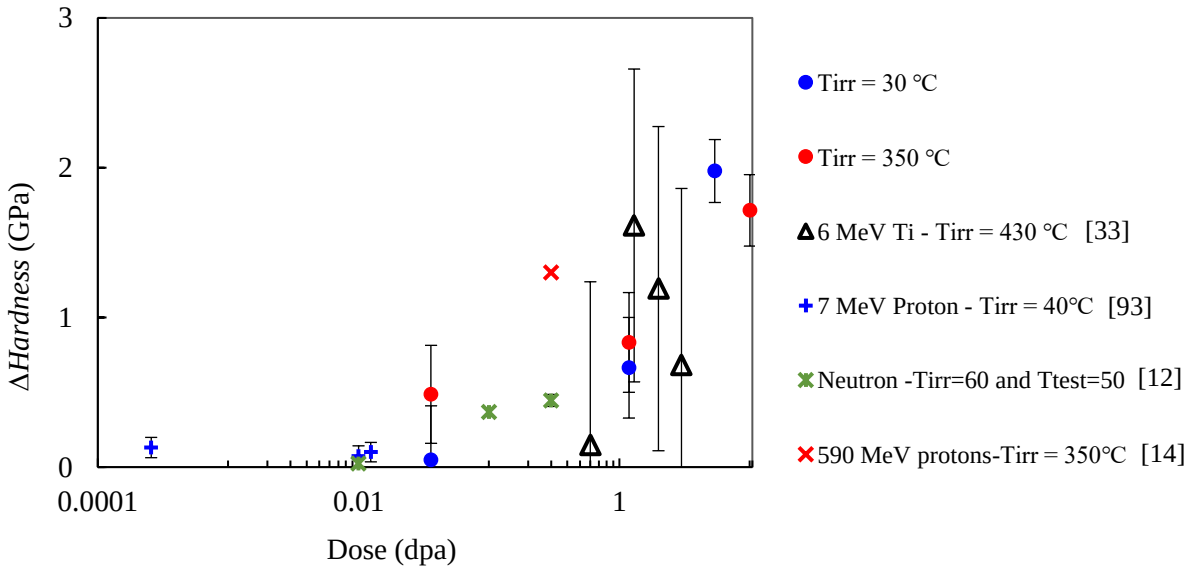

Figure 116. Change in hardness plotted for Ti-6Al-4V PM samples: Irradiated with 4 MeV Ar ion beams from this work (filled circles symbols); Irradiated with 6 MeV Ti ion beams from [33] (empty black triangle); Irradiated with 7 MeV proton beam from [93] (blue +); Irradiated with neutrons from [12] (green *); Irradiated with 590 MeV proton beam from [14] (red ×); The irradiation temperature for each set of samples were indicated in the legend.

5.2.1.3. Effect of the electronic excitation energy

Figure 117 shows a comparison between the hardness of the Ti–6Al–4V PM sample irradiated with a 36 MeVAr ion beam at 350 °C with and without the Ti-foil on the surface (see Figure 31). A higher hardening was observed for the sample with the Ti-foil on the surface characterized by a higher electronic excitation energy S_n on the surface (~ 0.25 keV nm^{-1}) and lower S_e (~1.4 keV nm^{-1}) compared to the sample without the Ti-foil (S_n ~ 0.015 keV nm^{-1} and S_e ~7.4 keV nm^{-1}). This difference suggested that the hardening in Ti–6Al–4V is mainly dependent on the ballistic effect (displacement of atoms as a result of the collision cascades) and that this alloy is resistant to the damage caused by high electronic excitations. Further investigations of the irradiation-induced hardening at the same irradiation dose but different electronic excitation energies would be required to confirm this result [11].

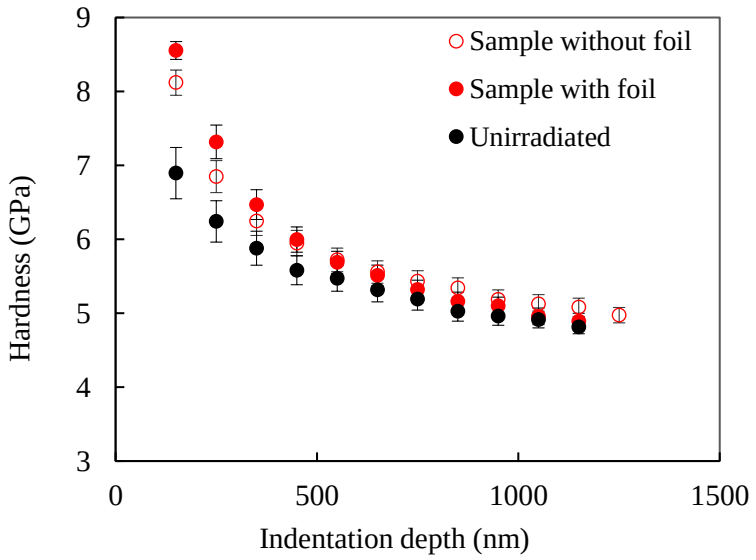

Figure 117. Hardness versus indentation depth for PM Ti–6Al–4V irradiated with a ^{36}Ar beam at a fluence of 1 × 10^{15} ions cm^{-2} and T = 350 °C with the CP–Ti foil (0.76 MeV) and without Ti-foil (36 MeV).

5.2.1.4. Effect of the irradiation dose and temperature on yield stress

Irradiation of metals at different temperatures increases the yield stress σ_y, especially for $T_{irr} < 0.3T_m$. In the case of the materials studied here, T_m is approximately 1600 ℃ [35] which results in $T_{irr} < 0.3T_m$ for irradiation temperatures equal to 30 ℃ and 350 ℃.

As outlined in 3.5.1. (Eq. 6), the radiation-induced hardening can be calculated through the change in hardness between the irradiated and unirradiated state:

$$\Delta H_{nano} = H_{irradiated} - H_{non\ irradiated} \quad \text{Eq. 15}$$

The change in hardness measured through Vickers indentation can be linked back to the change in nano hardness through the following equation [138, 166 - 167]:

$$H_v(\frac{\text{kg}}{\text{mm}^2}) = 0.01058 \times H_{nano}(GPa) \quad \text{Eq. 16}$$

This change in hardness can then be related to the change in yield stress $\Delta\sigma_y$ using Busby's approximation [114], with H_v being the hardness measured through the Vickers Hardness testing:

$$\Delta\sigma_y = 3.03\ \Delta H_v \quad \text{Eq. 17}$$

The resulting relationship between the change in yield stress and the change nano-hardness measured hardness is :

$$\Delta\sigma_y = 0.0320574 \times \Delta H_{\text{nano}} \quad \text{Eq. 17}$$

The change in yield stress ($\Delta\sigma_y$) was calculated for all irradiated samples. Figure 118 presents the calculated $\Delta\sigma_y$ for all samples irradiated with 4 MeV Ar ion beam.

At low temperatures, a significant increase in $\Delta\sigma_y$ was observed for both CP-Ti and PM Ti-6Al-4V with the former being slightly lower. At this low temperature, the irradiation hardening was due to the nucleation and growth of <a> and c-component dislocation loops only

[168]. The lower $\Delta\sigma_y$ for AM Ti-6Al-4V suggested a lower dislocation density compared to the other materials.

At the higher temperature of 350 ℃, the $\Delta\sigma_y$ was only calculated for CP-Ti and PM Ti-6Al-4V. The significant increase in yield stress for the PM Ti-6Al-4Vsuggests higher dislocation densities or radiation-induced precipitation. For this α+β alloy, an evolution of $\Delta\sigma_y$ as a function of temperature and irradiation dose was shown in Figure 119.

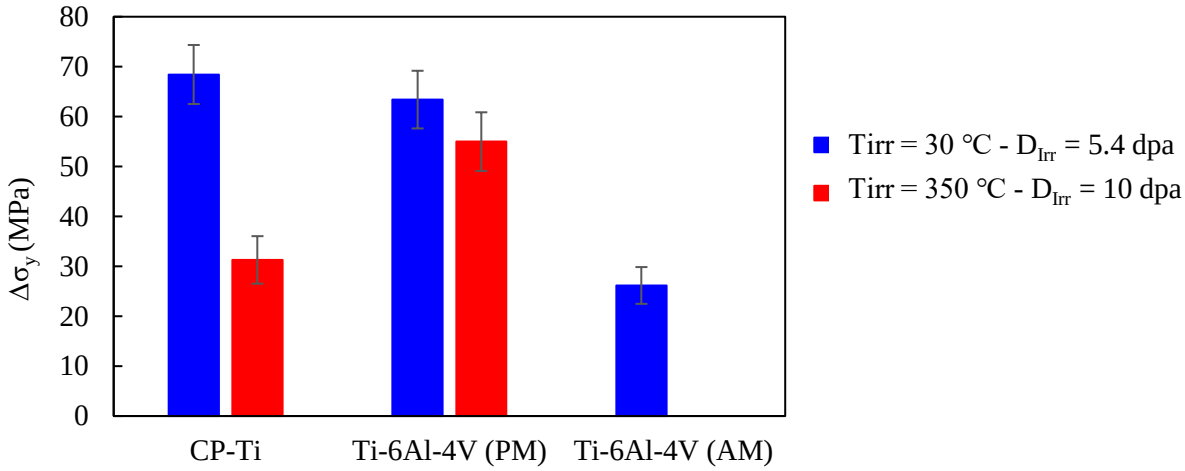

Figure 118. Change in yield stress Δσy calculated for samples irradiated with 4 MeV Ar ion beams at two different conditions: Irradiated at 30 ℃ up to a dose of 5.4 dpa; Irradiated at 350 ℃ up to a dose of 10 dpa.

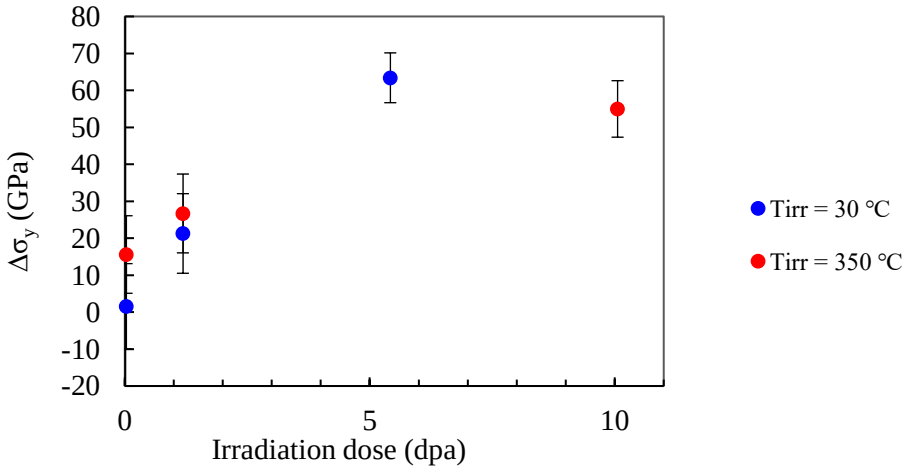

Figure 119. Change in yield strength calculated for AM or PM Ti-6Al-4V samples irradiated with Ar ion beams as a function of dose.

To better understand the effect of irradiation dose and temperature on the yield stress, the dispersed barrier hardening model was used. It is well established that irradiation induces barriers in the form of defect clusters, which impede dislocation motion. In the case of Ti alloys, <a> and c-component loops, as seen in this dissertation and [12 - 14, 33] and precipitates [17, 92], are considered to be dislocation barriers.

5.2.1.5. Correlating microstructure to the hardness: Application of the DBH model on CP Ti

Based on the DBH model, the change in yield stress is inversely proportional to the distance *l*, defined as the average obstacle spacing along the slip plane. Using Eq 10 and values of the defect number densities and equivalent diameter for <a> and c-component loops, distance *l* values were calculated for samples irradiated *in situ* with 1 MeV Kr ions and samples irradiated *ex situ* with 4 MeV Ar ion beams.

The calculated average <a> loops and c-component loops spacing along the slip plane were plotted in Figure 120. The error bars were calculated according to the propagation law for uncertainty [113] using the Eq. 18:

$$s_l = \sqrt{\left|\frac{\partial \mathrm{f}}{\partial \mathrm{a}}\right|^2 {s_a}^2 + \left|\frac{\partial \mathrm{f}}{\partial \mathrm{b}}\right|^2 {s_b}^2}$$

with: $f(a,b) = \frac{1}{\sqrt{\rho_n d}}$ Eq. 18

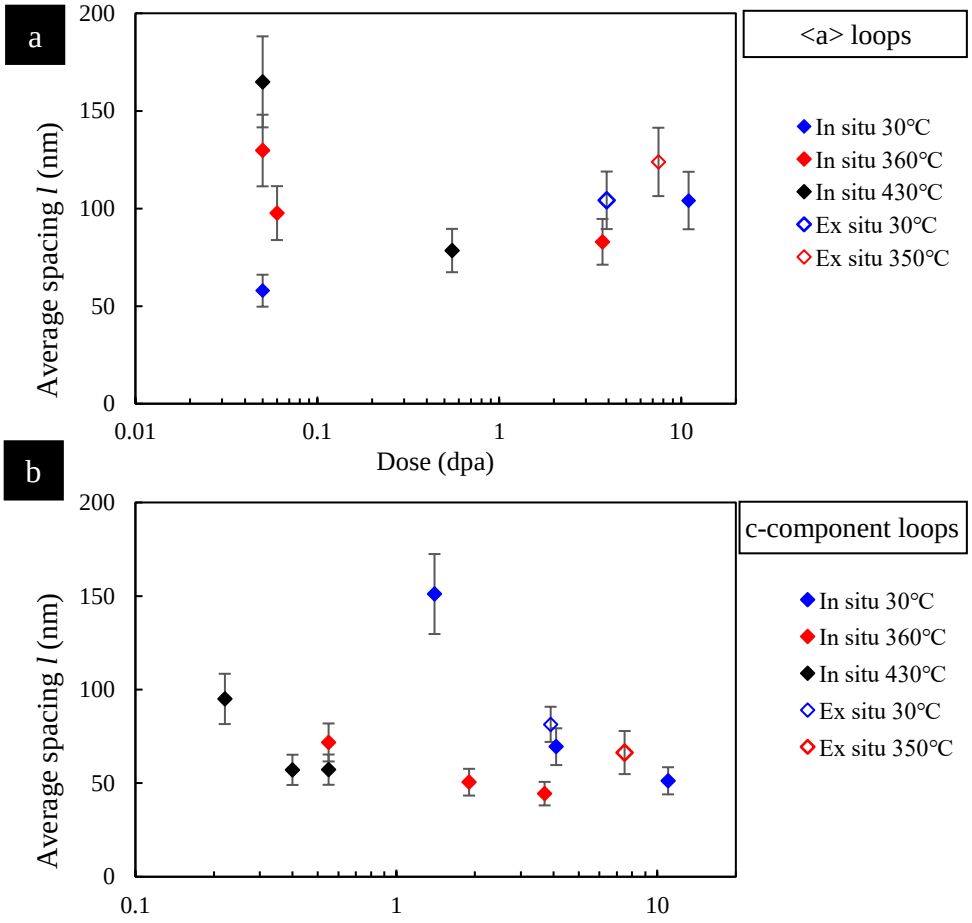

Figure 120. Average loops spacing along the slip plane, defined as distance l(nm), calculated for CP-Ti samples irradiated *in situ* with 1 MeV Kr ions and 4 MeV Ar ions at different temperatures. The irradiation temperature for each sample was indicated in the legend: a) <a> dislocation loops and b) c-component dislocation loops.

For <a> loops (see Figure 120-a), at the low dose of 0.05 dpa, the average spacing of 58 ± 8 nm at 30°C was the lowest resulting in an expected higher increase in yield stress. At high doses, the difference between samples irradiated at low and high temperatures was less significant.

The distance between c-component loops illustrated in Figure 120-b decreased with an increase of the dose for all temperatures. The rate of this decrease was lower as the dose increased. Since the strength of c-component loops as barriers in the DBH model is very low

compared to the strength of the <a> loops, 0.02 and 0.15, respectively, their contribution to the hardening will be less significant.

To better understand the contribution of <a> loops to the hardening, additional data points were collected from the literature. The average spacing, *l*, was calculated from the defect number densities and loop diameter data provided in [33] and [14]. The average spacing of <a> loops in CP-Ti irradiated with various particles (1 MeV Kr ion, 4 MeV Ar and 6 MeV Ti from [33]) and in high purity, Ti irradiated with 590 MeV protons from [14] is plotted in Figure 121. The same trend was observed at all temperatures, with an accelerated decrease in the <a> loop spacing at a low dose to reach a minimum and to increase again at a higher dose. The effect of the temperature was most significant at doses below 1 dpa, with the spacing *l* varying between 275 nm and 32 nm. At doses above 3 dpa, the temperature effect is less significant as the spacing, *l*, varied between 127 nm and 80 nm for all temperatures. At high temperatures, point defect recovery due to an enhanced diffusion causes an increased spacing between <a> loops.

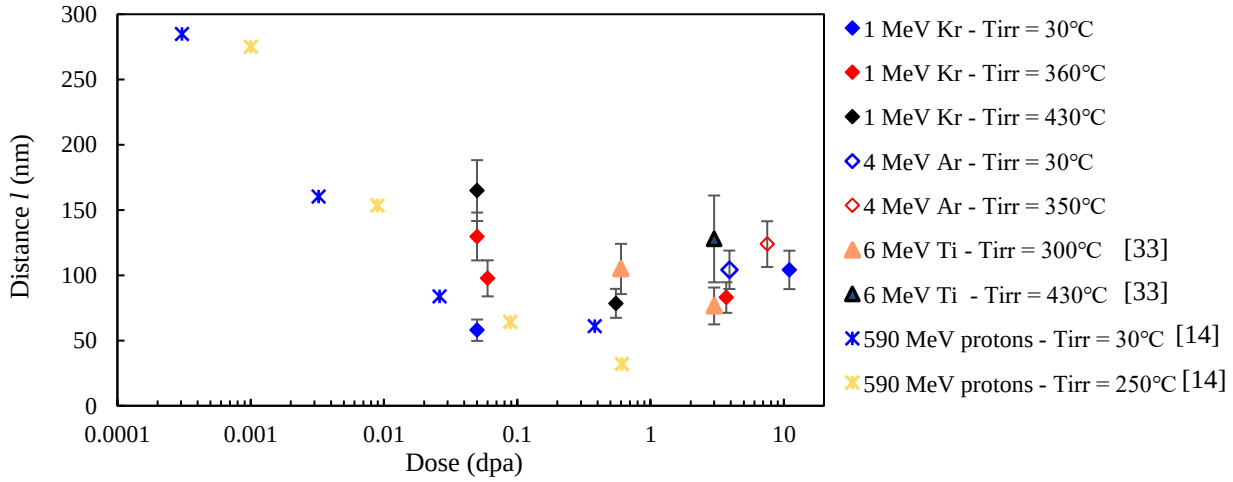

Figure 121. Average spacing for <a> dislocation loops plotted for Ti samples: Irradiated *in situ* with 1 MeV Kr ion beams (filled diamond symbols); Irradiated *ex situ* with 4 MeV Ar ion beams (empty diamond symbols); Irradiated *ex situ* with 6 MeV Ti ion beams from [33] (empty triangles); Irradiated with 590 MeV proton beam from [14] (*); The irradiation temperature for each set of samples were indicated in the legend.

To quantify the contributions of dislocation loops to hardening, two expressions were proposed in Eq. 11 (DBH) and Eq. 12 (modified DBH). A comparison between the experimental results obtained from the nano-indentation and the contributions to the change in yield stress due to the quantified <a> and c-component loops in CP-Ti samples irradiated with 4 MeV Ar beams is presented in Figure 122. The DBH expression provided the closest results to the measured hardness which confirmed that these dislocation loops are strong obstacles to the dislocation motion [13]. Additionally, the parameters suggested in Jouanny's work [33] seemed to provide consistent results for CP Ti.

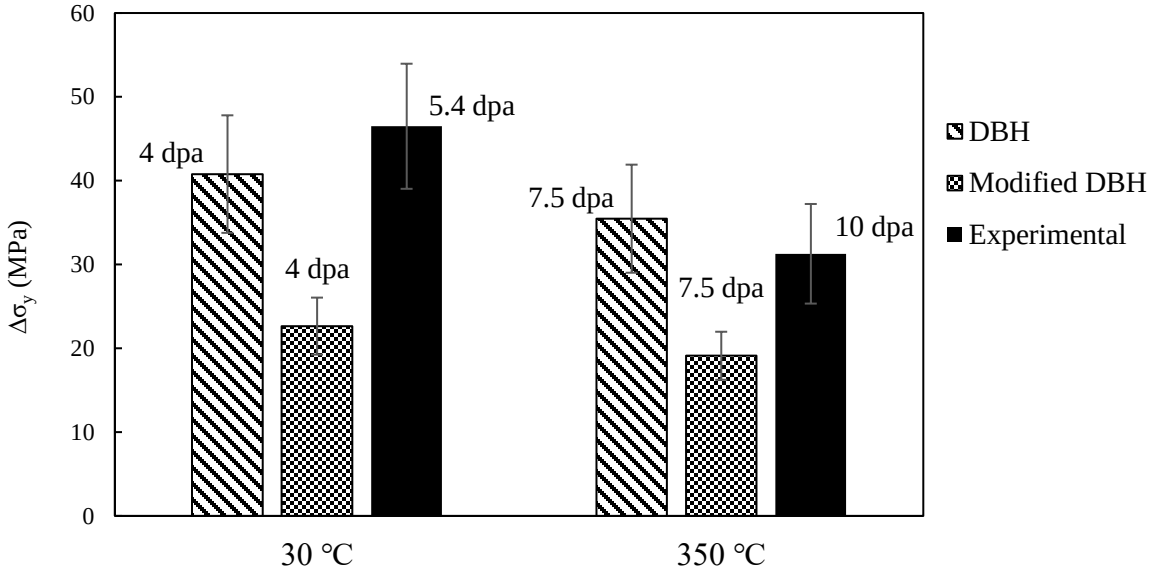

Figure 122. Comparison between change in yield stress in CP Ti irradiated with 4 MeV Ar ion 30℃ and 350℃: Contributions by the <a> and c-component loops calculated using DBH, labeled DBH in the legend; Contributions by the <a> and c-component loops calculated using the modified DBH, labeled Modified DBH in the legend; Values extracted from the nano-indentation results, labeled as 'Experimental' in the legend.

Using the data from [14] and the current work, the contributions of <a> and c-component loops to $\Delta\sigma_y$ were calculated for CP Ti (from current work) and high purity Ti [85] irradiated at 30 ℃ at different doses and are presented in Figure 123. Since c-component loops were only

observed after 1.4 dpa, the total contributions of <a> and c-component loops calculated by quadratic sum [116] were not significantly different from the contributions of <a> loops only.

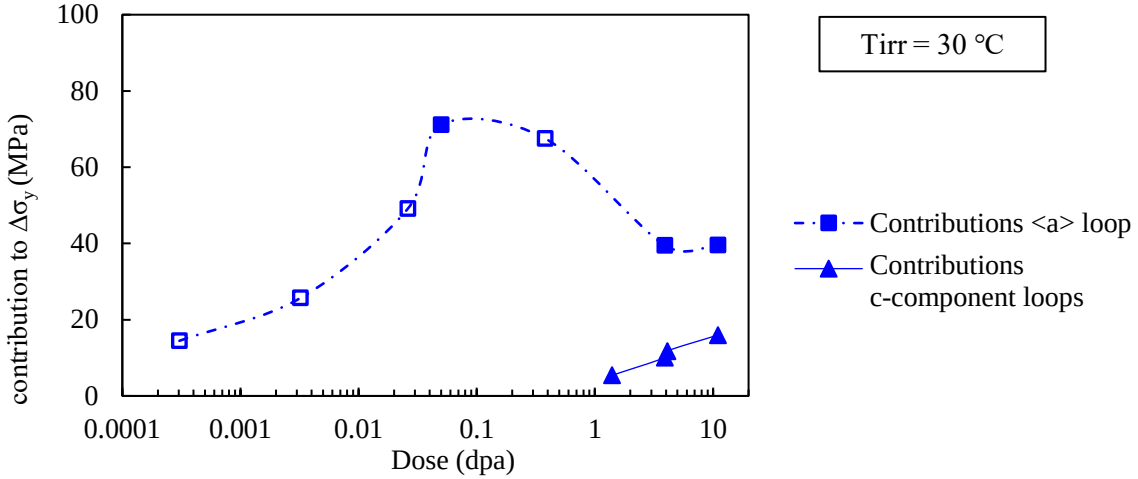

Figure 123. Contribution of <a> and c-component loops to the change in yield stress for Ti irradiated at 30 ℃. Full symbols are results from current work for CP Ti. The empty symbols were results for high purity Ti from [85].

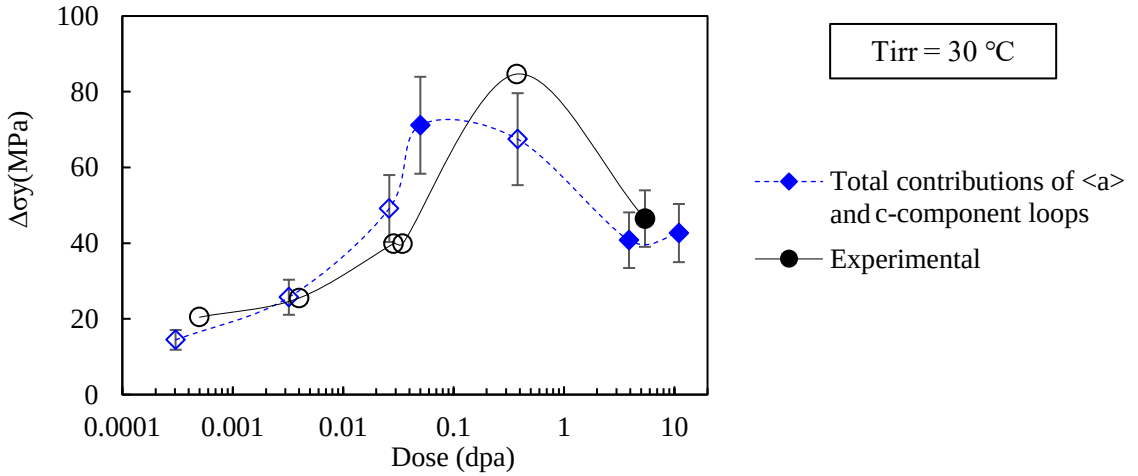

Figure 124. Good agreement between the contribution of both <a> and c-component loops to the change in yield stress and experimental measurements for Ti irradiated at 30 ℃. Full symbols were results from current work for CP Ti. The empty symbols are results for high purity Ti from [85].

In Figure 124, a good agreement between experimental measurements of the irradiation hardening (here represented by the increase in yield stress) in CP Ti irradiated at low

temperatures was found. Additionally, the effect of the alloying at this temperature (between CP Ti and high Purity Ti) and the dose rate was not significant.

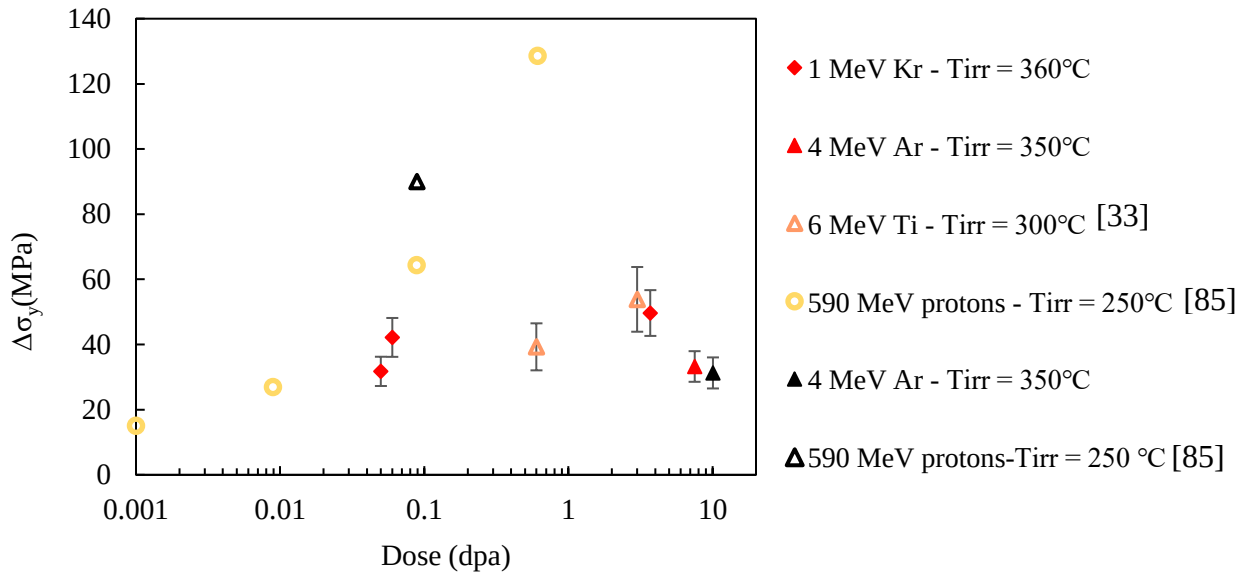

Figure 125. Contribution of <a> loops to the change in yield stress for Ti samples and experimental measurements for Ti irradiated at higher temperature: Black symbols represent results of mechanical testing and the colored symbols are the calculated contribution of <a> loops to hardening. The yellow, orange and red colors are assigned to irradiation temperatures of 250 ℃, 300 ℃ and 350 ℃ respectively.

At higher temperatures, the contributions of <a> dislocation loops to the hardening between 250 ℃ and 350 ℃ were plotted in Figure 125. At these temperatures, both the irradiation particle and the dose rate played essential roles in the evolution of <a> loop nucleation and growth and therefore contribute to the hardening. Lower dose rate irradiations, represented by 590 MeV proton irradiations [85], have resulted in both higher contributions to hardening from <a> loops at similar irradiation temperatures (~ 300 ℃).

In comparing the contributions of <a> loops at a dose of 0.6 dpa from 6 MeV Ti ions [33] and 590 MeV proton [85] irradiations, the observed significant difference was unexpected. Based on results from [33], the effect of the dose rate at this temperature was negligible in CP-Ti.

However since, the material used in the proton irradiation is a high purity Ti, this higher impurity content (see Table 20) may explain the higher hardening at higher irradiation temperature.

Table 20. Chemical composition of CP Ti in [33] and high purity Ti [85]

Elements	Ti	Fe	C	O	N	Ref
CP- Ti	99.801	0.02	0.006	0.17	0.003	[33]
High Purity Ti	99.999	-	-	-	-	[85]

5.2.1.6. Effect of the initial microstructure on the irradiation-induced hardening

One main focus of this study is to investigate the radiation damage in α-Ti grains in different materials: High purity Ti, CP Ti, Ti-6Al-4V PM and AM. Their microstructure, as shown in section 3.1, was very different. A comparison between the microstructure of materials used in the current work and from literature before irradiation is presented in Table 21.

Table 21. Comparison between the initial microstructure of the different materials

Material	Grain size	B-phase content (%vol)	Reference
CP Ti	20-40 µm Average size 30 µm	-	Current work
PM rolled Ti-6Al-4V	10-40 µm Average size 10.2 µm	7	Current work
AM Ti-6Al-4V	0.5 – 2 µm	14	Current work
CP Ti	60 µm	-	[15]
PM rolled Ti-6Al-4V	10 µm	10	[15]
High purity Ti	80 µm		[14]
Rolled Ti-6Al-4V	20 µm	13	[13]
CP Ti	10-30 µm	-	[150]
Rolled Ti-6Al-4V	10-30 µm	Not included	[150]
Rolled Ti-6Al-4V	20 µm	13	[12]

There was a large spread in the data across different temperatures and irradiation particles, as well as the spread of microstructures between the current study and in [12 – 15, 150].

At low temperatures*, the radiation hardening was not significantly different between samples with equiaxed α-phase grains at similar doses (see Figure 76 and Figure 124). The only material with a lamellar α-phase grain structure is the AM Ti-6Al-4V alloy and it exhibited lower radiation hardening at 30 °C (see Figure 76). The size of the α-phase lamellae in the AM alloy was ~ 10 times smaller than the α-phase grains observed in the conventionally rolled PM Ti-6Al-4V. A similar enhancement of radiation resistance was observed in forged Ti-6Al-4V, where smaller α-phase grain size led to less radiation hardening [169]. Additionally, in comparison with CP Ti and other near α alloys, the α+β phase alloy was more likely to become unstable and form precipitates under irradiation [16] such as V-rich precipitates ([16, 17, 88, 92]) causing a higher hardening in the α+β phase alloy.

At high temperatures, the radiation hardening depends strongly on the dose and the irradiation temperature. At 300 °C, the hardening in high purity Ti [85] was higher than in CP Ti [33] suggesting that higher impurity content improves the radiation hardening resistance. At 350 °C and for a dose of 5.4 dpa, the radiation hardening in PM Ti-6Al-4V was higher than CP Ti. At 430 °C, the hardening in CP Ti was slightly lower than for PM Ti-6Al-4V between doses of 0.6 and 3 dpa [33]. The comparison between CP Ti and Ti-6Al-4V PM suggests that the alloying elements in Ti-6Al-4V are detrimental to its radiation resistance at high temperatures. It would be interesting to investigate whether the lamellar structure in the AM alloy would help counteract this phenomenon.

* Irradiation temperature between 30 °C and 40 °C

CHAPTER 6
CONCLUSION

This dissertation work investigated the effect of heavy ion radiation damage on the microstructure and the nano-hardness of CP Ti and two Ti-6Al-4V alloys. To better understand the contributions of radiation-induced defects to the radiation hardening*, *in situ* TEM irradiations with Kr ion beams were performed at the IVEM-Tandem facility at Argonne National Laboratory. Observations of the nucleation and growth of <a> and c-component loops were reported and the dispersed barrier model was used to establish structure-mechanics relationships.

The following detailed conclusions can be drawn from this dissertation:

(1) The microstructure of the studied materials was significantly different. While the CP Ti exhibited a fully α-phase (hcp) microstructure containing equiaxed grains of 30 μm diameter, the PM rolled Ti-6Al-4V exhibited a lenticular α-phase microstructure (with widths between~10 and 40 μm) with mainly an intergranular β-phase. The AM Ti-6Al-4V material exhibited a lamellar α+β microstructure, where the width of the α-phase lamellae was between 0.5 μm and 2 μm, and their length varied between 2 and 20 μm.

(2) Radiation hardening was observed in all materials irradiated *ex situ* with Ar ion beams at 30 ℃ and 360 ℃. The increase in hardness was determined from the nanoindentation tests performed on the surface of the irradiated samples.

(3) Radiation hardening was insensitive to electronic excitation and was caused by the ballistic effect of ion irradiations. Hence a strong dose dependence was expected.

* Defined as the increase in hardeness as a result of exposure to irradiation.

(4) The irradiation dose and temperature dependence on hardening were studied for the PM Ti-6Al-4V. An increase in hardening was observed for both temperatures and for doses ranging from 0.1 to 10 dpa. At low doses, the radiation hardening was higher for the samples irradiated at 350 ℃ compared with those irradiated at 30 ℃. As the dose increased, the inverse was observed.

(5) The effect of the initial microstructure on the resistance to radiation-induced hardening was investigated using low-temperature irradiation with a 4 MeV Ar ion beam in the Ti-6Al-4V alloys. The measured hardness increased by 0.8 GPa for the AM alloy and 2 GPa in the PM alloy. The resistance to radiation hardening after low-temperature irradiation was, therefore, higher in the AM alloy due to the significant grain refinement.

(6) The effect of the alloying on the radiation resistance was investigated in conventionally rolled CP Ti and PM Ti-6Al-4V. After irradiation at 30 ℃ to a dose of 5.4 dpa, both materials exhibited similar hardening of approximately 2 GPa. However, a more significant increase in radiation hardening (~100%) was observed in the Ti-6Al-4V alloy after the same irradiation at 350 ℃ and for a dose up to 10 dpa. Increased radiation-induced precipitation in the Ti alloy is likely the cause for this difference.

(7) Observation of <a> loops were performed at 30 ℃, 360 ℃ and 430 ℃. At very low doses (up to 0.1 dpa), <a> loops appeared as black dots in BF TEM micrographs and had a bright contrast in DF micrographs. As the irradiation dose increased, these loops unfaulted and their size in the TEM foils increased at all the investigated irradiation temperatures. Loop growth occurred as a result of loop coalescence or the absorption of smaller new loops into larger loops. Alongside the already formed loops, new small defects were also present. Dislocation networks were only observed in the final damage structure at 430 ℃ both for CP Ti and AM Ti-6Al-4V.

At this temperature, loop diameters were larger for the AM Ti-6Al-4V alloy (12.5 nm) than CP Ti (8.5 nm).

(8) The present work showed that c-component loops were only observed after reaching a threshold incubation dose (TID). In CP Ti, these loops nucleated at much lower doses than Zr, and the TID decreased with increasing temperature: 1.4 dpa, 0.6 dpa and 0.24 dpa for irradiation temperatures of 30 ℃, 360 ℃ and 430 ℃, respectively. The Fe-rich precipitates observed in the current study in CP Ti (see Figure 58) could explain the lower TID values as opposed to those for the pure Zr, where no precipitates were found. The thermal and radiation-induced dissolution of precipitates are expected to increase the interstitial diffusion of Fe in the Ti matrix, thereby lowering the stacking fault energy of the Ti matrix and promoting the c-component loop nucleation. A lower TID value (0.22 dpa) was observed for AM Ti-6Al-4V at 360 ℃ compared to CP Ti, suggesting that alloying also enhanced c-component loop formation.

(9) Loop coalescence was the primary mechanism of c-component loop growth in CP Ti. The size of the loops and their defect number densities increased at 30 ℃ and 360 ℃ without showing signs of saturation up to a dose of 3.6 and 11 dpa. The foil irradiated at 430 ℃ seemed to reach a maximum loop size (20 nm) and density at the low dose of 0.55 dpa. In the AM Ti-6Al-4V, loops were significantly smaller than in CP Ti and were only quantified at the irradiation dose of 3.7 dpa.

(10) To better understand the effect of irradiation dose and temperature on the hardness, the dispersed barrier hardening model was used in CP Ti. The contributions of dislocation loops to the increase in yield stress at 30 ℃ and 360 ℃ were determined using the defect number densities and the loop diameters obtained from the TEM characterization. A good agreement between experimental measurements of the hardening in irradiated CP Ti and the calculated

contributions from loops was found. The barrier strength factors of <a> and c-component loops were validated to be 0.15 and 0.02, respectively confirming that <a> loops act as strong barriers to dislocation motion in ion irradiated Ti.

(11) A comparison of the current results with the literature indicated that at high temperatures, the presence of impurities rate plays an essential role in hardening. Significantly higher contributions from <a> loops to hardening were observed in pure Ti than CP-Ti. Further investigations at high temperatures are needed to understand this temperature, dose, dose rate, and alloying/microstructure dependence of radiation hardening in Ti alloys.

Although this dissertation addressed a few of the knowledge gaps identified in Chapter 2 (see 2.4), others were outside of the scope of this work. Furthermore, while some insights on the effect of dislocation loops and initial microstructure on the radiation resistance of Ti-alloys were offered, other parameters (grain orientation) and mechanisms (dissolution of impurity elements) could be further investigated.

(1) Bulk mechanical testing of neutron-irradiated Ti-alloys would allow for a better understanding of the dose/temperature dependence in Ti-alloys.

(2) The dissolution and segregation of impurity/alloying elements in irradiated Ti alloys:

To investigate the redistribution of elements like Fe [12] and their role in assisting the nucleation of c-component dislocation loops in CP Ti and Ti alloys, chemical analysis using a scanning transmission electron microscope (STEM) capable of high-resolution EDX spectrum imaging is beneficial. The redistribution of alloying elements was already successfully investigated in Zr alloys [170, 171] using an aberration-corrected (scanning) transmission electron microscope equipped with four EDX detectors. Atom Probe Tomography can also be used for this purpose.

(3) Orientation dependence

There is growing interest in the scientific community in investigating the effect of grain orientation on the radiation resistance of materials used in nuclear reactors. Some studies were already performed on tungsten [172] and beryllium [173]. In Ti, there is already an acknowledged orientation dependence of hardness in the unirradiated material [174]. Basal/ near basal orientation exhibit higher nanohardness in CP Ti [174]. As the diffusion in Ti is anisotropic as suggested by the DAD model, it would be interesting to investigate how it would affect irradiated Ti.

Combining EBSD characterization and nano-indentation testing would provide meaningful insights into the effect of grain orientation on the irradiation exposure.

BIBLIOGRAPHY

BIBLIOGRAPHY

[1] J.W. Davis, M.A. Ulrickson, R.A. Causey, Use of titanium in fusion components, J. Nucl. Mater. 212 (1994) 813–817.

[2] E. Hardin, T. HAGDU, D. Clayton, R. Howard, H. Greenberg, J. Blink, M. Sharma, M. Sutton, J. Carter, M. Dupont, Disposal Concepts/Thermal Load Management (FY11/12 Summary Report), FCRD-USED-2012-000219 REV. 1, 2012. http://curie.ornl.gov/printpdf/14 (accessed September 18, 2013).

[3] N. Simos, Composite Materials under Extreme Radiation and Temperature Environments of the Next Generation Nuclear Reactors, (2011). http://www.intechopen.com/books/metal-ceramic-and-polymeric-composites-for-various-uses/composite-materials-under-extreme-radiation-and-temperature-environments-of-the-next-generation-nucl (accessed September 18, 2013).

[4] V. Barabash, A. Peacock, S. Fabritsiev, G. Kalinin, S. Zinkle, A. Rowcliffe, J.-W. Rensman, A.A. Tavassoli, P. Marmy, P.J. Karditsas, F. Gillemot, M. Akiba, Materials challenges for ITER – Current status and future activities, J. Nucl. Mater. 367–370 (2007) 21–32. https://doi.org/10.1016/j.jnucmat.2007.03.017.

[5] B.S. Rodchenkov, A.V. Kozlov, Y.G. Kuznetsov, G.M. Kalinin, Y.S. Strebkov, Irradiation behaviour of titanium alloys for ITER blanket modules flexible attachment, J. Nucl. Mater. 307 (2002) 421–425.

[6] FRW. Stein, L.E. Ahle, S. Reyes, Beam Dump Design for the Rare Isotope Accelerator Fragmentation Line, Lawrence Livermore National Laboratory (2006), (n.d.).

[7] M. Avilov, A. Aaron, A. Amroussia, W. Bergez, C. Boehlert, T. Burgess, A. Carroll, C. Colin, F. Durantel, P. Ferrante, T. Fourmeau, V. Graves, C. Grygiel, J. Kramer, W. Mittig, I. Monnet, H. Patel, F. Pellemoine, R. Ronningen, M. Schein, Thermal, mechanical and fluid flow aspects of the high power beam dump for FRIB, Nucl. Instrum. Methods Phys. Res. Sect. B Beam Interact. Mater. At. 376 (2016) 24–27. https://doi.org/10.1016/j.nimb.2016.02.068.

[8] D.J. Morrissey, Status of the FRIB project with a new fragment separator, J. Phys. Conf. Ser. 267 (2011) 012001. https://doi.org/10.1088/1742-6596/267/1/012001.

[9] E.P. Abel, M. Avilov, V. Ayres, E. Birnbaum, G. Bollen, G. Bonito, T. Bredeweg, H. Clause, A. Couture, J. DeVore, M. Dietrich, P. Ellison, J. Engle, R. Ferrieri, J. Fitzsimmons, M. Friedman, D. Georgobiani, S. Graves, J. Greene, S. Lapi, C.S. Loveless, T. Mastren, C. Martinez-Gomez, S. McGuinness, W. Mittig, D. Morrissey, G. Peaslee, F. Pellemoine, J.D. Robertson, N. Scielzo, M. Scott, G. Severin, D. Shaughnessy, J. Shusterman, J. Singh, M. Stoyer, L. Sutherlin, A. Visser, J. Wilkinson, Isotope harvesting at FRIB: additional opportunities for scientific discovery, J. Phys. G Nucl. Part. Phys. 46 (2019) 100501. https://doi.org/10.1088/1361-6471/ab26cc.

[10] FRIB | Facility for Rare Isotope Beams | Michigan State University, (n.d.). https://frib.msu.edu/about/index.html (accessed January 23, 2020).

[11] A. Amroussia, M. Avilov, C.J. Boehlert, F. Durantel, C. Grygiel, W. Mittig, I. Monnet, F. Pellemoine, Swift heavy ion irradiation damage in Ti–6Al–4V and Ti–6Al–4V–1B: Study of the microstructure and mechanical properties, Nucl. Instrum. Methods Phys. Res. Sect. B Beam Interact. Mater. At. 365, Part B (2015) 515–521. http://dx.doi.org/10.1016/j.nimb.2015.09.029.

[12] S. Tähtinen, P. Moilanen, B.N. Singh, Effect of displacement dose and irradiation temperature on tensile and fracture toughness properties of titanium alloys, J. Nucl. Mater. 367–370 (2007) 627–632. https://doi.org/10.1016/j.jnucmat.2007.03.042.

[13] P. Marmy, T. Leguey, Impact of irradiation on the tensile and fatigue properties of two titanium alloys, J. Nucl. Mater. 296 (2001) 155–164.

[14] T. Leguey, N. Baluc, R. Schäublin, M. Victoria, Structure–mechanics relationships in proton irradiated pure titanium, J. Nucl. Mater. 307–311 (2002) 696–700. https://doi.org/10.1016/S0022-3115(02)01190-X.

[15] E. JOUANNY, Etude de l'évolution microstructurale sous irradiation aux ions Ti2+ de deux alliages de titane. Lien avec les propriétés mécaniques., PhD Thesis, Universite de Lorraine, 2017.

[16] P. Wilkes, G.L. Kulcinski, Heavy ion irradiation of a Ti-6Al-4V alloy, J. Nucl. Mater. 78 (1978) 427–430.

[17] S. Doriot, E. Jouanny, J. Malaplate, F. Dalle, L. Allais, T. Millot, M. Descoins, D. Mangelinck, M. Dehmas, Evolution of defects in Ti6-4 under Ti2+ ion irradiation: Focus on radiation-induced precipitates, J. Nucl. Mater. 511 (2018) 264–276. https://doi.org/koyama.

[18] M. Li, M.A. Kirk, P.M. Baldo, E.A. Ryan, TEM with in situ Ion Irradiation of Nuclear Materials: The IVEM-Tandem User Facility, Microsc. Microanal. 21 (2015) 437–438. https://doi.org/10.1017/S1431927615002986.

[19] M. Li, M.A. Kirk, P.M. Baldo, D. Xu, B.D. Wirth, Study of defect evolution by TEM with *in situ* ion irradiation and coordinated modeling, Philos. Mag. 92 (2012) 2048–2078. https://doi.org/10.1080/14786435.2012.662601.

[20] Y. Idrees, Z. Yao, M.A. Kirk, M.R. Daymond, In situ study of defect accumulation in zirconium under heavy ion irradiation, J. Nucl. Mater. 433 (2013) 95–107. https://doi.org/10.1016/j.jnucmat.2012.09.014.

[21] F. Onimus, L. Dupuy, F. Mompiou, In situ TEM observation of interactions between gliding dislocations and prismatic loops in Zr-ion irradiated zirconium alloys, Prog. Nucl. Energy. 57 (2012) 77–85. https://doi.org/10.1016/j.pnucene.2011.10.005.

[22] M. Kirk, X. Yi, M. Jenkins, Characterization of irradiation defect structures and densities by transmission electron microscopy, J. Mater. Res. 30 (2015) 1195–1201. https://doi.org/10.1557/jmr.2015.19.

[23] G.S. Was, Fundamentals of radiation materials science metals and alloys, Springer, Berlin, 2007. http://site.ebrary.com/id/10230196 (accessed August 8, 2013).

[24] C. Bassi, J.A. Peters, Effect of thermomechanical processing on microstructures and properties of titanium aluminide foils, Scr. Metall. Mater. 24 (1990) 1363–1368.

[25] R. Ding, Z.X. Guo, A. Wilson, Microstructural evolution of a Ti–6Al–4V alloy during thermomechanical processing, Mater. Sci. Eng. A. 327 (2002) 233–245.

[26] M. Žitňanský, L. Čaplovič, Effect of the thermomechanical treatment on the structure of titanium alloy Ti6Al4V, J. Mater. Process. Technol. 157–158 (2004) 643–649. https://doi.org/10.1016/j.jmatprotec.2004.07.151.

[27] D.E.J. Armstrong, T.B. Britton, Effect of dislocation density on improved radiation hardening resistance of nano-structured tungsten–rhenium, Mater. Sci. Eng. A. 611 (2014) 388–393. https://doi.org/10.1016/j.msea.2014.06.013.

[28] G.M. Cheng, W.Z. Xu, Y.Q. Wang, A. Misra, Y.T. Zhu, Grain size effect on radiation tolerance of nanocrystalline Mo, Scr. Mater. 123 (2016) 90–94. https://doi.org/10.1016/j.scriptamat.2016.06.007.

[29] A. Fitzner, J. Palmer, B. Gardner, M. Thomas, M. Preuss, J.Q. da Fonseca, On the work hardening of titanium: new insights from nanoindentation, J. Mater. Sci. 54 (2019) 7961–7974. https://doi.org/10.1007/s10853-019-03431-w.

[30] N. Swaminathan, P.J. Kamenski, D. Morgan, I. Szlufarska, Effects of grain size and grain boundaries on defect production in nanocrystalline 3C–SiC, Acta Mater. 58 (2010) 2843–2853. https://doi.org/10.1016/j.actamat.2010.01.009.

[31] B.N. Singh, M. Eldrup, S.J. Zinkle, S.I. Golubov, On grain-size-dependent void swelling in pure copper irradiated with fission neutrons, Philos. Mag. A. 82 (2002) 1137–1158. https://doi.org/10.1080/01418610208240021.

[32] B.N. Singh, Effect of grain size on void formation during high-energy electron irradiation of austenitic stainless steel, Philos. Mag. 29 (1974) 25–42. https://doi.org/10.1080/14786437408213551.

[33] E. Jouanny, Étude de l'évolution microstructurale sous irradiation aux ions Ti2+ de deux alliages de titane : lien avec les propriétés mécaniques, PhD Thesis, 2017. http://www.theses.fr/2017LORR0071/document.

[34] I.J. Polmear, Titanium alloys - Chapter 6, in: Light Alloys, Fourth Edition, Butterworth-Heinemann, Oxford, 2005.

http://www.sciencedirect.com/science/article/pii/B9780750663717500104 (accessed October 30, 2013).

[35] G. Welsch, E.W. Collings, B. Rodney, Materials Properties Handbook: Titanium Alloys, ASM International, 1993.

[36] H. Dammak, A. Dunlop, D. Lesueur, Phase transformation induced by swift heavy ion irradiation of pure metals, Nucl. Instrum. Methods Phys. Res. Sect. B Beam Interact. Mater. At. 107 (1996) 204–211.

[37] C. Leyens, M. Peters, eds., Titanium and Titanium Alloys: Fundamentals and Applications, 1st ed., Wiley, 2003. https://doi.org/10.1002/3527602119.

[38] W.G. Burgers, On the process of transition of the cubic-body-centered modification into the hexagonal-close-packed modification of zirconium, Physica. 1 (1934) 561–586.

[39] W.-F. Ho, A comparison of tensile properties and corrosion behavior of cast Ti–7.5Mo with c.p. Ti, Ti–15Mo and Ti–6Al–4V alloys, J. Alloys Compd. 464 (2008) 580–583. https://doi.org/10.1016/j.jallcom.2007.10.054.

[40] H. Li, D.E. Mason, Y. Yang, T.R. Bieler, M.A. Crimp, C.J. Boehlert, Comparison of the deformation behaviour of commercially pure titanium and Ti–5Al–2.5Sn(wt.%) at 296 and 728 K, Philos. Mag. 93 (2013) 2875–2895. https://doi.org/10.1080/14786435.2013.791752.

[41] I. Sabirov, M.T. Perez-Prado, J.M. Molina-Aldareguia, I.P. Semenova, G.Kh. Salimgareeva, R.Z. Valiev, Anisotropy of mechanical properties in high-strength ultra-fine-grained pure Ti processed via a complex severe plastic deformation route, Scr. Mater. 64 (2011) 69–72. https://doi.org/10.1016/j.scriptamat.2010.09.006.

[42] I.P. Semenova, V.V. Polyakova, G.S. Dyakonov, A.V. Polyakov, Ultrafine-Grained Titanium-Based Alloys: Structure and Service Properties for Engineering Applications, Adv. Eng. Mater. 22 (2020) 1900651. https://doi.org/10.1002/adem.201900651.

[43] S.H. Ahn, Y.B. Chun, S.H. Yu, K.H. Kim, S.K. Hwang, Microstructural refinement and deformation mode of Ti under cryogenic channel die compression, Mater. Sci. Eng. A. 528 (2010) 165–171. https://doi.org/10.1016/j.msea.2010.08.087.

[44] Y. Fan, W. Tian, Y. Guo, Z. Sun, J. Xu, Relationships among the Microstructure, Mechanical Properties, and Fatigue Behavior in Thin Ti6Al4V, Adv. Mater. Sci. Eng. 2016 (2016) 1–9. https://doi.org/10.1155/2016/7278267.

[45] J. Sieniawski, W. Ziaja, K. Kubiak, M. Motyk, Microstructure and Mechanical Properties of High Strength Two-Phase Titanium Alloys, in: J. Sieniawski (Ed.), Titan. Alloys - Adv. Prop. Control, InTech, 2013. http://www.intechopen.com/books/titanium-

alloys-advances-in-properties-control/microstructure-and-mechanical-properties-of-high-strength-two-phase-titanium-alloys (accessed October 30, 2013).

[46] W.E. Frazier, Metal Additive Manufacturing: A Review, J. Mater. Eng. Perform. 23 (2014) 1917–1928. https://doi.org/10.1007/s11665-014-0958-z.

[47] S. Liu, Y.C. Shin, Additive manufacturing of Ti6Al4V alloy: A review, Mater. Des. 164 (2019) 107552. https://doi.org/10.1016/j.matdes.2018.107552.

[48] M. Strantza, R. Vafadari, D. de Baere, B. Vrancken, W. van Paepegem, I. Vandendael, H. Terryn, P. Guillaume, D. van Hemelrijck, Fatigue of Ti6Al4V Structural Health Monitoring Systems Produced by Selective Laser Melting, Materials. 9 (2016) 106. https://doi.org/10.3390/ma9020106.

[49] C. de Formanoir, S. Michotte, O. Rigo, L. Germain, S. Godet, Electron beam melted Ti–6Al–4V: Microstructure, texture and mechanical behavior of the as-built and heat-treated material, Mater. Sci. Eng. A. 652 (2016) 105–119. https://doi.org/10.1016/j.msea.2015.11.052.

[50] S.L. Lu, H.P. Tang, Y.P. Ning, N. Liu, D.H. StJohn, M. Qian, Microstructure and Mechanical Properties of Long Ti-6Al-4V Rods Additively Manufactured by Selective Electron Beam Melting Out of a Deep Powder Bed and the Effect of Subsequent Hot Isostatic Pressing, Metall. Mater. Trans. A. 46 (2015) 3824–3834. https://doi.org/10.1007/s11661-015-2976-3.

[51] M. Shunmugavel, A. Polishetty, G. Littlefair, Microstructure and Mechanical Properties of Wrought and Additive Manufactured Ti-6Al-4V Cylindrical Bars, Procedia Technol. 20 (2015) 231–236. https://doi.org/10.1016/j.protcy.2015.07.037.

[52] C.G. Shirley, R.L. Chaplin, Evaluation of the Threshold Energy for Atomic Displacements in Titanium, Phys. Rev. B. 5 (1972) 2027–2029. https://doi.org/10.1103/PhysRevB.5.2027.

[53] C.A. English, M. Jenkins, Insight into Cascade Processes Arising from Studies of Cascade Collapse, Mater. Sci. Forum. 15–18 (1987) 1003–1022. https://doi.org/10.4028/www.scientific.net/MSF.15-18.1003.

[54] H.M. Simpson, A. Sosin, Defect mobility and reaction: Diffusional and rate theory formulations in one and three dimensions, Radiat. Eff. 3 (1970) 1–21. https://doi.org/10.1080/00337577008235611.

[55] R.E. Smallman, A.H.W. Ngan, Point Defect Behaviour, in: Mod. Phys. Metall., Elsevier, 2014: pp. 251–285. https://doi.org/10.1016/B978-0-08-098204-5.00006-7.

[56] R.E. Smallman, A.H.W. Ngan, Introduction to Dislocations, in: Mod. Phys. Metall., Elsevier, 2014: pp. 121–158. https://doi.org/10.1016/B978-0-08-098204-5.00004-3.

[57] G.S. Was, Radiation-Enhanced Diffusion and Defect Reaction Rate Theory, in: Fundam. Radiat. Mater. Sci. Met. Alloys, 2007: pp. 191–227. http://link.springer.com/content/pdf/10.1007/978-3-540-49472-0_5.pdf (accessed December 3, 2014).

[58] S.J. Zinkle, 1.03-Radiation-Induced effects on microstructure, Compr. Nucl. Mater. 1 (2012) 65–98.

[59] S.J. Rothman, Effects of irradiation on diffusion in metals and alloys, Applied Science Publishers Ltd, United Kingdom, 1983. http://inis.iaea.org/search/search.aspx?orig_q=RN:15038487.

[60] G.S. Was, T. Allen, Radiation-induced segregation in multicomponent alloys: Effect of particle type, Mater. Charact. 32 (1994) 239–255.

[61] M. Nastar, F. Soisson, Radiation-Induced Segregation, in: Compr. Nucl. Mater., Elsevier, 2012: pp. 471–496. https://doi.org/10.1016/B978-0-08-056033-5.00035-5.

[62] G.S. Was, T.R. Allen, RADIATION DAMAGE FROM DIFFERENT PARTICLE TYPES, in: K.E. Sickafus, E.A. Kotomin, B.P. Uberuaga (Eds.), Radiat. Eff. Solids, Springer Netherlands, Dordrecht, 2007: pp. 65–98. https://doi.org/10.1007/978-1-4020-5295-8_4.

[63] F. Aumayr, S. Facsko, A.S. El-Said, C. Trautmann, M. Schleberger, Single ion induced surface nanostructures: a comparison between slow highly charged and swift heavy ions, J. Phys. Condens. Matter. 23 (2011) 393001. https://doi.org/10.1088/0953-8984/23/39/393001.

[64] F. Onimus, J.L. Béchade, 4.01 - Radiation Effects in Zirconium Alloys, in: R.J.M. Konings (Ed.), Compr. Nucl. Mater., Elsevier, Oxford, 2012: pp. 1–31. https://doi.org/10.1016/B978-0-08-056033-5.00064-1.

[65] M. Griffiths, Evolution of microstructure in hcp metals during irradiation, J. Nucl. Mater. 205 (1993) 225–241.

[66] Y. Idrees, Microstructural evolution in Zr and Zr alloy Excel under ion irradiation., Library and Archives Canada = Bibliothèque et Archives Canada, 2014.

[67] Defect accumulation behaviour in hcp metals and alloys, J. Nucl. Mater. 276 (2000) 90–103. https://doi.org/10.1016/S0022-3115(99)00172-5.

[68] H. Föll, M. Wilkens, A simple method for the analysis of dislocation loops by means of the inside-outside contrast on transmission electron micrographs, Phys. Status Solidi A. 31 (1975) 519–524. https://doi.org/10.1002/pssa.2210310223.

[69] Intrinsic point defects in hexagonal close-packed metals, J. Nucl. Mater. 159 (1988) 122–148. https://doi.org/10.1016/0022-3115(88)90090-6.

[70] M. Griffiths, Faulkner, D, Styles, R.C, NEUTRON DAMAGE IN a-TITANIUM, J. Nucl. Mater. 119 (1983) 189–207.

[71] R.W. Gilbert, K. Farrell, C.E. Coleman, Damage structure in zirconium alloys neutron irradiated at 573 to 923 k, J. Nucl. Mater. 84 (1979) 137–148. https://doi.org/10.1016/0022-3115(79)90157-0.

[72] M.J. Makin, A.D. Whapham, F.J. Minter, Dislocation loops and hardening in neutron irradiated copper, Philos. Mag. 6 (1961) 465–468. https://doi.org/10.1080/14786436108235903.

[73] R.A. Holt, Mechanisms of irradiation growth of alpha-zirconium alloys, J. Nucl. Mater. 159 (1988) 310–338. https://doi.org/10.1016/0022-3115(88)90099-2.

[74] R.A. Holt, R.W. Gilbert, ⟨⟩ Component dislocations in annealed Zircaloy irradiated at about 570 K, J. Nucl. Mater. 137 (1986) 185–189. https://doi.org/10.1016/0022-3115(86)90218-7.

[75] M. Griffiths, Evolution of microstructure in hcp metals during irradiation, J. Nucl. Mater. 205 (1993) 225–241. https://doi.org/10.1016/0022-3115(93)90085-D.

[76] M. Griffiths, A review of microstructure evolution in zirconium alloys during irradiation, J. Nucl. Mater. 159 (1988) 190–218. https://doi.org/10.1016/0022-3115(88)90093-1.

[77] M. Griffiths, R.W. Gilbert, V. Fidleris, R.P. Tucker, R.B. Adamson, Neutron damage in zirconium alloys irradiated at 644 to 710 k, J. Nucl. Mater. 150 (1987) 159–168. https://doi.org/10.1016/0022-3115(87)90071-7.

[78] Y. Idrees, E.M. Francis, Z. Yao, A. Korinek, M.A. Kirk, M. Sattari, M. Preuss, M.R. Daymond, Effects of alloying elements on the formation of < *c* >-component loops in Zr alloy Excel under heavy ion irradiation, J. Mater. Res. 30 (2015) 1310–1334. https://doi.org/10.1557/jmr.2015.89.

[79] R.G. Faulkner, R.B. Jones, Z. Lu, P.E.J. Flewitt *, Grain boundary impurity segregation and neutron irradiation effects in ferritic alloys, Philos. Mag. 85 (2005) 2065–2099. https://doi.org/10.1080/14786430412331331853.

[80] N.Q. Lam, P.R. Okamoto, R.A. Johnson, Solute segregation and precipitation under heavy-ion bombardment, J. Nucl. Mater. 78 (1978) 408–418.

[81] Defects in Crystals - Introduction to Dislocations (Fifth Edition) - Chapter 1, (n.d.). http://www.sciencedirect.com/science/article/pii/B9780080966724000013 (accessed October 26, 2013).

[82] D. Hull, D.J. Bacon, Movement of Dislocations, in: Introd. Dislocations, Elsevier, 2011: pp. 43–62. https://doi.org/10.1016/B978-0-08-096672-4.00003-7.

[83] D.J. Bacon, F. Gao, Yu.N. Osetsky, The primary damage state in fcc, bcc and hcp metals as seen in molecular dynamics simulations, J. Nucl. Mater. 276 (2000) 1–12.

[84] R.B. Adamson, C.E. Coleman, M. Griffiths, Irradiation creep and growth of zirconium alloys: A critical review, J. Nucl. Mater. 521 (2019) 167–244. https://doi.org/10.1016/j.jnucmat.2019.04.021.

[85] T. Leguey *, N. Baluc, R. Schäublin, M. Victoria, Temperature dependence of irradiation effects in pure titanium, Philos. Mag. 85 (2005) 689–695. https://doi.org/10.1080/14786430412331319992.

[86] E. Jouanny, S. Doriot, J. Malaplate, M. Dehmas, L. Allais, M.L. Thuaut, T. Millot, Evolution of defects in titanium grade 2 under Ti $^{2+}$ ion irradiation: EVOLUTION OF DEFECTS IN TITANIUM GRADE 2 UNDER TI $^{2+}$ ION IRRADIATION, J. Microsc. 265 (2017) 275–286. https://doi.org/10.1111/jmi.12499.

[87] M. Griffiths, D. Gilbon, C. Regnard, C. Lemaignan, HVEM study of the effects of alloying elements and impurities on radiation damage in Zr-alloys, J. Nucl. Mater. 205 (1993) 273–283. https://doi.org/10.1016/0022-3115(93)90090-L.

[88] S. Tähtinen, P. Moilanen, B.N. Singh, Effect of displacement dose and irradiation temperature on tensile and fracture toughness properties of titanium alloys, J. Nucl. Mater. 367–370 (2007) 627–632. https://doi.org/10.1016/j.jnucmat.2007.03.042.

[89] S.M.L. Sastry, J.E. O' Neal, O. Izumi (Eds.), H. Kimura, Titanium '80, science and technology, in: Kyoto, Japan, 1980: p. 651. http://books.google.com/books/about/Titanium_80_science_and_technology.html?id=GLFPAQAAIAAJ (accessed April 14, 2015).

[90] D.T. Peterson, Swelling in neutron irradiated Titanium alloys, in: Eff. Radiat. Mater. 11th Int. Symp., American Society for Testing and Materials, Philadelphia, PA, 1982: p. 260. ay (accessed April 14, 2015).

[91] A. Kohyama, K. Asano, N. Igata, Neutron irradiation effects on electron-beam welded titanium and Ti-6Al-4V, J. Nucl. Mater. 141 (1986) 987–990.

[92] D.L. Plumton, G.L. Kulcinski, R.A. Dodd, Radiation induced precipitation in 9 MeV Al ion irradiated Ti-6A1-4V, J. Nucl. Mater. 144 (1987) 264–274.

[93] A. Dutta Gupta, P. Mukherjee, N. Gayathri, P. Bhattacharyya, M. Bhattacharya, A. Sarkar, S. Sen, M.K. Mitra, Proton irradiation studies on pure Ti and Ti-6Al-4V, Nucl. Instrum. Methods Phys. Res. Sect. B Beam Interact. Mater. At. 387 (2016) 63–72. https://doi.org/10.1016/j.nimb.2016.09.010.

[94] L. Kang, C. Yang, A Review on High-Strength Titanium Alloys: Microstructure, Strengthening, and Properties, Adv. Eng. Mater. 21 (2019) 1801359. https://doi.org/10.1002/adem.201801359.

[95] Hongmei Li, ANALYSIS OF THE DEFORMATION BEHAVIOR OF THE HEXAGONAL CLOSE-PACKED ALPHA PHASE IN TITANIUM AND TITANIUM ALLOYS, PhD disseretation, Michigan State University, 2013.

[96] K. Araci, D. Mangabhai, K. Akhtar, Production of titanium by the Armstrong Process®, in: Titan. Powder Metall., Elsevier, 2015: pp. 149–162. https://doi.org/10.1016/B978-0-12-800054-0.00009-5.

[97] S. Geneva, Additive manufacturing—general principles—terminology, ISO/ASTM. 52900 (2015).

[98] F. Mangano, L. Chambrone, R. van Noort, C. Miller, P. Hatton, C. Mangano, Direct Metal Laser Sintering Titanium Dental Implants: A Review of the Current Literature, Int. J. Biomater. 2014 (2014) 461534. https://doi.org/10.1155/2014/461534.

[99] M. Agarwala, D. Bourell, J. Beaman, H. Marcus, J. Barlow, Direct selective laser sintering of metals, Rapid Prototyp. J. 1 (1995) 26–36. https://doi.org/10.1108/13552549510078113.

[100] A.A. Antonysamy, J. Meyer, P.B. Prangnell, Effect of build geometry on the β-grain structure and texture in additive manufacture of Ti6Al4V by selective electron beam melting, Mater. Charact. 84 (2013) 153–168. https://doi.org/10.1016/j.matchar.2013.07.012.

[101] L. Ladani, Local and Global Mechanical Behavior and Microstructure of Ti6Al4V Parts Built Using Electron Beam Melting Technology, Metall. Mater. Trans. A. 46 (2015) 3835–3841. https://doi.org/10.1007/s11661-015-2965-6.

[102] X. Tan, Y. Kok, Y.J. Tan, G. Vastola, Q.X. Pei, G. Zhang, Y.-W. Zhang, S.B. Tor, K.F. Leong, C.K. Chua, An experimental and simulation study on build thickness dependent microstructure for electron beam melted Ti–6Al–4V, J. Alloys Compd. 646 (2015) 303–309. https://doi.org/10.1016/j.jallcom.2015.05.178.

[103] J.F. Ziegler, M.D. Ziegler, J.P. Biersack, SRIM – The stopping and range of ions in matter (2010), Nucl. Instrum. Methods Phys. Res. Sect. B Beam Interact. Mater. At. 268 (2010) 1818–1823. https://doi.org/10.1016/j.nimb.2010.02.091.

[104] D.B. Williams, C.B. Carter, Transmission electron microscopy: a textbook for materials science, Springer, New York; London, 2009.

[105] M.L. Jenkins, Characterisation of radiation-damage microstructures by TEM, J. Nucl. Mater. 216 (1994) 124–156. https://doi.org/10.1016/0022-3115(94)90010-8.

[106] M. Klinger, A. Jäger, *Crystallographic Tool Box* (*CrysTBox*): automated tools for transmission electron microscopists and crystallographers, J. Appl. Crystallogr. 48 (2015) 2012–2018. https://doi.org/10.1107/S1600576715017252.

[107] S. Suzuki, Features of Transmission EBSD and its Application, JOM. 65 (2013) 1254–1263. https://doi.org/10.1007/s11837-013-0700-6.

[108] J. Schindelin, I. Arganda-Carreras, E. Frise, V. Kaynig, M. Longair, T. Pietzsch, S. Preibisch, C. Rueden, S. Saalfeld, B. Schmid, J.-Y. Tinevez, D.J. White, V. Hartenstein, K. Eliceiri, P. Tomancak, A. Cardona, Fiji: an open-source platform for biological-image analysis, Nat. Methods. 9 (2012) 676–682. https://doi.org/10.1038/nmeth.2019.

[109] William D. Nix, Huajian Gao, Indentation size effects in crystalline materials: A law for strain gradient plasticity, J. Mech. Phys. Solids. 46 (1998) 411–425.

[110] P. Hosemann, D. Kiener, Y. Wang, S.A. Maloy, Issues to consider using nano indentation on shallow ion beam irradiated materials, J. Nucl. Mater. 425 (2012) 136–139. https://doi.org/10.1016/j.jnucmat.2011.11.070.

[111] C.D. Hardie, S.G. Roberts, A.J. Bushby, Understanding the effects of ion irradiation using nanoindentation techniques, J. Nucl. Mater. 462 (2015) 391–401. https://doi.org/10.1016/j.jnucmat.2014.11.066.

[112] J. Neter, M.H. Kutner, C.J. Nachtsheim, W. Wasserman, Applied Linear Statistical Models, Irwin, Chicago, 1996.

[113] P. Fornasini, The Uncertainty in Physical Measurements: An Introduction to Data Analysis in the Physics Laboratory, Springer New York, 2008. https://books.google.com/books?id=PBJgvPgf2NkC.

[114] J.T. Busby, M.C. Hash, G.S. Was, The relationship between hardness and yield stress in irradiated austenitic and ferritic steels, J. Nucl. Mater. 336 (2005) 267–278. https://doi.org/10.1016/j.jnucmat.2004.09.024.

[115] M.S. Beck, Dispersed barrier hardening in irradiated metals, (n.d.) 98.

[116] G.S. Was, Irradiation Hardening and Deformation, in: G.S. WAS (Ed.), Fundam. Radiat. Mater. Sci. Met. Alloys, Springer New York, New York, NY, 2017: pp. 669–733. https://doi.org/10.1007/978-1-4939-3438-6_12.

[117] R.E. Smallman, A.H.W. Ngan, Precipitation Hardening, in: Mod. Phys. Metall., Elsevier, 2014: pp. 499–527. https://doi.org/10.1016/B978-0-08-098204-5.00013-4.

[118] N.F. Mott, F.R.N. Nabarro, An attempt to estimate the degree of precipitation hardening, with a simple model, Proc. Phys. Soc. 52 (1940) 86–89. https://doi.org/10.1088/0959-5309/52/1/312.

[119] E. Orowan, Symposium on internal stresses in metals and alloys, Inst. Met. Lond. 451 (1948).

[120] D.R. Olander, Fundamental aspects of nuclear reactor fuel elements, 1976. https://doi.org/10.2172/7343826.

[121] G.I. Taylor, Plastic strain in metals, Plast. Strain Met. (1938) 307–324.

[122] J.A. Fellows, Second International Conference on The Strength of Metals and Alloys: Sponsored in 1970 by American Society for Metals in Asilomar, California, J. Compos. Mater. 4 (1970) 73–73. https://doi.org/10.1177/002199837000400106.

[123] S.J. Zinkle, Fundamental radiation effects parameters in metals and ceramics, Radiat. Eff. Defects Solids. 148 (1999) 447–477. https://doi.org/10.1080/10420159908229104.

[124] R. Onimus, J.-L. Béchade, C. Prioul, P. Pilvin, I. Monnet, S. Doriot, B. Verhaeghe, D. Gilbon, L. Robert, L. Legras, others, Plastic Deformation of Irradiated Zirconium Alloys: TEM Investigations and Micromechanical Modeling, J. ASTM Int. 2 (2005). http://www.astm.org/cgi-bin/scholar.cgi?JAI12424 (accessed April 20, 2015).

[125] Q. Dong, H. Qin, Z. Yao, M.R. Daymond, Irradiation damage and hardening in pure Zr and Zr-Nb alloys at 573 K from self-ion irradiation, Mater. Des. 161 (2019) 147–159. https://doi.org/10.1016/j.matdes.2018.11.017.

[126] X. Hu, T. Koyanagi, M. Fukuda, N.A.P.K. Kumar, L.L. Snead, B.D. Wirth, Y. Katoh, Irradiation hardening of pure tungsten exposed to neutron irradiation, J. Nucl. Mater. 480 (2016) 235–243. https://doi.org/10.1016/j.jnucmat.2016.08.024.

[127] S. Kojima, S.J. Zinkle, H.L. Heinisch, Radiation hardening in neutron-irradiated polycrystalline copper: Barrier strength of defect clusters, J. Nucl. Mater. 179–181 (1991) 982–985. https://doi.org/10.1016/0022-3115(91)90255-6.

[128] U.F. Kocks, The theory of an obstacle-controlled yield strength—Report after an international workshop, Mater. Sci. Eng. 27 (1977) 291–298. https://doi.org/10.1016/0025-5416(77)90212-9.

[129] H.M. Burte, Titanium Science and Technology: Proceedings, Plenum Publishing Corporation, 1973.

[130] J.H. Shen, Y.L. Li, Q. Wei, Statistic derivation of Taylor factors for polycrystalline metals with application to pure magnesium, Mater. Sci. Eng. A. 582 (2013) 270–275. https://doi.org/10.1016/j.msea.2013.06.025.

[131] M. Morita, O. Umezawa, Slip Deformation Analysis Based on Full Constraints Model for α-Titanium Alloy at Low Temperature, Mater. Trans. 52 (2011) 1595–1602. https://doi.org/10.2320/matertrans.L-M2011815.

[132] L.E. Rehn, P.R. Okamoto, R.S. Averback, Relative efficiencies of different ions for producing freely migrating defects, Phys. Rev. B. 30 (1984) 3073–3080. https://doi.org/10.1103/PhysRevB.30.3073.

[133] L.E. Rehn, H. Wiedersich, Freely-Migrating Defects: Their Production and Interaction with Cascade Remnants, Mater. Sci. Forum. 97–99 (1992) 43–58. https://doi.org/10.4028/www.scientific.net/MSF.97-99.43.

[134] L.K. Mansur, Correlation of neutron and heavy-ion damage, J. Nucl. Mater. 78 (1978) 156–160. https://doi.org/10.1016/0022-3115(78)90514-7.

[135] D. Connétable, J. Huez, É. Andrieu, C. Mijoule, First-principles study of diffusion and interactions of vacancies and hydrogen in hcp-titanium, J. Phys. Condens. Matter. 23 (2011) 405401. https://doi.org/10.1088/0953-8984/23/40/405401.

[136] E04 Committee, Test Methods for Determining Average Grain Size, ASTM International, n.d. https://doi.org/10.1520/E0112-96R04.

[137] T. Vilaro, C. Colin, J.D. Bartout, As-Fabricated and Heat-Treated Microstructures of the Ti-6Al-4V Alloy Processed by Selective Laser Melting, Metall. Mater. Trans. A. 42 (2011) 3190–3199. https://doi.org/10.1007/s11661-011-0731-y.

[138] M.F. Doerner, W.D. Nix, A method for interpreting the data from depth-sensing indentation instruments, J. Mater. Res. 1 (1986) 601–609. https://doi.org/10.1557/JMR.1986.0601.

[139] Y. Idrees, Z. Yao, M.A. Kirk, M.R. Daymond, In situ study of defect accumulation in zirconium under heavy ion irradiation, J. Nucl. Mater. 433 (2013) 95–107. https://doi.org/10.1016/j.jnucmat.2012.09.014.

[140] F. Long, Characterization of Deformation Mechanisms in Zirconium Alloys: Effect of Temperature and Irradiation, (2015). http://qspace.library.queensu.ca/handle/1974/12770 (accessed October 12, 2016).

[141] G. Monnet, B. Devincre, L.P. Kubin, Dislocation study of prismatic slip systems and their interactions in hexagonal close packed metals: application to zirconium, Acta Mater. 52 (2004) 4317–4328. https://doi.org/10.1016/j.actamat.2004.05.048.

[142] F. Onimus, I. Monnet, J.L. Béchade, C. Prioul, P. Pilvin, A statistical TEM investigation of dislocation channeling mechanism in neutron irradiated zirconium alloys, J. Nucl. Mater. 328 (2004) 165–179. https://doi.org/10.1016/j.jnucmat.2004.04.337.

[143] F. Onimus, J.L. Béchade, D. Gilbon, Experimental Analysis of Slip Systems Activation in Neutron-Irradiated Zirconium Alloys and Comparison with Polycrystalline Model Simulations, Metall. Mater. Trans. A. 44 (2013) 45–60. https://doi.org/10.1007/s11661-012-1463-3.

[144] A. Boyne, C. Shen, R. Najafabadi, Y. Wang, Numerical simulation of irradiation hardening in Zirconium, J. Nucl. Mater. 438 (2013) 209–217. https://doi.org/10.1016/j.jnucmat.2013.03.035.

[145] J.L. Brimhall, G.L. Kulcinski, H.E. Kissinger, B. Mastel, Microstructural analysis of neutron irradiated titanium and rhenium, Radiat. Eff. 9 (1971) 273–278. https://doi.org/10.1080/00337577108231060.

[146] J. Schindelin, I. Arganda-Carreras, E. Frise, V. Kaynig, M. Longair, T. Pietzsch, S. Preibisch, C. Rueden, S. Saalfeld, B. Schmid, J.-Y. Tinevez, D.J. White, V. Hartenstein, K. Eliceiri, P. Tomancak, A. Cardona, Fiji: an open-source platform for biological-image analysis, Nat. Methods. 9 (2012) 676. https://doi.org/10.1038/nmeth.2019.

[147] N. de Diego, Yu.N. Osetsky, D.J. Bacon, Structure and properties of vacancy and interstitial clusters in α-zirconium, J. Nucl. Mater. 374 (2008) 87–94. https://doi.org/10.1016/j.jnucmat.2007.07.011.

[148] M. Griffiths, R.W. Gilbert, The formation of c-component defects in zirconium alloys during neutron irradiation, J. Nucl. Mater. 150 (1987) 169–181. https://doi.org/10.1016/0022-3115(87)90072-9.

[149] A. Kohyama, K. Asano, N. Igata, Neutron irradiation effects on electron-beam welded titanium and Ti-6Al-4V, J. Nucl. Mater. 141 (1986) 987–990.

[150] A. Dutta Gupta, P. Mukherjee, N. Gayathri, P. Bhattacharyya, M. Bhattacharya, A. Sarkar, S. Sen, M.K. Mitra, Proton irradiation studies on pure Ti and Ti-6Al-4V, Nucl. Instrum. Methods Phys. Res. Sect. B Beam Interact. Mater. At. 387 (2016) 63–72. https://doi.org/10.1016/j.nimb.2016.09.010.

[151] F. Hegedüs, R. Brütsch, B. Oliver, P. Marmy, Fracture Toughness and Tensile Properties of the Titanium Alloys Ti6A14V and Ti5A12. 5Sn Before and After Proton and Neutron Irradiations at 150° C, Centre de recherches en physique des plasmas (CRPP), Ecole polytechnique fédérale, 2004. https://crppwww.epfl.ch/pubarchive/2004/LRP2004/lrp_789_04.pdf (accessed August 8, 2013).

[152] T. Ishida, E. Wakai, M. Hagiwara, S. Makimura, M. Tada, D.M. Asner, A. Casella, A. Devaraj, D. Edwards, R. Prabhakaran, D. Senor, M. Hartz, S. Bhadra, A. Fiorentini, M. Cadabeschi, J. Martin, A. Konaka, A. Marino, A. Atherthon, C.J. Densham, M. Fitton, K. Ammigan, P. Hurh, Study of the radiation damage effect on Titanium metastable beta alloy by high intensity proton beam, Nucl. Mater. Energy. 15 (2018) 169–174. https://doi.org/10.1016/j.nme.2018.04.006.

[153] G. Ayrault, Radiation-induced precipitation in single- and dual-ion irradiated Ti-6AI-4V, J. Nucl. Mater. 113 (1983) 1–13. https://doi.org/10.1016/0022-3115(83)90159-9.

[154] T.D. Gulden, I.M. Bernstein, Dislocation loops in irradiated zirconium, Philos. Mag. 14 (1966) 1087–1091. https://doi.org/10.1080/14786436608244779.

[155] D.J. Bacon, A review of computer models of point defects in hcp metals, J. Nucl. Mater. 159 (1988) 176–189. https://doi.org/10.1016/0022-3115(88)90092-X.

[156] R. Perez, H. Nakajima, F. Dyment, Diffusion in α-Ti and Zr, Mater. Trans. 44 (2003) 2–13. https://doi.org/10.2320/matertrans.44.2.

[157] Z. Guo, A.P. Miodownik, N. Saunders, J.-Ph. Schillé, Influence of stacking-fault energy on high temperature creep of alpha titanium alloys, Scr. Mater. 54 (2006) 2175–2178. https://doi.org/10.1016/j.scriptamat.2006.02.036.

[158] W.Z. Han, M.J. Demkowicz, E.G. Fu, Y.Q. Wang, A. Misra, Effect of grain boundary character on sink efficiency, Acta Mater. 60 (2012) 6341–6351. https://doi.org/10.1016/j.actamat.2012.08.009.

[159] O. El-Atwani, J.E. Nathaniel, A.C. Leff, K. Hattar, M.L. Taheri, Direct Observation of Sink-Dependent Defect Evolution in Nanocrystalline Iron under Irradiation, Sci. Rep. 7 (2017) 1836. https://doi.org/10.1038/s41598-017-01744-x.

[160] X.M. Bai, A.F. Voter, R.G. Hoagland, M. Nastasi, B.P. Uberuaga, Efficient Annealing of Radiation Damage Near Grain Boundaries via Interstitial Emission, Science. 327 (2010) 1631–1634. https://doi.org/10.1126/science.1183723.

[161] O. El-Atwani, A. Suslova, T.J. Novakowski, K. Hattar, M. Efe, S.S. Harilal, A. Hassanein, In-situ TEM/heavy ion irradiation on ultrafine-and nanocrystalline-grained tungsten: Effect of 3 MeV Si, Cu and W ions, Mater. Charact. 99 (2015) 68–76. https://doi.org/10.1016/j.matchar.2014.11.013.

[162] L.F. He, M. Gupta, M.A. Kirk, J. Pakarinen, J. Gan, T.R. Allen, In Situ TEM Observation of Dislocation Evolution in Polycrystalline UO2, JOM. 66 (2014) 2553–2561. https://doi.org/10.1007/s11837-014-1186-6.

[163] C. Fizanne-Michel, M. Cornen, P. Castany, I. Péron, T. Gloriant, Determination of hardness and elastic modulus inverse pole figures of a polycrystalline commercially pure titanium by coupling nanoindentation and EBSD techniques, Mater. Sci. Eng. A. 613 (2014) 159–162.

[164] L.Y. Chen, J.C. Huang, C.H. Lin, C.T. Pan, S.Y. Chen, T.L. Yang, D.Y. Lin, H.K. Lin, J.S.C. Jang, Anisotropic response of Ti-6Al-4V alloy fabricated by 3D printing selective laser melting, Mater. Sci. Eng. A. 682 (2017) 389–395. https://doi.org/10.1016/j.msea.2016.11.061.

[165] X. Wang, X. Gong, K. Chou, Scanning Speed Effect on Mechanical Properties of Ti-6Al-4V Alloy Processed by Electron Beam Additive Manufacturing, Procedia Manuf. 1 (2015) 287–295. https://doi.org/10.1016/j.promfg.2015.09.026.

[166] ISO., ISO 14577-4: 2007 Metallic Materials-Instrumented Indentation Tests for Hardness and Materials Parameters, Part 4: Test Methods for Metallic and Non-Metallic Coatings, (2007).

[167] Y. Takayama, R. Kasada, Y. Sakamoto, K. Yabuuchi, A. Kimura, M. Ando, D. Hamaguchi, H. Tanigawa, Nanoindentation hardness and its extrapolation to bulk-equivalent hardness of F82H steels after single- and dual-ion beam irradiation, J. Nucl. Mater. 442 (2013) S23–S27. https://doi.org/10.1016/j.jnucmat.2012.12.033.

[168] J. Silcox, P.B. Hirsch, Dislocation loops in neutron-irradiated copper, Philos. Mag. 4 (1959) 1356–1374. https://doi.org/10.1080/14786435908233371.

[169] S. Tähtinen, P. Moilanen, B.N. Singh, D.J. Edwards, Tensile and fracture toughness properties of unirradiated and neutron irradiated titanium alloys, J. Nucl. Mater. 307 (2002) 416–420.

[170] Y. Idrees, Z. Yao, J. Cui, G.K. Shek, M.R. Daymond, Zirconium hydrides and Fe redistribution in Zr-2.5%Nb alloy under ion irradiation, J. Nucl. Mater. 480 (2016) 332–343. https://doi.org/10.1016/j.jnucmat.2016.08.031.

[171] E.M. Francis, A. Harte, P. Frankel, S.J. Haigh, D. Jädernäs, J. Romero, L. Hallstadius, M. Preuss, Iron redistribution in a zirconium alloy after neutron and proton irradiation studied by energy-dispersive X-ray spectroscopy (EDX) using an aberration-corrected (scanning) transmission electron microscope, J. Nucl. Mater. 454 (2014) 387–397. https://doi.org/10.1016/j.jnucmat.2014.08.034.

[172] S. Das, H. Yu, E. Tarleton, F. Hofmann, Orientation-dependent indentation response of helium-implanted tungsten, Appl. Phys. Lett. 114 (2019) 221905. https://doi.org/10.1063/1.5097403.

[173] V. Kuksenko, S. Roberts, E. Tarleton, The hardness and modulus of polycrystalline beryllium from nano-indentation, Int. J. Plast. 116 (2019) 62–80. https://doi.org/10.1016/j.ijplas.2018.12.008.

[174] S. Panda, S.K. Sahoo, A. Dash, M. Bagwan, G. Kumar, S.C. Mishra, S. Suwas, Orientation dependent mechanical properties of commercially pure (cp) titanium, Mater. Charact. 98 (2014) 93–101. https://doi.org/10.1016/j.matchar.2014.10.011.